Title
Localized States in Driven Dissipative Systems with Time-Periodic Modulation

Author
Gandhi, Punit

Publication Date
2016

Peer reviewed|Thesis/dissertation

Localized States in Driven Dissipative Systems with Time-Periodic Modulation

by

Punit R Gandhi

A dissertation submitted in partial satisfaction of the

requirements for the degree of

Doctor of Philosophy

in

Physics

in the

Graduate Division

of the

University of California, Berkeley

Committee in charge:

Professor Edgar Knobloch, Chair
Professor Jonathan Wurtele
Associate Professor Jon Wilkening

Spring 2016

Localized States in Driven Dissipative Systems with Time-Periodic Modulation

Abstract

Localized States in Driven Dissipative Systems with Time-Periodic Modulation

by

Punit R Gandhi

Doctor of Philosophy in Physics

University of California, Berkeley

Professor Edgar Knobloch, Chair

The generalized Swift–Hohenberg equation is used to study the persistence and decay of localized patterns in the presence of time-periodic parametric forcing in one and two dimensions. A localized state that was stable with constant forcing may begin to breathe under periodic forcing, i.e. grow for part of the forcing cycle via nucleation of new wavelengths of the pattern followed by wavelength annihilation during another part of the cycle. The breathing dynamics occur as the forcing parameter exits the region of stability of the localized pattern on either side and the fronts that define the edges of the state temporarily depin. The parameters of the forcing determine if there will be net growth, a balance, or net decay on average.

A novel resonance phenomenon between the forcing period and the time required to nucleate one wavelength of the pattern outside the pinning region is identified. The resonances generate distinct regions in parameter space characterized by the net number of wavelengths gained or lost in one forcing cycle. Canard trajectories, in which the localized state follows an unstable solution branch for some amount of time before quickly jumping to a stable one, appear near the transitions between each region. In one dimension, the partitioning of the parameter space is well described by an asymptotic theory based on the wavelength nucleation/annihilation time near the boundaries of the region of stability. This theory leads to predictions that are qualitatively correct and, in some cases, provide quantitative agreement with numerical simulations.

The underlying resonance mechanism is a more general phenomenon and is also studied in the context of coupled oscillator systems with a periodically modulated Adler equation as a simple model. A strikingly similar partitioning of the parameter space is observed, with the resonances occurring this time between the period of the frequency modulation and the time for the generation of a phase slip.

To Heather, my partner on this long journey.

Contents

List of Figures

List of Tables

Acknowledgments

I have been fortunate to have wonderful mentors, collaborators, colleagues, friends and family support me through my time in Berkeley. My advisor Edgar Knobloch's passion for science, talent for asking the right questions, and ability to communicate scientific concepts with precision and clarity have been an inspiration to me. I am grateful for his guidance, patience and support during the time we have worked together. Cédric Beaume's combination of enthusiasm and practicality has made our collaboration a great experience. I thank him for his advice, his encouragement and his invaluable guidance in the art of numerics.

Thanks to Jonathan Wurtele for his continued advice and support both while I was his student and afterwards. I would also like to thank both Jonathan and Jon Wilkening for their patience and comments during the preparation of this dissertation.

I am indebted to Hsien-Ching Kao for his patience in helping me with the basics when I was just getting started. Thanks to Claudio Falcón for sharing his take on nonlinear physics with me, for being a gracious host during my visit to Chile, and for allowing me to turn knobs on his experiment. I have benefited from interesting and informative discussions with colleagues Yuval Zelnik, Michael Levy, Jianbo Xie, Benjamin Ponedel, Ari Zitin, and many others. Thanks to the Berkeley Compass Project for providing me a community within the physics department.

Finally, I am grateful to my family. My parents, my wife's parents and our extended family have always been there to share in our joy and provide a helping hand when we were struggling. I am especially grateful for the love of Naya, Nula and Heather that has kept me afloat during my time at Berkeley.

Financial support for this work has come in part by the National Science Foundation under grants DMS-1211953 and CMMI-1233692.

Chapter 1

Introduction

Rhythms are an integral part of our world, as has been documented in the context of biology in Arthur Winfree's book [1]. The time-periodic dynamics associated with these rhythms can be generated internally in oscillatory systems or can be externally imposed by a periodic drive. The dynamics of spatial patterns in the presence of such rhythms is the subject of this dissertation. The focus will be on spatially localized structures that consist of a patch of pattern embedded in some background state and subjected to time-periodic forcing.

1.1 Pattern formation

Patterns emerge in biology, chemistry and physics through a spontaneous or forced breaking of the continuous translation symmetry of the system. The systems of interest are typically dissipative and thus the patterns must be sustained by an external and often spatially uniform forcing. One important mechanism for generating patterns comes from Alan Turing's seminal paper [2] that describes a reaction-diffusion system consisting of two chemical species, an activator and a more quickly diffusing inhibitor. The activator stimulates a local increase in the production rate of both species while the inhibitor suppresses their production rate. Turing's mechanism, a type of *diffusion-driven instability*, relies on the difference in the rate of diffusion between the activator and inhibitor to destabilize a state that would be stable in the absence of diffusion.

In order to understand how a difference in diffusion rates can lead to a linear instability, we take a reaction-diffusion system of the form

$$U_t = D_u \nabla^2 U + f(U, V) \tag{1.1}$$

$$V_t = D_v \nabla^2 V + g(U, V), \tag{1.2}$$

where U and V are concentrations of the activator and inhibitor, respectively. We consider small perturbations $|u|, |v| \ll 1$ about a stationary state (U_0, V_0) consisting of spatially uniform concentrations so that $U = U_0 + u$ and $V = V_0 + v$. The system (1.1)-(1.2) can be

linearized about (U_0, V_0) to give

$$u_t = D_u \nabla^2 u + au - bv \tag{1.3}$$
$$v_t = D_v \nabla^2 v + cu - dv, \tag{1.4}$$

where

$$a = \left.\frac{\partial f}{\partial U}\right|_{(U_0,V_0)}, \quad b = -\left.\frac{\partial f}{\partial V}\right|_{(U_0,V_0)}, \quad c = \left.\frac{\partial g}{\partial U}\right|_{(U_0,V_0)}, \quad d = -\left.\frac{\partial g}{\partial V}\right|_{(U_0,V_0)}, \tag{1.5}$$

are positive coefficients in order for U and V to represent an activator and inhibitor, respectively. We can also define characteristic lengths $l_u = \sqrt{D_u/a}$ and $l_v = \sqrt{D_v/d}$ that give a measure of how far a peak in concentration of the activator and inhibitor will spread because of diffusion. Linear stability analysis shows that we must require $a < d$ and $ad < bc$ in order for (U_0, V_0) to be stable in the absence of diffusion ($D_u = D_v = 0$). When diffusion is present ($D_u, D_v > 0$), the uniform state becomes unstable to a spatially periodic state for $D_v/D_u > d/a > 1$. We can also express the condition in terms of diffusion length scales as $l_v > l_u$, which says that the inhibitor must diffuse farther than the activator in order for the instability to occur. When the uniform state is unstable, the magnitude of the wavenumber associated with the fastest growing mode is given by $k^2 = (l_u^{-2} - l_v^{-2})/2$ and is independent of the domain size.

We can gain some qualitative intuition about Turing's mechanism from the following argument. A localized perturbation that increases the concentration of the activator creates an increase in production of both the activator and inhibitor at that location. The inhibitor diffuses away from the area more quickly than the activator and thus the relative inhibitor concentration becomes high in the region surrounding the initial perturbation. Production of both the activator and inhibitor are therefore suppressed in this surrounding region and the activator becomes depleted there. The inhibitor, on the other hand, is continuously replenished by diffusion from the high concentration area at the location of the initial perturbation. The result is a region with an increased concentration of activator surrounded by a region of depressed activator concentration, and the mechanism is often referred to as local activation and long range inhibition [3]. The inhibitor concentration returns to the level of the uniform state once far enough away from the initial pertubation. This allows the activator concentration to build up again and process can repeat. Thus the uniform state can lose stability to patterns consisting of arrays of this type of structure. We note that care must be taken when applying the above qualitative argument as it may provide incorrect intuition about certain details such as the parameter dependence of the wavelength of the pattern generated from this instability.

While Turing originally proposed this mechanism as an explanation for the patterned growth of embryos during morphogenesis, there is no evidence of a significant difference in diffusion rates for the chemical species in this system or in most other biological contexts. In fact, Turing patterns were only produced in experiments about 40 years after Turing's original paper exactly because of the difficulties associated with engineering a system with sufficiently

different diffusion rates [4, 5]. The importance of Turing's work lies in the surprising result that an instability can arise from diffusion, normally thought to stabilize uniform states. Moreover, modern approaches to pattern formation rely heavily on Turing's idea of studying spatial patterns through linear instabilities of a spatially uniform state (see, e.g., Refs. [6, 7]). In the remainder of this section, we discuss several specific examples of pattern-forming systems.

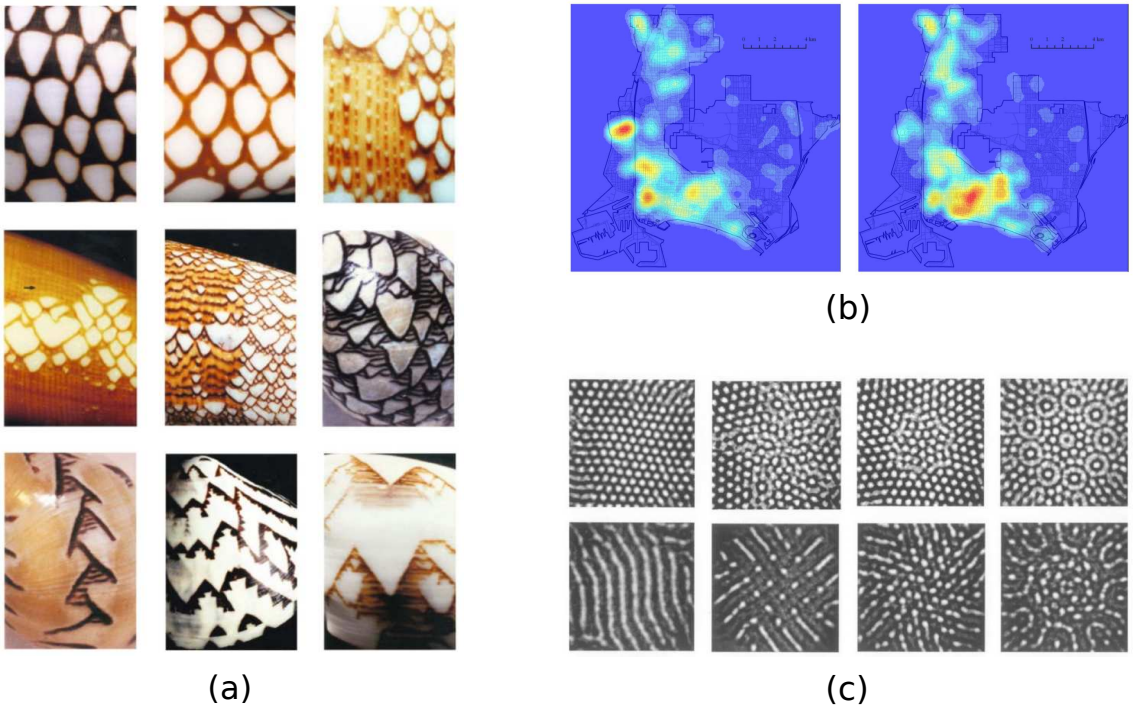

Figure 1.1: (a) Sea shell patterns taken from [8]. (b) Dynamic changes in residential burglary hotspots for two consecutive three-month periods beginning June 2001 in Long Beach, CA taken from [9]. (c) Experimentally observed patterns generated from a LCLV experiment taken from [10].

Population dynamics is concerned with patterns that form through the interactions of independently acting individuals. Agent-based models that rely on a set of simple rules governing the dynamics of a large number of independent agents have been used to successfully reproduce emergent social phenomena. Segregation models [11, 12], for example, have shown that such systems can self-organize spatially into groups with similar characteristics. An agent-based model that reduces to a system of reaction-diffusion equations in a continuum limit has been able to reproduce patterns of hotspots in criminal activity by coupling criminal agents to a field characterizing attractiveness for committing crime [9]. The model is based on empirical evidence that crime is self-excitatory and includes an effective long-range inhibition resulting from an assumed tendency for criminals to move in the

direction of increasing criminal activity. The continuum model does not correspond directly to an activator-inhibitor system, but the patterns form as a result of a difference in diffusion rates. As opposed to chemical systems in biology, it is physically plausible here for the criminal density to diffuse faster than the attractiveness for committing crime. Figure 1.1(b) shows data revealing dynamic hotspots in residential burglary in Long Beach, CA over two consecutive three-month periods.

Sea shells provide a beautiful example of a system that exhibits a remarkable diversity of patterns [8] (Fig. 1.1(a)) and, although there is only limited evidence that these are due to the Turing instability, reaction-diffusion models have been able to reproduce many of the patterns observed on the shells of mollusks. The underlying biological process is not understood completely, but it is thought that the two-dimensional patterns are actually a record of a one-dimensional pattern that evolves in time. The shell is created incrementally as the mollusk secretes material at the leading edge of the shell, laying down one line at a time. Recently, a neural feedback loop has been proposed as a mechanism for creating such patterns [13]. The mollusk reads in the previously generated pattern via sensory cells and uses this as a guide for its output. The model thus uses neural feedback instead of differences in diffusion rates to generate local activation and long range inhibition.

In contrast to the previous two examples, patterns in nonlinear optical media can be created and manipulated in table-top experiments. The pattern-forming mechanism in these types of experiments often relies on the conversion between phase modulation and amplitude modulation of light via nonlinear optical media and feedback. The feedback can be local or nonlocal and can be controlled with high precision. In a liquid crystal light valve (LCLV) experiment, for example, a laser beam passes through a thin layer of nematic crystal. It is reflected back and directed into a light valve to provide optical feedback that modulates the effective nonlinear index of refraction within the liquid crystal layer [14]. The sample patterns shown in Fig. 1.1(c) have been created experimentally in such a LCLV setup by allowing the feedback light to diffract and rotate relative to the incident light. While the mechanism for pattern formation in the LCLV system is fundamentally different from the mechanisms discussed previously, models of the system still predict the emergence of patterned states through linear instabilities of a uniform state.

1.2 Spatially localized patterns

Patterns often extend across the entire domain of the system, but can also be localized to a particular region of space even when the external forcing is uniform and isotropic. Indeed, all the systems mentioned in the previous section have been observed to generate stable localized states. Other commonly cited examples include time-dependent oscillons on vertically vibrated layers of granular material [15] or in photosensitive chemical systems under periodic illumination [16], current filaments in a gas discharge system [17] and localized bursts of neural activity used to encode short term memory [18, 19].

We will consider localized structures that consist of a patch of spatially periodic pattern

embedded in a homogeneous background. The theory behind the origin and properties of such structures is well understood, at least in one spatial dimension. The localized structures of primary interest are stationary and are described in terms of heteroclinic cycles connecting the homogeneous state to the patterned state and back again [20, 21]. Such cycles may be structurally stable, and so persist over an interval of parameter values located within the region of bistability between the homogeneous and spatially periodic states. This pinning region [22, 23] typically contains two or four families of homoclinic solutions connecting the homogeneous state to itself, organized within a "snakes-and-ladders" structure [24, 25]. These correspond to spatially localized states of ever greater length and accumulate on the heteroclinic cycle as their length increases. An excellent review of spatially localization in dissipative systems and its mathematical underpinnings is given in Ref. [26].

Figure 1.2: (a) Sub-Sahelian gapped landscape dominated by the shrub species *Combretum micranthum* G. Don in South-West Niger. Shrub crown radius and bare spots distance are approximately 1.75 m and 50 m (photography: N. Barbier). (b) Patch of *tiger bush* in Niger. Width of vegetated bands: approximately 50 m; width of bare soil bands: approximately 50 m (photography: courtesy of C. Valentin). (c) Example of *fairy circle* in the pro-Namib zone of the west coast of southern Africa (photography: courtesy of J. Vergeer). Figure and caption from R. Lefever [27].

Vegetation growth near the transition to desertification [28, 29, 30, 31, 32] provides an example of spatially localized states that experience time-dependent forcing. Localized structures and patchy patterns of the type shown in Fig. 1.2 have been observed in vegetation growth in semi-arid regions and these patterns experience intermittent fluctuations and periodic variations in growth conditions [33, 34, 35, 36]. The patterns result from the self-organization of individual plants in response to limited resources, e.g. water. It is thought that the underlying cause for the patterns involves positive feedback that allows for local activation and long range inhibition. For example, the presence of plants allows for more local infiltration of surface water into the soil to create local activation. The root system of the plant provides a mechanism for long range inhibition by drawing water away from the surrounding area thus making it less hospitable for other plants. Simple models describe the

system in terms of reaction-diffusion equations for biomass and water where periodic vegetation patterns are created through a Turing instability [37]. The biomass behaves like an activator while the lack of water behaves like an inhibitor. In these models localized patches of vegetation patterns are predicted in regions of bistability between a uniform state (either bare soil or uniform vegetation growth) and the periodic vegetation pattern. The effect of time-periodic precipitation on such localized states has been considered for a particular vegetation model in Ref. [36].

1.3 A model system for localized pattern formation

A "model organism" in the field of biology is useful when it provides insights about particular phenomena or processes that are applicable across a broad range of biological systems [38, 39]. For example, rats are used extensively as models in the study of both neuroscience and medicine while the fruit fly has long served as a model in the study of genetics. This approach allows for the development of highly refined tools and techniques for studying the relatively simple model organisms along with a detailed catalogue of practical knowledge about them. In the study of pattern formation, the Swift–Hohenberg equation (SHE) has taken on a role analogous to a model organism because of its relative simplicity and ability to capture the key features of a broad range of systems. In particular it exhibits a multitude of stable spatially localized patterns when bistability between a trivial state and a periodic state is present. Early studies of the bistable SHE [40, 41] demonstrated the existence of localized states through direct numerical simulation. More recently, Burke and Knobloch have provided a detailed understanding of the properties and dynamics of localized states in this system via a combination of theoretical analysis and numerical continuation [24, 25, 42].

Originally proposed as a model for Raleigh–Bénard convection [43], the SHE takes the form

$$\partial_t u = ru - \left(1 + \nabla^2\right)^2 u + N(u), \tag{1.6}$$

where u is a real field. In convection u represents the vertical velocity at the midplane of a thin layer of fluid that is heated from below, the forcing strength r is proportional to the temperature difference across the fluid, and $N(u)$ is typically a polynomial function of u that depends on the particular details of the system. The most commonly studied nonlinearity, which is also the one most relevant for Raleigh–Bénard convection, is $N(u) = -u^3$. In this context the trivial state $u = 0$ represents the conduction state in which the fluid remains motionless and this state is stable when the temperature difference is not too great ($r < 0$). For $r > 0$, the conduction state becomes unstable to convection in which the flow responsible for heat transport generates an alternating upward and downward velocity at the midplane. The resulting convection may be periodic and is then represented by a stationary spatially periodic solution P of Eq. (1.6) that is generated through a supercritical bifurcation at $r = 0$.

When $N(u)$ has competing nonlinear terms, the periodic state P can bifurcate subcritically and thus generate a region of bistability between P and $u = 0$. Two common choices

that allow for bistability are

$$N_{23}(u) = bu^2 - u^3 \tag{1.7}$$

$$N_{35}(u) = bu^3 - u^5, \tag{1.8}$$

where $b > 0$ is a free parameter. The nonlinearity N_{23} is the lowest order choice that allows for bistability through competing nonlinear terms while N_{35} is useful when considering systems that contain the "up-down" reflection symmetry $(x, u) \to (x, -u)$ present in Raleigh-Bénard convection.

Figure 1.3(a) shows the L^2 norm $\|u\| = \sqrt{\int_{-\Gamma/2}^{\Gamma/2} u^2(x)dx}$ of stationary localized solutions and the L^2 norm per period $\|u_P\| = \sqrt{\Gamma^{-1}\int_{-\Gamma/2}^{\Gamma/2} u_P^2(x)dx}$ of the stationary periodic state P of SHE with the nonlinearity N_{35} and $b = 2$ as a function of the forcing r. The periodic state P emerges subcritically from $u = 0$ and a *snakes-and-ladders* structure of localized states appears within the resulting region of bistability between P and $u = 0$ [42]. In addition to P, four branches $L_{0,\pi/2,\pi,3\pi/2}$ of localized states emerge from $u = 0$ at $r = 0$ [1] and sample solutions along these branches are shown in Fig. 1.3(b). The localized states on L_0 have a maximum at the center of the state and consist of half-integer numbers of wavelengths of the pattern. The branch L_π contains solutions with a minimum at the center and is related to L_0 by the reflection $(x, u) \to (x, -u)$ thus making the two solution branches indistinguishable when plotted in terms of the L^2 norm. The two additional branches $L_{\pi/2,3\pi/2}$ are comprised of antisymmetric states with integer numbers of wavelengths that are related by the same reflection $(x, u) \to (x, -u)$ and thus appear indistinguishable in Fig. 1.3(a) as well.

The four localized solutions branches emerging from $r = 0$ in the case of SHE with nonlinearity N_{35} are initially unstable and consist of solutions that evolve into exponentially localized pulses of the periodic state P as r decreases. The branches then begin to undergo repeated saddle-node bifurcations as they "snake" back and forth within the so-called pinning region (shaded in Fig. 1.3(a)). The saddle-nodes exponentially converge to a pair of values of r from the right that mark the edges of the pinning region and a half-wavelength is added to each side of the localized state for each back-and-forth excursion along the branch. The rungs of the snakes-and-ladders structure are comprised of asymmetric localized states that are created through pitchfork bifurcations.

The snakes-and-ladders structure for SHE with nonlinearity N_{23} is similar but consists of two instead of four intertwined snaking branches. The reflection symmetry $(x, u) \to (x, -u)$ is no longer present for the system and so stationary antisymmetric solutions branches of the form $L_{\pi/2,3\pi/2}$ no longer exist. A full wavelength is now added to each side of a localized state on L_0 and L_π for each back-and-forth excursion which results in states comprised of even and odd integer numbers of wavelengths of P, respectively.

[1] This assumes an infinite spatial domain $\Gamma = \infty$. On a finite domain $\Gamma < \infty$, these states appear through a secondary bifurcation along P. See Ref. [45] for a detailed discussion of this and other finite domain size effects.

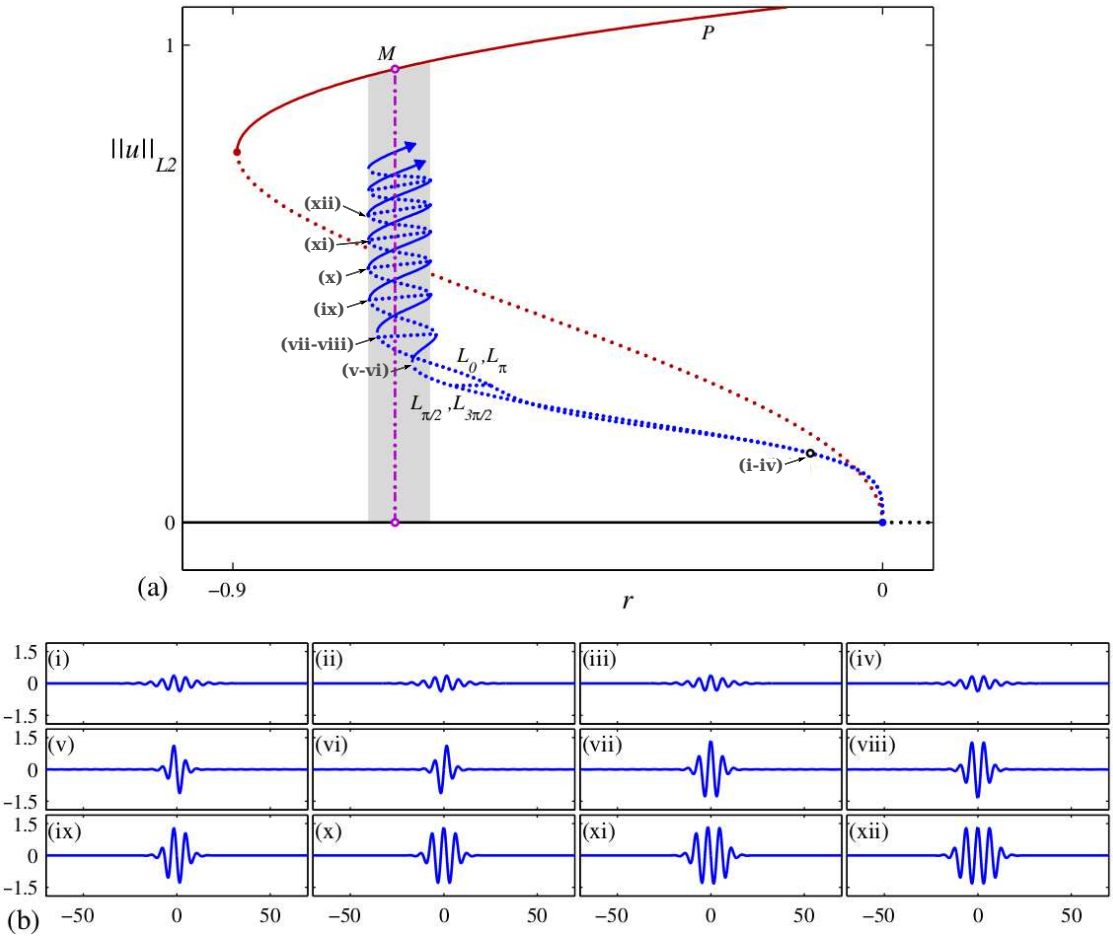

Figure 1.3: (a) Bifurcation diagram showing the snakes-and-ladders structure of localized states in the SHE with cubic-quintic nonlinearity N_{35} and $b = 2$. The localized states are plotted in terms of the L^2 norm while the periodic state P is plotted in terms of the L^2 norm per period. The periodic state P (red) bifurcates subcritically, creating a region of bistability between P and the trivial state $u = 0$ (black). Away from the origin the snaking branches (blue) are contained within the pinning region (shaded) approximately defined by $-0.7126 < r < -0.6267$. This pinning region straddles the Maxwell point M (pink dash-dot line) between P and $u = 0$. Solid (dotted) lines indicate stable (unstable) states. (b) Sample localized states along the snaking branch. First row, from left to right: profiles near onset on $L_{\pi/2}$, $L_{3\pi/2}$, L_0, L_π. Second row, from left to right: profiles at the first saddle-node on $L_{\pi/2}$, $L_{3\pi/2}$, L_0, L_π. Third row, from left to right: profiles at the third saddle nodes on $L_{\pi/2}$ and L_0, and the fifth saddle-nodes on $L_{\pi/2}$ and L_0. Taken from [44].

The SHE can be written in terms of a Lyapunov functional $\mathcal{F}[u]$, referred to as the *free*

energy,

$$u_t = -\frac{\delta \mathcal{F}[u]}{\delta u}, \qquad \mathcal{F}[u] = \frac{1}{\Gamma}\int_{-\Gamma/2}^{\Gamma/2} -\frac{1}{2}ru^2 + \frac{1}{2}\left[(1+\partial_x^2)u\right]^2 - V(u)\,dx, \tag{1.9}$$

where the function $V(u)$ is defined by $N = dV/du$. A straightforward calculation shows that

$$\frac{dF}{dt} = -\left(u_t\right)^2 \leq 0. \tag{1.10}$$

Thus, on a domain of finite spatial period all initial conditions approach a stationary state corresponding to a local minimum of the free energy. On an infinite domain, steadily moving front solutions are also possible. The free energy provides intuition about the existence and behavior of localized states in SHE: stable (unstable) solutions correspond to local minima (maxima) of $\mathcal{F}$. When the periodic state P bifurcates subcritically there exists a *Maxwell point* (pink dash-dot line in Fig. 1.3) at which the free energy of P matches the free energy of $u = 0$. At this point one expects coexistence of the two states based on energy arguments: a front separating the two states remains stationary since converting a part of the system from one state to the other will not lower the free energy. Near the Maxwell point, the front continues to remain stationary even though one of the two states is energetically favored. This is because the spatial structure of P generates an effective pinning potential that prevents the front from moving so as to lower the free energy [22]. This self-generated pinning potential allows localized states that are flanked by a pair of fronts to remain stationary over a finite parameter range. The difference in free energy between P and $u = 0$ generates a tilt in the effective pinning potential which results in depinning of the fronts when the system is far enough away from the Maxwell point. While the above argument relies on the gradient structure (Eq. (1.9)) of SHE, the snakes-and-ladders structure persists under perturbations to SHE that break the gradient structure [46]. A more detailed discussion of the applicability of SHE and related open questions can be found in Ref. [47].

While SHE was originally studied in connection with convection, the appearance of a snakes-and-ladders structure of localized states in a number of physical pattern-forming systems has breathed new life into the equation. It has become a model of choice for examining the properties and dynamics of spatially localized states and many consider it a kind of "normal form" or simplest description of this phenomenon.

1.4 Outline

Chapter 2 provides an overview of some underlying mathematical concepts along with references where more detail can be found. Chapter 3 describes the resonance phenomenon that is the main result of the thesis in the context of a simple ODE system with application to coupled oscillator systems [48]. The basic approach is then carried over to the study of spatially localized states in the one-dimensional quadratic-cubic SHE with time-periodic forcing

in Ch. 4 [49, 50, 51]. Chapter 5 describes ongoing progress toward extending the results of Ch. 4 to two-dimensional localized stripe patterns in SHE with cubic-quintic nonlinearity. The concluding chapter (Ch. 6) provides a summary along with an outlook for future work and potential applications. We also provide an appendix (App. A) describing the numerical methods that have been used in this dissertation.

Chapter 2

Background

Partial differential equations (PDEs) such as reaction-diffusion systems and the simpler Swift–Hohenberg equation (SHE) are often used to model the formation of spatial patterns that evolve in time. Many techniques for studying PDEs involve reducing the system to a set of ordinary differential equations (ODEs). Moreover, because the systems of interest are dissipative, the long-time dynamics approach attractors that form smaller and sometimes finite-dimensional subsets of the phase space. The two types of attractors of main interest to this dissertation are fixed points and periodic orbits. Fixed points are stationary solutions and can be studied by restricting the original system to the time-independent case thereby reducing PDEs in one spatial dimension to ODEs. This chapter reviews basic concepts from dynamical systems and bifurcation theory that provide a foundation for the results described in this dissertation. More detailed discussion of relevant topics can be found in, for example, Refs. [52, 53, 54, 55, 56].

2.1 Dynamical systems theory

We take a finite-dimensional *dynamical system* to be a set of n first-order ODEs of the form

$$\dot{\mathbf{u}} = f(\mathbf{u}, t; \boldsymbol{\mu}), \tag{2.1}$$

where $\mathbf{u} \in \mathbb{R}^n$ is a vector in the phase space that describes the state of the system, $\boldsymbol{\mu} \in \mathbb{R}^p$ is a set of p parameters that are fixed in time, and the dot represents derivative with respect to t. When the function $f : \mathbb{R}^n \times \mathbb{R} \times \mathbb{R}^p \to \mathbb{R}^n$ has no explicit time dependence, i.e. $f(\mathbf{u}, t; \boldsymbol{\mu}) = f(\mathbf{u}; \boldsymbol{\mu})$, we call the system *autonomous*. The nonautonomous case can be reduced to autonomous by extending the phase space to include t as a dynamical variable and reparametrizing the system in terms of a new dependent variable. Explicitly, we can extend Eq. (2.1) by defining $u_{n+1} = t$ and $\dot{t} = 1$, where the dot now represents derivative with respect to the new independent variable. We thus restrict the discussion that follows to the autonomous case unless otherwise noted. We shall see that it is sometimes useful to keep the time dependence explicit or even to think of the system as having a time-dependent parameter.

Trajectories $\mathbf{u}(t, \mathbf{u}_0)$ that solve Eq. (2.1) with the initial condition $\mathbf{u}(t_0) = \mathbf{u}_0$ can rarely be determined analytically for general nonlinear systems. Studying the properties of *fixed points* of the dynamical system where $\dot{\mathbf{u}}_{fp} = 0$, however, can provide quite a bit of information about the system's overall behavior. In particular, the dynamics near the fixed point can be described by linearizing about the fixed point to get

$$\dot{\mathbf{v}} = Df|_{fp}\mathbf{v} + \mathcal{O}(||\mathbf{v}||^2), \tag{2.2}$$

where $\mathbf{v} = \mathbf{u} - \mathbf{u}_{fp}$ is assumed to be small and $Df|_{fp}$ is the Jacobian

$$Df_{ij} = \frac{\partial f_i}{\partial u_j} \tag{2.3}$$

evaluated at the fixed point $\mathbf{u}_{fp}$. Truncated Eq. (2.2) is linear and the solution can be expressed in terms of eigenvalues λ_i and eigenvectors $\mathbf{w}_i$ of Df as

$$\mathbf{v}(t) = \sum_{i=1}^{n} \alpha_i \mathbf{w}_i e^{\lambda_i t}, \tag{2.4}$$

where the coefficients α_i are determined by the initial condition $\mathbf{v}(t_0) = \mathbf{u}_0 - \mathbf{u}_{fp}$. Because we assume f is a real-valued function, the eigenvalues come in complex conjugate pairs $(\lambda, \bar{\lambda})$ when not pure real. For *hyperbolic* fixed points in which $Re(\lambda_i) \neq 0$, the eigenvalues of Df_{fp} determine the types of dynamics near the fixed points and the time scales on which they occur. Indeed, the Hartman–Grobman theorem guarantees that the dynamical system behaves qualitatively the same as its linearization about a hyperbolic fixed point in a small neighborhood around this fixed point. Perturbations from the fixed point *decay* along stable directions with $Re(\lambda_i) < 0$ and the eigenspace spanned by the associated $\mathbf{w}_i$ is tangent to the stable invariant manifold $W^s(\mathbf{u}_{fp})$ comprised of all initial conditions $\mathbf{u}_0$ in the phase space that approach $\mathbf{u}_{fp}$ as $t \to +\infty$. Likewise, perturbations from the fixed point *grow* along *unstable* directions with $Re(\lambda_i) > 0$ and the eigenspace spanned by the associated $\mathbf{w}_i$ is tangent to the *unstable* invariant manifold $W^u(\mathbf{u}_{fp})$ comprised of all initial conditions $\mathbf{u}_0$ that approach $\mathbf{u}_{fp}$ as $t \to -\infty$. For nonhyperbolic fixed points, the remaining eigenspace spanned by eigenvectors with $Re(\lambda_i = 0)$ is tangent to the center invariant manifold $W^c(\mathbf{u}_{fp})$ which is discussed in Sec. 2.2.

A major focus of this dissertation is time-periodic dynamics. A *periodic orbit* of Eq. (2.1) is a solution that satisfies

$$\mathbf{u}_{po}(t + T) = \mathbf{u}_{po}(t) \tag{2.5}$$

for some period T. Just as with fixed points, linearizing about the orbit provides useful information such as the stability of the orbit. Defining $\mathbf{v} = \mathbf{u} - \mathbf{u}_{po}$ and assuming $||\mathbf{v}|| \ll 1$ gives

$$\dot{\mathbf{v}} = Df|_{po}(t)\mathbf{v} + \mathcal{O}(||\mathbf{v}||^2), \tag{2.6}$$

where $Df|_{po}(t)$ is the Jacobian evaluated along the periodic orbit and is thus T-periodic. Floquet's theoreom states that the solution to a linear system

$$\dot{\mathbf{v}} = A(t)\mathbf{v}, \tag{2.7}$$

where A is T-periodic can be written in the form

$$\mathbf{v}(t) = \sum_{j=1}^{n} \alpha_j e^{\sigma_j t}\mathbf{p}_j(t), \tag{2.8}$$

where $\mathbf{p}_j(t) = \mathbf{p}_j(t+T)$ is a periodic function, σ_j are known as the Floquet exponents, and α_j are constants determined from the initial condition. One can use the T-period map $\mathbf{v}_k = \mathbf{v}(kT)$ given by

$$\mathbf{v}_k = \sum_{j=1}^{n} \alpha_j \rho_j^k \mathbf{p}_j(T), \tag{2.9}$$

where $\rho_j = e^{\sigma_j T}$ are called the Floquet multipliers, to determine stability of the orbit $\mathbf{u}_{po}$. If $|\rho_j| < 1$ ($|\rho_j| > 1$), then the $\mathbf{u}_{po}$ is stable (unstable) to perturbations along the $\mathbf{p}_j(T)$ direction. A periodic orbit always has at least one marginal Floquet multiplier ($\rho = 1$) associated with perturbations along the trajectory. One other useful result from Floquet theory gives an expression for the product of the Floquet multipliers:

$$\prod_{j=1}^{n} \rho_j = \exp\left(\int_0^T \mathrm{tr}(A(s))ds\right), \tag{2.10}$$

or, equivalently, for the sum of the Floquet exponents:

$$\sum_{j=1}^{n} \sigma_j = \int_0^T \mathrm{tr}(A(s))ds. \tag{2.11}$$

2.2 Bifurcation theory

We have, up to now, discussed properties of the dynamics of a system given a particular set of parameter values. In many applications, however, we are interested in how the dynamics depend on parameters that correspond to experimental controls or environmental factors. It is often the case that, over most of the parameter space, fixed points of a dynamical system are *structurally stable* and thus small changes in parameters do not cause qualitative changes in the dynamics nearby. *Bifurcation theory* is interested in the complementary, and usually lower-dimensional, set in parameter space where small perturbations can produce radically different dynamics (see Ref. [57] for an introduction). Because the dynamics are qualitatively the same everywhere except when crossing this set of bifurcation points, understanding the

behavior nearby allows one to qualitatively map out the possible dynamics as a function of parameters.

Local bifurcations are completely captured by local analysis in the neighborhood of a fixed point while *global bifurcations* describe qualitative nonlocal changes in dynamics. A bifurcation point is often classified in terms of its *codimension* which, in practice, is defined as the minimum number of parameters that must be independently varied for the bifurcation to occur. Bifurcations of lower codimension are encountered more frequently, and many common codimension-one bifurcations can be described by one-dimensional systems. Moreover one can classify local bifurcations of general dynamical systems in terms of their simplest description within a small neighborhood of the fixed point undergoing a change. One can obtain a simplest description of the dynamics at a bifurcation point by (1) lowering the dimensionality through center manifold reduction and (2) reducing the number of nonlinear terms using a normal form transformation. These methods, described below, are typically applied at a bifurcation point in the parameter space and the behavior of the system for nearby parameter values is captured through a process known as unfolding.

Because hyperbolic fixed points are structurally stable, a local bifurcation must occur when the linearized system has eigenvalues with zero real part. *Center manifold reduction* leverages the associated separation of time scales to create a lower-dimensional description that faithfully reproduces the behavior of the full system. In particular, if we assume that a fixed point has no unstable eigenvalues so that $W^u = \emptyset$, then initial values in the neighborhood of the fixed point quickly evolve toward the center invariant manifold W^c where the dynamics takes place on a slower time scale. The center manifold theorem guarantees the reduced dynamics of the system restricted to the center manifold determines the dynamics of the full system in a small neighborhood of the fixed point as $t \to \infty$. The construction of the center manifold is a straightforward procedure that relies on parametrizing W^c in the full phase space in terms of vectors in the tangent space of W^c at the fixed point. As noted before, the tangent space of W^c at the fixed point is spanned by eigenvectors of the linearization of the system about the fixed point that have eigenvalues with zero real part.

After lowering the dimension of the description by restriction to the center manifold, one can often simplify the description further by transforming the system restricted to the center manifold into coordinates that remove as many nonlinear terms as possible. The resulting *normal form*, though not unique, is quite useful for studying and classifying bifurcations. The standard procedure involves computing the required nonlinear transformation order by order by solving a sequence of linear problems that are determined by the linearization of the system about the fixed point. While the normal form transformation formally preserves the dynamics of the system a truncation of the transformation at some order, which is what is computed in practice, may not. Also, the normal form transformation does not provide useful simplification for systems with $\dim(W^c) = 1$.

The simplified description of the original system at the bifurcation point that results from center manifold reduction and a normal form transformation must now undergo the process of *unfolding* in order to study the behavior of the system for nearby parameter values. The simplified system must be embedded in a family of systems with the number

of parameters equal to the codimension of the bifurcation. This can be done in practice by including additional linear and nonlinear terms in the system and defining their coefficients μ_j as dynamical variables with trivial evolution $\dot{\mu}_j = 0$. The process described here is not systematic and can rely on knowledge about the system, such as the existence of a trivial solution for all parameter values, to guide the choice of additional terms. Moreover, because it is based on a truncated normal form, it can be important to consider the effects of higher order terms once the dynamics of the unfolded bifurcation have been analyzed at a given order. We are now ready to review the normal forms of some common codimension-one bifurcations that appear throughout this dissertation.

Saddle-node bifurcation

The normal form of the *saddle-node bifurcation* is

$$\dot{u} = \mu \pm u^2, \tag{2.12}$$

which has fixed points when $u^2 = \mp\mu$. Taking the '$-$' case of the normal form Eq. (2.12),

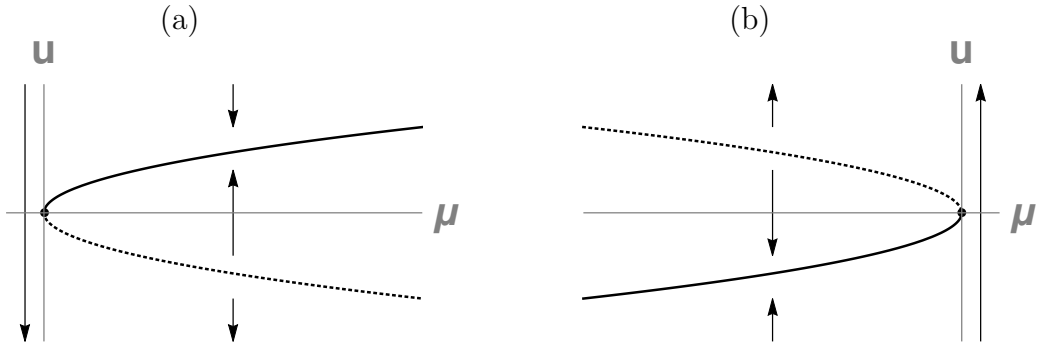

Figure 2.1: Bifurcation diagram for the saddle-node bifurcation described by (a) the '$-$' and (b) the '$+$' case of Eq. (2.12). Solid lines indicate stable steady state solutions while dotted lines indicate unstable steady state solutions.

we see that there are no fixed points for $\mu < 0$ and two fixed points $u_\pm = \pm\sqrt{\mu}$ for $\mu > 0$. Linearizing about the fixed points gives

$$\dot{v} = \mp 2u_\pm v, \tag{2.13}$$

and thus u_+ is stable while u_- is unstable. The bifurcation occurs at $\mu = 0$ when u_+ and u_- coincide as a single fixed point with a zero eigenvalue. We will find it useful to take the interpretation that the branch of fixed points defined by the curve $u^2 = \mu$ changes stability as it folds over at the bifurcation point. The '$+$' case behaves similarly and bifurcation diagrams for both cases are shown in Fig. 2.1. This is the generic codimension-one bifurcation.

Transcritical bifurcation

The *transcritical bifurcation* is given by the normal form

$$\dot{u} = \mu u \pm u^2. \tag{2.14}$$

Here $u = 0$ is a fixed point of the system for any value of μ and a second fixed point is given by $u = \mp\mu$. Linearization about the origin $u = 0$ gives $\dot{v} = \mu v$ while linearization

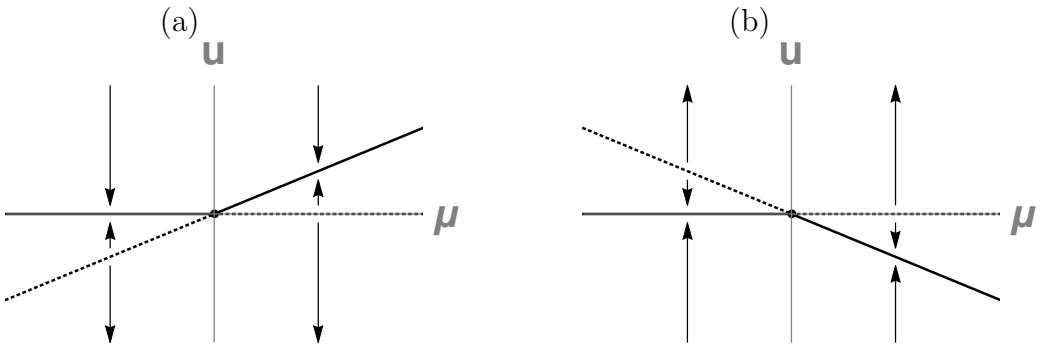

Figure 2.2: Bifurcation diagram for the transcritical bifurcation described by (a) the '−' and (b) the '+' case of Eq. (2.14). Solid lines indicate stable steady state solutions while dotted lines indicate unstable steady state solutions.

about $u = \mp\mu$ gives $\dot{v} = -\mu v$. There is therefore an exchange of stability between the two fixed points at the bifurcation at $\mu = 0$ where the two solution branches cross (Fig. 2.2). This bifurcation is codimension-one in systems that are required to maintain $u = 0$ as a fixed point, but is a codimension-two bifurcation generally. The introduction of a constant additive perturbation breaks the solution branches into either a pair of curves of fixed points with no bifurcation present or a pair of saddle-node bifurcations.

Pitchfork bifurcation

The *pitchfork bifurcation*, described by the normal form

$$\dot{u} = \mu u \pm u^3, \tag{2.15}$$

is codimension-one in, for example, systems that possesses the reflection symmetry $u \to -u$. Linearization about $u = 0$ gives $\dot{v} = \mu v$, and thus $u = 0$ is stable for $\mu < 0$ and unstable for $\mu > 0$. In the '−' case, known as *supercritical*, two additional stable branches of fixed points $u = \pm\sqrt{\mu}$ exist for $\mu > 0$ where $u = 0$ is unstable. In the *subcritical* pitchfork bifurcation described by Eq. (2.15) with a '+' the two solution branches $u = \pm\sqrt{-\mu}$ emerge from the bifurcation point into $\mu < 0$ and are unstable. These states coexist with the stable $u = 0$ solution. Bifurcation diagrams for the pitchfork bifurcation are shown in Fig. 2.3. A

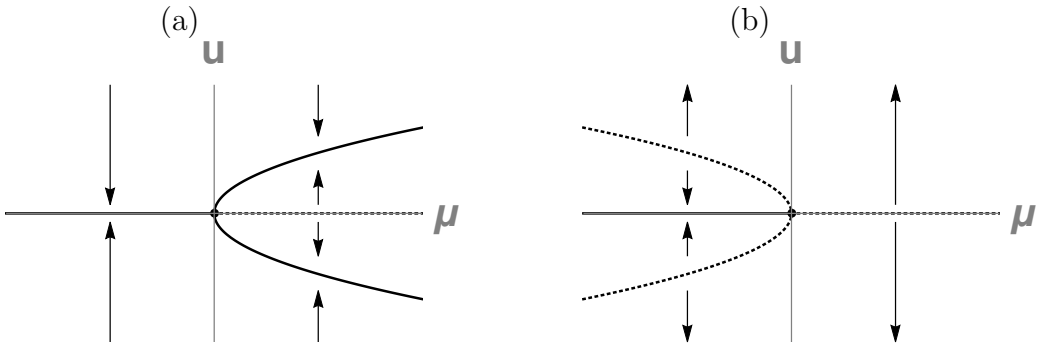

Figure 2.3: Bifurcation diagram for the pitchfork bifurcation described by (a) the '−' (supercritical) and (b) the '+' (subcritical) case of Eq. (2.15). Solid lines indicate stable steady state solutions while dotted lines indicate unstable steady state solutions.

constant perturbation breaks the pitchfork bifurcation into curves of fixed points and saddle-node bifurcations. This is actually a codimension-three bifurcation in general systems not constrained by any symmetry and can also break up into a transcritical bifurcation and saddle-node bifurcation under a quadratic perturbation.

Hopf bifurcation

The previous examples were all steady state bifurcations describing the creation, annihilation, and change of stability of fixed points. We now turn to the *Hopf bifurcation* (or Poincaré–Andronov–Hopf bifurcation), where a periodic orbit is born from a fixed point. This is the generic codimension-one oscillatory bifurcation in which a pair of complex conjugate eigenvalues crosses the imaginary axis transversally. The normal form is given in terms of the complex variable z by

$$\dot{z} = (\mu + i(\omega + a\mu))\, z \pm (1 + ib)|z|^2 z, \tag{2.16}$$

where μ is the bifurcation parameter as usual and $\omega, a, b \in \mathbb{R}$. For $\mu < 0$ the origin is a stable fixed point. At $\mu = 0$ the eigenvalues of the fixed point are pure imaginary $\lambda = \pm i\omega$. For $\mu > 0$ the eigenvalues begin to develop a positive real part and origin becomes unstable. For the case corresponding to '−' in Eq. (2.16) the periodic orbit emerges *supercritically* as a stable orbit coexisting with the unstable fixed point for $\mu > 0$. The '+' case, on the other hand, is a *subcritical* Hopf bifurcation in which the periodic orbit is unstable and coexists with the stable periodic orbit for $\mu < 0$. Example flows along with a bifurcation diagram for each case are shown in Fig. 2.4.

SNIPER bifurcation

As a final example, we discuss a second way in which periodic orbits are born that is relevant for synchronization in systems of coupled oscillators. The *SNIPER bifurcation* (saddle-

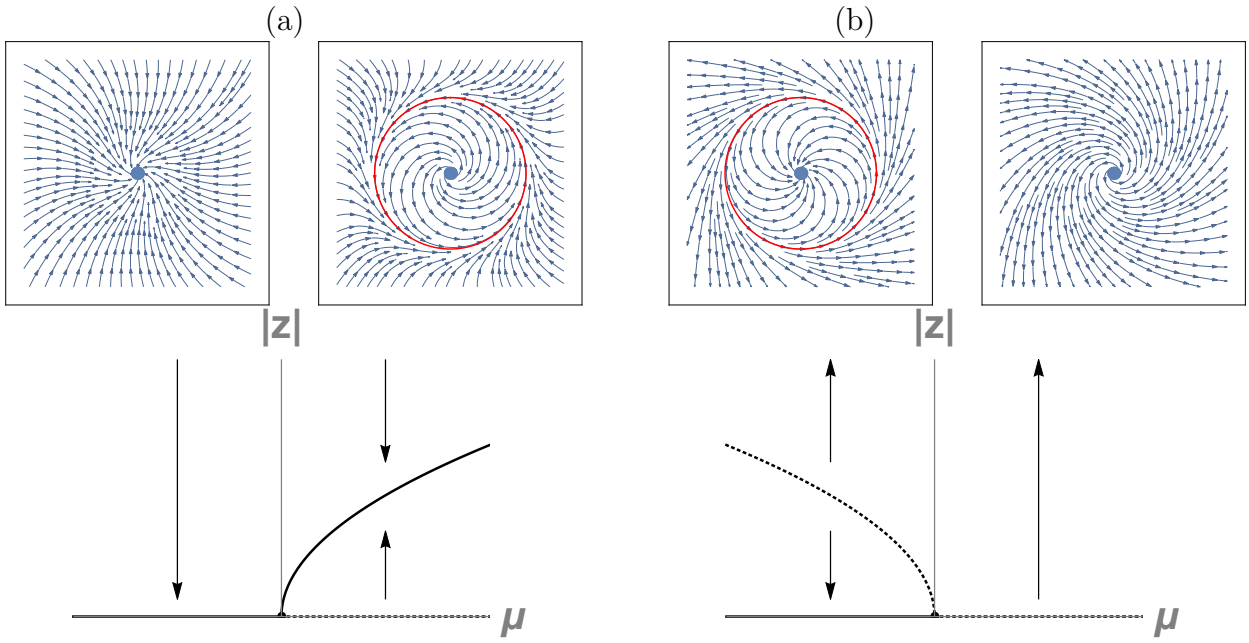

Figure 2.4: bifurcation diagrams and the flow field of the Hopf bifurcation described by (a) the '−' (supercritcal) and (b) the '+' (subcritical) case of Eq. (2.16) with $\omega = 1$, $a = 0.5$ and $b = 0.5$. For each case sample trajectories in the $(Re(z),Im(z))$ plane are shown in the top panel for $\mu = -1$ (left) and $\mu = 1$ (right). A dot marks the location of the fixed point at $z = 0$ and a red line indicates the trajectory of the periodic orbit when it exists. A representation of the bifurcation diagram in $|z|$ where the periodic orbit appears as a fixed point is also included for each case in the bottom panel. Here solid (dotted) lines indicate stable (unstable) fixed points or periodic orbits.

node infinite-period bifurcation), sometimes called SNIC (saddle-node on an invariant circle) bifurcation, is often described in polar coordinates [58] by

$$\dot{r} = r(1 - r^2) \tag{2.17}$$

$$\dot{\theta} = \mu - r\cos\theta. \tag{2.18}$$

The radial equation (2.17) has an unstable fixed point at the origin and a stable one at $r = 1$, and so the system always approaches the invariant circle $r = 1$. At $r = 1$, we can reduce the system to $\dot{\theta} = \mu - \cos\theta$. We find one stable fixed point and one unstable fixed point for θ satisfying $\mu = \cos\theta$ as long as $-1 < \mu < 1$. The bifurcation occurs at $\mu = 1$ and at $\mu = -1$ where a periodic orbit is created as the two fixed points annihilate locally along $r = 1$ in a saddle-node bifurcation. The trajectory follows the periodic orbit in the positive θ direction for $\mu > 1$ and the negative θ direction for $\mu < -1$. Figure 2.5 illustrates the bifurcation at $\mu = 1$ through phase portraits for different values of μ.

Unlike the previous examples which are purely local bifurcations of fixed points, the

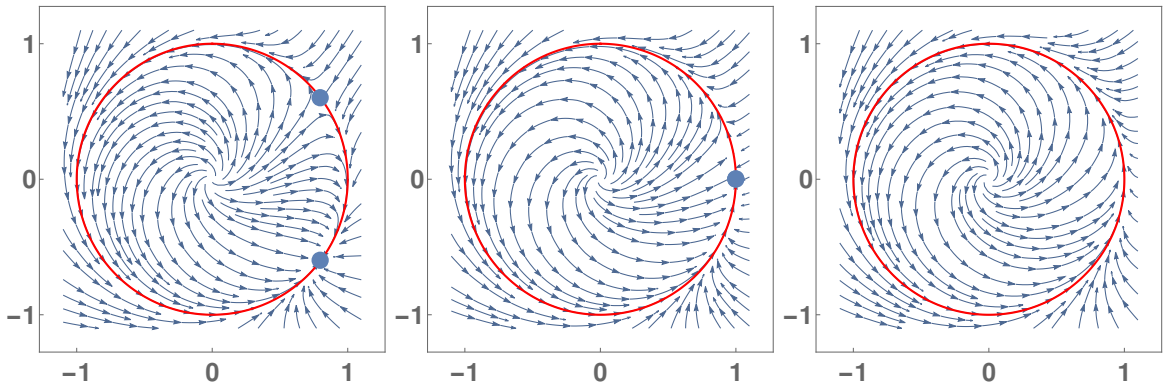

Figure 2.5: Phase portraits for Eqns. (2.17)-(2.18) with $\mu = 0.8$, 1.0 and 1.2. A SNIPER bifurcation occurs on the invariant circle $r = 1$ (shown in red) at $\mu = 1$ when the stable and unstable fixed points (blue dots) collide and a periodic orbit is created.

SNIPER bifurcation additionally has a global organization of the center-stable and center-unstable manifolds that is responsible for creating a periodic orbit. Local analysis of the saddle-node point of the system cannot distinguish the SNIPER bifurcation from a saddle-node bifurcation and many thus refer to the SNIPER as a global bifurcation [56]. The period of the orbit diverges like $(|\mu| - 1)^{-1/2}$ as $|\mu|$ decreases toward the bifurcation point, a very general feature of the scaling of characteristic times of dynamics near a saddle-node. This is in contrast to the logarithmic divergence of the period in truly global bifurcations that generate a periodic orbit such as a *homoclinic bifurcation* which occurs when an already existing saddle collides with a periodic orbit. In contrast to the SNIPER bifurcation, local analysis cannot even detect the occurrence of a homoclinic bifurcation.

The scaling of the period of the orbit created through a SNIPER bifurcation can be computed by directly integrating Eq. (2.18) at $r = 1$, but a more intuitive argument relies on the fact that the presence of the saddle-node is still "felt" after the fixed points collide. An eigenvalue of the system crosses zero at the bifurcation, and will thus be small nearby. This results in a slowing down of the dynamics near the point in phase space where the saddle point used to be. The *ghost* or saddle-node remnant acts as a bottleneck for the dynamics along the orbit and a majority of the time in the period is spent near this point.

As a side note, while the SNIPER bifurcation is a codimension-one, the slightly modified system

$$\dot{r} = r(\epsilon - r^2) \tag{2.19}$$

$$\dot{\theta} = \mu - r\cos\theta \tag{2.20}$$

generates a codimension-two bifurcation at $\epsilon = 0$ and $\mu = 0$ where the creation of the periodic orbit can be detected through local analysis.

2.3 Spatial dynamics

When considering stationary solutions to a PDE system on the real line, it is often useful to study the corresponding time-independent system where all time derivatives are set to zero. This restriction results in a set of ODEs that describes the *spatial dynamics* of the system. In this approach the position coordinate x is interpreted as a time-like independent variable of the dynamical system satisfied by time-independent solutions of the PDE system. Fixed points of the dynamical system correspond to stationary homogeneous solutions to the PDE system and periodic orbits describe stationary spatially periodic patterns. Stationary fronts are, in terms of spatial dynamics, heteroclinic trajectories that approach two different equilibria as $x \to \pm\infty$. Localized states can be thought of as homoclinic orbits that evolve away from an equilibrium as x increases from $-\infty$ before returning to it as $x \to \infty$. These localized states may approach the neighborhood of a second equilibrium in phase space and thus form approximate heteroclinic cycles consisting of two heteroclinic trajectories to and from the equilibria. In this case, the edges of the localized state correspond to fronts that connect one equilibrium state to another [22].

The issue with extending this approach to two or more spatial dimensions is that the equations describing the stationary solutions no longer reduce to a set of ODEs. The spatial dynamics interpretation thus requires accommodating multiple time-like variables. Moreover, the time-independent equations tend to be elliptic and there can be issues of ill-posedness as an initial value problem. Despite this, the spatial dynamics picture has provided useful insight for two-dimensional patterns in SHE [59].

Reversible dynamical systems and the Hamiltonian–Hopf bifurcation

A dynamical system (2.1) is said to be *reversible* if it is equivariant under the transformation $(t, u) \to (-t, \mathcal{R}u)$ where $\mathcal{R}^2 = id$ is called an *involution* [60, 61]. Intuitively, this describes systems where the backwards-time dynamics can be expressed in terms of the forwards-time dynamics. The simplest case of $\mathcal{R} = id$ describes a system that evolves the same forwards in time as it does backwards in time. Pattern-forming systems are often symmetric under spatial reflections $\mathcal{R}$ of the form $(x, \mathbf{u}) \to (-x, \mathcal{R}\mathbf{u})$, where $\mathcal{R}^2 = id$, and thus the dynamical system that describes their time-independent spatial trajectories is reversible. The SHE provides an example of one such system with reversible spatial dynamics, but because of its gradient structure (Eq. 1.9), the spatial dynamics are additionally Hamiltonian.

Reversibility constrains the possible configuration of the eigenvalues of fixed points invariant under the reflection $\mathcal{R}$. If λ is an eigenvalue of a fixed point in fix$\mathcal{R}$, then so is $-\lambda$. Moreover, if λ is complex then $\bar{\lambda}$ is also an eigenvalue since f is assumed to be a real-valued function. The characteristic polynomial that determines the spatial eigenvalues of the system can therefore be written as a function of λ^2 and the simplest nontrivial case is a

four-dimensional system with eigenvalues given by

$$\lambda^4 - b\lambda^2 + a = 0, \tag{2.21}$$

where a and b are real parameters. The nonzero eigenvalues of a fixed point satisfying $\mathbf{u}_{fp} = \mathcal{R}\mathbf{u}_{fp}$ come as either: (1) a quartet of complex eigenvalues, (2) two pairs of real eigenvalues, (3) a pair of real eigenvalues and a pair of imaginary eigenvalues or (4) two pairs of imaginary eigenvalues. The possible configurations of eigenvalues are mapped out as a function of a and b in Fig. 2.6 [62]. Along the curve $C_2 \cup C_3$ defined by $a = b^2/4$, there

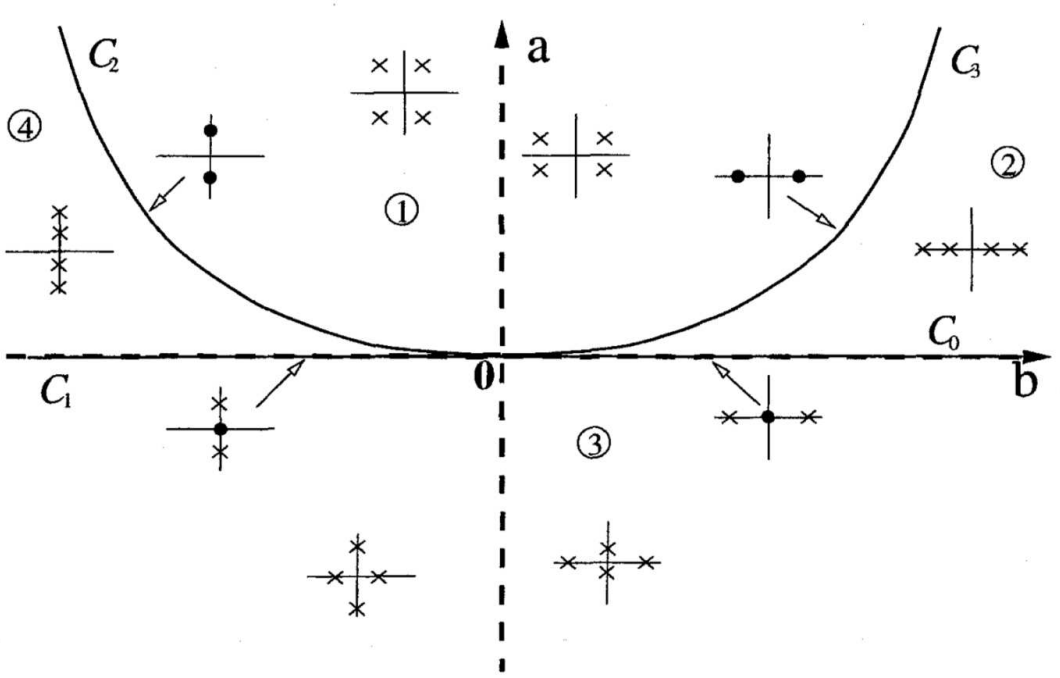

Figure 2.6: A map of the roots of $\lambda^4 - b\lambda^2 + a = 0$ in the (a, b) plane that correspond to the eigenvalues of a fixed point of a four-dimensional, reversible dynamical system. Four regions with distinct types of behavior are labeled and sample configurations of the roots in the complex plane are depicted throughout the parameter space. A Hamiltonian–Hopf bifurcation occurs along the curve C_2 defined by $b = -\sqrt{a}/2$. Taken from [62].

are two nonzero eignevalues $\lambda = \pm\sqrt{b/2}$ each with multiplicity two. During the transition through C_2 depicted in Fig. 2.7 where a complex quartet of eigenvalues collides pairwise at the imaginary axis and remain their afterwards (Fig. 2.7). This is known as a *Hamiltonian–Hopf bifurcation* (or reversible 1:1 resonance) which has been studied in detail in Refs. [63, 64, 21].

The Hamiltonian–Hopf bifurcation is an important mechanism for generating time-independent spatially periodic patterns in systems with reflection symmetry. The standard Hopf bifurcation occurs when a complex conjugate pair of eigenvalues $\lambda, \bar{\lambda}$ of a fixed point cross the

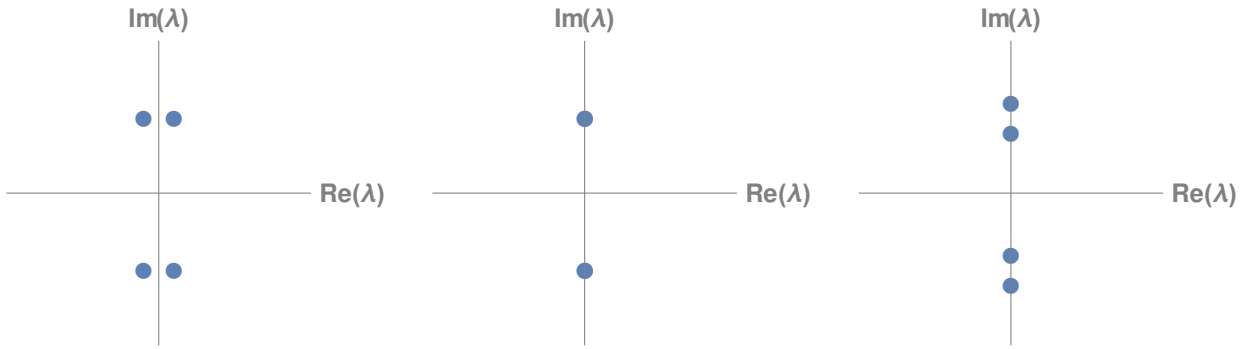

Figure 2.7: Eigenvalues of a system undergoing a Hamiltonian–Hopf bifurcation. The center panel indicates the bifurcation point at which periodic orbits are generated at the origin.

imaginary axis. In reversible systems, this pair becomes a quartet where $\pm\lambda$ and $\pm\bar{\lambda}$ each collide at the imaginary axis to become a pair of roots with multiplicity two. We can identify this bifurcation in SHE (1.6) by considering the dispersion relation that arises from its linearization about $u = 0$:

$$\sigma = r - (1 - k^2)^2, \tag{2.22}$$

where σ is the linear growth rate in time, k is the spatial wavenumber and the solution takes the form $u = A\exp(\sigma t + ikx) + c.c.$ for some amplitude $A \in \mathbb{C}$. The spatial eigenvalues of this time-independent state are determined from the marginal stability curve defined by $\sigma = 0$ and this maps onto a line in the (a, b) plane of Eq. (2.21) defined by $b = 2$ and $a = 1 + r$. The marginal equation (Eq. (2.22) with $\sigma = 0$) is solved by the four wavenumbers $k = \pm\sqrt{1 \pm \sqrt{r}}$ which form two pairs of real roots for k (corresponding to pure imaginary eigenvalues) when $r > 0$ and represent the wavenumbers of perturbations that are marginally stable in time. The eigenvalues collide pairwise at the imaginary axis at $r = 0$ to create a pair of double roots $k = \pm 1$ in a $1 : 1$ spatial resonance. For $r < 0$ the spatial eigenvalues have nonzero real part which is a prerequisite for the existence of fronts that connect to $u = 0$.

Homoclinic orbits and the heteroclinic tangle

The linear theory described above sets the stage for the study of homoclinic connections and thus spatially localized states. In order for an orbit homoclinic to a fixed point to exist, the fixed point must have at least one stable and one unstable spatial eigenvalue. Moreover, the stable and unstable manifolds associated with this fixed point must intersect in order for the trajectory to be able to approach the point as $x \to \pm\infty$. If, in addition, the codimension of the intersection of the manifolds is zero and the fixed point is hyperbolic, these homoclinic orbits are structurally stable and the associated localized states remain stationary over a finite parameter interval. For example, consider a fixed point from regions (1) or (2) of Fig. 2.6 with two-dimensional stable and unstable manifolds $\dim(W^{s,u}) = 2$.

The intersection of W^s and W^u is codimension-one in a generic four-dimensional system but codimension-zero when the system is reversible.

A series of homoclinic orbits can be organized around a heteroclinic cycle between a homogeneous state and a periodic state in a structure known as homoclinic snaking (cf. Fig. 1.3) [21, 65]. An excellent introduction to the heteroclinic tangle that lies at the heart of homoclinic snaking can be found in [66]. Consider intersections between the invariant manifolds of a fixed point which we choose to be 0 and a periodic orbit γ. We assume that both 0 and γ are fixed by the involution $\mathcal{R}$ and that $\dim(W^{u,s}(0)) = 2$. Owing to the symmetry $\mathcal{R}$, if we further assume that γ has one stable Floquet multiplier then it will also have one unstable multiplier and two $+1$ multipliers. The center-stable eigenspace is therefore three-dimensional and $W^s(\gamma)$ is thus also three-dimensional. The intersection of $W^u(0)$ and $W^s(\gamma)$ is therefore codimension-zero and thus structurally stable. Moreover reversibility implies the existence of another structurally stable intersection between $W^s(0)$ and $W^u(\gamma)$, i.e., a heteroclinic cycle exists over a finite parameter interval.

We now turn to homoclinic orbits in the Hamiltonian–Hopf bifurcation in order to study localized states in a region of bistability between a trivial state and spatially periodic one. This bifurcation is described by the normal form [64]

$$A' = ikA + B + iAP\left(|A|^2, K, \mu\right) \tag{2.23}$$

$$B' = ikB + iBP\left(|A|^2, K, \mu\right) + AQ\left(|A|^2, K, \mu\right), \tag{2.24}$$

where $A, B \in \mathbb{C}$, μ is a real bifurcation parameter, P and Q are polynomials with real coefficients, and $K = i(A\bar{B} - \bar{A}B)/2$. The normal form is equivariant under the reflection $(x, A, B) \to (-x, \bar{A}, \bar{B})$ and the phase rotation $(A, B) \to (A, B)e^{i\phi}$ for $\phi \in S^1$. Moreover, it is completely integrable with constants of motion

$$K = \frac{i}{2}(A\bar{B} - \bar{A}B) \tag{2.25}$$

$$H = |B|^2 - \int_0^{|A|^2} Q(u, K, \mu)du. \tag{2.26}$$

In the context of spatial dynamics, a quartet of complex spatial eigenvalues collide pairwise on the imaginary axis at $\pm ik$ where a bifurcation occurs in which spatially periodic states of wavenumber k are created.

The system (2.23)-(2.24) can be reduced to a single equation for $u = |A|^2$ by making use of the conserved quantities (2.25)-(2.26) and the fact that $u' = A\bar{B} + \bar{A}B$:

$$E = \frac{1}{2}(u')^2 + V(u), \tag{2.27}$$

where $E = 2K^2$ can be interpreted as the total energy of a one-dimensional particle in the potential

$$V(u) = -2u\left(H + \int_0^u Q(v, K, \mu)dv\right), \tag{2.28}$$

and the standard methods of classical mechanics can be applied to analyze the system. The fixed point at the origin $(A, B) = (0, 0)$ is given by $u = 0$ and the periodic orbits are represented by a single fixed point $u = u_{po}$. Orbits that are homoclinic to $u = 0$ must have $K = H = 0$. Homoclinic orbits appear when $V(u)$ has a local maximum at $u = 0$ and $V(u) > 0$ for some $u > 0$ to bound the orbit. When, in addition to a local maximum at $u = 0$, $u = u_{po}$ is also a local maximum and $V(0) = V(u_{po}) = 0$ with $V(u) < 0$ for $0 < u < u_{po}$ a heteroclinic cycle exists between $u = 0$ and $u = u_{po}$. Here we have assumed that u_{po} is in the set $K = H = 0$ as well. Sample effective potentials that allow for homoclinic and heteroclinic orbits are shown in Fig. 2.8.

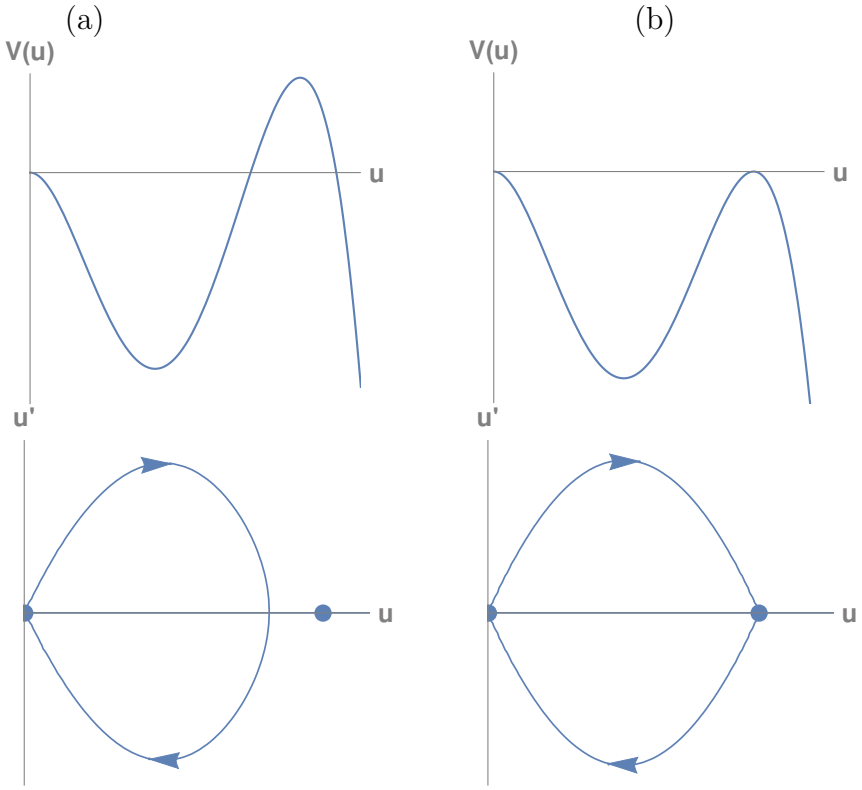

Figure 2.8: Sample effective potential (top) and the corresponding trajectory in (u, u') plane for cases where there exists (a) a homoclinic orbit to $u = 0$ at the origin, and (b) a heteroclinic orbit between $u = 0$ and another fixed point u_{po} representing periodic states.

While the normal form given by Eqs. (2.23)-(2.24) is completely integrable, many systems exhibiting a Hamiltonian–Hopf bifurcation such as SHE are not. We must therefore also consider persistence under perturbations of this system that break integrability. In what follows we make the assumption that the reversible system remains Hamiltonian and consider perturbations that break integrability. While this assumption is not strictly necessary, it does simplify the description significantly. The essential behavior remains unchanged even in cases where the Hamiltonian structure is also broken by the perturbations.

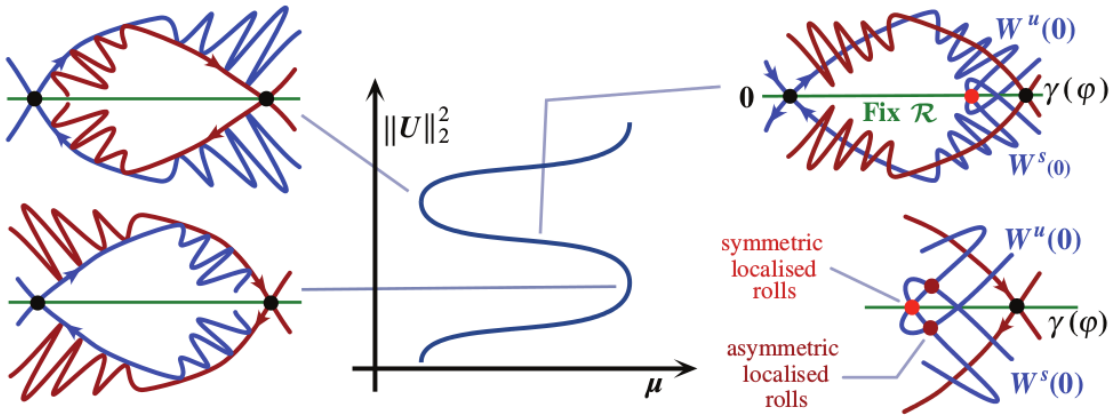

Figure 2.9: Schematic of the intersections of the unstable and stable manifolds of the fixed point $u = 0$ and the periodic orbit $\gamma(\phi)$ that lead to spatially localized states as homoclinic orbits to $u = 0$. Taken from Ref. [67].

Let us now consider what happens to the heteroclinic cycle under perturbations of the type described above. We select out a particular periodic orbit that is invariant under $\mathcal{R}$ and construct an appropriate two-dimensional Poincaré map within the zero level set of the Hamiltonian that contains both the trivial fixed point 0 and the point $\gamma(\phi)$ on the periodic orbit that is a fixed point of the map. Figure 2.9 shows phase portraits of the map with black dots representing the fixed points, which lie on the green line that represents the set invariant under the reflection $\mathcal{R}$. The blue lines represent the stable $W^s(0)$ and unstable $W^u(0)$ manifolds of the trivial state. As this is a map, an initial condition on $W^u(0)$ produces a sequence of points on the line that approach $\gamma(\phi)$ after an infinite number of forward iterations. The perturbation to the heteroclinic cycle causes the stable manifold of the periodic orbit $W^s(\gamma)$ (shown in red) to separate from $W^u(0)$. Under appropriate conditions, we expect an infinite number of transversal intersections of $W^u(0)$ and $W^s(\gamma)$ (top right panel): each intersection point is contained on both invariant manifolds and is thus mapped to other intersection points by forward and backward iterations. Moreover, forward iterations must approach $\gamma(\phi)$ since the intersections are on $W^s(\gamma)$ and backward iterations must approach 0 since the intersections are also on $W^u(0)$.

These intersections lie at the heart of the heteroclinic tangle and, along with the area-preserving property of Hamiltonian maps, cause $W^u(0)$ to oscillate wildly as it approaches $\gamma(\phi)$. Reversibility ensures that $W^s(0)$ behaves similarly near γ and intersects Fix$\mathcal{R}$ at the same point that $W^u(0)$ does. The intersections accumulate on $\gamma(\phi)$ and each one corresponds to a homoclinic orbit. Each additional oscillation of the manifold $W^u(0)$ corresponds to an additional period of the periodic orbit in the trajectory of the solution. As we are considering spatial dynamics, these homoclinic points correspond to spatially localized solutions that contain more and more wavelengths of the periodic pattern. We note that there are

also secondary intersections not on $\mathrm{Fix}\,\mathcal{R}$ which correspond to asymmetric localized states (bottom right panel of Fig. 2.9). These states appear on the rungs of the snakes-and-ladders structure described in Sec. 1.3. The heteroclinic tangle exists over a finite range of the bifurcation parameter μ and breaks as the stable ($W^s(\gamma)$) and unstable ($W^u(\gamma)$) manifolds of the periodic state become tangent to $W^u(0)$ and $W^s(0)$, respectively (left panels of Fig. 2.9). These points define the edge of the pinning region where the symmetric spatially localized states annihilate in fold bifurcations. The asymmetric states are also created and destroyed at these folds.

An analogous picture occurs near the origin where intersections of $W^s(\gamma)$ and $W^u(\gamma)$ accumulate on 0. Each intersection generates an orbit homoclinic to γ and each additional oscillation of the manifold $W^u(\gamma)$ corresponds to an additional period of the periodic orbit spent near 0. These orbits correspond to "holes" in an otherwise periodic pattern in which a certain number of wavelengths is replaced by the trivial $u = 0$ state.

The Swift–Hohenberg equation

The SHE has the minimum number of spatial derivatives for a robust heteroclinic cycle to occur, and thus provides a simple model for studying localized structures associated with homoclinic snaking. We emphasize that because it is a consequence of transversal intersections of manifolds the snakes-and-ladders structure is robust with respect to changes in parameters and even the equation. Indeed, examples of this snaking behavior have been identified in both gradient and nongradient systems, including buckling of slender structures [68, 23], shear flows [69], doubly diffusive convection [70, 71, 72], porous media convection [73] and rotating convection [74].

The spatial dynamics of SHE can be formulated using the free energy F given in Eq. (1.9) as a Lagrangian since $u_t = 0$. The equation of motion, the time-independent SHE, is given in terms of this second-order Lagrangian $F[u, u', u'']$ by

$$\frac{d^2}{dt^2}\frac{\partial F}{\partial u''} - \frac{d}{dt}\frac{\partial F}{\partial u'} + \frac{\partial F}{\partial u} = 0, \tag{2.29}$$

where the prime indicates derivative with respect to x and the nonlinear terms $N = dV/du$ of interest are quadratic-cubic (Eq. (1.7)) or cubic-quintic (Eq. (1.8)). The spatial dynamics conserve the quantity

$$H = -\frac{1}{2}(r-1)u^2 + (u')^2 - \frac{1}{2}(u'')^2 + u'u''' - V(u), \tag{2.30}$$

and this is in fact a Hamiltonian of the system [75]. The coordinate transformation

$$u = u, \qquad v = u', \qquad p_u = -u''' - 2u', \qquad p_v = u'', \tag{2.31}$$

puts the time-independent SHE into canonical form with two degrees of freedom. Equation (2.30) becomes

$$H = vp_u + \frac{1}{2}p_v^2 + v^2 + \frac{1}{2}(r-1)u^2 - V(u), \tag{2.32}$$

and the equations of motion are

$$u' = \frac{\partial H}{\partial p_u}, \quad p_u' = -\frac{\partial H}{\partial u}, \tag{2.33}$$

$$v' = \frac{\partial H}{\partial p_v}, \quad p_v' = -\frac{\partial H}{\partial v}. \tag{2.34}$$

As has already been noted, a Hamiltonian–Hopf bifurcation occurs for $u = 0$ at $r = 0$ where spatially periodic states u_{po} are created. We are interested in the case that these states bifurcate subcritically which occurs for $b > \sqrt{27/38}$ in the quadratic-cubic case with $N = N_{23}$ and for $b > 0$ in the cubic-quintic case with $N = N_{35}$. In this subcritical case, weakly nonlinear analysis can be used to locate a branch of homoclinic orbits of the type shown in Fig. 2.8(a) emerging from $r = 0$ along with the spatially periodic branch. Additionally, we can find a heteroclinic cycle between $u = 0$ and u_{po} through a higher-order calculation in the weakly subcritical limit where the nonlinear coefficient b is tuned to near the transition between subcritical and supercritical. This cycle occurs at the Maxwell point between the two states and the calculation predicts the cycle only exists at a single parameter value (Fig. 2.8(b)).

The weakly nonlinear calculation in this weakly subcritical limit fails to capture the persistence of the heteroclinic cycle because the multiple length scales approximation used decouples the dynamics of the envelope of the state from the phase of the periodic pattern at all finite orders. A calculation beyond all orders reveals that the heteroclinic tangle and thus homoclinic snaking does in fact occur, but only in an exponentially thin region around the Maxwell point [76, 77]. For larger values of the nonlinearity coefficient b the region of bistability increases and the structure persists on a larger parameter interval. The homoclinic snaking that results still surrounds the Maxwell point where a heteroclinic connection between $u = 0$ and u_{po} is expected, but occurs far away from the Hamiltonian–Hopf bifurcation and cannot be captured via weakly nonlinear analysis.

The wavelength of the stationary localized states varies across the snaking region. This variation is small (on the order of one percent) and the wavelength chosen by the state is not the one that minimizes the free energy F. This is a consequence of the fact that these states, which are orbits homoclinic to $u = 0$, are constrained to the $H = 0$ level set of the Hamiltonian. The dependence of the wavelength on the parameter r matches what one might intuitively expect from energy considerations: the state is compressed and the wavelength is smaller when $u = 0$ is energetically favored while the state expands and the wavelength is longer when u_{po} is energetically favored.

2.4 Parametric resonance

A dynamical system exhibiting oscillations typically responds strongly to an external periodic forcing when the frequency of the drive is commensurate (or nearly commensurate)

with an intrinsic frequency of the system. This phenomenon, known as *resonance*, is ubiquitous throughout the physical world and the simplest model of a parametrically driven linear oscillator captures the essential dynamics in many cases when the forcing is parametric. Consider a rigid pendulum whose pivot is vertically vibrated and is undergoing small oscillations about one of the two fixed points of the system. The equation of motion follows a Mathieu equation (see, e.g., Ref. [78]) of the form

$$\ddot{u} + (a - 2q\cos 2t)u = 0. \tag{2.35}$$

Time has been scaled to the half the frequency of the external drive, $\omega = \sqrt{|a|}$ is a characteristic timescale for dynamics of the system and q characterizes the vibration amplitude of the pivot. We begin the discussion by asking the question: under what conditions will the oscillations about $u = 0$ remain bounded near $u = 0$ for all time? In the absence of an external drive ($q = 0$), the oscillations are stable for $a > 0$ which corresponds to the system linearized about the standard configuration for a pendulum. The case of $a < 0$, on the other hand, describes an inverted pendulum where the system has been linearized about the unstable upright position which, as we shall see, can actually be stabilized by the vibration.

From Floquet's theorem (Eq. (2.8)) we see that the solution takes the form

$$u = e^{\sigma_1 t}p_1(t) + e^{\sigma_2 t}p_2(t), \tag{2.36}$$

where $p_j(t)$ are π-periodic functions. Applying Eq. (2.11) (or using reversibility under $(t, u) \to (-t, u)$) implies that $\sigma_1 + \sigma_2 = 0$. Moreover, if the Floquet exponents are complex, they must be complex conjugate pairs: $\sigma_2 = \bar{\sigma}_1$. We also note that the exponents are not unique, $\sigma_j \to \sigma_j + in/2$ is also a multiplier because the additional term just adds an $n\pi$ periodic multiplicative factor which can be absorbed by p_j. Therefore, the Floquet multipliers must be pure real, pure imaginary or complex of the form $\sigma_j = \eta_j + in/2$ where $\eta_1 = -\eta_2$ are real. They cannot be general complex numbers because the above conditions imply $Re(\sigma_j) = -Re(\sigma_j)$ when $Im(\sigma_j) \neq in/2$. Because $\sigma_1 = -\sigma_2$ the condition for stability is that $Re(\sigma_j) = 0$. The Floquet exponents are given by $\pm i\omega$ when $q = 0$, $a > 0$ and they are in general functions of q. We consider an asymptotic expansion of the exponents near $q = 0$ for $a > 0$ and write the exponent as $\sigma = i\omega + q\sigma_1 + q^2\sigma_2 + \mathcal{O}(q^3)$. There are regions of instability near $\omega = n/2$, or equivalently near $a = n^2/4$.

A multiple scales analysis (see Ref. [52]) can be used to compute approximations of the solutions within the region of instability. However if we are just interested in finding the boundaries between regions of stability and instability, we can make use of the fact that the solutions will be periodic with period $n\pi$ along these transition curves. We look near the region of instability by making the expansions $a = n^2/4 + qa_1 + q^2a_2 + \ldots$ and $u = u_0 + qu_1 + q^2u_2 + \ldots$. We can apply standard perturbation theory as in Ref. [53] to find solutions with period $n\pi$ by removing secular terms at each order. Alternatively, we can use the Poincaré–Lindstedt method as in Ref. [79]. Both methods approximate the regions of instability by finding the edges near $a = n^2/4$ for $q \ll 1$. Within these so-called *Arnold tongues* a small amplitude periodic drive can excite large oscillations of the pendulum

when the frequency is tuned to be near resonance. Figure 2.10 shows numerically computed tongues that open as a increases and lead to regions of instability caused by resonances between the natural oscillation period and vibration period. We see that the shaded regions of stability where small oscillations remain bounded near $u = 0$ extend to $a < 0$. Thus a fine-tuning of parameters to within one of these regions can stabilize an inverted pendulum with a periodic forcing.

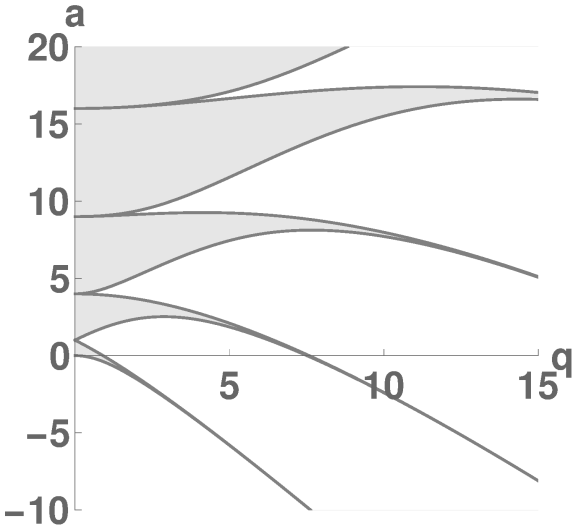

Figure 2.10: Stability diagram for the Mathieu equation (2.35) showing the opening of resonance tongues as the amplitude a of vibration increases. The state $u = 0$ is unstable in the white regions while oscillations about $u = 0$ remain bounded for all time in the gray regions and $u = 0$ is therefore stable there.

2.5 Phase oscillators and synchronization

Many situations are described by a system of coupled oscillators that each exhibit stable time-periodic motion and the seminal work of Winfree [80] provides a framework for studying such systems in biology. When weakly coupled, the oscillators can adjust their frequency and relative phase to undergo a collective motion through a process called *synchronization*. Frequency synchronization or frequency entrainment occurs when oscillators with different intrinsic periods all execute periodic motion with a common frequency. In phase synchronization or phase locking, the oscillators align the phase of their oscillation cycles with one another such that the phase difference remains constant. Synchronization has been famously studied in the context of fireflies [81] where large groups of phase-locked fireflies have been observed to flash in phase across a large field. It is theorized to be key to healthy cardiac dynamics [82] but also the root of Parkinson's disease in neural dynamics [83]. When the coupling is weak, coupled oscillator systems can often be described just in terms of the

phases of the individual oscillators. We explicitly describe the reduction for two oscillators presented in Ref. [84], and this approach extends to N oscillators in a straightforward way.

Consider a dynamical system composed of two nearly identical coupled oscillators

$$\dot{\mathbf{u}}_1 = f(\mathbf{u}_1) + \epsilon f_1(\mathbf{u}_1) + \epsilon g(\mathbf{u}_1, \mathbf{u}_2) \tag{2.37}$$

$$\dot{\mathbf{u}}_2 = f(\mathbf{u}_2) + \epsilon f_2(\mathbf{u}_2) + \epsilon g(\mathbf{u}_2, \mathbf{u}_1), \tag{2.38}$$

where $\dot{\mathbf{u}} = f(\mathbf{u})$ has a stable T-periodic orbit $\mathbf{u}_{po}$, g is the coupling function, f_j describe possible small differences in the oscillators, and $\epsilon \ll 1$. The first step in the reduction process is to transform the system into a phase coordinate ϕ along the limit cycle $\mathbf{u}_{po}$ that satisfies

$$\dot{\phi} = 1. \tag{2.39}$$

Physically, this map takes the nonuniform motion along the limit cycle to a motion at constant speed around a circle. The next step is to extend the mapping from the limit cycle into a small neighborhood around it. This allows us to associate a phase to orbits in the presence of small perturbations ϵp introduced by heterogeneities in the oscillators and the coupling. This extension is accomplished via the *sensitivity function* or the *phase response curve* $\mathbf{Z}(\phi)$. One can gain some intuition about $\mathbf{Z}$ by using the definition based on the concept of isochrons [80, 85]. The phase is extended off the periodic orbit as follows: the phase associated with a point off the periodic orbit is the phase of the initial condition on the periodic orbit that it approaches as $t \to \infty$ when both are time-evolved. The set of all points with the same phase defined in this way is called an *isochron*. We can then compute the phase response curve $\mathbf{Z} = \nabla\phi$ with components given by $Z_j = \partial\phi/\partial u_j$ in terms of the extended phase $\phi(\mathbf{u})$ that is now defined on a neighborhood of the phase space around $\mathbf{u}_{po}$. The phase response curve $\mathbf{Z}(\phi)$ is often computed in practice by numerically solving

$$\frac{d\mathbf{Z}}{d\phi} = -\{Df|_{po}\}^T \mathbf{Z} \tag{2.40}$$

with the normalization condition that $\mathbf{Z}(\phi) \cdot f(\mathbf{u}_{po}(\phi)) = 1$. See Ref. [86] for an overview of this adjoint approach and other standard methods for computing $\mathbf{Z}(\phi)$.

Writing the original coupled oscillator system in terms of the phase variables and making use of the definition of the phase response curve, we get

$$\dot{\phi}_1 = 1 + \epsilon \mathbf{Z}(\phi_1) \cdot p_1\left(\mathbf{u}_{po}(\phi_1), \mathbf{u}_{po}(\phi_2)\right) \tag{2.41}$$

$$\dot{\phi}_2 = 1 + \epsilon \mathbf{Z}(\phi_2) \cdot p_2\left(\mathbf{u}_{po}(\phi_2), \mathbf{u}_{po}(\phi_1)\right), \tag{2.42}$$

where the perturbation function is given by $p_i(\mathbf{u}, \mathbf{v}) = f_i(\mathbf{u}) + g(\mathbf{u}, \mathbf{v})$. By defining new slow phase variables $\theta_j = \phi_j - t$ that track the phases in a frame rotating with the unperturbed oscillation frequency and averaging over the fast timescale with period T, we can reduce the system to the form

$$\dot{\theta}_1 = \omega_1 + \Gamma(\theta_1 - \theta_2) \tag{2.43}$$

$$\dot{\theta}_2 = \omega_2 + \Gamma(\theta_2 - \theta_1), \tag{2.44}$$

where, for $j \neq k$,

$$\omega_j = \frac{1}{T}\int_0^T \mathbf{Z}(\theta_j + t) \cdot f_j\left(\mathbf{u}_{po}(\theta_j + t)\right) dt \tag{2.45}$$

$$\Gamma(\theta_j - \theta_k) = \frac{1}{T}\int_0^T \mathbf{Z}(\theta_j + t) \cdot g\left(\mathbf{u}_{po}(\theta_j + t), \mathbf{u}_{po}(\theta_k + t)\right) dt, \tag{2.46}$$

and the dot represents the standard vector dot product. Taking the difference of the two equations allows for the system to be expressed in terms of a single variable $\psi = \theta_1 - \theta_2$ as

$$\dot{\psi} = r + (\Gamma(\psi) - \Gamma(-\psi)), \tag{2.47}$$

where $r = \omega_1 - \omega_2$. It is clear that only the odd component of Γ, which we denote as Γ_o, contributes and the equation finally reduces to

$$\dot{\psi} = r + 2\Gamma_o(\psi). \tag{2.48}$$

This reduction method can be applied to N oscillators to produce a system of N coupled phase equations in the form

$$\dot{\theta}_j = \omega_j + \sum_{k=1}^{N} \Gamma_{jk}(\theta_j - \theta_k). \tag{2.49}$$

A great amount of analytic progress can be made under the simplifying assumption that $\Gamma_{jk}(\psi) = (K/N)\sin\psi$. The result

$$\dot{\theta}_j = \omega_j - \frac{K}{N}\sum_{k=1}^{N} \sin(\theta_j - \theta_k) \tag{2.50}$$

is known as the Kuramoto model [87] and effectively takes the simplest odd functional form for Γ_{jk} along with the assumption that the oscillators are globally coupled (every oscillator is coupled to every other) with equal strength. Kuramoto was able to simplify the system by defining the complex order parameter

$$Re^{i\Phi} = \frac{1}{N}\sum_{j=1}^{N} e^{i\theta_j}, \tag{2.51}$$

where $0 \leq R \leq 1$ and $0 \leq \Phi < 2\pi$ are mean field quantities that characterize the synchronization of the motion of the individual oscillators and give their average phase, respectively. This allows for the system to be written as

$$\dot{\psi}_j = \omega_j - \dot{\Phi} - KR\sin\psi_j, \tag{2.52}$$

where $\psi_j = \theta_j - \Phi$. These equations have an effective coupling strength KR and frequency parameter $\omega_j - \dot{\Phi}$ that depend on the order parameter and can, in general, be time-dependent.

The new phase variables ψ_j represent the phase difference of each oscillator from the average phase of the system Φ. The oscillations only couple to each other through the dynamics of the order parameter.

Equations (2.52) represent a reduced description of N weakly coupled oscillators in terms of just their phases. The collective behavior of the oscillator system can now be studied through the order parameter (Eq. (2.51)). An equation determining the dynamics of R and Φ can be developed by enforcing a self-consistency condition on the system [87, 84]. In particular, the equality in the definition of the order parameter (Eq. (2.51)) must hold when the solutions to Eq. (2.52) for each of the phases are substituted into the right-hand side.

2.6 Relaxation oscillations and the canard explosion

Canards trajectories were first discovered by Benoît in 1981 [88] and subsequently analyzed via singular perturbation theory in Ref. [89]. The defining characteristic is that the trajectory follows an unstable manifold for some amount of time before quickly jumping to a stable one. Canards appear in the transition from small amplitude oscillations to relaxation oscillations and mixed-mode oscillations that are of great interest for spiking and bursting in neural models [90] and for oscillating chemical reactions [91]. They also play a role in the creation of shocks in traveling waves of advection-reaction-diffusion systems [92], and may be relevant for wound healing [93] and solar winds [94]. However, very little work has been done on canards trajectories in PDE systems where a reduced ODE description does not exist.

The classical example of canards occurs during the transition from small amplitude oscillations to large amplitude relaxation oscillations in the van der Pol equation,

$$\frac{d^2x}{d\tau^2} - \mu(1-x^2)\frac{dx}{d\tau} + x = a, \tag{2.53}$$

with large damping $\mu \gg 1$ and constant external forcing strength a. We can make use of the Liénard transformation by defining a new variable z with

$$\mu\frac{dz}{d\tau} = \frac{d^2x}{d\tau^2} - \mu(1-x^2)\frac{dx}{d\tau} \tag{2.54}$$

so that Eq. (2.53) simply becomes $\mu dz/d\tau + x = a$. Upon integration of Eq. (2.54), the van der Pol equation can be recast as the dynamical system

$$\frac{dx}{d\tau} = \mu(z + x - x^3/3) \tag{2.55}$$

$$\mu\frac{dz}{d\tau} = a - x. \tag{2.56}$$

The large damping results in slow-fast dynamics in the system, and we can analyze the behavior on slow and fast time scales separately by introducing an appropriately scaled time and considering the limiting case $\mu \to \infty$.

In order to capture the dynamics that occur on short time scales, we rewrite the system in terms of a fast time $t = \mu\tau$ and a small parameter $\epsilon = 1/\mu^2 \ll 1$. The resulting fast dynamics is given by the system

$$\frac{dx}{dt} = (z + x - x^3/3) \tag{2.57}$$

$$\frac{dz}{dt} = \epsilon(a - x). \tag{2.58}$$

The dynamics of the limiting case ($\epsilon = 0$) for the fast system reduces to trajectories that follow lines of constant z and stationary points along

$$z_c(x) = -x + x^3/3. \tag{2.59}$$

This so-called critical manifold $z_c(x)$ has a local maximum (minimum) at $x = -1$ ($x = 1$) and is attracting (repelling) for $|x| > 1$ ($|x| < 1$). We will find it useful to segment this curve into three pieces: $z_c^-(x)$ indicates the attracting section on $x < -1$, $z_c^u(x)$ indicates the repelling section on $-1 < x < 1$, and $z_c^+(x)$ indicates the attracting section on $x > 1$. Considering $0 < \epsilon \ll 1$ will add corrections to the manifold of stationary points of the fast dynamics but an initial condition (x_0, z_0) will still evolve on a time scale $t \sim \mathcal{O}(\mu^{-1})$ toward a point within a small ($\sim \mathcal{O}(\mu^{-2})$) neighborhood of (x_c, z_0) on one of the two attracting sections of the critical manifold where x_c is defined by $z_0 = z_c^{\pm}(x_c)$.

The long-time dynamics of the system can be examined by writing Eqs. (2.55)-(2.56) in terms of a slow time $T = \tau/\mu$ and the same small parameter $\epsilon = 1/\mu^2 \ll 1$:

$$\epsilon\frac{dx}{dT} = (z + x - x^3/3) \tag{2.60}$$

$$\frac{dz}{dT} = a - x. \tag{2.61}$$

The limiting case ($\epsilon = 0$) of the resulting slow system is restricted to $z_c(x)$ where the dynamics are determined by $dz/dT = a - x$. Considering $0 < \epsilon \ll 1$ again introduces corrections such that trajectory, upon entering a small neighborhood around $z_c^{\pm}$, drifts slowly within this neighborhood and only exits near $x = \pm 1$. The fixed point of this limiting case at $(x, z) = (a, -a + a^3/3)$ is also a fixed point of the full system and will be stable for $|a| > 1$ and unstable for $|a| < 1$.

Figure 2.11 summarizes the dynamics of the van der Pol oscillator as a function of $a > 0$. We note that the results extend to $a < 0$ with use of the symmetry $(x, z, a) \to (-x, -z, -a)$. The fixed point at $x = a$ will be stable for $a > 1$ and all trajectories will approach this point upon entering the neighborhood of z_c^+. A Hopf bifurcation occurs at $a = 1$ in which small amplitude oscillations are born at the local minimum of $z_c(x)$ at $x = 1$. These small amplitude oscillations exist for a narrow parameter interval before transitioning to relaxation oscillation consisting of fast jumps in x with fixed z separated by a slow drift along the attracting sections $z_c^{\pm}$. The trajectories followed by these relaxation oscillations can be

constructed by gluing together the drift from the slow system and the jumps from the fast system via matched asymptotics. The large amplitude relaxation oscillations persist all the way to the unforced case $a = 0$.

The transition between small amplitude oscillations and relaxation oscillations has an exponentially thin width ($\Delta a \sim e^{-\mu^2}$) and occurs through a sequence of canards that spend a significant amount of time drifting along the repelling section $z_c^u(x)$. As a decreases just below $a = 1$, the trajectory of a small amplitude oscillations drifts along $z_c^u(x)$ for an increasing amount of time before jumping back to $z_c^+(x)$. This continues until a maximal canard is reached in which the trajectory traverses the entire repelling section $z_c^u(x)$ before jumping back to $z_c^+(x)$. As a decreases below this point, the trajectory follows $z_c^u(x)$ for a decreasing amount of time and now jumps to $z_c^-(x)$ instead of $z_c^+(x)$. The trajectory then tracks $z_c^-(x)$ until $x = -1$ before jumping to back to $z_c^+(x)$. The end of the canard explosion occurs when the trajectory no longer drifts along $z_c^u(x)$ and instead jumps directly from $z_c^+(x)$ to $z_c^-(x)$ and back.

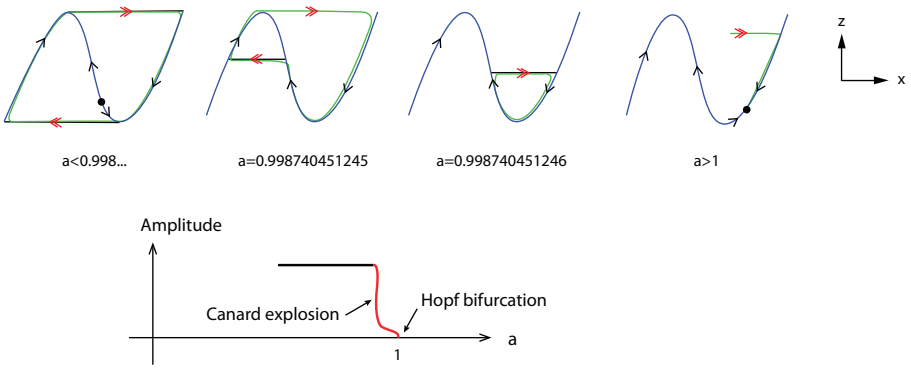

Figure 2.11: Transition from no oscillations to small amplitude oscillations to relaxation oscillations near $a = 1$ in the van der Pol oscillator with $\mu = 10$. A supercritical Hopf bifurcation occurs at $a = 1$ and a canard explosion appears in an exponentially small neighborhood of $a = 0.998740451245$ as small amplitude oscillations transition to relaxation oscillations. A bifurcation diagram of oscillation amplitude as a function of a is shown in the bottom panel while sample trajectories in the (x, z) plane are shown in the top panels. Taken from [95].

Chapter 3

Phase locking and phase slips in systems with time-periodic modulation

The main focus of this dissertation is the dynamics of spatially-localized patterns in spatially-extended systems with time-periodic forcing. The underlying resonance mechanism at play in these systems, however, is a more general phenomenon that appears even in simple dynamical systems. This chapter, which describes work published in [48], uses the Adler equation to explore the effects of time-periodic frequency modulation in the context of synchronization of coupled oscillators. This work serves to demonstrate the framework used to study spatially extended systems with time-periodic parameters in later chapters. Moreover, a deeper level of theoretical and numerical analysis is possible here and many of the insights gained transfer over to the spatially extended cases considered in Chs. 4 and 5. Finally, this chapter opens the door to further study of the role of this resonance mechanism in applications that can be described by systems of coupled oscillators.

The Adler equation [96]

$$\dot{\theta} = r - \sin\theta \tag{3.1}$$

has been used to describe phase synchronization between a pair of coupled oscillators. In this case $\theta \equiv \phi_1 - \phi_2$ represents the difference in the phases ϕ_j of the two oscillators and r represents the normalized frequency difference. When $|r| < 1$ the equation describes a phase-locked state; when $|r| > 1$ the phase difference increases or decreases monotonically, corresponding to repeated phase slips. The transition between these two states is an example of a SNIPER bifurcation [56] and the phase slip period diverges like $1/\sqrt{r-1}$ as r decreases towards $r = 1$.

The nonautomous equation (3.1) with $r = r(t)$ and $r(t)$ a periodic function of time thus describes the effects of temporal modulation of the SNIPER bifurcation. Such modulation is of interest since for part of the modulation cycle the oscillators may be phase-locked while for the rest of the cycle they may undergo phase slips. In this chapter we show that the

interplay between these two states is complex, and characterize the resulting behavior for both high and low frequency modulation $r(t)$; the intermediate case in which the modulation period is comparable to the phase slip period is of particular interest and is also investigated here in detail.

The nonautonomous Adler equation arises in a number of applications. First and foremost it arises in systems of driven identical active rotators [97, 98] or, equivalently, driven arrays of Josephson junctions [99] described by the equations

$$\dot{\phi_j} = \omega(t) - \sin\phi_j - K\sum_{m=1}^{M}\sin(\phi_j - \phi_m). \tag{3.2}$$

Here ω relates to the intrinsic frequency of the individual rotators and K measures their coupling strength. In terms of the Kuramoto order parameter $R\exp i\Phi \equiv \sum_{m=1}^{M}\exp i\phi_m$, this system can be written in the equivalent form

$$\dot{\theta_j} = \omega(t) - \dot{\alpha} - K\tilde{R}\sin\theta_j, \tag{3.3}$$

where $\theta_j \equiv \phi_j - \alpha$, $K\tilde{R} = \sqrt{1+(KR)^2+2KR\cos\Phi}$ and $\tan\alpha = KR\sin\Phi(1+KR\cos\Phi)^{-1}$. Since R and $\dot{\Phi}$ are in general functions of time [100] the quantities $\tilde{R}$ and α will also be functions of time and these are determined by the collective dynamics of the remaining $M-1$ oscillators. When M is large the latter are unaffected by the behavior of an individual oscillator, and $\tilde{R}$ and α can therefore be assumed to be given. The dynamics of each oscillator are thus described by an Adler equation with a time-dependent effective frequency and a time-dependent effective coupling constant. The latter dependence can be removed using the simple substitution $d\tau = K\tilde{R}\,dt$ provided $K(t)$ remains bounded away from zero.

Nonautonomous effects also arise in phase-coupled oscillator systems of Kuramoto type [87] and these are of interest in neural models. In models of this type the coupling strength K_{jk} between oscillators j and k is taken to be a function of time, reflecting either evolution of the network [101, 102, 103, 104, 105] or the effects of a drug, during anesthesia, for example [106]. The simplest model of this type,

$$\dot{\phi_j} = \omega - K(t)\sum_{m=1}^{M}\sin(\phi_j - \phi_m), \tag{3.4}$$

can be written in the equivalent form

$$\dot{\theta_j} = \omega - \dot{\Phi} - K(t)R(t)\sin\theta_j, \tag{3.5}$$

where $\theta_j \equiv \phi_j - \Phi$. Thus the dynamics of each individual oscillator are determined by the global behavior of the system through the quantities KR and Φ. When M is large both R

and Φ may be taken as given, independent of the behavior of the oscillator j. The resulting system can be cast in the form

$$\theta_j' = \tilde{\omega}(\tau) - \sin\theta_j, \tag{3.6}$$

where the prime denotes differentiation with respect to a new time τ, $d\tau = KR\,dt$, and $\tilde{\omega}(\tau) = [\omega/K(\tau)R(\tau)] - \Phi'(\tau)$, with $K(\tau) \equiv K[t(\tau)]$, $R(\tau) \equiv R[t(\tau)]$ etc. It suffices, therefore, to consider the effects of a time-dependent effective frequency only. Related models arise in systems with frequency adaptation [107]. An excellent review of the origin of nonautonomous effects in the Kuramoto model and its variants can be found in [108].

Finally, the nonautonomous Adler equation also describes a single resistively shunted Josephson junction driven by a biased AC current [109]. Theoretical investigations of this equation, motivated by observations of Shapiro steps [110] in the supercurrent, have illuminated a wealth of mode-locking behavior [111, 112, 113]. Large arrays of coupled Josephson junctions are thus amenable to the same type of analysis as active rotator systems [99, 114].

The chapter is organized as follows. In the next section we summarize the basic properties of the Adler equation with and without time-periodic modulation. In Sec. 3.2 we study, under a variety of conditions, periodic orbits of the nonautonomous Adler equation that take the form of oscillations about a phase-locked state. In Sec. 3.3 we study the so-called phase-winding trajectories describing repeated phase slips and identify the regions in parameter space where different states of this type are found. In Sec. 3.4 we show that an adiabatic analysis describes accurately the resulting parameter space not only for low modulation frequencies but in fact remains accurate far outside of this regime. Section 3.5 provides a brief summary of the results and discusses potential applications of the theory.

3.1 The Adler equation

The Adler equation (3.1) with constant r has several symmetries of interest. The equation is invariant under complete rotations $\mathcal{W} : \theta \to \theta + 2\pi$, and time translations $\mathcal{T}_\tau : t \to t + \tau$ by an arbitrary real τ. In addition, it is invariant under the phase symmetry $\mathcal{P}_0 : (t, \theta) \to (-t, \pi - \theta)$ and the parameter symmetry $\mathcal{R}_0 : (r, \theta) \to -(r, \theta)$. As already mentioned, the fixed points or equilibria of Eq. (3.1) correspond to phase-locking between the two oscillators, and these exist in the parameter interval $|r| < 1$:

$$\theta_{eq} = \sin^{-1} r. \tag{3.7}$$

If θ is defined mod 2π, this condition determines two branches of equilibria that merge in a saddle-node bifurcation at $r = \pm 1$ and are related by $\mathcal{P}_0$. One of these branches is stable and can be identified by the condition $\partial_r \theta_{eq} > 0$ while the other is unstable and is characterized by $\partial_r \theta_{eq} < 0$. No fixed points exist for $|r| > 1$: θ increases monotonically when $r > 1$ and decreases monotonically when $r < -1$. When θ is defined mod 2π the resulting trajectories are both periodic in time and the steady-state SNIPER bifurcations at $r = \pm 1$ generate periodic orbits, a consequence of the global organization of the stable and unstable manifolds of the fixed points.

In the present work we find it convenient to think of θ as a variable defined on the real line. When this is done the equation has an infinite number of stable and unstable equilibria that differ in the number of 2π turns relative to an arbitrary origin $\theta = 0$. We refer to these turns as phase slips since one of the two oscillators is now ahead of the other by an integer number of 2π rotations. Trajectories outside of the phase-locked region will incur positive or negative phase slips with frequency

$$\omega_0 = \sqrt{r^2 - 1}. \tag{3.8}$$

This frequency approaches zero in a characteristic square root manner as $|r|$ approaches $|r| = 1$ from above [56].

When the frequency parameter r oscillates in time,

$$r = r_0 + a\sin(2\pi t/T), \tag{3.9}$$

the system retains the winding symmetry $\mathcal{W}$, while the translation symmetry becomes discrete $\mathcal{T} : t \to t + T$. The phase symmetry now includes a time shift, $\mathcal{P} : (t, \theta) \to (T/2 - t, \pi - \theta)$. The parameter symmetry takes the form $\mathcal{R} : (r_0, a, \theta) \to -(r_0, a, \theta)$. There is also an additional parameter symmetry $\mathcal{S} : (t, a) \to (t + T/2, -a)$. We remark that, as already explained, any time-dependence in the coupling parameter $K > 0$ can be removed by a simple transformation, and this parameter is therefore scaled to unity.

Depending on the amplitude a and the period T of the frequency modulation (3.9) the solutions of the resulting equation take the form of oscillations about a phase-locked state or describe repeated phase slips in which the phase difference θ drifts with a nonzero mean speed. We identify below a series of resonances between the modulation period T and the time scale for the generation of a phase slip. The resulting parameter space structure is determined using a combination of numerical simulations, numerical continuation [115] and asymptotic methods. Regions with an integer number of phase slips per period are separated by regions with noninteger numbers of phase slips and include canard trajectories that drift along unstable equilibria. Both high and low frequency modulation is considered. We do not consider noise-triggered phase slips.

3.2 Periodic orbits

Phase-locked states of the autonomous system (3.1) may undergo phase slips in the presence of modulated frequency while remaining phase-locked on average. For such solutions the number of negative phase slips balances the number of positive phase slips over one modulation cycle. Figure 3.1 shows the bifurcation diagram for the nonautonomous Adler equation (3.1) with the periodic modulation (3.9) along with sample trajectories at two points on the solution branches, both superposed on the corresponding equilibrium solutions of the autonomous system, i.e., $r = r_0$. The solution branches *snake*, i.e., they undergo repeated back-and-forth oscillations as the parameter r_0 varies. The extrema of these oscillations

correspond to the SNIPER bifurcations at $r = \pm 1$; the equilibria with a positive slope correspond to stable solutions while those with a negative slope are unstable. Thus along the branch of equilibria stability changes at every fold.

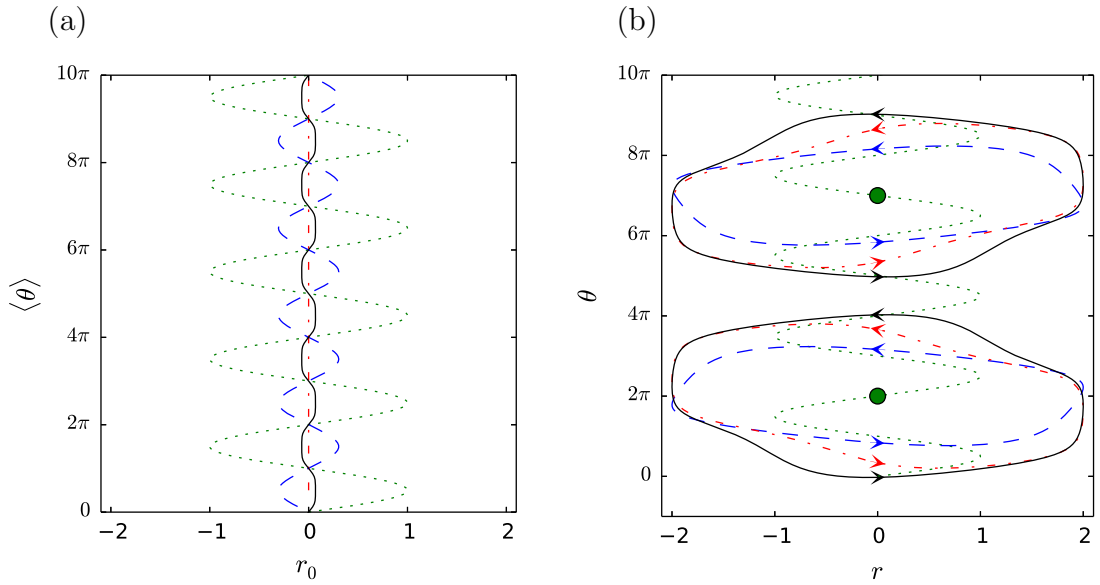

Figure 3.1: (a) Bifurcation diagram showing the average phase $\langle\theta\rangle \equiv T^{-1}\int_0^T \theta(t)\,dt$ of periodic orbits in the periodically modulated Adler equation as a function of r_0 when $a = 2$ and $T = 15$ (blue dashed line), $T \approx 23.01$ (red dash-dotted line) and $T = 25$ (black solid line). (b) Sample trajectories, in corresponding line type, in the (r, θ) plane for solutions with $r_0 = 0$ and $\langle\theta\rangle = 2\pi$ and 7π, superposed on the branch of equilibria of the autonomous system ($a = 0$), represented by a green dotted line.

The trajectories shown in Fig. 3.1(b) are periodic, with period T, and their bifurcation structure parallels that of the phase-locked states in the autonomous system: the solutions snake within an r_0 interval determined by a pair of folds on either side as shown in Fig. 3.1(a). The amplitude of this oscillation and its shape depends on the period T of the forcing which also affects the solution stability. For example, for $\langle\theta\rangle = 2\pi$ and $r_0 = 0$, the solution of the autonomous problem is stable, but becomes unstable for $T = 15$ as most of the periodic orbit tracks the unstable branch of the autonomous problem, before becoming stable again for $T = 25$. A numerical computation of the Floquet multiplier $\exp\left[-\int_0^T \cos\theta(t)dt\right]$ for the Adler equation linearized about the periodic orbit during the continuation procedure confirms that the upward (downward) sloping portions of the solution branch remain stable (unstable) all the way to the folds.

The presence of the symmetries allows us to generate other solutions from the one calculated. Figure 3.2 shows the four different orbits produced by applying the eight different symmetries generated by $(\mathcal{I}, \mathcal{R}, \mathcal{P}, \mathcal{S})$: $\mathcal{I}, \mathcal{R}, \mathcal{P}, \mathcal{S}, \mathcal{RP}, \mathcal{RS}, \mathcal{PS}, \mathcal{RPS}$ to a periodic orbit ob-

tained for $r_0 = 0.2$, $T = 15$ and $a = 2$. These periodic orbits lie on the same solution branch in Fig. 3.1(a). The symmetry $\mathcal{S}$ acts like the identity, the time shift compensating for the sign reversal of a. Application of $\mathcal{T}$ does not produce new orbits, and we can shift any periodic orbit to higher or lower values of θ by multiples of 2π using powers of $\mathcal{W}$. We take advantage of the latter to avoid overlap among the different solutions shown in Fig. 3.2.

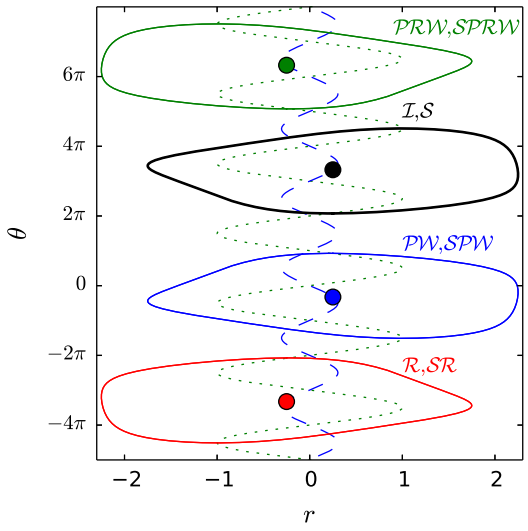

Figure 3.2: The four distinct orbits of the periodically modulated Adler equation generated by applying the symmetries $(\mathcal{I}, \mathcal{R}, \mathcal{P}, \mathcal{S})$ to the stable periodic orbit computed for $T = 15$, $r_0 = 0.2$, and $a = 2$. A sequence of orbits with $\theta \to \theta + 2\pi n$ can be found by applying $\mathcal{W}^n$ to each of the four solutions. These orbits lie on the branch displayed in Fig. 3.1(a) for $T = 15$. The symmetry $\mathcal{W}$ has been applied in order to prevent overlap between the four distinct orbits. The equilibria of the autonomous system ($a = 0$) are shown as a green dotted line.

Figure 3.3 shows how the existence region of the periodic orbit, labeled PO, evolves with T. Numerical continuation of the folds at the two edges of PO reveals a series of *pinched regions* in which the folds "cross" and the PO region is reduced to the single value $r_0 = 0$. This accounts for the switch in the orientation of the branch as T increases (see Fig. 3.1(a)). We call the sections between the pinched regions *sweet spots*. Within each of these sweet spots, the number of positive and negative phase slips during one cycle is the same, and the orbits are therefore qualitatively similar. The resulting structure, shown in Fig. 3.3(a), is reminiscent of the structure observed in [49]. Figure 3.3(b) shows the amplitude of the oscillation in θ for periodic orbits at $r_0 = 0$ as a function of the period T. The figure reveals that N positive and negative phase slips can occur even when $\Delta\theta = \theta_{\max} - \theta_{\min} < 2\pi N$. This is a consequence of the fact that the two successive saddle-nodes at $r = \pm 1$ are separated by a phase difference of π. Figure 3.4 shows a series of periodic orbits that transition from zero to one positive and one negative phase slip as a (equivalently T) increases.

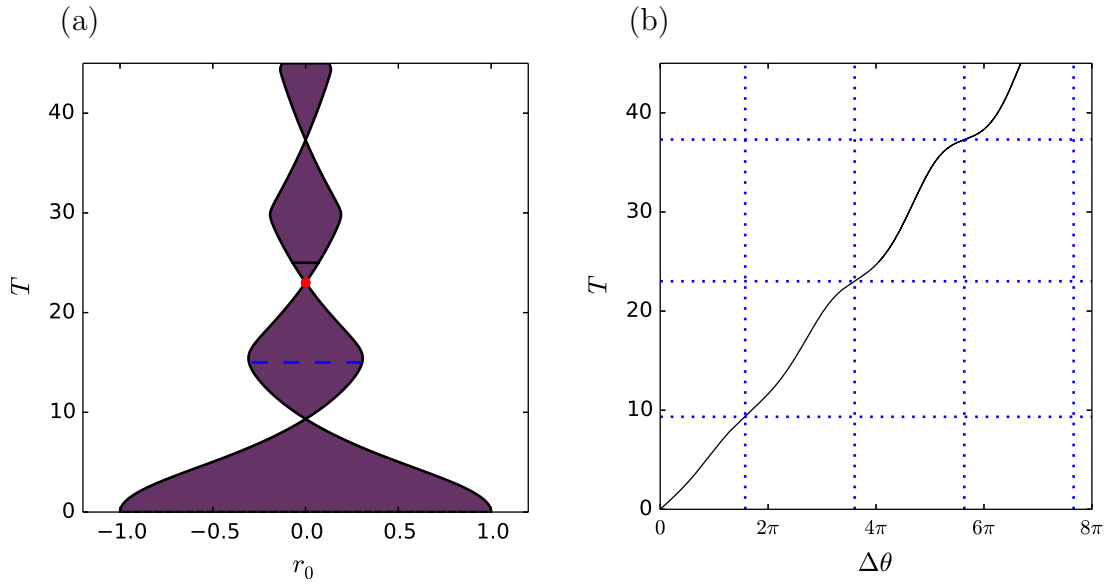

Figure 3.3: (a) Locus of the folds that define the boundary of the PO region in the (r_0, T) plane of the periodically modulated Adler equation. The horizontal dashed and solid lines indicate the values of T corresponding to the branches of periodic orbits computed in Fig. 3.1(a). (b) The amplitude $\Delta\theta \equiv \theta_{\max} - \theta_{\min}$ of a periodic orbit with $r_0 = 0$ and $a = 2$ as function of the period T. The dotted horizontal lines correspond to the pinched regions at $T \approx 9.33$, 23.01 and 37.31 in panel (a); at these the corresponding periodic orbits are characterized by $\Delta\theta \approx 4.95$, 11.32 and 17.71 and deviate from multiples of 2π by $(2\pi n - \Delta\theta)/2\pi \approx 0.21$, 0.20, 0.18, respectively.

Birth of periodic orbits

To understand the effect of a time-dependent frequency parameter on the dynamics of phase-locked oscillators, we start out by considering the high-frequency modulation limit of the Adler equation (3.1) with the time-periodic modulation (3.9). We write $T = 2\pi\epsilon/\omega$, where $\epsilon \ll 1$, and $\omega \sim \mathcal{O}(1)$ is a suitably scaled frequency, and define the fast time ϕ by $\omega t = \epsilon\phi$. The Adler equation becomes

$$\omega\partial_\phi\theta = \epsilon(r_0 + a\sin\phi - \sin\theta - \partial_t\theta). \tag{3.10}$$

We assume that $\theta(\phi, t) = \theta_0(\phi, t) + \epsilon\theta_1(\phi, t) + \epsilon^2\theta_2(\phi, t) + \ldots$ and carry out the calculation order by order. The leading order equation shows that $\theta_0 = \psi_0(t)$ is independent of the fast oscillation time. The $\mathcal{O}(\epsilon)$ equation yields, after integration over the fast period of the forcing,

$$\partial_t\psi_0 = r_0 - \sin\psi_0. \tag{3.11}$$

Thus, at leading order, the averaged system follows an autonomous Adler equation with constant forcing equal to the average of the periodically modulated case.

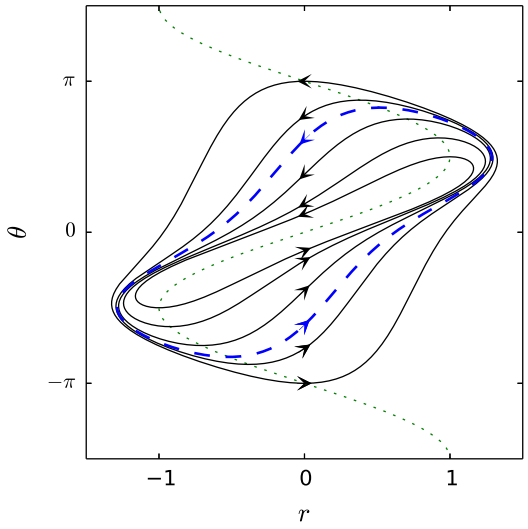

Figure 3.4: A series of periodic orbits (solid black) of the periodically modulated Adler equation for $T = 25$, $r_0 = 0$ and increasing values of a, corresponding to increasing oscillation amplitude $\Delta\theta = \pi, 5\pi/4, 3\pi/2, 7\pi/4, 2\pi$, superposed on top of the bifurcation diagram of the phase-locked solutions of the autonomous system $a = 0$ (green dotted line). The transition from zero phase slips to one positive and one negative phase slip is indicated by a dashed blue line and corresponds to $a \approx 1.29$ and $\Delta\theta \approx 1.65\pi$.

The solution at order ϵ reads

$$\theta_1(\phi, t) \equiv -\frac{a}{\omega}\cos\phi + \psi_1(t), \tag{3.12}$$

where ψ_1 is determined through the solvability condition at the next order. This next order equation reads

$$\omega\partial_\phi\theta_2 = -\theta_1\cos\theta_0 - \partial_t\theta_1, \tag{3.13}$$

and integration over the fast period gives the solvability condition

$$\partial_t\psi_1 = -\psi_1\cos\psi_0. \tag{3.14}$$

The solution at order ϵ^2 is thus

$$\theta_2(\phi, t) = \tfrac{a}{\omega^2}\sin\phi\cos\psi_0(t) + \psi_2(t), \tag{3.15}$$

while the order ϵ^3 equation reads

$$\omega\partial_\phi\theta_3 = -\theta_2\cos\theta_0 + \tfrac{1}{2}\theta_1^2\sin\theta_0 - \partial_t\theta_2, \tag{3.16}$$

leading to a solvability condition for ψ_2:

$$\partial_t\psi_2 + \psi_2\cos\psi_0 = \tfrac{a^2}{4\omega^2}\sin\psi_0 + \tfrac{1}{2}\psi_1^2\sin\psi_0. \tag{3.17}$$

To study the average dynamics, we define the period-averaged phase

$$\psi = (2\pi)^{-1} \int_0^{2\pi} \left(\theta_0 + \epsilon\theta_1 + \epsilon^2\theta_2\right) d\phi. \tag{3.18}$$

This expression is accurate to order $\mathcal{O}(\epsilon^2)$. Summing the solvability conditions now yields the equation

$$\partial_t \psi = r_0 - \left(1 - \tfrac{a^2T^2}{16\pi^2}\right) \sin\psi + \mathcal{O}(T^3), \tag{3.19}$$

where we have replaced ω/ϵ by $2\pi/T$. Thus, in the high-frequency limit, the averaged dynamics follows an Adler equation for which the amplitude of the nonlinear term that characterizes the coupling strength between the two oscillators decreases in proportion to $(aT)^2$. The phase-locked region of the averaged equation (3.19) that defines the PO region for the time-dependent Adler equation thus exists for $|r_0| = 1 - (aT/4\pi)^2$, and the introduction of high-frequency modulation narrows the width of the phase-locked region in the parameter r_0 by $2(aT/4\pi)^2$.

Death of periodic orbits

Asymptotic analysis near the folds that define the edges of PO can provide some insight into the break-up of the periodic orbits. We consider perturbations about the marginally stable orbit at the left ($r_0 = r_-$) and right ($r_0 = r_+$) edges of PO for a given modulation frequency $\omega = 2\pi/T$ and amplitude a, namely Eq. (3.1) with $r = r_0 + a\sin\omega t$, where $r_0 = r_\pm + \epsilon^2\mu$ and $\epsilon \ll 1$. We use multiple time scales by introducing a slow time $\tau = \epsilon t$ on which the system incurs net phase slips and expand the phase variable as $\theta = \theta_0 + \epsilon\theta_1 + \epsilon^2\theta_2 + \ldots$.

The leading order equation, $\partial_t\theta_0 = r_\pm + a\sin\omega t - \sin\theta_0$, is solved by the marginally stable periodic orbit, which we have computed numerically via continuation. The $\mathcal{O}(\epsilon)$ equation is

$$\partial_t\theta_1 + \theta_1\cos\theta_0 = -\partial_\tau\theta_0 \tag{3.20}$$

which has a solution of the form $\theta_1 = A\exp\left(-\int\cos\theta_0 dt\right)$ for a slowly-varying amplitude A as θ_0 does not depend on the slow time. At $\mathcal{O}(\epsilon^2)$, the equation reads

$$\partial_t\theta_2 + \theta_2\cos\theta_0 = \mu + \frac{1}{2}\theta_1^2\sin\theta_0 - \partial_\tau\theta_1. \tag{3.21}$$

The existence of a solution in θ_2 that is T-periodic requires that the solvability condition

$$\partial_\tau A = \mu\alpha_1 + \frac{1}{2}\alpha_2 A^2 \tag{3.22}$$

be satisfied where the coefficients can be computed numerically from the integrals

$$\alpha_1 = \frac{1}{T}\int_0^T \exp\left(\int\cos\theta_0 dt\right) dt, \qquad \alpha_2 = \frac{1}{T}\int_0^T \sin\theta_0 \exp\left(-\int\cos\theta_0 dt\right) dt. \tag{3.23}$$

Thus, just outside PO, the system will incur *net* phase slips with a frequency of

$$\Omega_{\text{slip}} = \sqrt{2|\alpha_1\alpha_2(r_0 - r_\pm)|}. \tag{3.24}$$

Figure 3.5 shows a comparison of this frequency as a function of r_0 with simulations near the right edge of PO for $T = 15$, where $r_+ \approx 0.305$, and $\alpha = \sqrt{2|\alpha_1\alpha_2|} \approx 1.163$. The coefficient that describes the square root dependence of the frequency on the distance from the left edge of PO will be identical to the one computed for the right edge owing to the symmetry $\mathcal{R}$.

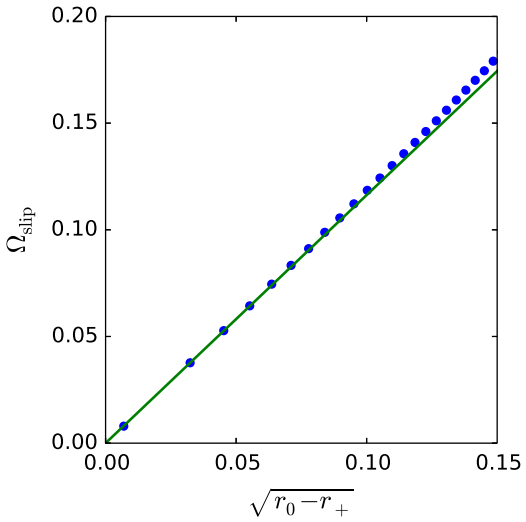

Figure 3.5: (a) A plot of the frequency Ω_{slip} at which phase slips of the periodically modulated Adler equation occur just outside of PO as a function of distance $\sqrt{r_0 - r_+}$ from the right edge when $a = 2$ and $T = 15$. The solid green line is the prediction in Eq. (3.24) from asymptotic theory while the blue dots are computed from time simulations.

The asymptotics of sweet spots

When large excursions of the forcing parameter are allowed during a high-frequency cycle, a balance is struck that allows a finite number of phase slips to occur. We keep $T = 2\pi\epsilon/\omega$ but link the amplitude of the forcing to the frequency by $a = \rho/\epsilon \equiv 2\pi\rho/\omega T$. Upon defining the fast time-scale $\phi = \omega t/\epsilon$, the Adler equation becomes

$$\omega\partial_\phi\theta - \rho\sin\phi = \epsilon(r_0 - \sin\theta - \partial_t\theta). \tag{3.25}$$

Using an asymptotic series of the form $\theta(\phi, t) = \theta_0(\phi, t) + \epsilon\theta_1(\phi, t) + \epsilon^2\theta_2(\phi, t) + \ldots$ and solving the leading order equation we obtain

$$\theta_0(\phi, t) = -\tfrac{\rho}{\omega}\cos\phi + \psi_0(t). \tag{3.26}$$

The evolution of ψ_0 is determined from a solvability condition at next order. Since the order ϵ equation reads

$$\omega\partial_\phi\theta_1 = r_0 + \sin\left(\tfrac{\rho}{\omega}\cos\phi - \psi_0\right) - \partial_t\psi_0, \tag{3.27}$$

the required solvability condition is

$$\partial_t\psi_0 = r_0 - J_0(\tfrac{\rho}{\omega})\sin\psi_0, \tag{3.28}$$

where J_0 is the Bessel function of the first kind. The averaged dynamics thus follow an autonomous Adler equation with a constant frequency and a coupling strength given by $J_0(\rho/\omega) = J_0(aT/2\pi)$. The boundaries of the PO region are thus defined by $r_0 = \pm J_0(aT/2\pi)$ and these oscillate in r_0 as aT increases with an amplitude that decreases with increasing T (Fig. 3.6). The location of the pinched regions is thus determined by the zeros

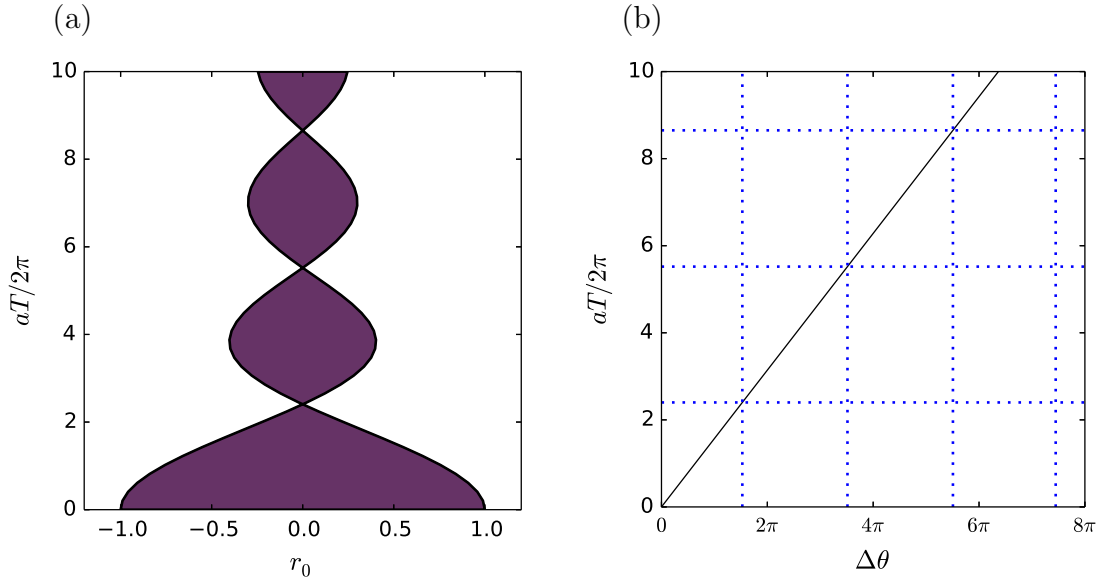

Figure 3.6: (a) The PO region in the (r_0, aT) parameter plane corresponding to stable phase-locked solutions of the periodically modulated Adler equation when the modulation has high frequency and a large amplitude. (b) The leading order amplitude $\Delta\theta \equiv \theta_{\max} - \theta_{\min}$ of a periodic orbit at $r_0 = 0$ as a function of $aT/2\pi$. Horizontal dotted lines correspond to the first three pinched regions which coincide with the zeros of $J_0(aT/2\pi)$: $aT/2\pi \approx 2.40$, 5.52 and 8.65.

of $J_0(aT/2\pi)$. Between these are the sweet spots where periodic orbits exist over the finite range $|r_0| < |J_0(aT/2\pi)|$. The reversal of orientation of the folds seen in Fig. 3.1(a) is analogous to sign changes of $J_0(aT/2\pi)$ in this high frequency, large amplitude limit, as shown in Fig. 3.6.

Amplitude dependence

We now examine how periodic solutions within PO behave as a function of the amplitude of the modulation by fixing $r_0 = 0$ and performing numerical continuation in a (Fig. 3.7). As long as r_0 is in the interior of PO, each value of a admits two periodic orbits on a 2π interval for $\langle\theta\rangle$. One is stable, one is unstable, and they are related by the phase symmetry $\mathcal{P}$. The symmetries of the system further imply that the locations of these orbits at $r_0 = 0$ are fixed at $\langle\theta\rangle = m\pi$ for $m \in \mathbb{Z}$ and such solutions persist for all values of a (horizontal lines in panel (a) of Fig. 3.7). The pinched regions where the PO boundaries cross (Fig. 3.3(a)) and the snaking branch becomes vertical (red dash-dotted line in Fig. 3.1(a)) correspond to codimension two points in the (a, T) plane; at these points a continuum of periodic orbits parametrized by the phase average $\langle\theta\rangle$ is present. Thus when $r_0 = 0$ the periodic orbits create the grid-like bifurcation diagram shown in Fig. 3.7(a). This grid structure breaks apart into isolated loops of solutions as soon as $r_0 \neq 0$, and gaps between the regions of existence of periodic orbits begin to emerge (cf. Fig. 3.3(a)). The loops that emerge from the breakup of the rectangular grid structure at $r_0 = 0$ when $r_0 \neq 0$ shrink to zero with increasing a (or T), as expected from Fig. 3.3(a). Numerical continuation of the boundary of the PO region as a function of a when $r_0 = 0.1$ and $T = 25$ reveals that periodic orbits persist only to $a \approx 14.5$.

Figure 3.8[A-E] shows solutions for $r_0 = 0$ at the parameter values indicated in Fig. 3.7(a) by red dots labeled with the corresponding capital letter. The equilibria for the autonomous problem are shown for reference (dotted line). These reveal that the periodic orbits alternately track branches of unstable and stable equilibria for part of each oscillation cycle (orbits A, B, C), and likewise for C, D, E. Since orbits that track stable equilibria are expected to be stable when the drift along such equilibria is sufficiently slow, we expect that orbits B and D are stable while A, C and E are unstable. This expectation is confirmed by explicit stability calculations.

Canards

Figure 3.9 shows periodic orbits from the first vertical solution branch in Fig. 3.7(a) corresponding to the dark blue dots not labeled with capital letters. These periodic orbits all have the same value of $a \approx 1.2$ and correspond to pinched zone solutions with $\langle\theta\rangle = \pi$, $5\pi/4$, $3\pi/2$, $7\pi/4$ and 2π. These solutions illustrate how the periodic orbit expands to larger $\langle\theta\rangle$ while tracking the equilibria of the autonomous system. These are beginning to reveal characteristics of the so-called canard states familiar from studies of slow-fast systems. For example, the third panel shows an orbit that slowly tracks a branch of stable equilibria towards lower θ and smaller r followed by tracking a branch of unstable equilibria towards yet smaller θ but increasing r, before an abrupt transition near the right fold that restores the original θ value essentially instantaneously, i.e., at essentially constant r. This difference in timescales is not as pronounced in the last panel of Fig. 3.9 but can be enhanced by increasing the modulation period.

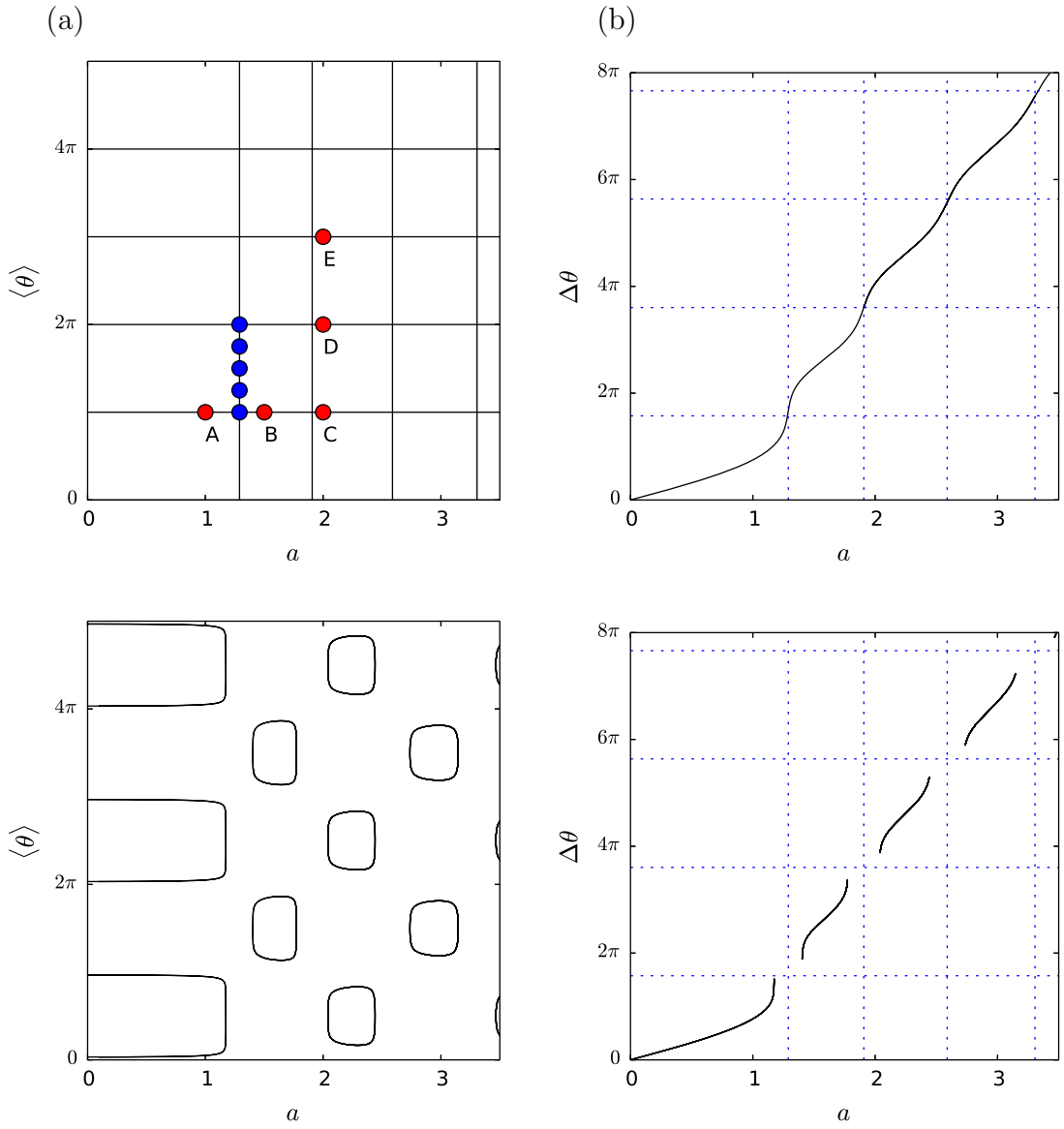

Figure 3.7: Bifurcation diagrams showing (a,c) the average phase $\langle\theta\rangle \equiv T^{-1}\int_0^T \theta(t)dt$ (solid lines) and (b,d) the oscillation amplitude $\Delta\theta \equiv \theta_{\max} - \theta_{\min}$ of periodic orbits of the periodically modulated Adler equation as a function of a when $r_0 = 0$ and $T = 25$. The solutions shown in (a) collapse onto a single curve when plotted in terms of $\Delta\theta$ in (b). When $r_0 = 0.1$ and $T = 25$, the grid structure of (a) separates into isolated loops shown in (b) that collapse onto disconnected line segments when plotted in terms of $\Delta\theta$ in (d).

Figure 3.10 shows typical "two-headed" canard trajectories with a clear separation of timescales, obtained for $T = 100$, $r_0 = 0$ and slightly different modulation amplitudes a.

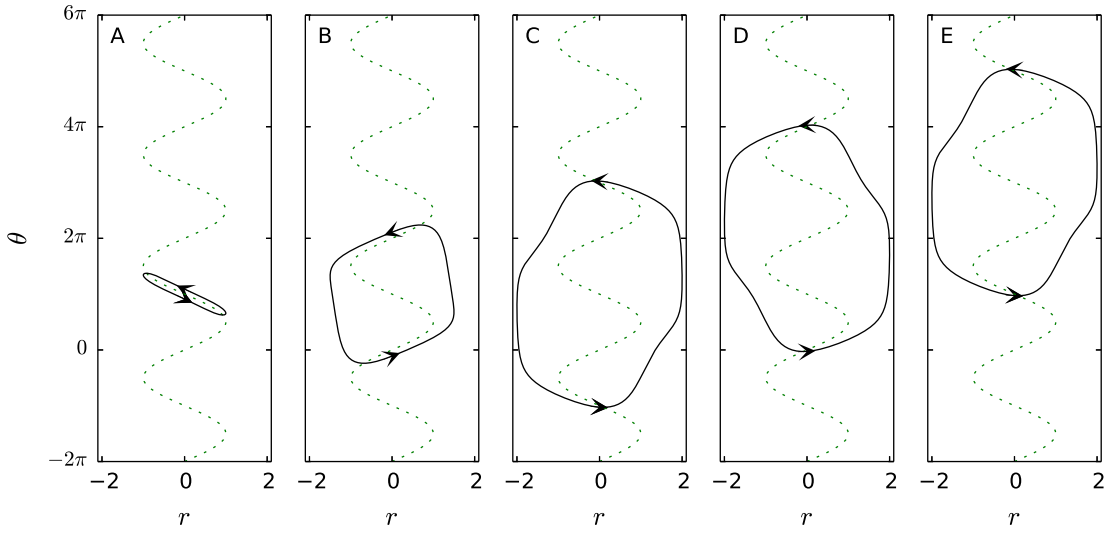

Figure 3.8: (A)-(C) Periodic orbits of the periodically modulated Adler equation with $\langle\theta\rangle = \pi$ in the (r, θ) plane when $r_0 = 0$, $T = 30$ and $a = 1,\ 1.5,\ 2$. (C)-(E) Periodic orbits with $\langle\theta\rangle = \pi,\ 2\pi,\ 3\pi$ in the (r, θ) plane when $r_0 = 0$, $T = 30$ and $a = 2$. The orbits shown here correspond to the red dots in Fig. 3.7(a) labeled with capital letters.

The two canards with the smallest values of a (red, yellow) appear just below the transition from no phase slips to one positive and negative phase slip that occurs at the first pinched zone of PO and spend the majority of their trajectory tracking a stable equilibrium. The next two canards (green, light blue) appear just above the first pinched zone and both incur one positive and negative phase slip within the phase-locked region $|r| < 1$. A majority of the time along these canard trajectories is spent tracking unstable equilibria. These four canard trajectories illustrate the transition of a stable orbit within the lowest region of PO to an unstable orbit within the first sweet spot such as the dark blue trajectory that tracks unstable equilibria through the entire orbit.

Increasing the amplitude a slightly further leads the canard to overshoot the right saddle-node and can make it depart from the branch of unstable equilibria upwards, i.e., in the opposite direction as compared to the solutions for slightly smaller a. The latter case leads to a different type of canard: the system jumps from the unstable solution branch to the upper branch of stable equilibria, which it then follows downward in θ. After reaching the upper left fold of the equilibria the trajectory jumps to the lower left fold and thereafter follows the lower unstable equilibria towards larger r, resulting in the same sequence of transitions but now as r increases. The resulting solution is periodic but is characterized by phase slips that take place inside the phase-locked region $|r| < 1$. This behavior is exemplified by the outer canard trajectory (purple) in Figs. 3.10(a); the associated $\dot{\theta}$ displays an inverse peak, as shown in Fig. 3.10(b). This canard appears as a approaches the second pinched

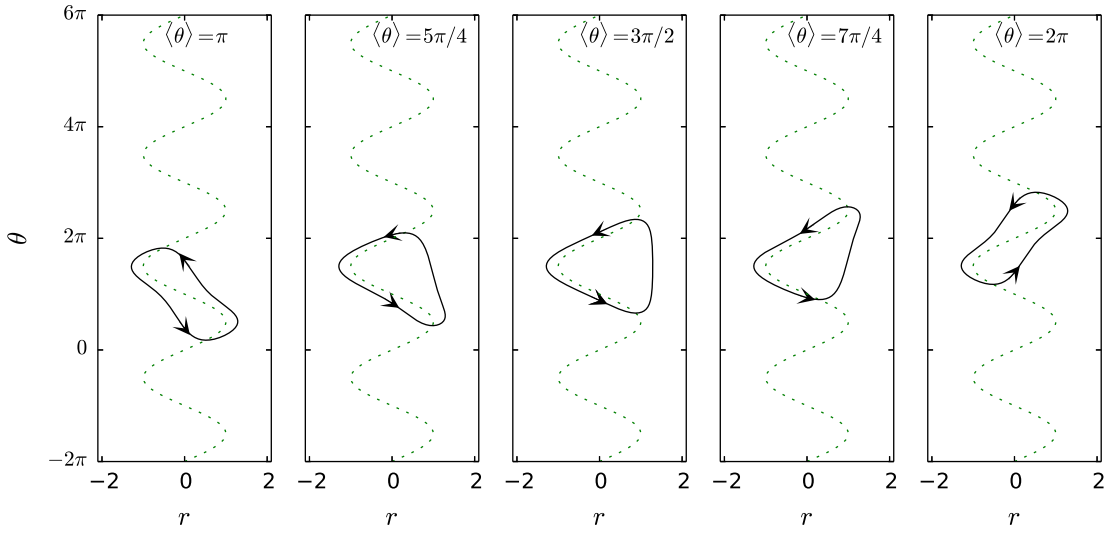

Figure 3.9: Periodic orbits of the periodically modulated Adler equation along the first vertical solution branch in Fig. 3.7 in the (r, θ) plane when $r_0 = 0$, $T = 25$ and $a \approx 1.2$. These solutions are characterized by $\langle\theta\rangle$ that is a fraction of 2π, viz. π, $5\pi/4$, $3\pi/2$, $7\pi/4$ and 2π. The orbits shown here correspond to the unlabeled blue dots in Fig. 3.7(a).

zone and begins the transition to a stable orbit with two positive and negative phase slips.

Figure 3.11 shows the corresponding canard trajectories with the same parameter values as in Fig. 3.10 but opposite stability properties. In particular, the transition from unstable periodic orbit with no phase slips to stable periodic orbit with one positive and negative phase slip is depicted by the orbits with the four smallest values of a (red, yellow, green, light blue).

Canard trajectories with additional time separation along the stable and unstable manifolds can be achieved by increasing T further. For example, Fig. 3.12 shows several "two-headed" canard trajectories obtained for $T = 300$.

3.3 Winding trajectories

Outside of the phase-locked region of the Adler equation with constant frequency parameter ($r_0 \in [-1, 1]$, $a = 0$) there exist winding solutions that complete phase slips with the frequency given by Eq. (3.8). The introduction of a modulation in r with period T (Eq. 3.9, $a \neq 0$) generates winding solutions even when the average value r_0 lies within $[-1, 1]$. This occurs for values of r_0 outside of PO (but $|r_0| < 1$), and is a consequence of an imbalance between positive and negative phase slips.

We define the *winding number* of a trajectory in the modulated system as the average

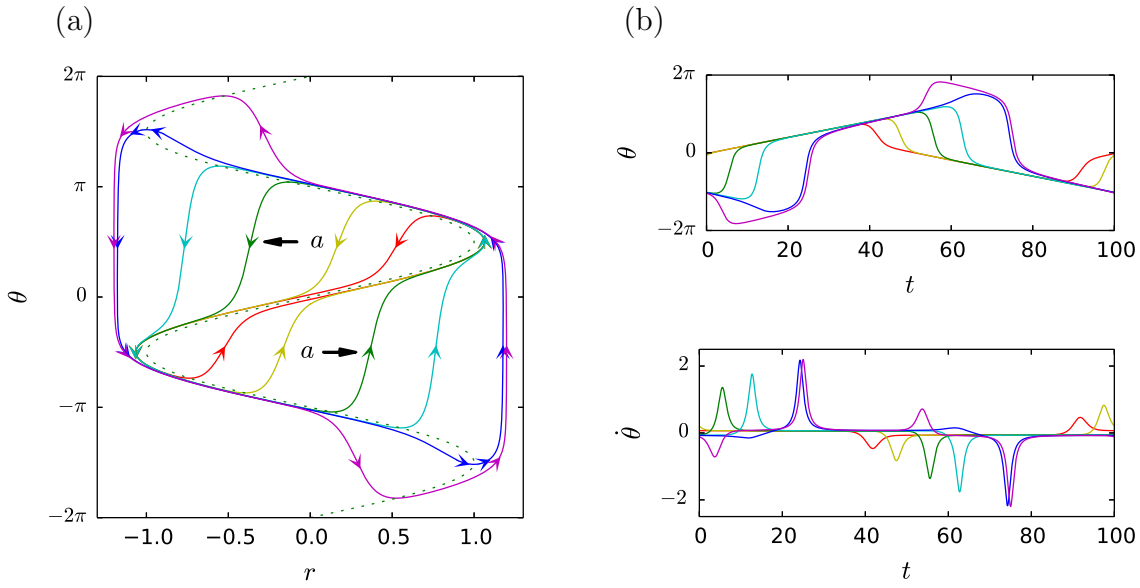

Figure 3.10: (a) Two-headed canard trajectories $\theta(r)$ of the periodically modulated Adler equation for $r_0 = 0$, $T = 100$ and $a \approx 1.064807$, 1.064872, 1.064876, 1.066086, 1.177531 and 1.198182. The red and yellow orbits with the smallest values of a appear in the lowest region of PO and track stable equilibria over a majority of the orbit. The remaining four (green, light blue, dark blue, purple) appear within the first sweet spot of PO and track unstable equilibria over a majority of the orbit. (b) The corresponding solutions $\theta(t)$ and $\dot{\theta}(t)$.

number of net phase slips per period,

$$N = \lim_{m\to\infty} \frac{\theta(mT) - \theta(0)}{2\pi m} \tag{3.29}$$

with $m \in \mathbb{Z}$. Figure 3.13 shows solution branches with integer winding numbers $N = 1, 2, 3$ when $a = 2$ and $T = 25$ (solid lines). These were computed by numerical continuation as a boundary value problem with the constraint that $\theta(T) - \theta(0) = 2\pi N$. Trajectories with integer winding number exist over finite ranges of the parameter r_0. Solutions displaying an extra positive phase slip over each modulation cycle have winding number $N = 1$; these exist for $r_{1,\min} \approx 0.1 < r_0 < r_{1,\max} \approx 0.4$. To the right of this interval lie solutions with winding number $N = 2$, extending from $r_{2,\min} \approx 0.4$ to $r_{2,\max} \approx 0.6$. Solutions with higher integer winding number exist beyond this point as exemplified by the $N = 3$ solutions in Fig. 3.13.

Resonance tongues

The parameter range containing integer winding solutions forms through the opening of resonance tongues as the modulation amplitude a increases from zero. We write, following

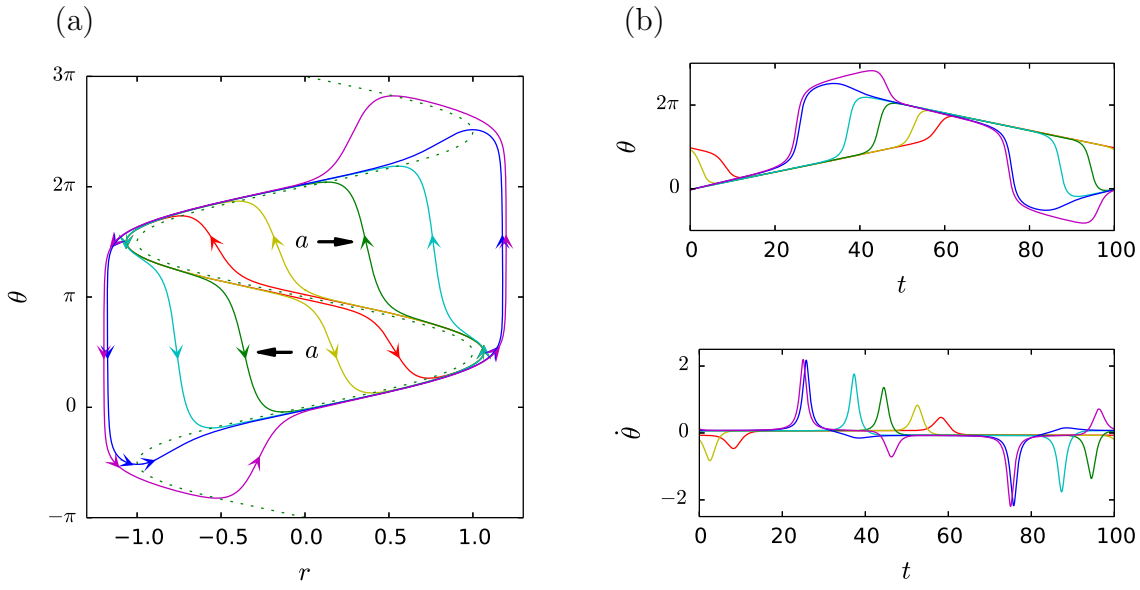

Figure 3.11: (a) Two-headed canard trajectories $\theta(r)$ of the periodically modulated Adler equation for $r_0 = 0$, $T = 100$ and $a \approx 1.064807$, 1.064872, 1.064876, 1.066086, 1.177531 and 1.198182. These orbits have the same parameter values as those in Fig. 3.10 but opposite stability properties. The red and yellow orbits with the smallest values of a appear in the lowest region of PO and track unstable equilibria over a majority of the orbit. The remaining four (green, light blue, dark blue, purple) appear within the first sweet spot of PO and track stable equilibria over a majority of the orbit. (b) The corresponding solutions $\theta(t)$ and $\dot{\theta}(t)$.

Ref. [112], $x = \tan\theta/2$ to put the Adler equation in the form

$$\dot{x} = \frac{1}{2}r - x + \frac{1}{2}rx^2. \tag{3.30}$$

The Riccati transformation $x = -2\dot{y}/ry$ now generates a second order linear equation for the variable $y(t)$:

$$\ddot{y} + \left(1 - \frac{\dot{r}}{r}\right)\dot{y} + \frac{r^2}{4}y = 0. \tag{3.31}$$

Using the standard transformation $y = ze^{-\frac{1}{2}\int 1 - \frac{\dot{r}}{r}dt}$ we finally obtain the Hill equation

$$\ddot{z} + \left[\frac{r^2}{4} + \frac{\ddot{r}}{2r} - \frac{\dot{r}^2}{2r^2} - \frac{1}{4}\left(1 - \frac{\dot{r}}{r}\right)^2\right] z = 0. \tag{3.32}$$

Substituting the time-dependent frequency parameter r specified in Eq. (3.9) and assuming $a \ll 1$ yields the Mathieu equation

$$\ddot{z} + \left(\frac{r_0^2 - 1}{4} + \frac{a}{2r_0}\sqrt{\omega^2 + (r_0^2 - \omega^2)^2}\sin(\omega t - \xi)\right) z + \mathcal{O}(a^2) = 0, \tag{3.33}$$

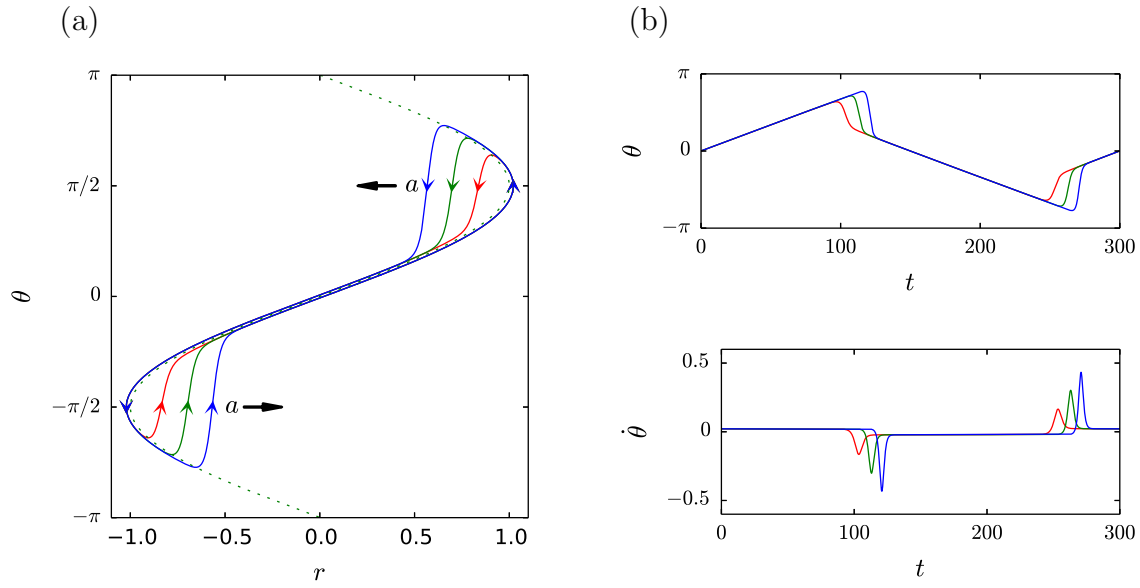

Figure 3.12: Two-headed canard trajectories of the periodically modulated Adler equation computed by numerical continuation of periodic orbits in the parameter a. The parameters are $r_0 = 0$, $T = 300$ and $a \approx 1.02115308$, 1.02116560, 1.02116562.

where $\omega \equiv 2\pi/T$ and $\tan\xi \equiv (r_0^2 - \omega^2)/\omega$. Phase slips in the original Adler equation correspond to divergences of x; these in turn correspond to zero crossings of y and z.

The resonance tongues grow in this asymptotic limit according to the characteristic curves of the above Mathieu equation. We compare these asymptotic predictions with the numerical computation of the resonance tongues through two-parameter continuation of folds on the branches of winding solutions. The tongues associated with the 1:1, 2:1, and 3:1 resonances between the winding frequency and the modulation frequency are shown in Fig. 3.14 alongside the predictions from the characteristic curves of the Mathieu equation (3.33).

The resonance tongues enter farther into the phase-locked region $|r_0| < 1$ as a increases. We observe that as a increases the location of the tongues begins to depart from the Mathieu equation predictions, as noted already in the context of Josephson junction models (Ch. 11 of Ref. [109]). In particular, the interaction of these tongues with their negative winding counterparts leads to qualitative changes: for $a > 1.29$, the width of the 1:1 resonance tongue stops growing monotonically and its left boundary turns abruptly from $r_0 \approx 0$ to larger r_0; at $r_0 \approx 0.25$, $a \approx 1.57$ the tongue collapses to a single point before growing again. This situation repeats as a increases and the tongue therefore describes a succession of sweet spots and pinched regions. The same behavior is observed for the subsequent resonance tongues: the 2:1 resonance tongue starts to shrink at $r_0 \approx 0.25$, $a \approx 1.57$ and collapses to a point at $r_0 \approx 0.50$, $a \approx 1.86$, etc.

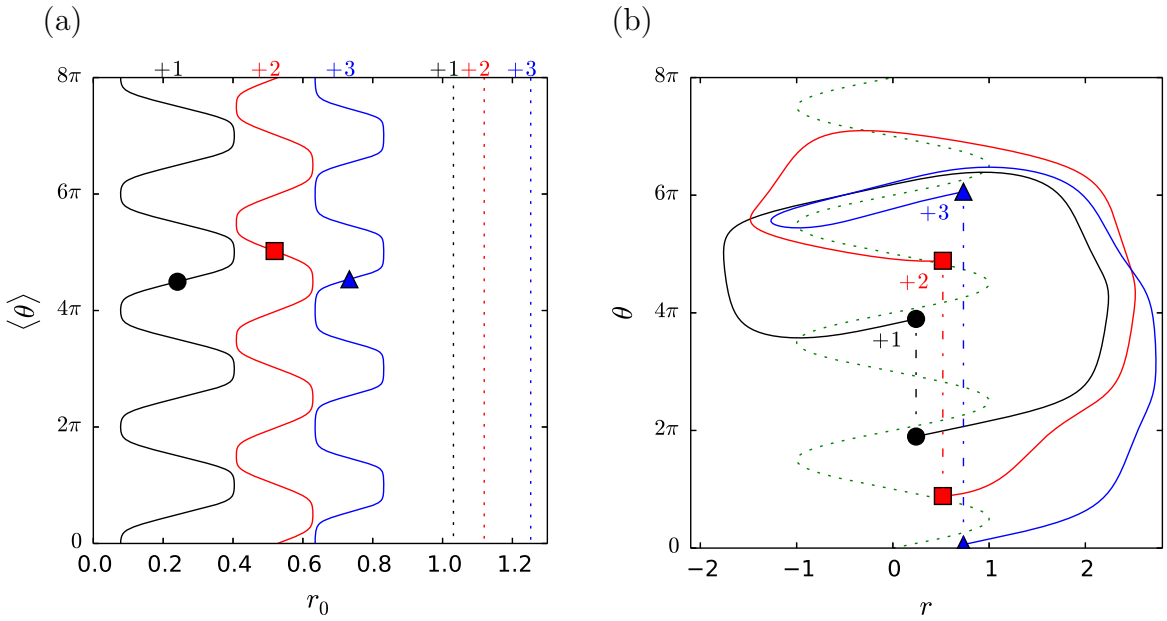

Figure 3.13: (a) The phase $\langle\theta\rangle \equiv T^{-1}\int_0^T \theta(t)\,dt$ averaged over T of winding orbits of the periodically modulated Adler equation as a function of r_0 when $a = 2$ and $T = 25$. Since θ is no longer periodic all points with the same $\langle\theta\rangle$, mod 2π, at a particular value of r_0 lie on the same trajectory. The black (with circle), red (with square) and blue (with triangle) branches have winding numbers $N = 1,\ 2,\ 3$, respectively. The branches of solutions with the same winding numbers but constant frequency parameter $r = r_0$ are shown as (vertical) dotted lines. (b) Sample winding trajectories corresponding to the colored symbols in panel (a).

Partitioning of the parameter space

The parameter plane (r_0, T) can be partitioned in terms of winding number by following the folds of the N:1 resonant winding trajectories such as those shown in Fig. 3.13. The resulting partitioning of parameter space is shown in Fig. 3.15. To obtain this figure the branches with winding numbers $1 \le N \le 7$ were continued in r_0 for $a = 2$ and $T = 5$, followed by continuation of the saddle-nodes on these branches in the parameters r_0 and T. The region PO of periodic orbits was computed in a similar way for completeness. The sweet spot and pinching structure of regions with constant integer winding number that begins to emerge in Fig. 3.14(a) can also be seen as T increases for fixed a. The width of these sweet spots decreases with T. For infinite periods, any small departure from the symmetry axis $r_0 = 0$ leads to the dominance of positive or negative phase slips over the other.

Thus the parameter plane is partitioned into regions with solutions displaying zero, one, two or more net phase slips per cycle. Each of these regions possesses a structure similar to that of the PO region with zero net phase slips. The first region to the right of PO

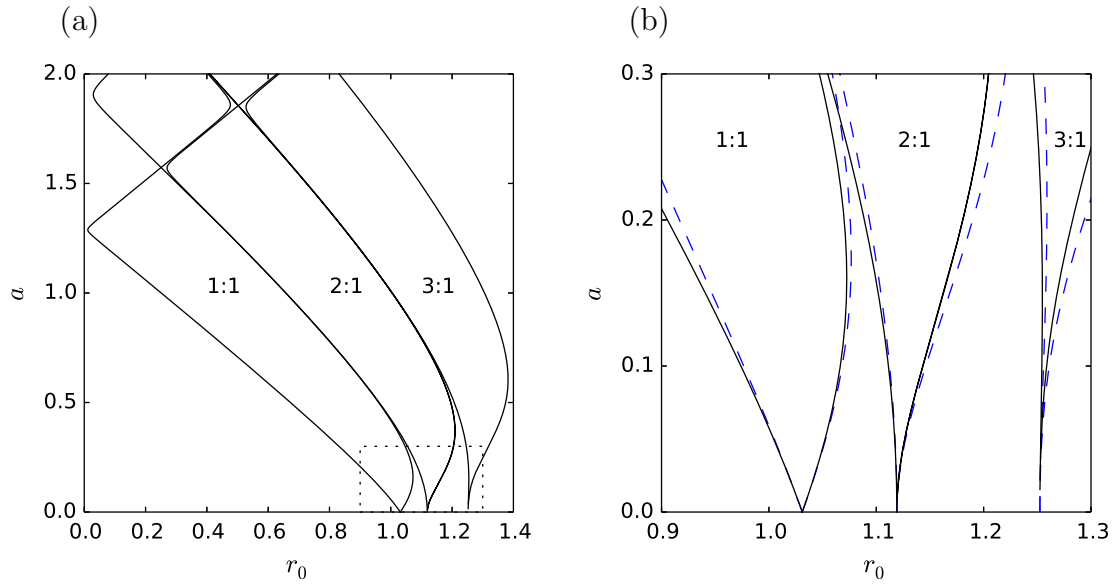

Figure 3.14: (a) Resonance tongues for the 1:1, 2:1 and 3:1 resonances between the winding frequency and the modulation frequency in the (r_0, a) plane of the periodically modulated Adler equation when $T = 25$. The resonance tongues correspond to the solution branches shown in Fig. 3.13 with 1, 2 and 3 phase slips per period of the modulation cycle, respectively. The boxed region in the lower right of panel (a) is replotted in panel (b) along with the predictions for the location of the tongues from Eq. (3.33) in dashed lines.

corresponds to solutions that undergo one extra positive phase slip within each period of the modulation. The first sweet spot of this band, at low T, corresponds to solutions that complete one positive and no negative phase slip per cycle; the second sweet spot, further up, consists of solutions that complete two positive phase slips and one negative phase slip per cycle, etc. The second region on the right corresponds to solutions that undergo two extra positive phase slips, and so on as r_0 increases. All these regions have a similar structure as the modulation period T increases. They all correspond to the resonance tongues in Fig. 3.14 and are separated by transition zones with solutions that have a non-integer winding number. These transition zones narrow as T increases and solutions within them can have periods that are a multiple of the modulation period, or not be periodic at all. Solutions with negative winding number are found in analogous regions obtained by reflection in $r_0 = 0$.

Figure 3.16 shows the winding number between PO and the 1:1 resonance tongue as computed from time simulations averaged over 5000 modulation periods $T = 25$. The figure shows that the winding number increases monotonically and smoothly within this transition zone, as expected on the basis of theoretical considerations [112]. However, modifications of the nonautonomous Adler equation, such as the inclusion of an inertial term or a more general time dependence, can generate subharmonic resonances that populate the transition

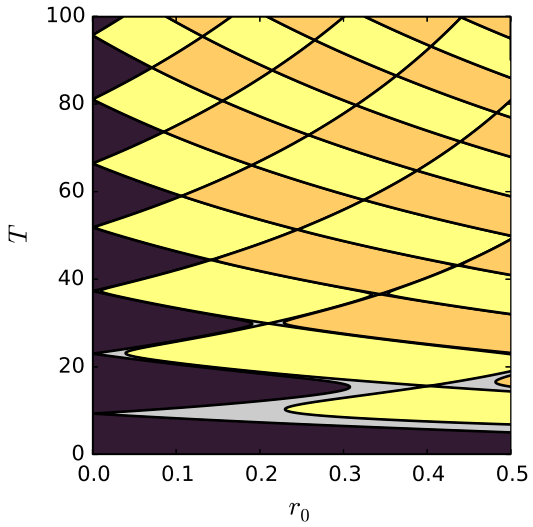

Figure 3.15: Average winding number per period T of the frequency parameter shown in the (r_0, T) plane of the periodically modulated Adler equation for $a = 2$. No net phase slips occur over the course of a modulation period in the dark region to the left; the alternating lighter yellow and darker orange regions to the right indicate $1, 2, 3, \ldots$ net phase slips as r_0 increases. The (lightest) gray transition zones have non-integer winding numbers. Trajectories with negative winding number are located in regions obtained by reflection in $r_0 = 0$.

zones [109]. Subharmonic resonances have also been observed to produce a devil's staircase type structure in the related problem of spatially localized states in the periodically forced Swift–Hohenberg equation (Fig. 4.12).

Asymptotic formation of sweet spots

We can extend the above predictions by analyzing the limit in which the trajectory barely exits the phase-locking region $-1 < r < 1$ but the modulation period is slow enough that phase slips still take place. Explicitly, we take $r(t) = \epsilon^2\mu + (1 + \epsilon^2\rho)\sin\epsilon^2\omega t$, where $\epsilon^2\mu$ represents a small offset of the average value of $r(t)$ from $r_0 = 0$. We introduce the slow time scales $\tau = \epsilon t$ and $\Phi = \epsilon^2\omega t$ and employ an asymptotic expansion of the form $\theta = \theta_0 + \epsilon\theta_1 + \epsilon^2\theta_2 + \ldots$.

At leading order, the Adler equation (3.1) gives $\sin\theta_0 = \sin\Phi$ for which we choose the stable phase locked solution $\theta_0 = \Phi + 2\pi n$ that has no τ dependence. The alternate choice, $\theta_0 = \pi - \Phi + 2\pi n$, produces unstable periodic orbits or unstable winding trajectories. At order ϵ, we obtain the equation $\partial_\tau\theta_0 = -\theta_1\cos\theta_0$. When $\theta_0 \neq \pi/2 + \pi n$, $\theta_1 = 0$ in order to

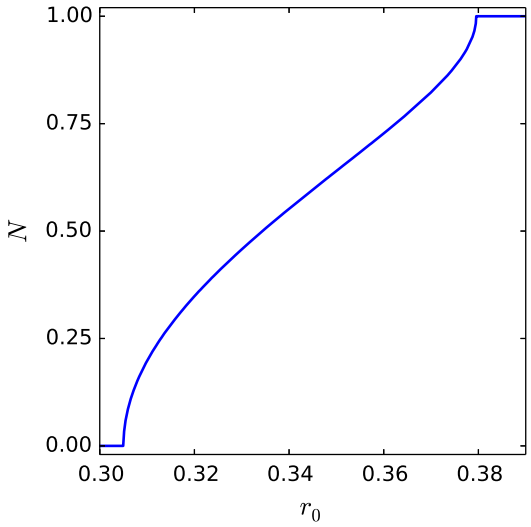

Figure 3.16: The winding number N as a function of r_0 across the transition zone between PO and the 1:1 resonance tongue of the periodically modulated Adler equation with $T = 15$ and $a = 2$.

satisfy the condition that θ_0 be independent of τ. At order ϵ^2, we obtain

$$\theta_2 \cos\theta_0 = \mu + \rho \sin\Phi + \tfrac{1}{2}\theta_1^2 \sin\theta_0 - \partial_\tau \theta_1 - \omega \partial_\Phi \theta_0, \tag{3.34}$$

leading to the second order correction

$$\theta_2 = (\mu - \omega)\sec\Phi + \rho \tan\Phi \tag{3.35}$$

provided that $\theta_0 \neq \pi/2 + \pi n$.

To examine the dynamics near $\theta_0 = \pi/2 + n\pi$ where the system is transitioning between phase-locked dynamics and winding, we take the slow time to be $\Phi = \pi/2 + \epsilon\phi$. Equation (3.1) then becomes

$$\epsilon\omega\partial_\phi\theta = \epsilon^2\mu + (1 + \epsilon^2\rho)\cos\epsilon\phi - \sin\theta. \tag{3.36}$$

The leading order and order ϵ equations are identical to the general case above while θ_1 is determined from the order ϵ^2 equation,

$$\theta_2 \cos\theta_0 = \mu + \rho - \tfrac{1}{2}\phi^2 + \tfrac{1}{2}\theta_1^2 \sin\theta_0 - \omega\partial_\phi\theta_1, \tag{3.37}$$

which differs from Eq. (3.34). Since $\theta_0 = \pi/2$ the Riccati transformation $\theta_1 = -2\omega\partial_\phi\psi/\psi$ transforms this equation into the Weber equation

$$\partial_\phi^2\psi = -\tfrac{1}{2\omega^2}(\mu + \rho - \tfrac{1}{2}\phi^2)\psi. \tag{3.38}$$

We now use a matching procedure to connect the relevant solution of this equation to the case when $\Phi \neq \pi/2 + n\pi$. Noting that $\theta_1(\Phi) \to 0$ as $\Phi \to \pi/2 + n\pi$, we choose our solution such that $\theta_1 \to 0$ as $\phi \to -\infty$. This matching condition is satisfied by the parabolic cylinder function [116] $\psi = D_\nu(s)$, where

$$\nu = \frac{\mu + \rho}{2\omega} - \frac{1}{2}, \qquad s = \frac{\phi}{\sqrt{\omega}}. \tag{3.39}$$

Each zero $s = s_0$ of $\psi = D_\nu(s)$ corresponds to one phase slip. Care must be taken in interpreting these results since the zeros of ψ correspond to divergences of θ_1 and thus a breakdown of the asymptotic series used to obtain Eq. (3.38). The above calculation holds between the asymptotic breakdowns where $\theta_1(\tau)$ diverges, so a complete trajectory can be constructed by "gluing" solutions across each individual phase slip. Thus ψ can be used to describe a series of phase slips via this gluing process.

The number of zeros of ψ corresponds to the number of phase slips and thus determines which solution branch the system will follow upon re-entering the phase-locked region $\pi/2 < \Phi < 3\pi/2$. In particular, $[n_+]$ phase slips are undergone when

$$[n_+] - \tfrac{1}{2} < \frac{\mu + \rho}{2\omega} < [n_+] + \tfrac{1}{2}. \tag{3.40}$$

More generally, we can express the number of positive (negative) phase slips that occur near the boundaries of the phase-locked region in terms of the parameters of the problem as

$$[n_\pm] = \begin{cases} \pm \left[\frac{(a \pm r_0 - 1)T}{4\pi} \right] & (a \pm r_0 - 1) \geq 0 \\ 0 & (a \pm r_0 - 1) < 0, \end{cases} \tag{3.41}$$

where the square bracket indicates rounding to the nearest integer. The predictions of this theory match well with time simulations for $a = 1.005$, as seen in Fig. 3.17. The simulations employed a fourth order Runge–Kutta scheme for 12 periods of the modulation using the initial condition $\theta(0) = \sin^{-1} r_0$. The winding number was computed from $2\pi N = (\theta(12T) - \theta(2T))/10$ as a function of the parameters r_0 and T. Time simulations were used in place of numerical continuation because the extremely long time scales make continuation a computationally challenging task. Owing to symmetry the PO region is always centered on $r_0 = 0$, and states with negative winding number are found in regions obtained by reflection in $r_0 = 0$.

The figure reveals the formation of sweet spots in this limit whenever $a > 1$. When $a < 1$, there are two distinct sets of resonance bands – one set formed by regions with a fixed number of positive phase slips n_+, and the other by regions with a fixed number of negative phase slips n_-. At $a = 1$ the two sets of resonance bands both asymptote to $r_0 = 0$ as $T \to \infty$ (Fig. 3.18(a)). The sweet spot and pinching structure emerges through the intersections of these resonance bands that take place once $a > 1$ (Fig. 3.18(b,c)). In particular, the pinched region separating the n and $n+1$ sweet spots in PO is located at $(a-1)T/4\pi = n + 1/2$ and marks the transition from n to $n + 1$ positive and negative phase slips within a modulation cycle.

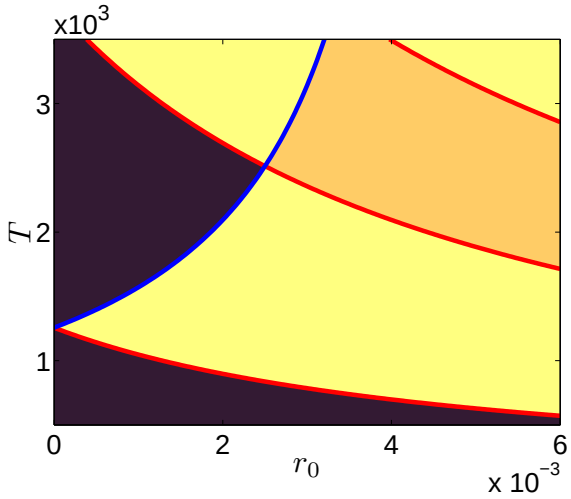

Figure 3.17: Average winding number per period T of the frequency parameter shown in the (r_0, T) plane of the periodically modulated Adler equation for $a = 1.005$. Colors represent results from numerical simulation: no net phase slips occur over the course of a modulation period in the dark region to the left; the alternating yellow and orange regions to the right indicate $1, 2, 3, \ldots$ net phase slips as r_0 increases. The red (negative slope) and blue (positive slope) lines mark the transitions between the regions of constant n_+ and n_- as predicted by the asymptotic theory (Eq. (3.41)). Trajectories with negative winding number are located in regions obtained by reflection in $r_0 = 0$.

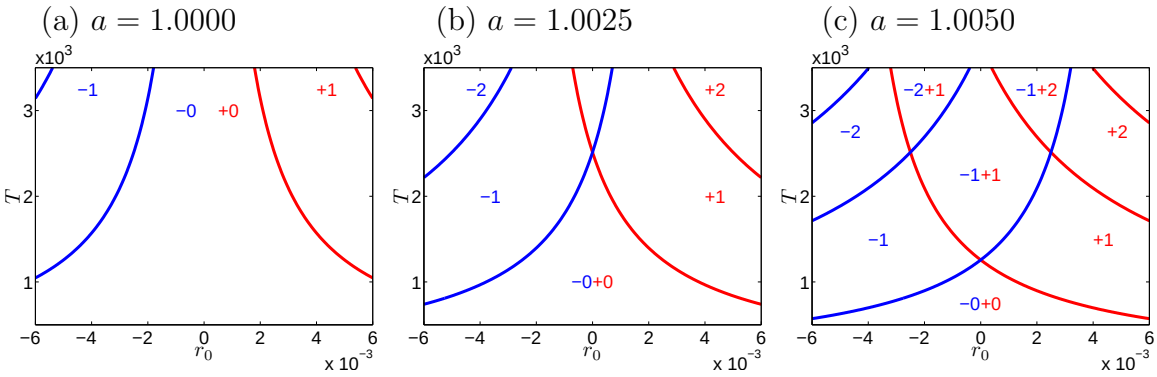

Figure 3.18: Transitions between the regions of constant n_+ (red, negative slope) and n_- (blue, positive slope) in the (r_0, T) plane of the periodically modulated Adler equation as predicted by the asymptotic theory (Eq. (3.41)) for $a = 1.0000,\ 1.0025,\ 1.0050$, respectively. A sweet spot and pinching structure begins to emerge as a increases.

3.4 Adiabatic theory

We now consider a more general time-dependence for the parameter r, but assume it varies slowly enough that we can treat the dynamics quasi-statically: $r = r(2\pi t/T)$ with $T \gg 1$.

In this adiabatic limit, two distinct types of dynamics arise: slow dynamics that track the steady state phase-locked solution when $-1 \lesssim r(2\pi t/T) \lesssim 1$ and a fast phase rotation with an adiabatically varying parameter when $|r(2\pi t/T)| \gtrsim 1$. No matter how low the frequency is, there is always an intermediate regime around the transition from a phase-locked state to rotation where the phase rotation is slow enough that it occurs on the same scale as the parameter drift. We apply WKB theory [52] to capture the dynamics in each of the two regions separately and provide a condition for matching the solution across the transitions at $r \approx \pm 1$.

We start with Eq. (3.32) but assume that $r = r(\omega t)$ with $\omega \ll 1$. We do not need to specify the form of $r(\omega t)$. We transform this equation into a standard form for WKB theory by recasting it in terms of the slow time $\phi = \omega t$:

$$z'' + \frac{1}{\omega^2}\left(\frac{r^2-1}{4} + \frac{\omega r'}{2r} + \frac{\omega^2 r''}{2r} - \frac{3\omega^2 (r')^2}{4r^2}\right) z = 0. \tag{3.42}$$

The system transitions from a phase-locked state to winding near $r^2 - 1 \sim \mathcal{O}(\omega)$, and we can use the standard WKB ansatz $z = A z_{\mathrm{WKB}} = A \exp(iS/\omega) + \text{c.c.}$, where A is an arbitrary complex constant determined from initial conditions and/or matching procedure when we are away from these points. We suppose that $S = S_0 + \omega S_1 + \dots$ and match orders to solve for each S_i.

Making the WKB substitution generates, at leading order,

$$S_0'^2 = \frac{r^2-1}{4}. \tag{3.43}$$

The leading order WKB solution, in terms of the original time scale, is $z = A \exp\left(\pm \frac{i}{2} \int \sqrt{r^2-1} dt\right)$. The equation at next order is, after simplification,

$$-2S_0' S_1' + iS_0'' + \frac{r'}{2r} = 0, \tag{3.44}$$

yielding

$$S_1 = \frac{1}{2}\left(i \log \sqrt{r^2-1} \mp \tan^{-1}\left(\frac{1}{\sqrt{r^2-1}}\right)\right), \tag{3.45}$$

depending on the choice of root for S_0.

Including this correction, the solution becomes

$$z = \frac{A}{(r^2-1)^{1/4}} \exp \pm \tfrac{i}{2}\left(\int \sqrt{r^2-1} dt - \tan^{-1} \frac{1}{\sqrt{r^2-1}}\right). \tag{3.46}$$

When $r < 1$, we find it convenient to rewrite the expression for S_1 as

$$S_1 = \frac{i}{2}\left(\log \sqrt{1-r^2} \pm \log \frac{1+\sqrt{1-r^2}}{r}\right), \tag{3.47}$$

and the solution now takes the form

$$z = \frac{A}{(1-r^2)^{1/4}} \left(\frac{1+\sqrt{1-r^2}}{r} \right)^{\mp 1/2} \exp \mp \tfrac{1}{2} \int \sqrt{1-r^2} dt. \tag{3.48}$$

Near a transition point $r = 1$ (we take it to be at $t = 0$), we suppose that $r \approx 1 + \alpha t$, where $\alpha = \dot{r}(0) = \omega r'(0)$ is a constant. To leading order, the equation becomes

$$\ddot{z} + \frac{\alpha}{2}(t+1)z = 0, \tag{3.49}$$

which has solutions in terms of the Airy functions $\mathrm{Ai}(s)$ and $\mathrm{Bi}(s)$ [116], where $s = -\left(\frac{\alpha}{2}\right)^{1/3}(t+1)$.

We will further assume $\alpha > 0$ so that the transition occurs as the system leaves the phase-locked region and enters the winding region and remind the reader that

$$\tan \frac{\theta}{2} = -\frac{2}{r}\frac{\dot{z}}{z} + \frac{1}{r}\left(1 - \frac{\dot{r}}{r}\right). \tag{3.50}$$

We consider the solution within the phase-locked region that follows, for $t < 0$, the stable steady-state solution branch $\theta = \sin^{-1} r$, corresponding to taking the negative root of S_0. Thus, Eq. (3.48) reduces to

$$z = \frac{A_{\mathrm{pl}}}{(1-r^2)^{1/4}} \left(\frac{1+\sqrt{1-r^2}}{r} \right)^{1/2} \exp \tfrac{1}{2} \int \sqrt{1-r^2} dt, \tag{3.51}$$

where A_{pl} depends on the choice of initial condition. In terms of θ, expression (3.51) reads

$$\tan \frac{\theta}{2} = \frac{1-\sqrt{1-r^2}}{r} \left(1 - \frac{\dot{r}}{r(1-r^2)}\right). \tag{3.52}$$

In order to match solutions across the transition region, we must take the $t \to 0$ (equivalently $r \to 1$ limit of this solution and match it to the $t \to -\infty$ (equivalently $s \to \infty$) limit of the Airy function solution of Eq. (3.49). This procedure selects the Airy function Ai with amplitude proportional to A_{pl}. On the other side, the winding solution coming from Eq. (3.46) can be matched to the Airy solution when written in the form

$$z = \frac{A_{\mathrm{w}}}{(r^2-1)^{1/4}} \cos \frac{1}{2} \left(\int \sqrt{r^2-1} dt - \tan^{-1} \frac{1}{\sqrt{r^2-1}} \right), \tag{3.53}$$

where $A_{\mathrm{w}} = A_{\mathrm{w}}(A_{\mathrm{pl}})$. The matching is achieved by comparing the $r \to 1$ ($t \to 0$) limit of expression (3.53) to the $t \to \infty$ ($s \to -\infty$) limit of the Airy function obtained in the matching procedure with the phase-locked solutions. Expression (3.53) yields:

$$\tan \frac{\theta}{2} = \frac{1}{r}\left[1 + \sqrt{r^2-1} \tan \frac{1}{2}\left(\int \sqrt{r^2-1} dt - \tan^{-1} \frac{1}{\sqrt{r^2-1}} \right)\right] \left(1 - \frac{\dot{r}}{r(r^2-1)}\right). \tag{3.54}$$

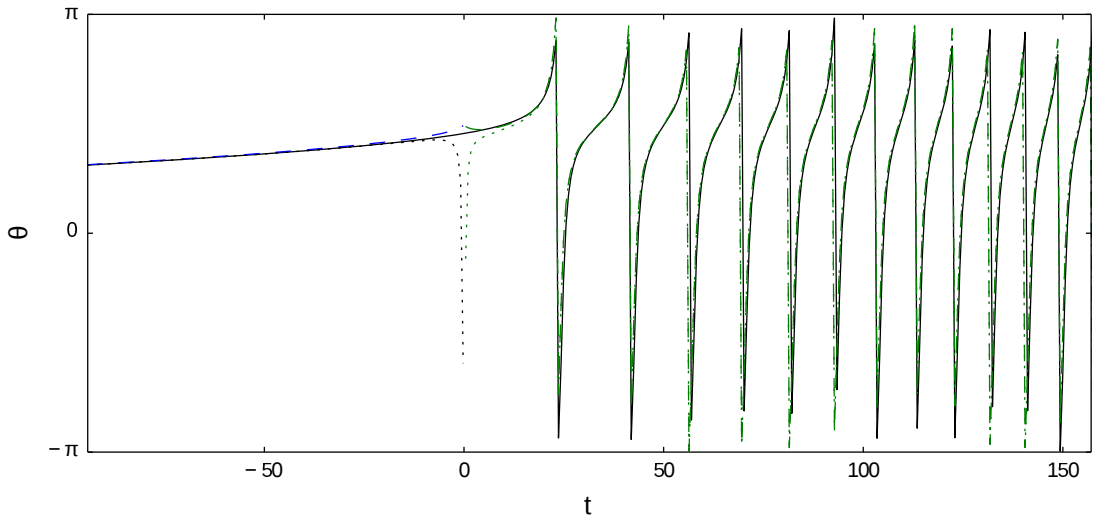

Figure 3.19: The phase $\theta(t)$ mod(2π) near the transition from a phase-locked state to winding from a time simulation of the periodically modulated Adler equation with $T = 2\pi \times 10^3$, $a = 2$, and $r_0 = 0$ (black solid line). The simulation represents the evolution of θ in the time window $[-100, 160]$ of a converged periodic orbit for which $t = 0$ corresponds to $r = 1$. The dashed lines are computed using the adiabatic predictions (3.52) and (3.54) without the "subdominant" term proportional to $\dot{r}$ while the dotted lines take it into account. Predictions in the phase-locked (winding) regime are shown in blue (green) for $t < 0$ ($t > 0$).

Figure 3.19 shows a comparison of the WKB solution in terms of θ with a periodic orbit obtained through simulation with $r(t) = 2\sin(10^{-3}t + \pi/6)$.

The results obtained from the WKB approximation in the limit of a slowly-varying frequency parameter can be generalized using a theorem that places bounds on the number of zeros of solutions to linear second order differential equations. Given an equation of the form

$$\ddot{z} + q(t)z = 0 \tag{3.55}$$

with $q(t) > 0$ in C^2 and bounded, such that $\dot{q}(t) = o\left(q^{3/2}(t)\right)$ as $t \to \infty$, it can be shown [117] that the number of zeros $[n]$ between $0 \le t \le T$ for a given solution $z(t) \neq 0$ is bounded by

$$\left|\pi[n] - \int_0^T \sqrt{q(t)}dt\right| \le \pi + \int_0^T \left|\frac{5\dot{q}^2}{16q^{5/2}} - \frac{\ddot{q}}{4q^{3/2}}\right| dt. \tag{3.56}$$

It follows that when $\dot{q} \ll 1$

$$\pi[n] \sim \int_0^T \sqrt{q(t)}dt \qquad \text{as} \quad T \to \infty, \tag{3.57}$$

thereby reproducing the quasi-static prediction from WKB theory. In the case of the Adler equation, the corresponding frequency parameter is given by

$$q(t) = \frac{r^2 - 1}{4} + \frac{\dot{r}}{2r} + \frac{\ddot{r}}{2r} - \frac{3\dot{r}^2}{4r^2}. \tag{3.58}$$

The conditions on r for the applicability of the bound within the time interval of interest are that $|q(t)| > 0$, $r \in C^4$ and is bounded. We can make some further approximations in the limit that $r = r(\omega t)$ is slowly varying, i.e., $\omega \ll 1$, and the first condition reduces to $|r| + \mathcal{O}(\omega) > 1$. In this adiabatic limit, the integral in the bound becomes

$$\int \sqrt{q(t)}dt = \int \frac{\sqrt{r^2-1}}{2}dt - \tan^{-1}\frac{1}{\sqrt{r^2-1}} + \mathcal{O}(\omega). \tag{3.59}$$

The bound on the number of zeros of the Hill equation translates into a bound on the number of phase slips incurred by a solution to the Adler equation over a given time interval where $q(t) > 0$, i.e., when $r(t)$ is outside of the phase-locking region. We define $n_\pm$ by the integral

$$n_\pm = \frac{1}{\pi}\int_{\mathcal{T}_\pm} \sqrt{q(t)}dt \tag{3.60}$$

over the time interval $\mathcal{T}_\pm$ spent with $q(t) > 0$ and $r(t) > 1$ ($r(t) < -1$) for n_+ (n_-). The bound described above restricts the number of phase slips over $\mathcal{T}_\pm$ to either rounding up or down ($\lfloor n_\pm \rfloor$ or $\lceil n_\pm \rceil$) to order $\mathcal{O}(\omega)$. This is a generalization of the WKB solution in the sense that the bound can apply even when the slowly-varying assumption does not hold. Some care must be taken when applying this bound as $q \to \infty$ as $r \to 0$. The bound applies to positive and negative phase slips separately in order to place a bound on the winding number of a particular trajectory.

The WKB approximation can be used to predict the partitioning of the parameter space by winding number (see Fig. 3.15) by computing the net winding number $N = [n_+] + [n_-]$, where

$$n_\pm = \pm\frac{T}{2\pi^2}\int_{\phi_\pm}^{\pi/2} \sqrt{(r_0 \pm a\sin\phi)^2 - 1}\, d\phi, \tag{3.61}$$

and $r_0 \pm a\sin\phi_\pm = 1$. The first correction from WKB theory cancels because the system always enters and exits the phase-locked region at the same value of r. Replacing the expression in the square root with $q(t)$ provides a way to estimate the winding number from the bound. Figure 4.21 shows a comparison of the resulting prediction with the numerical results in Fig. 3.15. We see that the adiabatic theory agrees well with the numerical results far beyond the low frequency limit for which it was constructed, a conclusion supported by the generalization (3.56).

3.5 Discussion

This chapter has investigated the dynamics of two coupled oscillators when the frequency difference is modulated in time. The same equation describes a multitude of other sys-

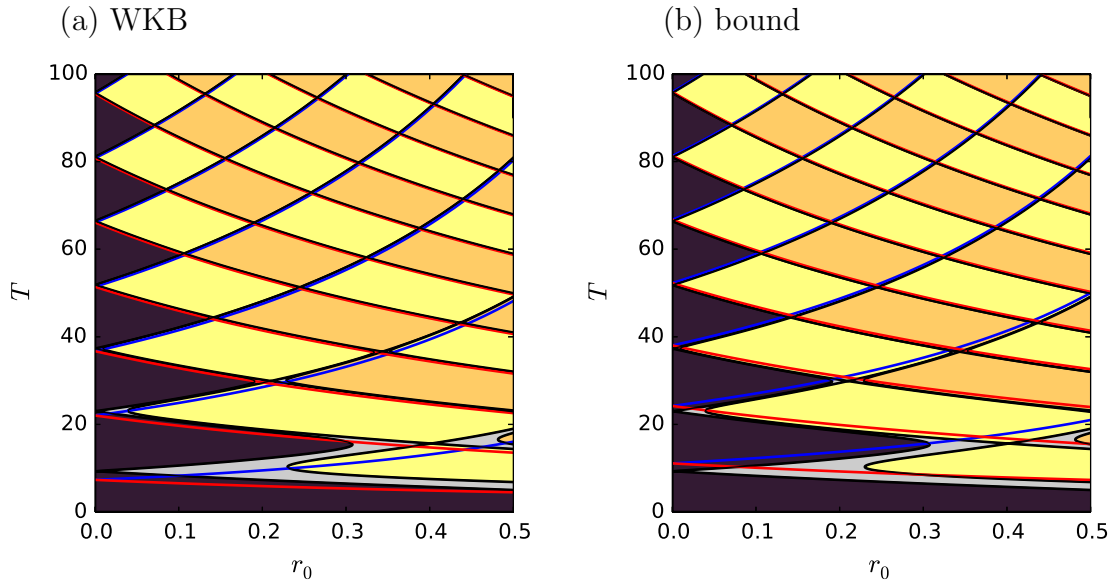

Figure 3.20: Average winding number per period T of the frequency parameter shown in the (r_0, T) plane of the periodically modulated Adler equation for $a = 2$. Colors represent results from numerical simulation: no net phase slips occur over the course of a modulation period in the dark region to the left; the alternating lighter yellow and darker orange regions to the right indicate $1, 2, 3, \ldots$ net phase slips as r_0 increases. The red/blue (negative/positive slope) lines represent predictions of adiabatic theory. The left panel shows the prediction based on the WKB approximation (Eq. (3.61)) while the right panel shows the prediction based on the bound in Eq. (3.57).

tems, ranging from Josephson junctions to systems of large numbers of coupled oscillators. Specifically, the Adler equation [96] with a sinusoidally varying frequency parameter has been studied. The frequency modulation introduces two new parameters into the problem, in addition to the mean frequency difference r_0: the amplitude a and the period T of the modulation. While the autonomous Adler equation leads to phase locking for $-1 \leq r_0 \leq 1$ and persistent drift for $|r_0| > 1$, we have unveiled much richer dynamics that take place when frequency modulation is activated: the phase-locked solutions turn into periodic orbits and the phase difference θ between the oscillators becomes a periodic function of time. The region PO of the existence of these periodic orbits is centered around $r_0 = 0$ and exhibits a succession of sweet spots as a or T increases, interspersed with pinched regions where the width of PO vanishes. The width of these sweet spots decreases with increasing a and T. On either side of PO one finds regions within which the solution grows or decays by one, two, etc. phase slips per modulation cycle. These regions have the same basic structure as the PO region, and are separated by exponentially thin transition zones where the number of phase slips fluctuates from cycle to cycle. This intricate behavior is a consequence of a

sequence of resonances between the time needed for a phase slip and the period of the modulation, and can be described, in an appropriate regime, in terms of an interaction between n:1 and $-n$:1 resonance tongues.

Canard orbits form an essential part of this picture [118]. These are present in the vicinity of the boundaries of the PO region and consist of trajectories that drift along a branch of stable equilibria for part of the cycle; after reaching a fold at which the equilibria lose stability the trajectory drifts for a time along the branch of unstable equilibria, instead of detaching, before an abrupt jump back to a stable equilibrium. Equation (3.38) describes the emergence of such trajectories for low frequency modulation with mean near $r_0 = 0$ and amplitude slightly larger than $a = 1$; Fig. 3.21 shows several examples of the predicted canard solutions, for comparison with the "larger" periodic canard orbits computed numerically in Sec. 3.2.

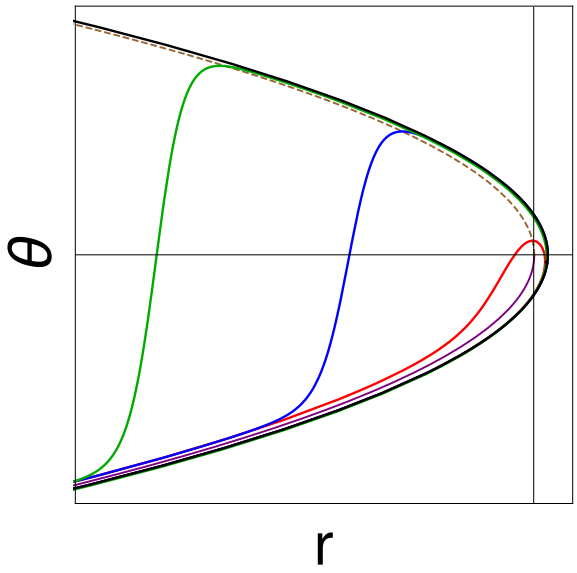

Figure 3.21: Canard behavior in the periodically modulated Adler equation near $r = 1$ in the limit $T \gg 1$ as predicted by Eq. (3.38) for $\nu = -10^{-1}$ (red, inner), -10^{-6} (blue, middle), -10^{-12} (green, outer) and 0 (black). In terms of the parameters of the original problem $\nu \equiv \dfrac{1}{4\pi T}(r_0 + a - 1) - \dfrac{1}{2}$; the horizontal and vertical scales are $r - 1 \sim 1/T$ and $\theta - \pi/2 \sim 1/\sqrt{T}$. The stable (solid purple) and unstable (dashed brown) stationary solutions to the autonomous problem are shown for reference.

Similar behavior has been observed in the partial differential equation description of the dynamics of spatially localized states [49]. In this work, which is described in Ch. 4 the quadratic-cubic Swift–Hohenberg equation (SHE23) is forced in a time-periodic manner and a similar partitioning of parameter space is observed. The reason for this similarity can be traced to the nature of the motion, under parametric forcing, of fronts connecting

a spatially periodic state of SHE23 to the trivial, homogeneous state: the front motion is analogous to repeated phase slips, with each "phase slip" corresponding to a nucleation or annihilation event that adds or subtracts one wavelength of the pattern at either end of the localized structure. However, the resulting partitioning of the parameter space is not symmetric owing to a lack of symmetry between positive and negative "phase slips." An adiabatic theory of the type described here works equally well in SHE23 and its predictions are in excellent agreement with the results of numerical simulations [50]. Indeed SHE23 also displays canards associated with the transitions between different states [51].

The work presented here has a direct application to Josephson junctions driven by an AC current. In the overdamped limit such junctions are modeled by Eq. (3.1) [109], with r representing the external drive and θ the phase difference of the Ginzburg–Landau order parameter across the gap. The so-called supercurrent across the gap is proportional to $\sin\theta$ while the voltage produced corresponds to the derivative $\dot{\theta}$. In this context, phase-locking and phase-slips are closely related to the existence of Shapiro steps [110] for a single Josephson junction. Related dynamics arise in arrays of Josephson junctions that are globally coupled via an LRC circuit [114]. These systems provide a physical realization of the phase-coupled oscillator models at the beginning of this chapter. Using the reduction method of Ref. [99] that has been developed in the context of Josephson junctions, the system of M oscillators in Eq. (3.3) can be recast into the three-dimensional dynamical system

$$\gamma' = \gamma(1-\gamma^2)\cos\Theta, \tag{3.62}$$

$$\Theta' = \gamma r - \sin\Theta, \tag{3.63}$$

$$\Psi' = -\sqrt{1-\gamma^2}\sin\Theta, \tag{3.64}$$

where the prime denotes a derivative with respect to a variable τ defined by $\gamma d\tau = K\tilde{R}dt$ and the time-dependent frequency parameter $\gamma r \equiv \gamma\omega/K\tilde{R} - \alpha'$. Thus the collective dynamics described by Eq. (3.63) also obey an Adler equation, although it has to be solved self-consistently with Eq. (3.62). The solution to Eq. (3.2) in terms of these collective variables is given by

$$\tan\left[\frac{1}{2}(\phi_j - \alpha - \Theta)\right] = \sqrt{\frac{1+\gamma}{1-\gamma}}\tan\left[\frac{1}{2}(\psi_j - \Psi)\right], \tag{3.65}$$

where the ψ_j are constants of motion. The phase Θ is related to the Kuramoto order parameter $R\exp i\Phi \equiv \sum_{m=1}^{M}\exp i\phi_m$ through

$$\left[(1-\gamma^2)\frac{\partial\mathcal{H}}{\partial\gamma} - i\frac{\sqrt{1-\gamma^2}}{\gamma}\frac{\partial\mathcal{H}}{\partial\Psi}\right]\exp(i\Theta) = R\exp\left[i(\Phi-\alpha)\right], \tag{3.66}$$

where

$$\mathcal{H} = \sum_{m=1}^{M}\log\left[\frac{1-\gamma\cos(\psi_m-\Psi)}{\sqrt{1-\gamma^2}}\right]. \tag{3.67}$$

Phase portraits of the dynamics projected onto the (Θ, γ) plane are shown in Fig. 3.22. The oscillators are synchronized for the case depicted in panel (a), while they are not for the case in panel (b).

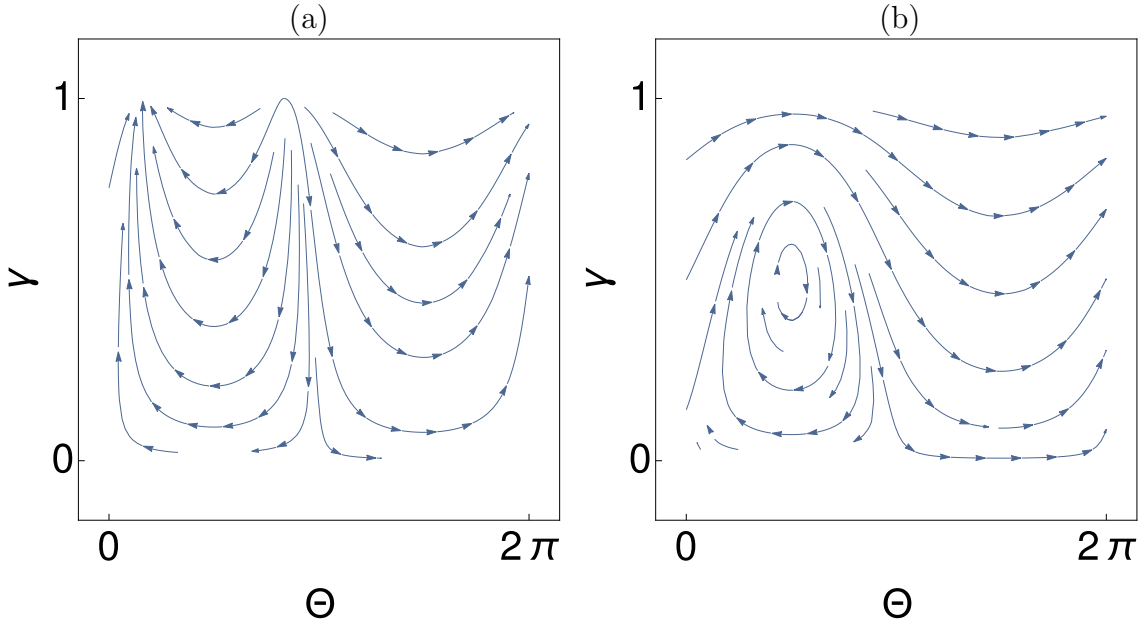

Figure 3.22: Phase portraits of Eqns. (3.62)-(3.64) in the (Θ, γ) plane. (a) $r = 0.5$ (b) $r = 2$.

We see that, while the reduction assumes $\gamma < 1$, the dynamics of the system follows the Adler equation in the $\gamma \to 1$ limit. Noting that Ψ is uncoupled from γ and Θ and defining $\alpha = \gamma/\sqrt{1-\gamma^2}$ allows one to further simplify the description of the dynamics to a dynamical system with Hamiltonian

$$H = r\sqrt{1-\alpha^2} - \alpha \sin\Theta. \tag{3.68}$$

Weakly coupled systems can often be decomposed into two parts with part A obeying dynamics that are largely insensitive to the dynamics of part B. In these circumstances it often suffices to consider system B on its own but with prescribed time-dependence arising from the coupling to A. This is the case, for example, in globally coupled phase oscillator systems, in which each oscillator responds to the global dynamics of the system but the global dynamics are insensitive to the details of the dynamics of an individual oscillator. These systems have properties closely related to the periodically modulated Adler equation studied here. For these reasons we anticipate applications of the techniques developed here to studies of synchronization in oscillator networks. Considering a time-dependent parameter r in the system described by Eq. (3.68) may also provide additional insight into the response of systems of globally coupled oscillators to time-periodic modulation.

Chapter 4

Localized states in systems with time-periodic forcing

Localized states are encountered in systems with a fluctuating or noisy background [119, 120, 121, 122] as well as in periodically driven systems [15, 123, 124, 125, 126, 127, 128]. Temporal forcing has, in general, a number of consequences. In extended systems it may destabilize existing patterns or lead to resonant excitation of new patterns and a variety of phase-locking phenomena [129, 130]. In addition, new structures may be generated by rapid switching between two coexisting attractors [131, 132]. Localized structures may be impacted in two different ways. First, the temporal forcing may render existing localized structures time-dependent, and second, it may generate bistability between a homogeneous state and an extended parametrically driven spatially periodic pattern. The latter case creates a parameter regime where spatially localized time-dependent patterns may be found [133].

In this chapter we focus on time-independent systems supporting spatially localized states and study the effect of time-periodic forcing on these states. For reasons described in Sec. 1.3, we adopt the quadratic-cubic Swift–Hohenberg equation (SHE23) as our model system for localized states. We identify a number of new structures in this system when subjected to time-periodic forcing, including time-dependent breathing states and structures that grow or shrink in an episodic manner. In particular, we identify a resonance phenomenon between the forcing period and the times required to nucleate and annihilate wavelengths of the pattern. This resonance leads to a complex partitioning of the parameter space whose structure can be understood qualitatively, and in some cases quantitatively, using appropriate asymptotics.

The main numerical results of this chapter along with an adiabatic theory were first published in Ref. [49] with a more detailed analysis of the underlying resonance mechanism appearing in Ref. [50]. The properties of canard trajectories associated with the transitions between the partitions of the parameter space were further expanded upon in Ref. [51]. The story is similar to that described for the periodically modulated Adler equation in Ch. 3. The spatial extent of the state plays the role of the phase variable, pinning of the fronts that define the edges of the state plays the role of phase-locking and wavelength nucleations (annihilations) play the role of positive (negative) phase slips.

This chapter is organized as follows. In the next section we summarize pertinent results concerning dynamics of localized states in the autonomous SHE23. In Sec. 4.2 we consider the effect of high frequency temporal forcing of this equation, and then in Sec. 4.3 we focus on the different breathing states present for intermediate frequencies. Low frequency forcing is considered in Sec. 4.4 and in Sec. 4.5 we discuss canard trajectories that track an unstable equilibrium for some time before quickly jumping to a stable one. Finally, we provide brief conclusions in Sec. 4.6. We map out the parameter space of SHE23 using time-simulations instead of numerical continuation as was done in Ch. 3. We are able to analytically study many of the limits considered in Ch. 3 for the periodically forced Adler equation, though the situation is complicated here by the fact that we are dealing with a PDE. These complications make the analysis more challenging both numerically and analytically, but also allow for interesting dynamics not present in the simpler ODE model.

4.1 The quadratic-cubic Swift–Hohenberg equation

The SHE23 serves as a model for pattern formation in a broad range of physical systems. This equation which, in one dimension, takes the form

$$u_t = ru - \left(1 + \partial_x^2\right)^2 u + bu^2 - u^3, \tag{4.1}$$

describes the dynamics of a real field $u(x,t)$ in time. The parameter r specifies the strength of the forcing while the parameter $b > \sqrt{27/38}$ determines the extent of the bistability region between the trivial state $u \equiv 0$ and the patterned state $u_p(x)$, $u_p(x) = u_p(x + 2\pi)$ for all x.

In analogy with Eq. (3.9), we consider the time-depending forcing

$$r = r_0 + \rho \sin \omega t, \tag{4.2}$$

where r_0 is the average value of the forcing, ρ is the amplitude of modulation, and $T = 2\pi/\omega$ is the period. Note that this type of parametric forcing leaves the trivial state $u = 0$ unchanged. In the following we take $b = 1.8$ [134, 135] and use periodic boundary conditions on a domain of $\Gamma = 80\pi$ (i.e. 40 characteristic wavelengths), unless otherwise noted. In addition we impose the symmetry $x \to -x$ of SHE23 on all solutions of the system thereby focusing on *even* solutions. This procedure allows us to perform computations on the half domain. We integrate the equation forward in time using a fourth order exponential time differencing scheme [136] on an equidistributed mesh. Our calculations are performed in Fourier space and fully dealiased. In cases where a larger domain was necessary, the spatial density of grid points is kept constant. Steady state solutions of the constant forcing case were computed using the numerical continuation software AUTO [115]. Appendix A provides a more detailed discussion of the numerical methods used.

Stationary localized states

For $b = 1.8$ and $r \equiv r_0$, a spatially periodic solution u_p bifurcates subcritically from $u = 0$ at $r = 0$. The periodic state passes through a saddle-node at $r_{sn} \approx -0.3744$ gaining stability

and creating a region of bistability with $u = 0$ in $-0.3744 < r < 0$. The Maxwell point between the trivial state $u = 0$ and the periodic state u_p is located at $r_M \approx -0.3126$ within the bistability region. The pinning or snaking region $r_- < r < r_+$ straddles this point ($r_- \approx -0.3390$, $r_+ \approx -0.2593$), and contains a pair of intertwined branches (Fig. 4.1a) of even parity spatially localized states with maxima (L_0) or minima (L_π) at $x = 0$ as described in Sec. 1.3 and with more detail in Ref. [24]. In a finite domain, snaking continues until the domain is (almost) filled with pattern. The solution branches then exit the pinning region and terminate on branches of periodic states near their saddle-node. Throughout this

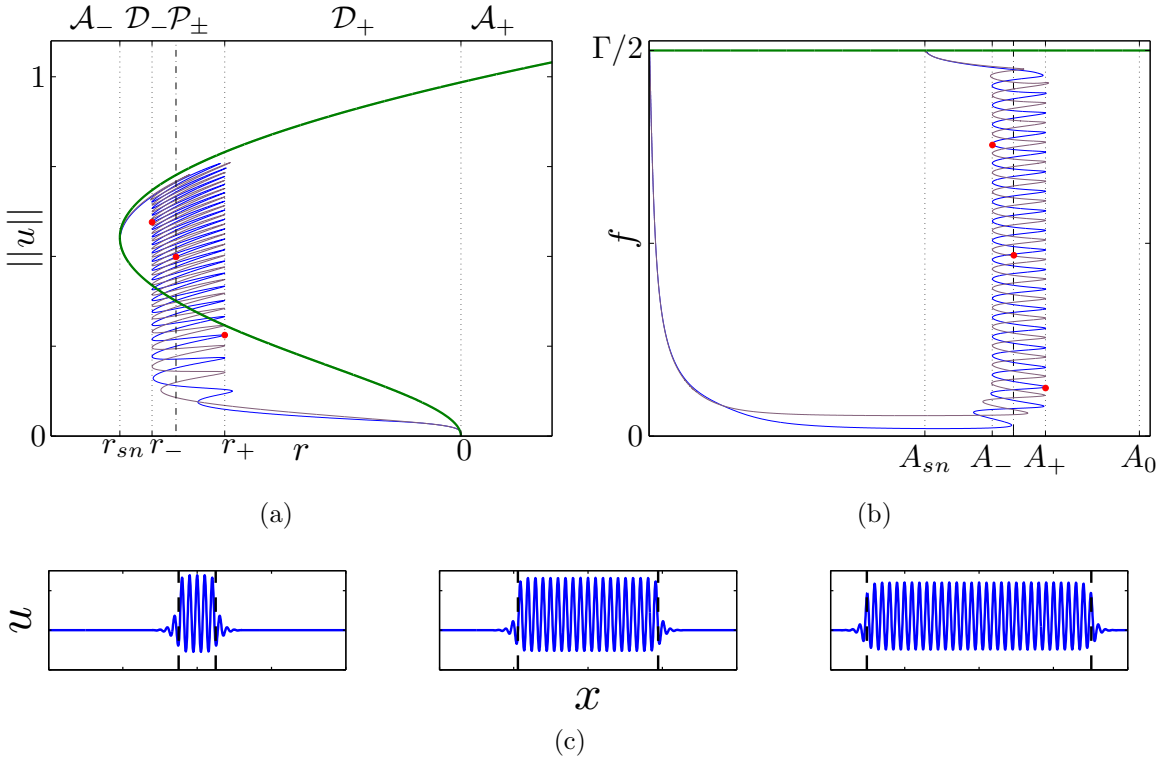

Figure 4.1: (a) Bifurcation diagram showing the normalized L^2 norm $||u|| = \sqrt{\frac{1}{\Gamma}\int_{-\Gamma/2}^{\Gamma/2} u^2\, dx}$ of time-independent solutions of SHE23 as a function of the constant forcing parameter r. Vertical dashed lines delimit the amplitude regime $\mathcal{A}_-$, the depinning regimes $\mathcal{D}_\pm$ and the pinning region $\mathcal{P}_\pm$. The characteristics of each regime are described in the text. (b) The same as (a) but projected on the amplitude $A = \max_x(u)$ and the position $f > 0$ of the right front, as defined in the text. (c) Solutions $u(x)$ corresponding to the red circles in (a) and (b), with black dashed lines indicating the locations $x = \pm f$ of the fronts.

chapter we present our results in terms of the amplitude of the pattern, $A = \max_x(u)$, and the location $x = f$ of the front connecting the pattern to the homogeneous state relative to

the axis of symmetry $x = 0$ of the pattern,

$$f = 2\frac{\int_0^{\Gamma/2} xu^2\, dx}{\int_0^{\Gamma/2} u^2\, dx}. \tag{4.3}$$

Figure 4.1 shows a comparison of the steady state solutions represented in the (A, f) plane to the standard $(r, ||u||)$ bifurcation diagram along with sample solutions. As the amplitude A of snaking localized solutions is comparable to that of the periodic state at the same parameter values, larger values of f indicate broader localized structures. However, between the pinning region and $r = 0$ the solutions broaden to fill the available domain as their amplitude decreases to zero. Thus f increases without bound as $A \to 0$.

Temporal dynamics of localized initial conditions

The gradient structure of SHE23 ensures that spatially localized initial conditions eventually settle on a steady state that is a local mininum of the free energy

$$\mathcal{F}[u] = \frac{1}{\Gamma}\int_{-\Gamma/2}^{\Gamma/2} -\frac{1}{2}ru^2 + \tfrac{1}{2}\left[(1+\partial_x^2)u\right]^2 - \frac{1}{3}bu^3 + \frac{1}{4}u^4\, dx. \tag{4.4}$$

The type of steady state and the transient leading to it depend on r and the initial condition. The relevant regimes organized around the presence of steady spatially localized states can be identified in Fig. 4.1 and are summarized below:

1. Regime $\mathcal{A}_-$: $r < r_{sn}$. Only the trivial state is stable. The dynamics is dominated by an overall amplitude (or body) mode and the amplitude of any localized initial condition decays homogeneously to zero.

2. Regime $\mathcal{D}_-$: $r_{sn} \le r \le r_-$. Two stable states are present: $u = 0$ and u_p, with $\mathcal{F}[0] < \mathcal{F}[u_p]$. Spatially localized initial conditions evolve via a depinning (or edge) mode responsible for the progressive loss of spatial periods while keeping their amplitude constant. The solution collapses to the trivial state only when its extent becomes comparable to one wavelength.

3. Regime $\mathcal{P}_\pm$: $r_- \le r \le r_+$. There is a large number of coexisting stable and unstable states: trivial, spatially periodic and spatially localized with different numbers of periods. The long-time behavior of the system is determined by the basins of attraction of the stable states and hence by the initial conditions provided.

4. Regime $\mathcal{D}_+$: $r_+ \le r \le 0$. The situation is similar to that in $\mathcal{D}_-$ but this time $\mathcal{F}[u_p] < \mathcal{F}[0]$. Spatially localized initial conditions nucleate additional wavelengths under the influence of the depinning mode, and in periodic domains evolve into the spatially periodic state.

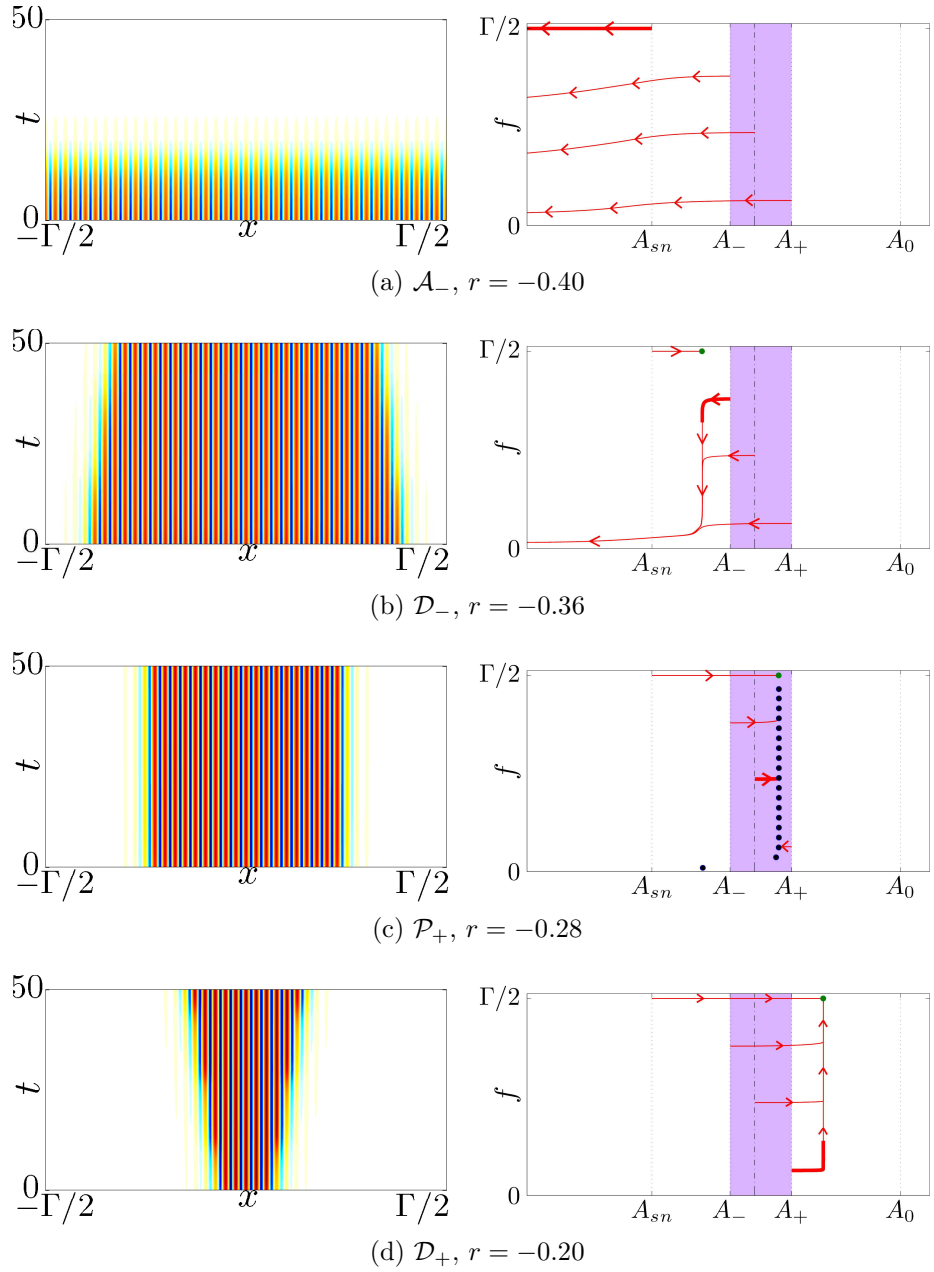

(a) $\mathcal{A}_-$, $r = -0.40$

(b) $\mathcal{D}_-$, $r = -0.36$

(c) $\mathcal{P}_+$, $r = -0.28$

(d) $\mathcal{D}_+$, $r = -0.20$

Figure 4.2: Space-time plots (left panels) and sample phase space trajectories (right panels) illustrating the dynamics of localized solutions of L_0 type in the different parameter regimes of SHE23 with constant forcing in Fig. 4.1, initialized with different values of r. Green dots indicate stable periodic states for the given forcing while blue dots indicate stable localized states. The purple region shows the pinning region.

5. Regime $\mathcal{A}_+$: $r > 0$. The only stable state is the spatially periodic state.

These regimes are depicted in the phase portraits in Fig. 4.2. The computations use L_0 localized solutions from the snaking region, hereafter $u_0(x)$, as initial conditions. These evolve first in A to the appropriate amplitude, followed by depinning if r falls outside the pinning region.

If $r = r_\pm + \delta$, where $|\delta| \ll 1$, the resulting front propagates at an overall constant speed determined by the nucleation time $T^{\rm dpn} \propto |\delta|^{-1/2}$ computed in reference [24]. In this calculation, the solution takes the form $u(x,t) = u_0(x) + \sqrt{|\delta|}a(t)v_\pm(x) + \mathcal{O}(|\delta|)$, where a is the time-dependent amplitude associated with the eigenmode $v_\pm$ that is responsible for triggering a nucleation (+) or annihilation (−) event. The equation that governs the dynamics of a is

$$\alpha_1 \dot{a} = \sqrt{|\delta|}(\alpha_2 \,\mathrm{sgn}(\delta) + \alpha_3 a^2), \tag{4.5}$$

where $\mathrm{sgn}(\delta)$ is the sign of δ and the coefficients α_j for each of the two cases ($r_\pm$) are computed numerically from the following integrals:

$$\alpha_1 = \int_0^{\Gamma/2} v_\pm(x)^2\, dx, \quad \alpha_2 = \int_0^{\Gamma/2} v_\pm(x)u_0(x)\, dx, \quad \alpha_3 = \int_0^{\Gamma/2} v_\pm(x)^3(b - 3u_0(x))\, dx. \tag{4.6}$$

We now discuss the solutions describing a nucleation event near r_+, where $\alpha_3 > 0$; analogous arguments apply in the vicinity of r_-, where $\alpha_3 < 0$. Within the pinning region, $\delta < 0$, a pair of stable and unstable steady state solutions u_0 is present, corresponding to the vicinity of a fold on the right of the snaking branch L_0 (Fig. 4.3(b)) and all initial conditions approach the stable state or diverge. Outside of the pinning region, $\delta > 0$, there are no stable solutions and the amplitude $a \to \infty$ for all initial conditions. The upper panels of Fig. 4.3(a,c) show typical trajectories $a(t)$ corresponding to the dynamics represented by the arrows in Fig. 4.3(b), with the right panel showing three successive nucleation events. We approximate the time between depinning events, i.e. the nucleation time $T_+^{\rm dpn}$, as the time interval between successive asymptotes where a diverges.

Near the fold of the snaking branch L_0 and to its right ($0 < \delta \ll 1$) the system undergoes dynamics on the time scale $\delta^{-1/2}$ [24] and thus $T_+^{\rm dpn} = \mathcal{O}(\delta^{-1/2})$. Upon leaving the vicinity of the fold (i.e. when $a \to \infty$), the system transitions toward the next fold on the snaking branch (Fig. 4.3) before slowing down again. This transition corresponds to a nucleation event that adds a wavelength to each side of $u_0(x)$ and the process repeats at successive folds. Since the structure of $v_+(x)$ is almost independent of the length $2f$ of the localized state (it is an edge mode) the resulting process is periodic, a fact that can be highlighted by introducing the Riccati variable q defined by $a = -\alpha_1\dot{q}/\alpha_3\sqrt{|\delta|}q$. In terms of q, Eq. (4.5) becomes the oscillator equation $\ddot{q} + \delta\Omega_+^2 q = 0$, where $\Omega_+^2 \equiv \alpha_2\alpha_3/\alpha_1^2 > 0$. The lower panels of Fig. 4.3(a,c) show the oscillator amplitude $q(t)$ corresponding to the $a(t)$ solutions shown just above. In summary, we have the generation of periodic dynamics through the collision of two fixed points at $\delta = 0$ and the period of the motion scales like $T \sim 1/\sqrt{\delta}$. A similar discussion applies to annihilation events near $r = r_-$. It is in this sense that we call the fold bifurcations at the edges of the pinning region SNIPER bifurcations and can think of the Adler equation as a qualitative description of the front dynamics. However, care must be

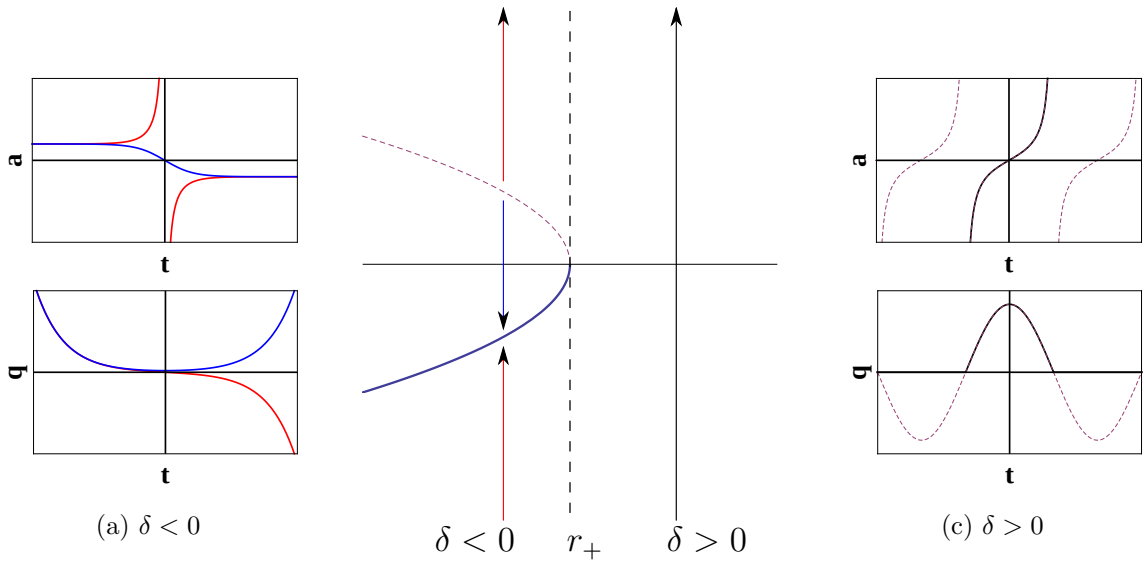

(a) $\delta < 0$

(b) Stability diagram

(c) $\delta > 0$

Figure 4.3: Amplitude of the depinning mode of SHE23 with constant forcing in terms of $a(t)$ (upper panels) and $q(t)$ (lower panels) near r_+ for (a) $\delta < 0$ and (c) $\delta > 0$; (b) shows the corresponding bifurcation diagram. Panels in (c) show three successive nucleation events corresponding to times where $a(t) \to \infty$ (top panel) or $q(t) = 0$ (lower panel).

taken in the interpretation of this equation, because $q \to 0$ implies $a \to \infty$ while Eq. (4.5) breaks down already when $a = \mathcal{O}(\delta^{-1/2})$. Despite this caveat we shall find the variable q useful since it highlights the possibility of a temporal resonance when SHE23 is periodically forced in time. It also provides a clear analogy to the periodically modulated Adler equation discussed in Ch. 3.

Figure 4.4 compares the leading order theoretical prediction $T_+^{\rm dpn} = \pi/\sqrt{\delta}\Omega_+$ obtained from Eq. (4.5) (dashed lines) with numerical simulations of SHE23. The theory works well for $0 < \delta \ll 1$ but improved agreement can be obtained using a numerical fit to the results of the simulations. Motivated by the leading order theory we seek a fit of the form $(T^{\rm dpn})^{-1} = \sum \sigma_n \delta^{n/2}$, $n \geq 1$, and compute the coefficients σ_n using the method of least squares. A fifth order truncation accounts accurately for the results in Fig. 4.4 even when $r \sim r_{sn}$. The figure shows the nucleation time in $\mathcal{D}_+$ (red) and annihilation time in $\mathcal{D}_-$ (blue). The symbols represent results from simulations, the dashed lines represent the prediction from the leading order asymptotic theory, while the solid lines represent the fifth order numerical fit. The times $T^{\rm col}$ for a marginally stable periodic state at r_{sn} (black crosses) and a localized state at r_- (black diamonds) to reach the trivial state by amplitude decay in $\mathcal{A}_-$ are shown in black. The black dashed line represents the leading order asymptotic theory applied to the periodic state near r_{sn}. The coefficients σ_n for both the asymptotic theory and the fifth order numerical fit for our choice of parameters are summarized in table 4.1. We will find

that the numerical fit is required for quantitative agreement between the theory presented in Sec. 4.4 and numerical simulations presented in Sec. 4.3. However, the theory cannot be applied directly to localized states in $\mathcal{A}_-$ since these states undergo both amplitude decay *and* depinning.

	Ω	σ_1	σ_2	σ_3	σ_4	σ_5
$T_+^{\rm dpn}$	0.5285	0.1687	0.1141	0.7709	-0.4000	0.0803
$T_-^{\rm dpn}$	0.7519	0.2381	-0.8445	33.37	-306.4	1067
$T_{sn}^{\rm col}$	0.7705	0.4829	-1.738	10.62	-35.00	48.31
$T_{\rm loc}^{\rm col}$	-	0.2081	0.4431	2.962	-34.15	79.52

Table 4.1: Values of the coefficients σ_j determined from a least squares fit of the depinning/collapse time to simulations of SHE23 with constant forcing of the form $T^{-1} = \sum_{n=1}^{5} \sigma_n |r - r_{\pm,sn}|^{n/2}$. The frequency Ω is calculated numerically from the integrals in Eq. (4.6) in each case.

4.2 The high frequency limit

We begin our study of the effects of time-periodic forcing on localized states by considering the limit of fast oscillations. We first consider the case when the frequency of the forcing cycle is so fast that the motion of the fronts does not permit nucleation/annihilation of additional/existing periods. We then increase the amplitude of the forcing cycle so that the structure remains unpinned for an appreciable amount of time.

The averaged system

The qualitative behavior of Eq. (4.1) is unchanged when the forcing frequency is high enough that insufficient time is spent outside of the pinning region for depinning to occur. The effect of the periodic forcing in this case is small, producing rapid amplitude fluctuations of the existing localized states. We introduce the effective Maxwell point $\bar{r}_M$ using the relation

$$\langle \mathcal{F}[u] \rangle = 0, \tag{4.7}$$

where the brackets indicate an average over the forcing cycle. We assume that the periodic forcing occurs at a high frequency, $\omega \to \omega/\epsilon$, where $\epsilon \ll 1$ and define a fast timescale $\phi = \omega t/\epsilon$. We seek solutions of Eq. (4.1) in the form $u(x,t) = u_0(x,t,\phi) + \epsilon u_1(x,t,\phi) + \epsilon^2 u_2(x,t,\phi) + \ldots$, satisfying

$$\omega \partial_\phi u = \epsilon \left[(r_0 + \rho \sin\phi) u - \left(1 + \partial_x^2\right)^2 u + b u^2 - u^3 - \partial_t u \right], \tag{4.8}$$

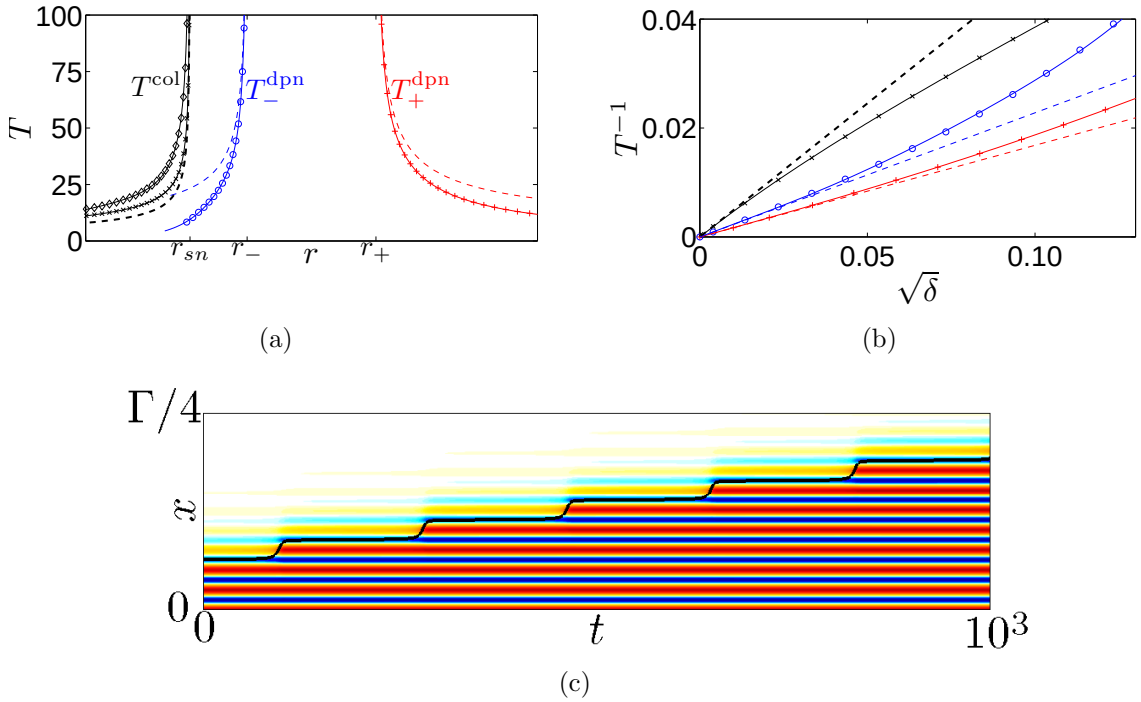

Figure 4.4: For SHE23 with constant forcing, (a) the time between nucleation events ($T_+^{\rm dpn}$, red crosses), annihilation events ($T_-^{\rm dpn}$, blue circles) and the time for the spatially periodic state to collapse to the trivial state ($T_{sn}^{\rm col}$, black crosses) as functions of the parameter r, starting from marginally stable L_0 solutions at $r = r_+$, $r = r_-$ and the periodic state at $r = r_{sn}$, respectively. The symbols show results from direct numerical simulations, the solid lines are fits to this data, and the dashed lines are predictions from the leading order theory in [24]. The corresponding results for the collapse time for a localized state at r_- are also shown ($T_{\rm loc}^{\rm col}$, black diamonds). (b) Comparison between numerical data (circles/crosses) and the leading order theory (dashed lines), showing $(T_\pm^{\rm dpn})^{-1}$ as a function of the square root of the distance δ from the pinning region. The corresponding fifth order fits are shown using solid lines. (c) A space-time representation of a simulation at $r \approx -0.2583$ ($\delta \approx 0.001$) initialized using a marginally stable localized solution at r_+, with red representing high values and blue low values of $u(x)$. The solid black line shows the instantaneous front position $x = f(t)$.

where t is the original timescale on which the averaged dynamics take place, and assume that $\rho, r_0, b, \omega = \mathcal{O}(1)$. The leading order equation $(u_0)_\phi = 0$ gives $u_0(x,t,\phi) = A_0(x,t)$. At order $\mathcal{O}(\epsilon)$, we obtain

$$\omega\partial_\phi u_1 = (r_0 + \rho\sin\phi)u_0 - \left(1+\partial_x^2\right)^2 u_0 + bu_0^2 - u_0^3 - \partial_t u_0. \tag{4.9}$$

The solvability condition requires that the integral over a single period of the fast oscillation of the right side of Eq. (4.9) vanishes. This condition yields the governing equation for A_0:

$$\partial_t A_0 = r_0 A_0 - \left(1+\partial_x^2\right)^2 A_0 + bA_0^2 - A_0^3. \tag{4.10}$$

Thus, in the limit of a high frequency forcing cycle with order unity amplitude, the leading order behavior follows the time-independent SHE23. Corrections arise at second order, as we now show.

Equations (4.9) and (4.10) show that the $\mathcal{O}(\epsilon)$ correction to the leading order behavior is given by

$$u_1(x,t,\phi) = -\tfrac{\rho}{\omega}\cos\phi A_0(x,t) + A_1(x,t). \tag{4.11}$$

At $\mathcal{O}(\epsilon^2)$ we obtain

$$\omega\partial_\phi u_2 = (r_0+\rho\sin\phi)u_1 - \left(1+\partial_x^2\right)^2 u_1 + 2bu_0u_1 - 3u_0^2u_1 - \partial_t u_1 \tag{4.12}$$

leading to the solvability condition

$$\partial_t A_1 = r_0 A_1 - \left(1+\partial_x^2\right)^2 A_1 + 2bA_0A_1 - 3A_0^2A_1. \tag{4.13}$$

Similarly, the second order correction to the solution takes the form

$$u_2 = \frac{\rho^2}{4\omega^2}\cos 2\phi A_0(x,t) - \frac{\rho}{\omega^2}\sin\phi\left(bA_0(x,t)^2 - 2A_0(x,t)^3\right) - \frac{\rho}{\omega}\cos\phi A_1(x,t) + A_2(x,t), \tag{4.14}$$

and we obtain, at $\mathcal{O}(\epsilon^3)$,

$$\omega\partial_\phi u_3 = (r_0+\rho\sin\phi)u_2 - \left(1+\partial_x^2\right)^2 u_2 + 2bu_0u_2 - 3u_0^2u_2 + bu_1^2 - 3u_0u_1^2 - \partial_t u_2, \tag{4.15}$$

yielding

$$\partial_t A_2 = r_0 A_2 - \left(1+\partial_x^2\right)^2 A_2 + b(2A_0A_2 + A_1^2) - 3(A_0^2A_2 + A_0A_1^2) - \tfrac{1}{2}\left(\tfrac{\rho}{\omega}\right)^2 A_0^3. \tag{4.16}$$

We can define an averaged variable with error at order $\mathcal{O}(\epsilon^3)$ that describes the dynamics on the long timescale:

$$A \equiv \frac{1}{2\pi}\int_0^{2\pi}\left(u_0 + \epsilon u_1 + \epsilon^2 u_2\right)\, d\phi = A_0 + \epsilon A_1 + \epsilon^2 A_2. \tag{4.17}$$

On summing the solvability conditions, we obtain the following equation for the dynamics of the averaged variable

$$\partial_t A = r_0 A - \left(1+\partial_x^2\right)^2 A + bA^2 - \left[1 + \frac{1}{8\pi^2}\left(\rho T\right)^2\right] A^3 + \mathcal{O}(T^3), \tag{4.18}$$

where, for clarity, we have introduced the period of the forcing cycle $T \equiv 2\pi\epsilon/\omega$. The result is an SHE23 with a modified cubic term.

We find that the averaged Maxwell point of the system, defined by Eq. (4.7), is in fact the Maxwell point of the averaged system (4.18). This can be checked explicitly by noting that

$$\bar{\mathcal{F}}[A] = \langle \mathcal{F}_0[u_0 + \epsilon u_1 + \epsilon^2 u_2] \rangle + \mathcal{O}(\epsilon^3), \tag{4.19}$$

where $\bar{\mathcal{F}}$ is the free energy of the averaged system with periodic forcing, $\mathcal{F}_0$ is the free energy of the system with a constant forcing r_0, and the average is over a forcing cycle. Furthermore,

$$\bar{\mathcal{F}}[A] = \mathcal{F}_0[u_0] + \frac{\rho^2 T^2}{32\pi^2\Gamma} \int_{-\Gamma/2}^{\Gamma/2} u_0^4 \, dx + \mathcal{O}(T^3), \tag{4.20}$$

implying that the free energy in the fluctuating system is greater than that of the system with constant forcing r_0. We can use this expression to calculate the frequency-induced shift of the Maxwell point explicitly by finding the value of r where $\bar{\mathcal{F}}[A] = 0$. Because the periodic forcing has increased the energy of the spatially periodic state, the Maxwell point of the averaged system necessarily shifts to the right ($\bar{r}_M > r_M$) to compensate while the boundaries of the pinning region also shift to the right. Following [24] we obtain

$$\bar{r}_\pm = r_\pm + \frac{\rho^2 T^2}{8\pi^2} \frac{\int_{-\Gamma/2}^{\Gamma/2} u_0^3 v_\pm \, dx}{\int_{-\Gamma/2}^{\Gamma/2} u_0 v_\pm \, dx}. \tag{4.21}$$

Here u_0 is the marginally stable solution of the constant forcing system at $r_\pm$, and $v_\pm$ are the eigenmodes of the linearized problem at $r_\pm$ responsible for wavelength nucleation/annihilation. Both integrals are positive and we find that

$$2\bar{p} \equiv \bar{r}_+ - \bar{r}_- \approx 2p - 0.0039(\rho T)^2, \tag{4.22}$$

where $p = (r_+ - r_-)/2$ is the half-width of the pinning region in the constant forcing case. Thus the introduction of the periodic forcing *shrinks* the width of the pinning region and shifts it to the right.

Large amplitude forcing

We may repeat the above calculation in the case $\rho \to \rho/\epsilon$ so that we are now dealing with fast oscillations with a large amplitude. This allows the system to spend enough time outside of the pinning region for depinning to take place. However, in this limit, a large fraction of the forcing cycle is actually spent in the amplitude decay/growth regimes $\mathcal{A}_\pm$, and thus the leading order dynamics will not be comprised simply of nucleation and annihilation events. This regime is described by the equation

$$\omega\partial_\phi u - \rho\sin(\phi)u = \epsilon\left[r_0 u - \left(1 + \partial_x^2\right)^2 u + bu^2 - u^3 - \partial_t u\right], \tag{4.23}$$

where $r_0, b, \rho = \mathcal{O}(1)$, and we look for solutions in the form $u = u_0 + \epsilon u_1 + \epsilon^2 u_2 + \dots$. At leading order we obtain $(\omega u_0)_\phi - \rho \sin(\phi) u_0 = 0$, with solution

$$u_0(x,t,\phi) = e^{-(\rho/\omega)\cos\phi} A_0(x,t). \tag{4.24}$$

At $\mathcal{O}(\epsilon)$, the governing equation becomes

$$\omega \partial_\phi u_1 - \rho \sin(\phi) u_1 = r_0 u_0 - \left(1 + \partial_x^2\right)^2 u_0 + b u_0^2 - u_0^3 - \partial_t u_0. \tag{4.25}$$

Imposing the requirement that u_1 is periodic on the fast timescale leads to the solvability condition $\int \mathrm{RHS}\, e^{(\rho/\omega)\cos\phi}\, d\phi = 0$, where RHS stands for the right-hand side of Eq. (4.25), and an evolution equation for A_0:

$$\partial_t A_0 = r_0 A_0 - \left(1 + \partial_x^2\right)^2 A_0 + b I_0(\tfrac{\rho}{\omega}) A_0^2 - I_0(\tfrac{2\rho}{\omega}) A_0^3. \tag{4.26}$$

Here $I_0(x)$ is the modified Bessel function of the first kind. Thus the slowly evolving amplitude A_0 of the leading order solution u_0 satisfies an SHE23 with modified coefficients.

The correction u_1 to the leading order solution can be found by integrating Eq. (4.25) using the integrating factor $e^{(\rho/\omega)\cos\phi}$ and substituting in Eqs. (4.24) and (4.26):

$$u_1(x,t,\phi) = \tfrac{1}{\omega} e^{-(\rho/\omega)\cos\phi} \left[J(\tfrac{\rho}{\omega}, \phi) b A_0(x,t)^2 - J(\tfrac{2\rho}{\omega}, \phi) A_0(x,t)^3 + \omega A_1(x,t) \right], \tag{4.27}$$

where A_1 is yet to be determined. The time-dependent coefficients, which are periodic in the fast time ϕ, are given in terms of the integral

$$J(\gamma, \phi) = \int_0^\phi \left[e^{-\gamma \cos\psi} - I_0(\gamma) \right] \mathrm{d}\psi, \tag{4.28}$$

where $\gamma = \rho/\omega$, $2\rho/\omega$. At $\mathcal{O}(\epsilon^2)$ we obtain

$$\omega \partial_\phi u_2 - \rho \sin(\phi) u_2 = r_0 u_1 - \left(1 + \partial_x^2\right)^2 u_1 + 2 b u_0 u_1 - 3 u_0^2 u_1 - \partial_t u_1 \tag{4.29}$$

and the solvability condition can be written in the form

$$\begin{aligned} \frac{1}{2\pi} \int_0^{2\pi} \mathrm{d}\phi \Big[r_0 - \left(1 + \partial_x^2\right)^2 - \partial_t + 2b e^{-(\rho/\omega)\cos\phi} A_0(x,t) - 3 e^{-2(\rho/\omega)\cos\phi} A_0(x,t)^2 \Big] \\ \times \left(J(\tfrac{\rho}{\omega}, \phi) b A_0(x,\tau)^2 - J(\tfrac{2\rho}{\omega}, \phi) A_0(x,\tau)^3 + A_1(x,\tau) \right) = 0. \end{aligned} \tag{4.30}$$

The solvability condition can be simplified by defining the integral

$$K(\sigma, \gamma, \phi) = \int_0^\phi e^{-\sigma \cos\psi} J(\gamma, \psi)\, \mathrm{d}\psi \tag{4.31}$$

and noting that $K(\sigma, \gamma, 2\pi) = 0$. The result is

$$\partial_t A_1 = \left[r_0 - \left(1 + \partial_x^2\right)^2 \right] A_1 + 2 b I_0(\tfrac{\rho}{\omega}) A_0 A_1 - 3 I_0(\tfrac{2\rho}{\omega}) A_0^2 A_1. \tag{4.32}$$

We can now define the averaged amplitude $A \equiv A_0 + \epsilon A_1$ by

$$I_0\left(\tfrac{\rho}{\omega}\right) A = \frac{1}{2\pi}\int_0^{2\pi} u_0 + \epsilon u_1 \, \mathrm{d}\phi \,; \tag{4.33}$$

this amplitude satisfies the equation

$$\partial_t A = r_0 A - \left(1 + \partial_x^2\right)^2 A + b I_0(\tfrac{\rho}{\omega}) A^2 - I_0(\tfrac{2\rho}{\omega}) A^3 + \mathcal{O}(\epsilon^2). \tag{4.34}$$

Thus there is no additional correction at $\mathcal{O}(\epsilon)$ and the averaged dynamics follows a Swift–Hohenberg equation with modified nonlinear coefficients up to $\mathcal{O}(\epsilon^2)$.

In contrast to the $\rho \sim \mathcal{O}(1)$ case, the cubic nonlinearity is now dramatically increased relative to the quadratic one. This results in a rapid decrease in the region of bistability of the averaged equation (4.34) as ρ/ω increases. For $b = 1.8$, the region of bistability disappears at $\rho/\omega \approx 7.02$ when the bifurcation that creates the periodic state transitions from subcritical to supercritical. Thus the region of existence of periodic orbits in the high frequency, large amplitude limit narrows as it shifts towards increasing r_0 and eventually disappears at $r_0 = 0$ when $\rho/\omega \approx 7.02$. Figure 4.5 shows the predicted edges of the region of existence of localized states that remain stationary on average in the $(r_0, \rho/\omega)$ plane for $b = 1.8$.

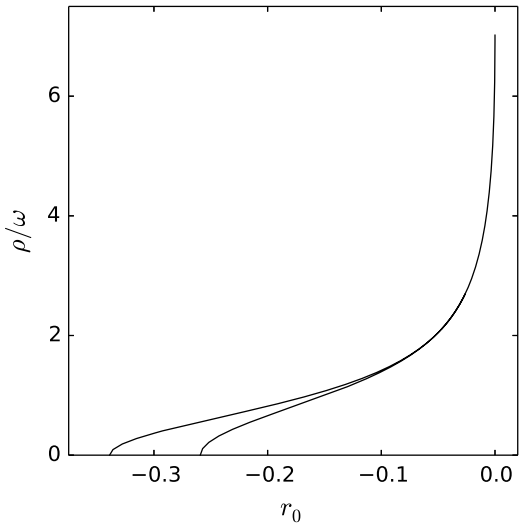

Figure 4.5: The edges of the region where localized states remain stationary on average in the large amplitude, high frequency limit of SHE23 with time-periodic forcing as predicted by Eq. (4.34). The $(r_0, \rho/\omega)$ plane is depicted with using the parameter $b = 1.8$. This region in the analogous limit for the periodically modulated Adler equation is shown in Fig. 3.6.

We note that the result in this high frequency, large amplitude limit qualitatively differs from the analogous limit for the nonautonomous Adler equation presented in Sec. 3.2

(compare Fig. 3.6 to Fig. 4.5). The amplitude dynamics that occur outside of the region of bistability in SHE23 are responsible for the demise of localized states that remain stationary on average in this limit. This is manifested by the appearance of modified Bessel functions in Eq. (4.26) for SHE23 as opposed to the Bessel function found in Eq. (3.28) for the Adler equation.

4.3 Intermediate frequencies: Breathing localized structures

We now move away from the high frequency limit and investigate parameter combinations that permit depinning. For this purpose we consider parameter excursions that allow the system to traverse $\mathcal{P}_\pm$ and spend a significant time in both $\mathcal{D}_+$ and $\mathcal{D}_-$, i.e., we take $r_- < r_0 < r_+$, and $\rho > p$, where $p \equiv (r_+ - r_-)/2$ is the half-width of the pinning region. The resulting structures oscillate in width and amplitude and we refer to them as "breathing" localized structures. The numerical results of this section rely on time-simulation as opposed to numerical continuation that was employed for the computation of periodic orbits and winding trajectories in the periodically modulated Adler equation (Ch. 3).

The fate of stable localized initial conditions

Figure 4.6 shows sample results for $\rho = 0.1$, $r_0 = -0.28$, in each case starting from the same stable spatially localized L_0 solution of the time-independent problem $r \equiv r_0$. The figure shows that, depending on T, the solution can undergo growth/decay through a depinning-like process (Fig. 4.6(a,c)), decay to the trivial state via an amplitude mode (Fig. 4.6(d)), or take the form of a periodic orbit corresponding to a localized solution with no net motion of the fronts (Fig. 4.6(b)). Moreover, the growth/decay of new wavelengths can occur regularly from one period of the forcing to the next, or in a seemingly irregular way. In particular, Fig. 4.6(a) shows a growth scenario for $T = 50$ in which the solution grows in length by one wavelength on each side after approximately three cycles of the forcing. This process is irregular in the sense that the number of nucleation and decay events is not constant from one period of the forcing to the next. It is also interesting to note that this simulation does not reach the spatially periodic state, but instead approaches an oscillating state with a defect at the edge of the periodic domain. In contrast, Fig. 4.6(c), obtained for $T = 250$, shows a very regular pattern of five nucleations events followed by six decay events during the course of each forcing cycle, resulting in an overall decay of the state. Finally, Fig. 4.6(d) for $T = 350$ shows an initial growth phase followed by abrupt amplitude decay to the trivial state.

Although the wavelength of a localized solution depends on the forcing parameter r, it is always near the preferred wavelength 2π, and thus f undergoes abrupt jumps by approximately 2π whenever the fronts depin. These jumps are most evident during the growth phase since the time between nucleations is longer than the time between annihilations. The

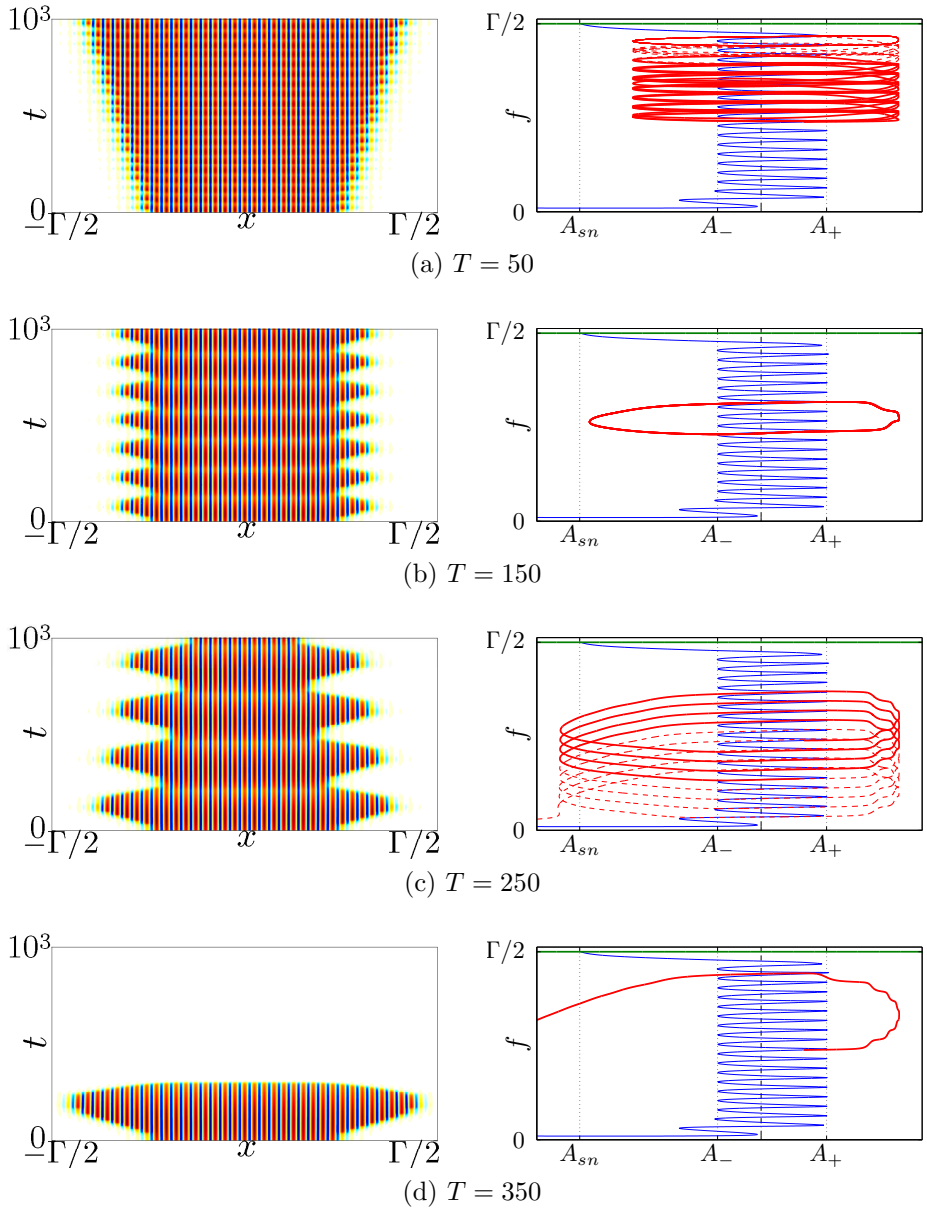

(a) $T = 50$

(b) $T = 150$

(c) $T = 250$

(d) $T = 350$

Figure 4.6: Space-time plots (left panels) and the corresponding phase space trajectories (right panels) for solutions of the periodically forced SHE23 with $r(t) = -0.28 + 0.1\sin(2\pi t/T)$, $b = 1.8$, initialized using an L_0 solution at $r = -0.28$. The red dashed lines in the right panels correspond to evolution past the time window represented in the left panels, while the green lines represent spatially periodic solutions of the time-independent case. The period T is indicated below each plot. The trajectory in (a) terminates on time-periodic defect state.

results shown in Fig. 4.6 are independent of the length of the initial stable state selected for the simulation, provided that $6\pi \lesssim f \lesssim \Gamma/2 - 6\pi$ throughout the simulation, i.e., provided the structure remains well localized. We likewise report that the initial phase of oscillation does not affect the dynamics.

We distinguish periodic orbits from growing and decaying orbits using the instantaneous front velocity V_f defined by the relation $V_f \equiv \dot{f}$. We look at the averaged front velocity $\langle V_f \rangle$ over a cycle period (calculated for oscillation periods for which $6\pi \lesssim f \lesssim \Gamma/2 - 6\pi$ and disregarding the first oscillation period), and consider an orbit periodic if $|\langle V_f \rangle| < 10^{-4}$ (corresponding to no net nucleation or annihilation within a time period of about 6×10^4 units). For example, the orbit shown in Fig. 4.6(b) is deemed periodic since $|\langle V_f \rangle|$ falls below the cut-off value of 10^{-4} after 12 periods of the forcing cycle (in fact $|\langle V_f \rangle|$ is still decreasing, even after the 1800 units of time). For decaying and growing orbits, the average change in the front position $\langle \Delta f \rangle$ over one cycle helps distinguish the regular behavior in Fig. 4.6(c) where $\langle \Delta f \rangle / 2\pi \approx 1.0108$ from the irregular dynamics in Fig. 4.6(a) where $\langle \Delta f \rangle / 2\pi \approx 0.3087$: regular dynamics translate into $\langle \Delta f \rangle$ close to an integer number of nucleation/decay events ($\langle \Delta f \rangle \approx 2n\pi$).

Spatially localized periodic orbits

We now investigate the existence of periodic orbits like the state exemplified in Fig. 4.6(b). For $\rho = 0.1$, we do a parameter scan varying the mean forcing amplitude $r_- \leq r_0 \leq r_+$ in steps of $\Delta r_0 = 10^{-4}$ and the oscillation period $10 \leq T \leq 400$ in steps of $\Delta T = 1$. At each point a simulation is run to calculate $\langle V_f \rangle$ initialized with a steady state localized solution at $r \equiv r_0$. In most cases the simulations were run for 2000 units of time (4000 units were necessary for the longer oscillation periods). The results are shown in Fig. 4.7. The region where $|\langle V_f \rangle| < 10^{-4}$ is labeled *PO* and corresponds to parameter values at which periodic orbits are found. For short periods T for which there is insufficient time for nucleation or annihilation within a cycle, the region of periodic orbits spans nearly the whole pinning region (bottom part of Fig. 4.7). With increasing T the range of existence of periodic orbits narrows as predicted by the theory in Sec. 4.2 for fast oscillations but does not do so monotonically. The figure reveals that *sweet spots* where the range is larger than in the *pinched regions* above and below occur at regular intervals of the forcing cycle period. For $\rho = 0.1$, the pinched regions are separated by $\Delta T \approx 43$. The region of existence of periodic orbits is asymmetric owing to major differences in the depinning dynamics in regimes $\mathcal{D}_-$ and $\mathcal{D}_+$. Moreover, the region slants to higher values of the forcing as the period T increases, a property that is related to the additional time spent in regime $\mathcal{A}_-$ during the decay phase. Region *PO* eventually asymptotes to $r_0 \approx -0.2744$ as $T \to \infty$, the threshold for entering regime $\mathcal{A}_-$, where amplitude decay takes over from depinning as the leading mode of decay. In contrast to the high frequency case, here the Maxwell point determined from the time-averaged free energy moves to lower values of r and is no longer a good predictor of the region of periodic orbits. Despite this, the high frequency prediction of the width of the pinning region in Eq. (4.22) remains within $\sim 10\%$ of the results of numerical simulation with $\rho = 0.1$

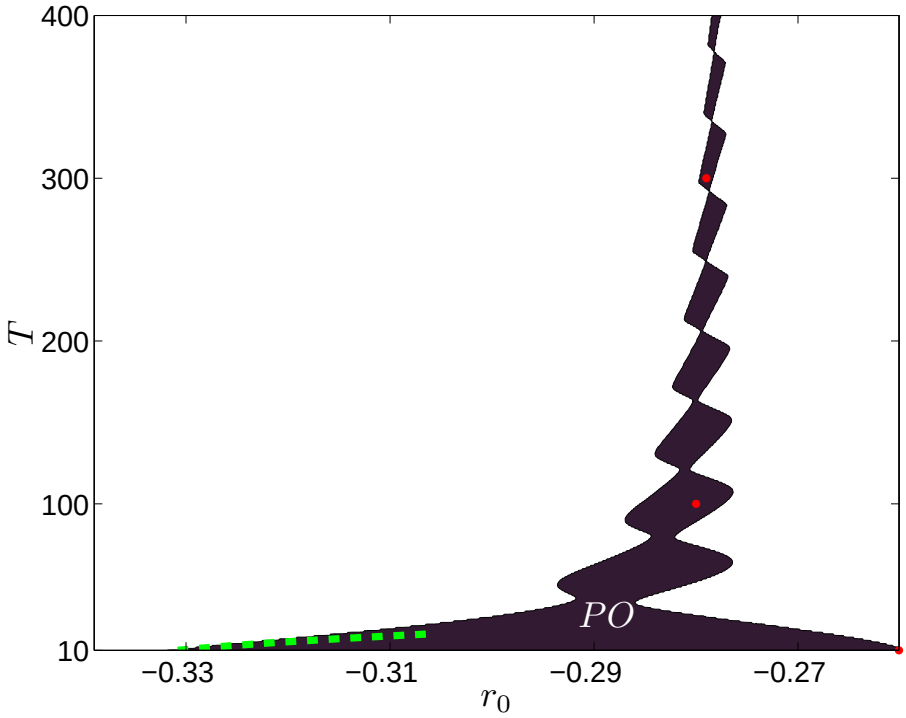

Figure 4.7: Diagram showing the region of existence of periodic orbits PO (shaded region) of the periodically forced SHE23 as defined by $|\langle V_f \rangle| < 10^{-4}$ for oscillation amplitude $\rho = 0.1$. The simulations are initialized with a L_0 solution that is stable for constant forcing r_0. The range of r_0 shown corresponds to the pinning interval (r_-, r_+) in the time-independent case. The three dots (lower right corner, 2nd and 7th sweet spots from bottom) indicate parameter values for the periodic orbits shown in Fig. 4.8. The green dashed line shows the predicted location of the left edge of PO for $10 \leq T \leq 20$ from the high-frequency theory of Sec. 4.2.

and $T = 10$, even though the $\omega \gg 1$ assumption no longer applies. Numerical continuation indicates that the analogous pinched regions for the Adler equation in fact narrow to a single point (cf. Fig. 3.3). The first several pinched regions of SHE23, on the other hand, have a finite width up to the precision at which we are able to compute the periodic orbits and the location of the pinching in parameter space. It is unclear whether this discrepancy is real or just an artifact of the numerics.

Figure 4.8 shows three different stable periodic orbits from different sweet spots, corresponding to $T = 10$, 100 and 300. The left panels indicate that these solutions are converged to machine precision and do not seem to suffer from slow instabilities, while the remaining panels provide insight into the balance between growth and decay over the course of the cycle period. Figure 4.8(a), for $T = 10$, shows a periodic pulsation in amplitude but no front motion. Figure 4.8(b), for $T = 100$, reveals a periodic orbit characterized by both amplitude and front oscillation as does Fig. 4.8(c) for $T = 300$. The $T = 100$ orbit, which is located in

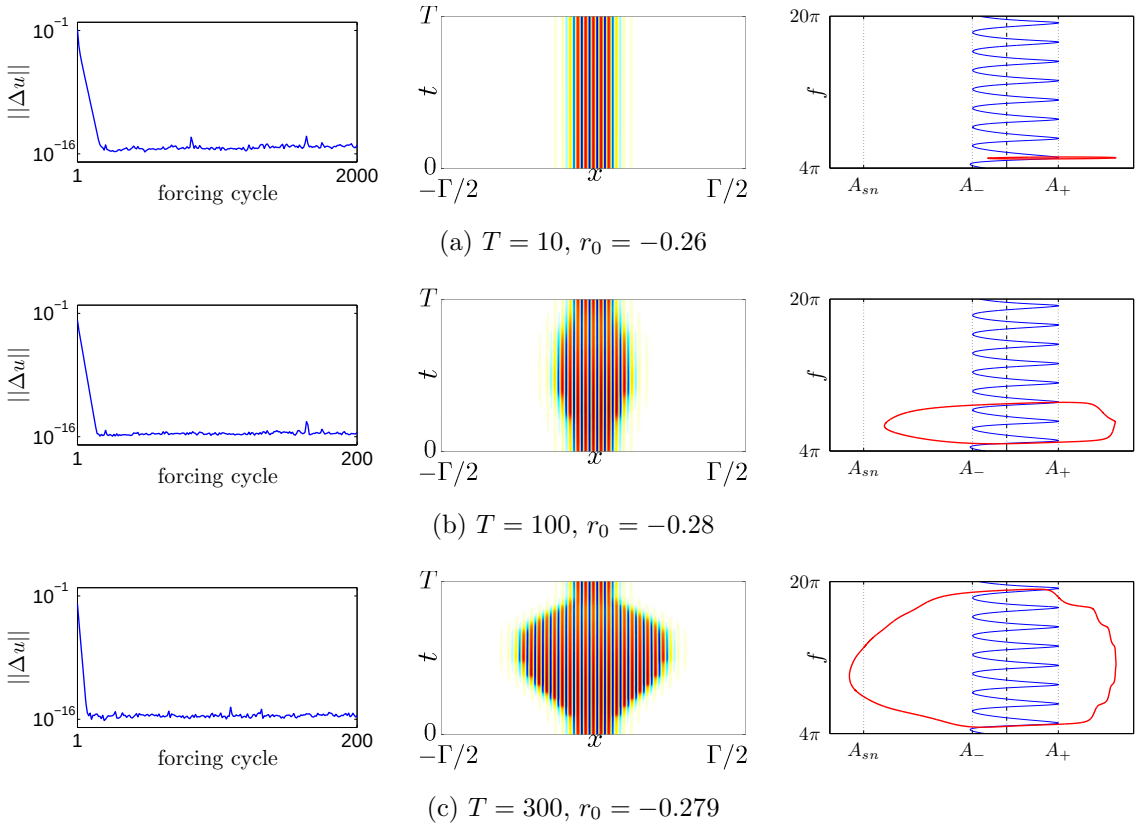

Figure 4.8: Periodic orbits of the periodically forced SHE23 for three parameter combinations: The normalized L^2 norm of the difference of two solutions exactly one period apart showing convergence to machine precision (left panels), space-time plots of the corresponding converged solution over one cycle period (middle panels), and the (A, f) trajectory of the converged solution (right panels).

the *second* fully formed sweet spot from the bottom of Fig. 4.7, undergoes *two* nucleation events followed by *two* decay events during the course of each forcing cycle. The $T = 300$ example is from the 7th sweet spot and undergoes 7 nucleation/decay events per cycle and shows that the nucleations occurring during the growth phase of the forcing between $t \approx 50$ and $t \approx 150$ are significantly slower than the decay between $t \approx 200$ and $t \approx 250$. Note that periodic orbits are present despite entering $\mathcal{A}_-$, something that is only possible because of the short amount of time spent in this regime.

We also examined the dependence of the region PO on the amplitude of oscillation, ρ. The results for $T \leq 200$ (Fig. 4.9) show that as ρ increases, the sweet spots span an increasingly smaller interval in the period T and thus a larger variety of periodic orbits can be observed within a given range of T as ρ increases. In addition, the whole sweet spot structure asymptotes more quickly towards $r_0 = -0.2744$ as ρ increases.

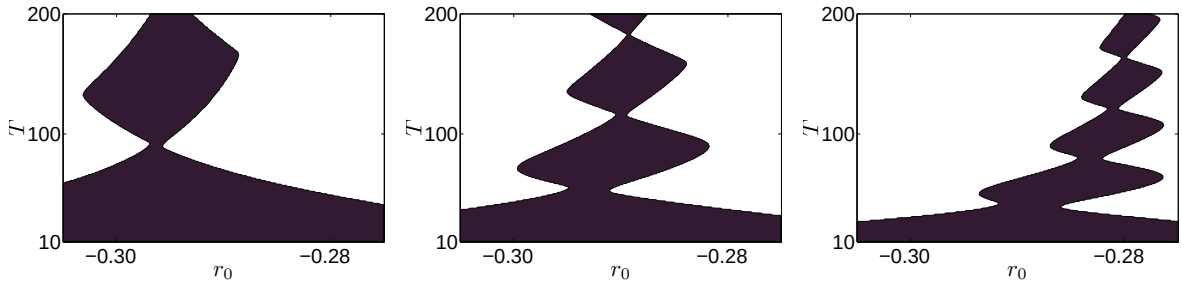

(a) $\rho = 0.06$ (b) $\rho = 0.08$ (c) $\rho = 0.10$

Figure 4.9: Region of existence of periodic orbits in the periodically forced SHE23 when (a) $\rho = 0.06$, (b) $\rho = 0.08$, (c) $\rho = 0.1$, using the same color code as in Fig. 4.7.

Structures undergoing net growth or decay

The existence of the periodic orbits discovered above is closely related to the dynamics of the fronts connecting the localized patterned state to the background state, suggesting that we can use the net displacement $\langle \Delta f \rangle$ of the fronts within a forcing cycle to classify the growing/decaying solutions. We therefore calculated $\langle \Delta f \rangle$ on the same grid as that used to find the periodic orbits PO, starting from narrower localized states to the right of PO and broader localized states to the left of PO, all stable. In some cases (e.g. for $T > 200$), a domain of twice and sometimes four times the size used in the PO calculations was necessary to capture enough oscillations.

The results are summarized in Fig. 4.10. The different colored regions are determined by the conditions $(n - 0.25)2\pi < \langle \Delta f \rangle < (n + 0.25)2\pi$, $n = \pm 1, \pm 2, \ldots$ and represent regions where regular behavior is observed. The zones between these regions (shown in gray) are "transition zones" that will be discussed below. The figure shows that the region of existence of the periodic orbits is surrounded by regions of decay (to the left) and growth (to the right). Beginning in the periodic orbit region PO and moving to the right (increasing r_0), the first region encountered (O_{+1}) corresponds to growth by one wavelength on either side of the pattern per cycle. The next region (O_{+2}) corresponds to growth by two wavelengths on either side, and so on for the subsequent regions which we refer to as O_n, where n is a positive integer. The regions to the left of PO correspond to decay instead of growth. The closest region to PO, O_{-1}, exhibits one wavelength decay on either side of the pattern per cycle and so on for O_n, $n < -1$. Each of these regions is separated from its neighbor by a transition zone where irregular dynamics are observed and displays the same sweet spot and pinching structure as the PO region: the regions expand and contract successively as T increases. Some insight into this structure can be gained by looking at the number q (m) of wavelengths gained (lost) on each side of a localized structure during an excursion of the trajectory into regime $\mathcal{D}_+$ ($\mathcal{D}_-$). A sketch of the corresponding results in Fig. 4.11 shows that areas corresponding to the gain (loss) of a fixed number of wavelengths during a $\mathcal{D}_+$ ($\mathcal{D}_-$) excursion form bands, and that the intersections of these bands define subregions

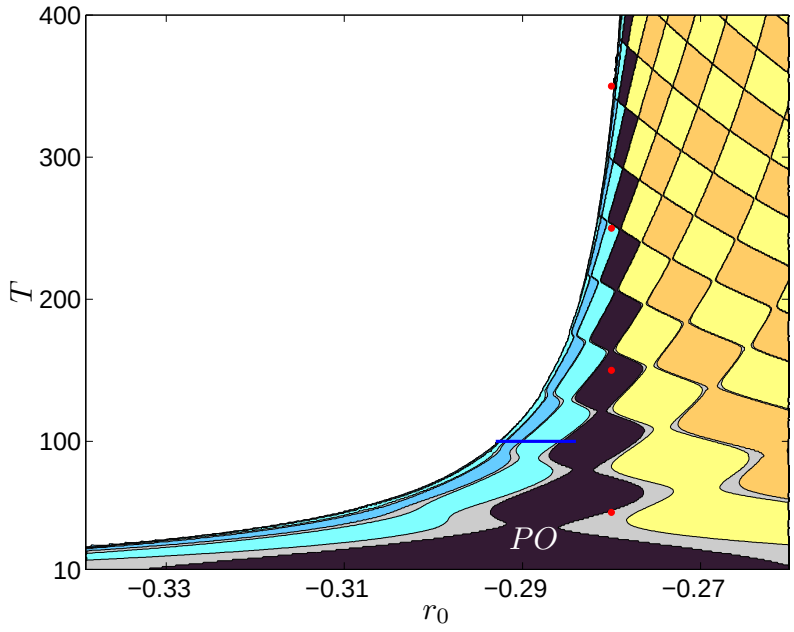

Figure 4.10: The number of spatial periods added/lost per cycle for localized states of the periodically forced SHE23 with an oscillation amplitude $\rho = 0.1$. The simulations were initialized with L_0 localized solutions that are stable at r_0 in the time-independent system. The central dark region corresponds to PO (cf. the shaded region in Fig. 4.7). The light blue region to the left corresponds to decay by one wavelength on each side of the localized state per cycle, the next to decay by two wavelengths per cycle etc. The regions to the right of PO correspond instead to net growth by one wavelength, two wavelengths etc. on each side of the localized state per cycle. The large white region to the left indicates the location of decay to the trivial state within one cycle period. Transition zones where irregular behavior is observed are shown in gray. The dots indicate the location in parameter space of the solutions plotted in Fig. 4.6 while the horizontal line refers to a region that is studied in Fig. 4.13.

labeled ${}^{-m}O_n^{+q}$, where $n = q-m$, corresponding to net gain or loss of n wavelengths per cycle resulting from the annihilation of m wavelengths followed by the nucleation of q wavelengths (Fig. 4.11(c)). This procedure allows us to assign a unique label to each subregion in the parameter plane (excluding the transition zones in between). Spending more time or going farther into $\mathcal{D}_+$ ($\mathcal{D}_-$) will result in more nucleations (annihilations) over a forcing cycle because more time is spent outside of the pinning region. This explains the evolution of the ${}^{-m}O_n^{+q}$ structure as r_0 increases: the time spent in $\mathcal{D}_+$ increases and the time spent in $\mathcal{D}_-$ decreases. Similarly, as the period T of the forcing increases, more time is spent in both $\mathcal{D}_+$ and $\mathcal{D}_-$, resulting in an increase of both q and m. This translates into larger oscillations in

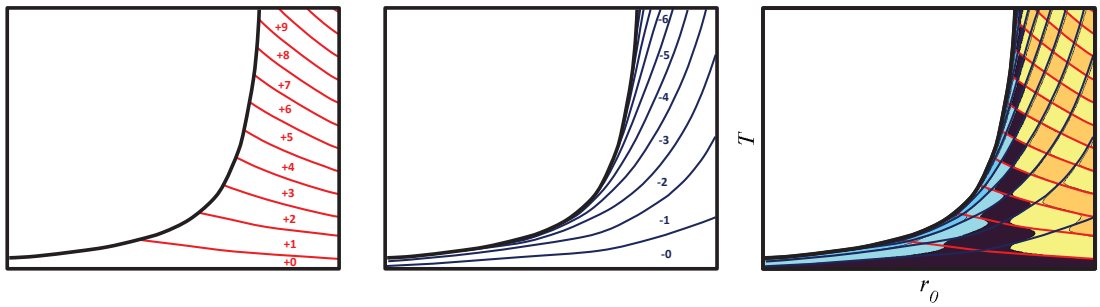

(a) (b) (c)

Figure 4.11: Sketch of the sweet spot classification scheme for the periodically forced SHE23. The lines indicate transitions between the number of wavelengths gained in (a) and lost in (b) on each side of the localized pattern during one cycle period. These lines are superimposed over the data from numerical simulations in (c) as a means to classify the regions of growth and decay.

the location of the fronts of the localized structures for longer periods. Finally we can gain intuition about the cliff beyond which localized solutions collapse to the trivial state within a single forcing cycle by considering the length of time spent in the regime $\mathcal{A}_-$. This region is characterized by the time required for solutions to decay to the homogeneous state. As the cycle period increases, the center of oscillation that allows the system to just reach this threshold time is pushed further to the right. So the edge of the cliff moves to increasing values of r_0 as the cycle period T increases.

The transition zones narrow as the period T increases, and a closer look reveals a complex structure resembling a devil's staircase, a characteristic feature of mode-locking. Figure 4.12 shows $\langle f \rangle$ within the transition zone between PO and O_{+1} at $T = 80$ calculated on a domain of 160 spatial periods using a grid of r_0 values with spacing $\Delta r_0 = 10^{-5}$. The results reveal the presence of increasingly thin regions in which n wavelengths are gained/lost from either side of the localized structure within N cycles. These regions thus correspond to fractional growth/decay of the solutions suggesting a complex structure on all scales. We note that this structure does not appear in the analogous transition zones of the periodically modulated Adler equation as subharmonic resonances do not exist (cf. Fig. 3.16). It does, however, appear in variants of the periodically modulated Adler equation such as those that include a second derivative term [109]. Whether there are regions of nonperiodic dynamics corresponding to irrational numbers cannot be determined through simulations, but the small amplitude asymptotic results of this section seem to indicate that they form a dense subset of the transition zone.

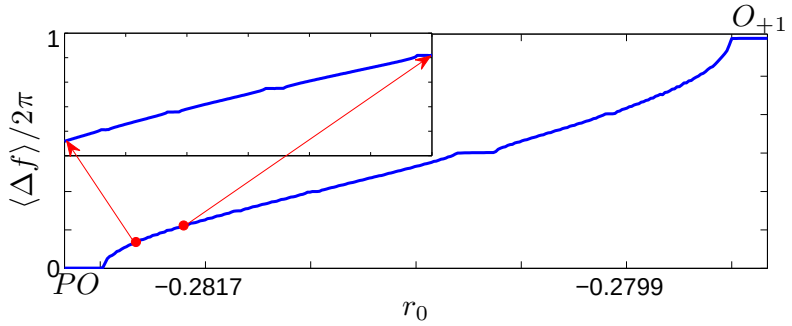

Figure 4.12: The quantity $\langle \Delta f \rangle / 2\pi$ in the transition zone between PO and O_{+1} of the periodically forced SHE23 with $T = 80$ exhibits a structure characteristic of a devil's staircase (see inset).

Amplitude decay

In addition to the depinning-like dynamics observed in the colored regions outside of PO in Fig. 4.10, amplitude decay occurs in the white region. In this region the initial localized solution collapses to the trivial state within a single forcing cycle. The boundary of this region is formed by the accumulation of the depinning bands identified in Fig. 4.11(b).

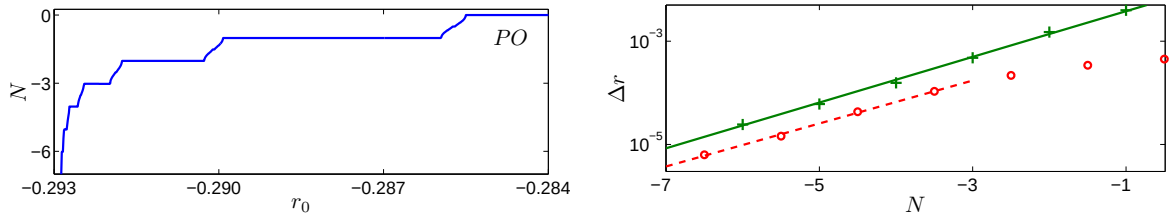

(a) (b)

Figure 4.13: (a) The quantity $N \equiv \langle \Delta f \rangle / 2\pi$, representing the shift in the front location averaged over a cycle period, as a function of r_0 in the periodically forced SHE23 with $T = 100$ (Fig. 4.10, horizontal line). (b) Length of the plateaus (green crosses) and of the transition regions between them (red circles) as determined from (a), shown in a semilog plot, together with linear approximations to the data (straight lines, given in the text). The plateaus are plotted at integer values of N while the transition zones between plateaus $N = n$ and $N = n + 1$ are taken to correspond to $N = n + 0.5$.

We look more carefully at the accumulation point of the decay bands in Fig. 4.13. The plateaus correspond to the loss of integer numbers of wavelengths per forcing cycle. Figure 4.13(a) shows that the width of the plateaus as well as of the transition zones between

them decreases as one approaches the accumulation point, while Fig. 4.13(b) shows the width Δr of the plateaus and the transition zones as a function of N, the number of wavelengths lost per cycle ($N < 0$). The data obtained shows that both these widths decrease exponentially with increasing $|N|$ and are consistent with the fits

$$\Delta r_P(N_P) = 0.01056\, e^{1.0188 N_P}, \tag{4.35}$$

$$\Delta r_T(N_T) = 0.003307\, e^{0.9584 N_T}, \tag{4.36}$$

where Δr_P (resp. Δr_T) denotes the width of the plateau corresponding to the loss of N_P wavelengths per cycle (resp. width of the transition zone between the pair of closest integers to N_T). To obtain these fits we used all the data in Fig. 4.13(b) on the plateau widths but only the transition zones between $N = -6.5$ and $N = -3.5$. To consider even smaller values of N would have required considerably more numerical effort without improving substantially the accuracy of the fit, while values of N closer to 0 lead to departures from the asymptotic regime. Both formulas show similar exponential decrease, thereby confirming the presence of an abrupt "cliff" at the accumulation point (Fig. 4.13(a)). Furthermore, we see that the width of the transition zones tends to about 1/3 of that of the plateaus as $|N|$ increases.

Asymptotic theory: small oscillations

To understand the structure of the parameter plane in Fig. 4.10 we need to understand the process of depinning in the time-dependent system. For this purpose we will consider parameter excursions that take the system outside of the pinning region long enough for a nucleation or annihilation event to occur. We therefore suppose that $r \to r_+ + \epsilon^2(\delta + \rho \sin \epsilon\omega t)$ for which the oscillation period is of the same order as the nucleation time. The theory developed here is a straightforward extension of the small amplitude resonance tongue calculation of Sec. 3.3 for the periodically modulated Adler equation and an analogous calculation near r_- produces similar results. In this regime the problem is governed by the equation

$$\partial_t u = \left(r_+ + \epsilon^2(\delta + \rho \sin \epsilon\omega t)\right) u - \left(1 + \partial_x^2\right)^2 u + bu^2 - u^3. \tag{4.37}$$

Since the dynamics takes place on an $\mathcal{O}(\epsilon^{-1})$ timescale we define the slow timescale $\tau = \epsilon t$ and write $\partial_t \to \epsilon \partial_\tau$. We look for a solution in the form $u = u_0 + \epsilon u_1 + \epsilon^2 u_2 + \ldots$, obtaining, at leading order,

$$r_+ u_0 - \left(1 + \partial_x^2\right)^2 u_0 + b u_0^2 - u_0^3 = 0. \tag{4.38}$$

As a result we pick u_0 to be a localized solution at a saddle-node bifurcation of the snaking branch in the time-independent case. In this case u_0 is stationary but only marginally stable. At $\mathcal{O}(\epsilon)$, we obtain

$$\partial_\tau u_0 = r_+ u_1 - \left(1 + \partial_x^2\right)^2 u_1 + 2b u_0 u_1 - 3u_0^2 u_1. \tag{4.39}$$

Since u_0 is stationary, u_1 must be of the form of a zero eigenvector of SHE23 linearized about the saddle-node solution. The relevant eigenvector v_+ corresponds to wavelength addition

and is symmetric with respect to $x \to -x$. Since we focus on states that do not drift we can ignore the marginal but antisymmetric eigenvectors corresponding to translation and phase. Thus $u_1 = a(\tau)v_+$.

To determine the amplitude a we must go to $\mathcal{O}(\epsilon^2)$. At this order, the equation is

$$\partial_\tau u_1 = r_+ u_2 - \left(1 + \partial_x^2\right)^2 u_2 + 2bu_0u_2 - 3u_0^2u_2 + (\delta + \rho\sin\omega\tau)u_0 + bu_1^2 - 3u_0u_1^2. \tag{4.40}$$

The solvability condition for u_2 is [24]

$$\alpha_1\dot{a} = \alpha_2(\delta + \rho\sin\omega\tau) + \alpha_3 a^2, \tag{4.41}$$

with the coefficients α_j calculated from the integrals defined in Eq. (4.6).

We can turn this equation into a Mathieu equation using the Riccati transformation $a = -\alpha_1\dot{q}/\alpha_3 q$, obtaining

$$\ddot{q} = -\Omega_+^2\left(\delta + \rho\sin\omega\tau\right)q, \qquad \delta > 0, \tag{4.42}$$

where $\Omega_+^2 \equiv \alpha_2\alpha_3/\alpha_1^2 > 0$ with α_j evaluated at r_+ (cf. Sec. 4.1). Thus $\Omega_+ \approx 0.5285$. The same procedure at the left boundary of the pinning region leads to an equation for the dynamics of the annihilation mode amplitude as a function of the distance δ from the boundary, $r_0 = r_- + \delta$:

$$\ddot{q} = \Omega_-^2\left(\delta + \rho\sin\omega\tau\right)q, \qquad \delta < 0, \tag{4.43}$$

where we have set $a = \alpha_1\dot{q}/\alpha_3 q$. The integrals α_j are now evaluated at $r = r_-$ and $\Omega_- = \sqrt{-\alpha_2\alpha_3/\alpha_1^2} \approx 0.7159$.

We can make use of the known properties of the solutions of the Mathieu equation to understand the origin of the resonances between the forcing frequency ω and the characteristic depinning frequency $\sqrt{\delta}\Omega_+$. The properties of Eq. (4.42) are summarized in the standard stability diagram for the Mathieu equation [78] shown in Fig. 4.14 in terms of the scaled distance from the boundary of the pinning region δ/ρ and the scaled oscillation period $\Omega_+\sqrt{\rho}T/\pi$. The shaded zones indicate that the solutions of (4.42) are bounded for all time, while the solutions are unbounded in the white bands. In terms of the amplitude a in Eq. (4.41), the shaded areas correspond to transition zones where a non-integer number of nucleation events occurs during each cycle of the forcing. In fact, nonperiodic dynamics occur for irrational values of the associated Mathieu characteristic exponent within these zones. The first white band on the far left corresponds to stable periodic orbits that do not undergo nucleation. The state undergoes one nucleation per oscillation in the white band immediately to the right, and the number of nucleations per oscillation increases by integer values within each subsequent white band.

We remark (cf. Sec. 4.1) that care must be taken in interpreting the solutions to Eqs. (4.42) and (4.43) since the zeros of $q(\tau)$ correspond to solutions of Eq. (4.41) that diverge to $\pm\infty$. During this process higher order nonlinearities enter Eq. (4.41) with the result that the Riccati transformation no longer yields a linear equation. Thus the solutions of Eqs. (4.42) and (4.43) in fact fail to describe the depinning process near the zeros of $q(\tau)$,

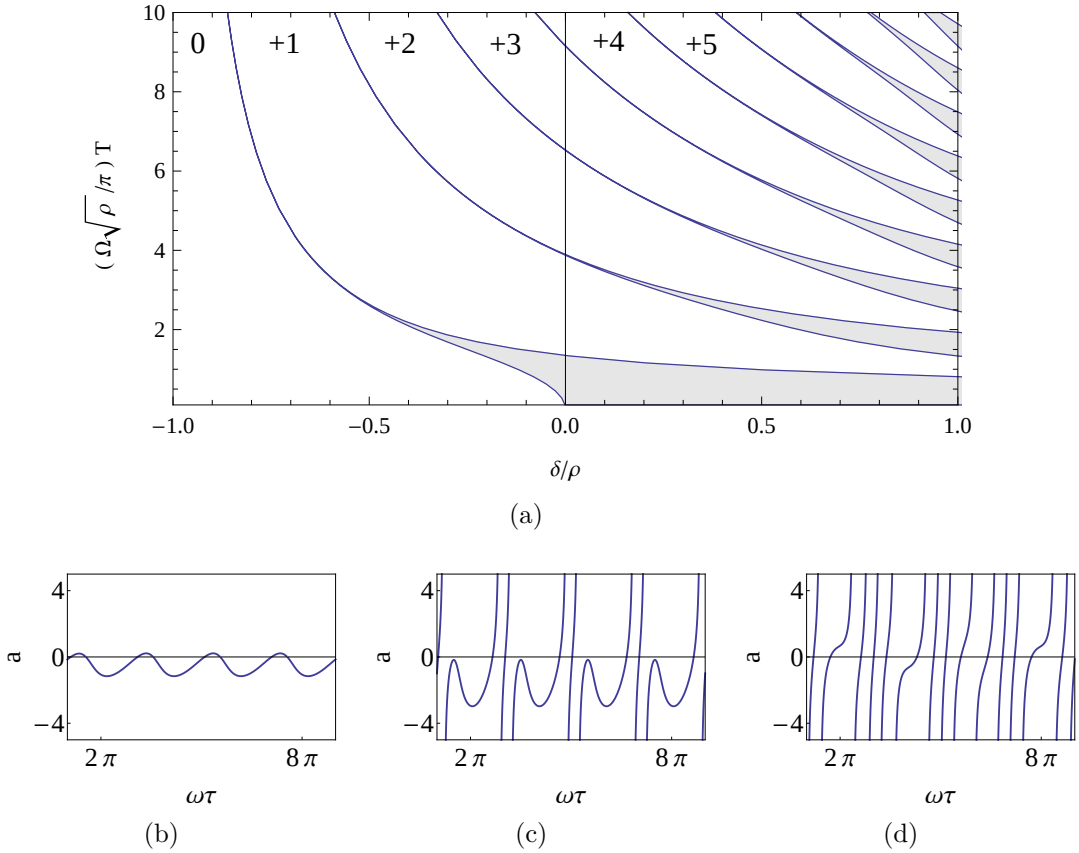

Figure 4.14: (a) The stability diagram for Eq. (4.42). The white bands correspond, from left to right, to states that undergo exactly 0,1,2,3,... nucleation events per forcing cycle. A non-integer number of nucleations per cycle occurs in the gray transition zones in between. (b) Sample solution $a(\tau)$ within the 0 region when $\delta = -\rho/2$, $T = 2\pi/\Omega_+\sqrt{\rho}$. (c) Sample solution $a(\tau)$ within the +2 region when $\delta = 0$, $T = 6\pi/\Omega_+\sqrt{\rho}$. (d) Sample solution $a(\tau)$ within the transition region between regions +3 and +4 when $\delta = \rho$, $T = 4\pi/\Omega_+\sqrt{\rho}$. Nucleation events correspond to divergences in $a(\tau)$.

and the corresponding solution $a(\tau)$ is determined by "gluing" together a series of individual nucleation events. However, as suggested by the description in Eqs. (4.42) and (4.43), the resulting nucleation process is indeed periodic, albeit in the frame moving with the front $x = f(\tau)$.

Asymptotic theory: formation of sweet spots and pinching

With intuition gained from the small amplitude theory we now consider the case of large parameter oscillations that take the system just outside of the pinning region, but with a long enough period that there is time for depinning to occur. The analogous calculation

for the periodically modulated Adler equation is described in Sec. 3.3 and produces similar results. Because the system spends only a small fraction of the forcing cycle outside of $\mathcal{P}_\pm$, we require the forcing cycle period to be yet longer, $T = \mathcal{O}(\epsilon^{-2})$, in order that depinning takes place. We therefore define the slow timescale $\mathcal{T} = \epsilon^2 t$ and write the forcing parameter in the form

$$r = r_c + \epsilon^2 r_2 + (p + \epsilon^2 \delta) \sin\left(\epsilon^2 \omega t\right), \tag{4.44}$$

where $r_c \equiv (r_+ + r_-)/2$ corresponds to the center of the pinning region, and $p \equiv (r_+ - r_-)/2$ is its half-width. This choice allows for the oscillations to take the system just outside of the pinning region on both sides where depinning can be described quantitatively; the small offset represented by r_2 is included for greater generality, as is illustrated in the schematic in Fig. 4.15(a). A periodic orbit from a simulation, colored according to the value of the forcing parameter r is also shown.

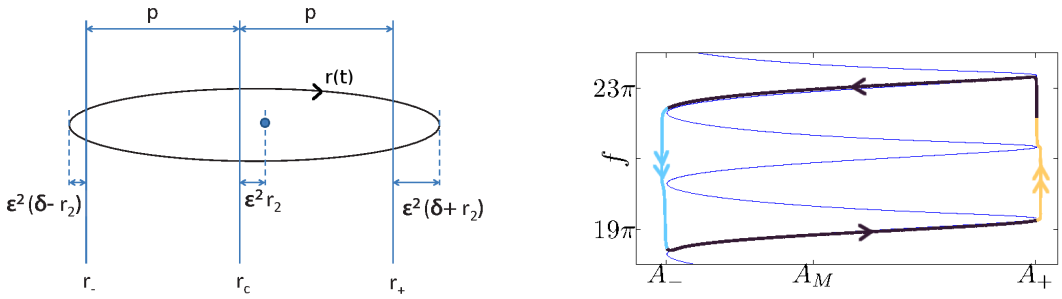

(a) (b)

Figure 4.15: (a) A schematic of the forcing function $r(t)$ used in the asymptotic theory in the $(r, \dot{r})$ plane. (b) A periodic orbit of the periodically forced SHE23 with $\rho = p + 10^{-3}$, $T = 5000$, and $r_0 = -0.299$. The orbit is colored by the magnitude of r: purple corresponds to $\mathcal{P}_\pm$ (slow phase), orange to $\mathcal{D}_+$ (fast phase), and blue to $\mathcal{D}_-$ (fast phase).

We anticipate that in the above setup nucleation will occur on the faster timescale $\tau = \mathcal{O}(\epsilon^{-1})$ and so look for solutions in the form $u = u_0 + \epsilon u_1 + \epsilon^2 u_2 + ...$, where $u_j \equiv u_j(x, \tau, \mathcal{T})$. Writing $\partial_t = \epsilon \partial_\tau + \epsilon^2 \partial_\mathcal{T}$, we obtain at leading order

$$\left[r_c + p \sin(\omega \mathcal{T}) - (1 + \partial_x^2)^2\right] u_0 + b u_0^2 - u_0^3 = 0. \tag{4.45}$$

Thus we can choose $u_0(x, \mathcal{T})$ to be a stable localized solution of the time-independent SHE23 within the pinning region, with $\mathcal{T}$ determining the value of the forcing parameter within this region. The solutions follow the corresponding segment of the L_0 branch (Fig. 4.15(b)) as long as $\pi(n - 1/2) < \omega \mathcal{T} < \pi(n + 1/2)$, for any integer n. As we will see, special care must be taken near the extrema of the forcing cycle when the system leaves the pinning region and the dynamics take place on the faster timescale τ.

The $\mathcal{O}(\epsilon)$ correction reads

$$\left[r_c + p\sin(\omega\mathcal{T}) - (1+\partial_x^2)^2 + 2bu_0 - 3u_0^2\right] u_1 = 0. \tag{4.46}$$

When $\omega\mathcal{T} = (2n+1/2)\pi$ (resp. $(2n+3/2)\pi$), the quantity u_1 solves the linearized SHE23 at r_+ (resp. r_-) with symmetric solution v_+ (resp. v_-), i.e. the depinning mode responsible for growth (resp. decay) of the localized pattern. In contrast, when $(n-1/2)\pi < \omega\mathcal{T} < (n+1/2)\pi$, no reflection-symmetric marginally stable modes are present. To examine the dynamics near r_+ we take the slow time to be $\omega\mathcal{T} = \pi/2 + \epsilon\theta$; a similar procedure can be carried out near r_- by taking $\omega\mathcal{T} = 3\pi/2 + \epsilon\theta$, and subsequent cycles of the forcing can be handled in the same way. The time derivative now becomes $\partial_t = \epsilon\omega\partial_\theta$ and the $\mathcal{O}(\epsilon)$ equation (4.46) becomes

$$\left[r_+ - (1+\partial_x^2)^2 + 2bu_0 - 3u_0^2\right] u_1 = \omega\partial_\theta u_0. \tag{4.47}$$

Since u_0 is the marginally stable localized solution at r_+ it follows that $\partial_\theta u_0 = 0$ and hence that $u_1 = a(\theta)v_+(x)$.

At $\mathcal{O}(\epsilon^2)$ we obtain

$$\left[r_+ - (1+\partial_x^2)^2 + 2bu_0 - 3u_0^2\right] u_2 = \omega\partial_\theta u_1 - (b-3u_0)u_1^2 - (r_2 + \delta - \tfrac{1}{2}p\theta^2)u_0, \tag{4.48}$$

for which the solvability condition is

$$\alpha_1\omega a' = \alpha_2(r_2 + \delta - \tfrac{1}{2}p\theta^2) + \alpha_3 a^2, \tag{4.49}$$

where the prime denotes the θ derivative and the coefficients α_j are determined by the integrals in Eq. (4.6).

Using the transformation $a = -\alpha_1\omega q'/\alpha_3 q$, we obtain a linear oscillator problem with a time-dependent frequency,

$$q'' = -\frac{p\Omega_+^2}{2\omega^2}\left(\theta_+^2 - \theta^2\right) q, \tag{4.50}$$

where $\theta_+^2 = 2(r_2+\delta)/p$ and, as before, $\Omega_+^2 = \alpha_2\alpha_3/\alpha_1^2$. The system exits $\mathcal{P}_+$ when $r_2 + \delta > 0$, and in this case $[-\theta_+, \theta_+]$ corresponds to the time interval spent in $\mathcal{D}_+$. We now use a matching procedure to connect this solution to the case when $\omega\mathcal{T} \neq \pi/2$, noting that $u_1(x,\mathcal{T}) \to 0$ as $\omega\mathcal{T} \to \pi/2$, so that the solution remains stable as it approaches the boundary of the pinning region. Since the leading order solution for large $|\theta|$ is given by $a(\theta) \approx \sqrt{p\alpha_2/2\alpha_3}|\theta|$ we require that $a(\theta) \to \sqrt{p\alpha_2/2\alpha_3}\theta < 0$ as $\theta \to -\infty$. The solution of Eq. (4.50) satisfying this requirement can be written in terms of parabolic cylinder functions [116], $q = D_\nu(z)$, where

$$\nu = \frac{\sqrt{p}\Omega_+\theta_+^2}{2\sqrt{2}\omega} - \frac{1}{2}, \qquad z = -(2p)^{1/4}\sqrt{\frac{\Omega_+}{\omega}}\theta. \tag{4.51}$$

Each zero $z = z_0$ of $q = D_\nu(z)$ corresponds to a nucleation event, since a diverges to $\pm\infty$ as $z \to z_0$. To determine the outcome of such an event we must consider the limit as $\theta \to \infty$ to match the $\dot{r} > 0$ phase of the forcing cycle with the $\dot{r} < 0$ phase that follows. This will tell

us what branch the solution follows for $\pi/2 < \omega\mathcal{T} < 3\pi/2$. The parabolic cylinder function behaves like

$$D_\nu(z) \to \tfrac{\sqrt{2}\pi}{\Gamma[-\nu]}|z|^{-(\nu+1)}e^{z^2/4} \tag{4.52}$$

for real $z \to -\infty$, where $\Gamma[-\nu]$ is the Gamma function evaluated at $-\nu$. Examining the sign of $\Gamma[-\nu]$ shows that as long as ν is not a positive integer, $a \to \sqrt{p\alpha_2/2\alpha_3}\theta > 0$ in this limit, and the solution does indeed settle on the nearest stable localized solution. The special cases for which ν is a positive integer correspond to the solution landing exactly on an unstable solution.

We can get a very simple expression for the number of nucleation events that occur near r_+ by counting the number of real zeros of $D_\nu(z)$ for a given ν. We start by noting that for $z \to \infty$ ($\theta \to -\infty$), $D_\nu(z)$ approaches zero from above. When $\nu < 0$, there are no real zeros and $D_\nu(z) > 0$ for all z. Equation (4.52) shows that in the limit that $z \to -\infty$, the sign of $D_\nu(z)$ depends on the sign of $\Gamma[-\nu]$. For $\nu < 0$, the sign is positive and $D_\nu(z) \to +\infty$ as $z \to -\infty$ without crossing zero. At $\nu = 0$, $\Gamma[-\nu] = \infty$ and $D_\nu(z) \to 0$ from above; there are still no zero crossings. For $0 < \nu < 1$, there will be one zero crossing as $D_\nu(z) \to -\infty$ as $z \to -\infty$. The number of zeros continues to increase by one each time there is a sign change in $\Gamma[-\nu]$ so that for $n - 1 < \nu < n$, there will be $n > 0$ zeros of $D_\nu(z)$. Therefore there will be n_+ nucleation events if

$$n_+ - \tfrac{1}{2} < \frac{\Omega_+ T}{2\pi\sqrt{2p}}(r_0 + \rho - r_+) < n_+ + \tfrac{1}{2}, \tag{4.53}$$

where we have re-expressed the condition in terms of the amplitude $\rho \equiv p + \epsilon^2\delta$, offset $r_0 \equiv r_c + \epsilon^2 r_2$, and the period $T \equiv 2\pi/\epsilon^2\omega$. A similar relation applies for the number of annihilations $n_- < 0$:

$$n_- - \tfrac{1}{2} < \frac{\Omega_- T}{2\pi\sqrt{2p}}(r_0 - \rho - r_-) < n_- + \tfrac{1}{2}. \tag{4.54}$$

The above conditions also reveal the presence of bifurcation delay, as expected of a nonautonomous bifurcation problem. This delay manifests itself in the shift of the critical value $r_2+\delta = 0$ for the presence of a fold to the threshold value determined by $\nu = 0$, viz., $r_2+\delta = \omega/\sqrt{2p}\Omega_+$: the system enters $\mathcal{D}_+$ by as much as $\omega/\sqrt{2p}\Omega_+$ without triggering a nucleation event. Figure 4.16(b,c) show the amplitude a as a function of the scaled time $(2p)^{1/4}\Omega_+\theta/\omega$ just before and after this threshold. The transition between these two cases involves canard trajectories [118]. The discontinuous jump in Fig. 4.16(c) represents a nucleation event and is obtained by gluing together two separate asymptotic calculations near different, but adjacent saddle-nodes on the same snaking branch. The same "inertial" effect is observable even when the system does not leave $\mathcal{P}_+$, i.e., $\delta + r_2 < 0$. Using the property

$$D_\nu(z) \to \sqrt{2^\nu\pi}\left(\frac{1}{\Gamma[(1-\nu)/2]} - \frac{\sqrt{2}z}{\Gamma[-\nu/2]} - \frac{(1+2\nu)z^2}{4\Gamma[(1-\nu)/2]}\right), \qquad z \to 0, \tag{4.55}$$

we see that even when the system just barely reaches the boundary of the pinning region, $r_2 + \delta = 0$, the perturbation $a(\theta)$ remains finite (Fig. 4.16(a)). Indeed the minimum value of $a(\theta)$ occurs for $\theta > 0$ instead of $\theta = 0$. In fact $a(\theta)$ can be calculated explicitly in terms of parabolic cylinder functions using the relation

$$\frac{dD_\nu(z)}{dz} = \tfrac{1}{2} z D_\nu(z) - D_{\nu+1}(z). \tag{4.56}$$

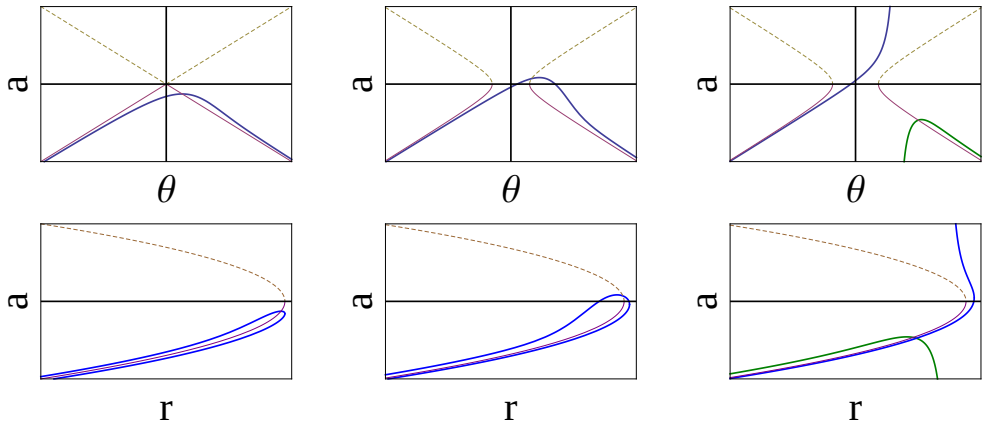

(a) $\nu = -0.5$ (b) $\nu = -0.1$ (c) $\nu = 0.1$

Figure 4.16: A plot of the amplitude $a(\theta)$ of the $\mathcal{O}(\epsilon)$ correction $u_1(x)$ to the solution that is marginally stable at $r = r_+$ as a function of a scaled $\mathcal{O}(\epsilon)$ time near the boundary of the pinning region for different values of $\nu = \frac{\sqrt{p}\Omega_+\theta_+^2}{2\sqrt{2}\omega} - \frac{1}{2}$. The time $\theta = 0$ corresponds to the peak of the forcing cycle where "inertial" effects are expected. The thin solid (dashed) line shows the amplitude a for the stable (unstable) localized solution as functions of r but replotted in terms of the time θ. Below each frame is a schematic representation of the trajectory of the amplitude a as a function of the forcing parameter r. The stable (unstable) steady state branches of the constant forcing case are shown in solid (dashed) lines for reference. (a) $\nu = -0.5$: the system does not leave the pinning region, but there are still deviations from the stable state. (b) $\nu = -0.1$: the system exits the pinning region, but not far enough for nucleations to occur. (c) $\nu = 0.1$: the system penetrates into $\mathcal{D}_+$ past the threshold for a nucleation to occur (represented by a discontinuous jump).

In the parameter regime analyzed here, the system tracks a given stable localized state with a delay in r of up to $\mathcal{O}(\epsilon^2)$ for most of the forcing cycle. All of the interesting dynamics occur within a small time interval when the system visits the vicinity of the boundary of the pinning region. If it ventures far enough outside of this boundary, nucleation/annihilation events begin to take place after a delay. Once the system reenters the pinning region, the system settles on the nearest stable but longer/shorter localized structure. The settling

process also happens within the vicinity of the boundary of the pinning region and there may or may not be an additional nucleation/annihilation event during this settling, depending on where in the process the system was upon re-entering the pinning region $\mathcal{P}_\pm$.

To understand the structure of growing, steady-state, and decaying solutions in this limit, we need only compare the growth from depinning that occurs near $\omega\mathcal{T} = \pi/2$ to the decay from depinning that occurs near $\omega\mathcal{T} = 3\pi/2$. The formation of the sweet spot and pinching structure of the stationary solutions can be predicted by balancing the growth on the right of the pinning region to the decay on the left as we shall now see.

The number of nucleation events n_+ given by Eq. (4.53) and annihilation events $-n_-$ given by Eq. (4.54) during one forcing period can be summarized by:

$$n_\pm = \begin{cases} \left[\frac{\Omega_\pm T}{2\pi\sqrt{2p}}(r_0 \pm \rho - r_\pm)\right] & \text{if } \pm(r_0 \pm \rho - r_\pm) > 0 \\ 0 & \text{if } \pm(r_0 \pm \rho - r_\pm) \le 0 \end{cases}, \tag{4.57}$$

where the brackets indicate rounding to the nearest integer and come from the settling of the state to a stable localized solution upon re-entry into the pinning interval.

For $\rho - p < 0$, the resonance bands associated with the left and right edges of the pinning interval are disjoint but asymptotically approach $r_0 = r_c$ as $T \to \infty$ for $\rho = p$. For $\rho - p > 0$, an asymptotically small sweet spot and pinching structure begins to form as a result of successive crossing between the resonance bands, as shown in Fig. 4.17.

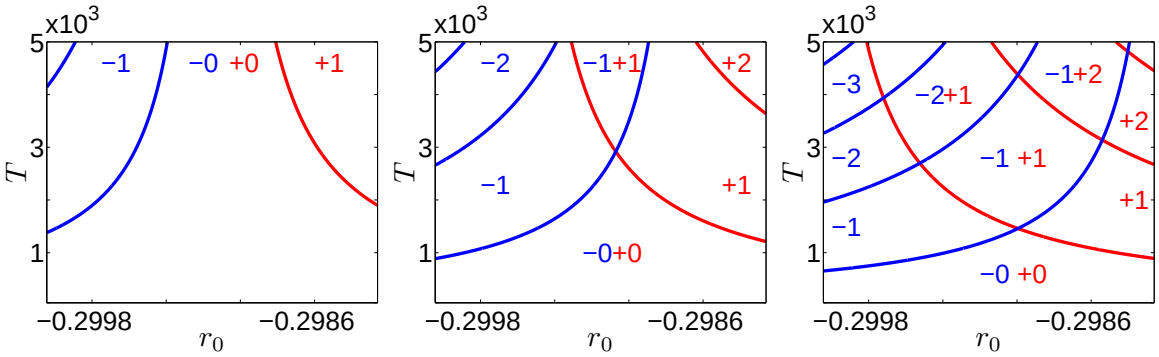

(a) $\rho - p = 0$ (b) $\rho - p = 0.0005$ (c) $\rho - p = 0.001$

Figure 4.17: Predictions from the asymptotic theory for the periodically force SHE23, Eq. (4.57). The blue (resp. red) lines correspond to parameter values where n_- (resp. n_+) changes.

The prediction of Fig. 4.17(c) where $\rho = p + 10^{-3}$ is compared with numerical simulation in Fig. 4.18, and shows excellent quantitative agreement. Specifically, the colored regions are determined by numerical simulation (the colored regions shown in Figs. 4.18 to 4.20 correspond to $2\pi(n-0.5) < \langle \Delta f \rangle < 2\pi(n+0.5)$ for $n = 0, \pm 1, \pm 2, \ldots$) and these match the coding scheme of Fig. 4.10 without the gray transition zones, while the red and blue lines

are predictions for the transitions between the various regions of the classification scheme detailed in Fig. 4.11. Note, however, that the values of r_0 in Fig. 4.18 span only about 1/40th of the pinning region of the constant forcing system: the sweet spot–pinched structure here is asymptotically small as a result of our choice of ρ.

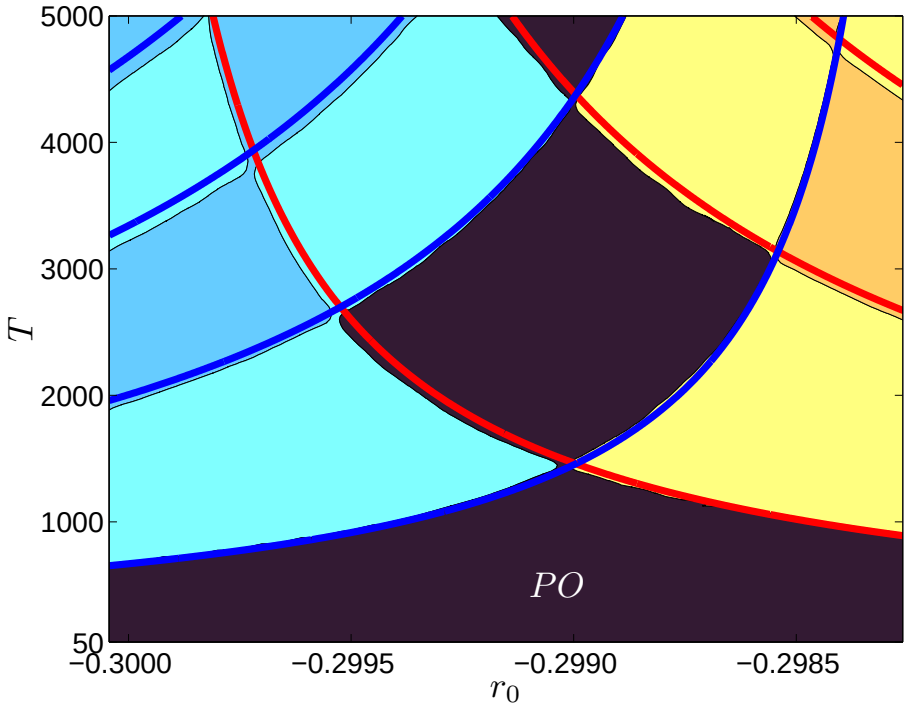

Figure 4.18: A comparison of the asymptotic theory (Eq. (4.57)) (red/blue lines) with numerical simulations (colors) for the periodically forced SHE23 with $\rho = p + 10^{-3} \approx 0.04$. The dark region corresponds to the region PO. The red (blue) lines indicate transitions in the number of nucleations (decays) that occur during one forcing cycle.

Figure 4.19 shows the (r_0, ρ) parameter plane for $T = 100$ and $T = 200$, along with an extension of the predictions from the above asymptotic theory (Eqs. (4.53) and (4.54)). The extension has been computed by replacing $\sqrt{p}$ in the denominator of the expressions by $\sqrt{\rho}$ as a means for correcting for the cases when $\rho \not\approx p$. The modified theory is able to accurately predict the location of the transition between the zero and ± 1 bands well outside of the limit in which it was derived, owing to the fact that the first nucleation/annihilation event necessarily occurs near the edge of the pinning region.

We note that PO and the O_n resonance bands slant towards increasing r_0 as ρ increases, and this is expected given that annihilation events happen more rapidly than nucleation events for the same distance in forcing parameter r outside of the pinning region in SHE23 with constant forcing. Within PO, the system must at minimum reach $\mathcal{D}_-$ if at least one nucleation event occurs. This condition, $r_0 - \rho < r_-$, provides a strict maximum bound on

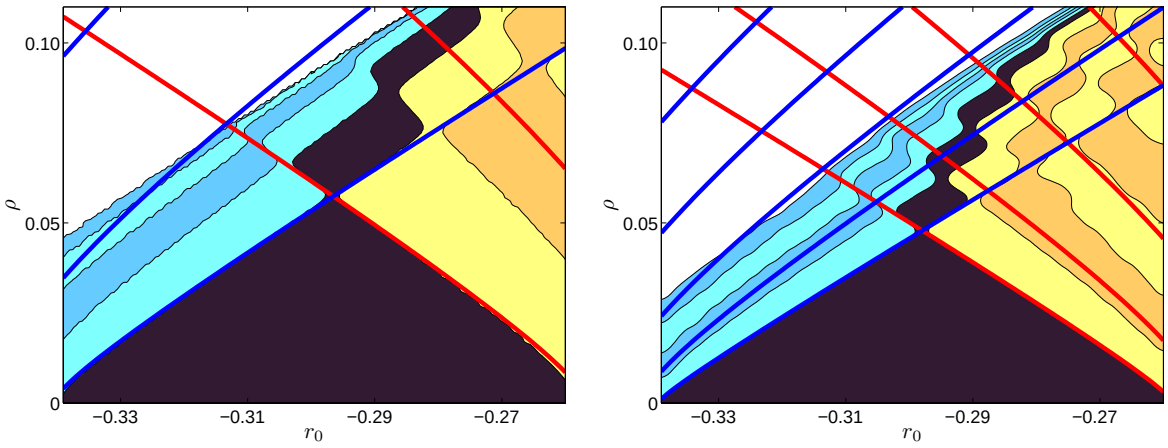

(a) $T = 100$ (b) $T = 200$

Figure 4.19: For the periodically forced SHE23, the number of spatial periods gained/lost in one forcing cycle when (a) $T = 100$ and (b) $T = 200$. All simulations were initialized with stable L_0 solutions at the corresponding r_0 in the constant forcing case. The dark region labeled *PO* indicates the location of periodic orbits and corresponds to the dark region in Fig. 4.7. The light blue region immediately to the left indicates decay by one wavelength on each side of the localized structure per forcing cycle, the next region to the loss of two wavelengths per cycle, and so on. The solution grows by one wavelength on each side of the localized structure per forcing cycle in the region immediately to the right of the dark region, and so on. The white region to the left indicates solutions that collapse to the trivial state within one cycle.

the value of r_0 where *PO* can exist that is approached in the limit that $T^-_{\rm dpn} \ll T^+_{\rm dpn}$. A minimum bound can be found from noting that the system cannot go too far into $\mathcal{A}_-$. In the limit that the amplitude collapse time $T^{\rm col}_{sn} \to 0$ this reduces to the condition $r_0 - \rho > r_{sn}$. The numerical simulations show that *PO* nearly reaches the maximum bound after the first pinched region for both $T = 100$ and $T = 200$ while it nears the minimum bound for $T = 200$ around the fourth pinched region. Above about $\rho \approx 0.1$ the $T = 200$ *PO* region approximately parallels the minimum bound. The periodic orbits remain centered within the pinning region $r_- < r_0 < r_+$ for the entire region mapped out for both cases in Fig. 4.19. It would be interesting to continue the calculation to larger values of rho to see what happens to *PO*. The high frequency, large amplitude limit considered at the end of Sec. 4.2 predicts that *PO* will disappear in a codimension-two point at $r_0 = 0$ and $\rho T/2\pi \approx 7.02$. The dynamics related to the demise of *PO* seems to be related to the amplitude mode and *PO* in Fig. 4.19(b) is clearly beginning to feel the effect from $\mathcal{A}_-$.

4.4 The low-frequency limit: Adiabatic theory

In this section we consider the remaining case, that of low-frequency forcing. In this regime we may neglect inertial effects that can cause delays in the onset of depinning or allow for the completion of depinning events within the pinning region. We note that, by applying the technique of matched asymptotics (see, for example, [137]), we can estimate the depinning delay to be $\sim |dr/dt|^{-1/3}$ where the derivative is evaluated at $r_\pm$. The analogous theory is described in much greater detail for the simpler case of the periodically modulated Adler equation in Sec. 3.4.

Sweet spot structure

Using the adiabatic approximation described above, the number $n_\pm$ of nucleation/annihilation events over the course of a forcing cycle can be estimated from the expression

$$n_\pm = \pm \int_{\mathcal{T}_\pm} \frac{dt}{T_\pm^{\rm dpn}(t)}, \tag{4.58}$$

where $\mathcal{T}_\pm$ is the time spent outside of the pinning region and $T_\pm^{\rm dpn}(t)$ is the time between nucleation/annihilation events of the constant forcing problem with parameter $r(t)$. The super/subscript + (resp. −) refers to regime $\mathcal{D}_+$ (resp. $\mathcal{D}_-$). We assume that the dynamics within the pinning region allow the system to either complete the nucleation process (corresponding to rounding $n_\pm$ up), or settle back down to the state already reached (corresponding to rounding $n_\pm$ down). We also suppose that the threshold between completing a nucleation event or settling back corresponds to $n_\pm + 1/2$ and will use brackets, e.g. $[n_\pm]$, to denote the nearest integer. We recall that leading order asymptotics near the edge of the pinning region predict that $(T_\pm^{\rm dpn})^{-1} = \Omega_\pm \delta_\pm^{1/2}/\pi$ [24] and use this prediction together with the assumption $r(t) = r_0 + \rho \sin 2\pi t/T$ to obtain

$$n_\pm = \pm \frac{2\sqrt{2\rho}\Omega_\pm T}{\pi^2} \left[E\left(\tfrac{1-\eta_\pm}{2}\right) - \tfrac{1+\eta_\pm}{2} K\left(\tfrac{1-\eta_\pm}{2}\right) \right], \tag{4.59}$$

where $\eta_\pm = |r_0 - r_\pm|/\rho < 1$ and

$$K(\mathrm{m}) = \int_0^{\pi/2} \frac{1}{\sqrt{1 - \mathrm{m}\sin^2\theta}}\, d\theta \qquad E(\mathrm{m}) = \int_0^{\pi/2} \sqrt{1 - \mathrm{m}\sin^2\theta}\, d\theta. \tag{4.60}$$

are the complete elliptic integrals of the first and second kind [116].

The predictions of the adiabatic theory in Eq. (4.59) are shown in Fig. 4.20 for $\rho = p + 10^{-3} \approx 0.04$ and $\rho = 0.1$. The red and blue lines indicate transitions between adjacent values of $[n_+]$ and $[n_-]$, respectively. The plot in Fig. 4.20(a) is colored according to the simulation results to emphasize the quantitative accuracy of the adiabatic prediction for $\rho = p + 10^{-3}$. The accuracy of these predictions diminishes with increasing ρ as shown in

Fig. 4.20(b) for $\rho = 0.1$ (cf. Fig. 4.10), although the predicted sweet spot and pinching structure continues to resemble the simulations. The dark region in this graph corresponds to the predicted location of PO based on the theory (Eq. (4.59)), i.e., PO is the region where $[n_+] + [n_-] = 0$. The predictions for the $\rho = 0.1$ case fail in three ways: (i) the pinched

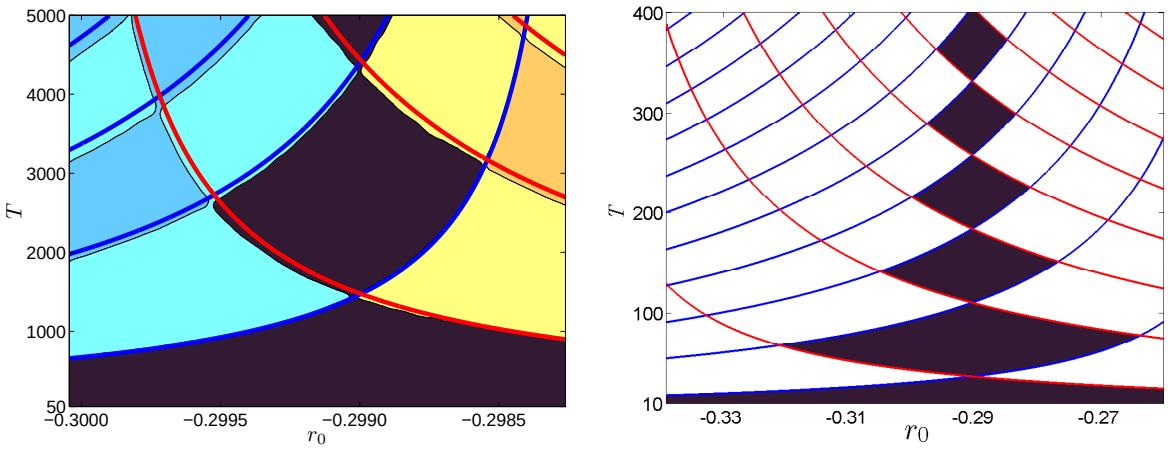

(a) $\rho = p + 10^{-3}$, theory and simulation

(b) $\rho = 0.1$, theory only

Figure 4.20: Predictions from adiabatic theory for the periodically force SHE23 using the asymptotic approximation Eq. (4.59) for the depinning time when (a) $\rho = p + 10^{-3} \approx 0.04$ and (b) $\rho = 0.1$. The colors in (a) refer to the numerical simulation results for the locations of PO (dark), O_{+n} (alternating yellow and orange), and O_{-n} (alternating shades of blue). The dark region in (b) is the adiabatic theory prediction of the PO region.

regions are spaced too far apart, (ii) there is no cliff demarcating the dominance of overall amplitude decay, and (iii) the region PO does not slant as in the simulations (Fig. 4.10). The qualitative disagreement occurs because of a breakdown of the asymptotic prediction for $T_{\pm}^{\mathrm{dpn}}$ when the system enters too far into regions $\mathcal{D}_{\pm}$. In addition to the quantitative disagreement of the depinning times, the theory omits the amplitude mode that destroys the localized states in $\mathcal{A}_-$. We can account for (i) by making use of numerical fits in place of the asymptotic theory for $T_{\pm}^{\mathrm{dpn}}$ as described in Fig. 4.4 and can also extend the theory to include predictions about the cliff mentioned in (ii) as described in the next section. The theory cannot, however, account for (iii) as the slanting is a result of the coupling between the amplitude and depinning modes which we have neglected.

The cliff

We can approximate the dynamics of the overall amplitude decay of a localized state in $\mathcal{A}_-$ by computing the time $T_{sn}^{\mathrm{col}}(r)$, $r < r_{sn}$, for a solution initialized with the periodic state at r_{sn} to decay to the trivial state. This calculation mirrors the asymptotic calculation for

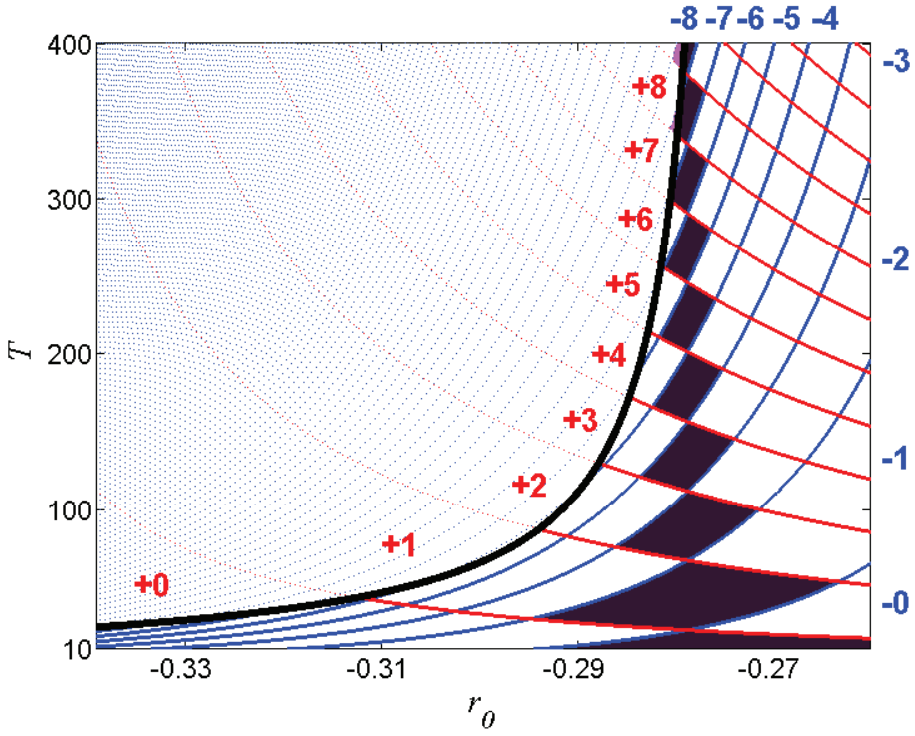

Figure 4.21: Adiabatic prediction in the (r_0, T) plane of the decay versus nucleation dynamics of a spatially localized initial condition of SHE23 with time-periodic forcing. Positive (resp. negative) numbers represent $[n_+]$ (resp. $[n_-]$), the change in the number of wavelengths due to nucleation (resp. annihilation) events during one cycle. The results are obtained using the relation (4.59) with $\rho = 0.1$ and $b = 1.8$. The figure is plotted over the same r_0 interval as Fig. 4.10.

$T_{\pm}^{\rm dpn}$. For $r = r_{sn} + \delta_{\rm col}$, $|\delta_{\rm col}| \ll 1$, we find

$$(T_{sn}^{\rm col})^{-1} \approx \frac{\Omega_{sn}}{2\pi} |\delta_{\rm col}|^{1/2}. \tag{4.61}$$

Substituting $T_{sn}^{\rm col}$ into Eq. (4.58) in place of $T_{\pm}^{\rm dpn}$ leads to an equation analogous to Eq. (4.59) for $n_{\rm col}$. Since $n_{\rm col}$ is at most one we assume that the threshold for the solution to decay irrevocably is $n_{\rm col} = 1/2$. This procedure yields a prediction for the location of the cliff in parameter space. For improved numerical accuracy for forcing cycles that penetrate far into $\mathcal{A}_-$, a numerical fit is useful (Fig. 4.4). Figure 4.21 reveals the dramatic improvement in the (r_0, T) phase diagram that results from this procedure applied to $T_{\pm}^{\rm dpn}$. We have also replaced the leading order theory for $T_{sn}^{\rm col}$ with a numerical fit to $T_{\rm loc}^{\rm col}$ to obtain an improved prediction for the cliff (bold black line). The hybrid adiabatic theory augmented with numerical fits from simulations of the system under constant forcing is in remarkably good agreement with the simulations even for $\rho = 0.1$. The predicted extent in T of the

sweet spots is $\triangle T \approx 45$, independently of T, which is within 5% of the value computed from simulations, viz., $\triangle T \approx 43$. In addition, the predicted period at which the cliff occurs for a given value of r_0 deviates from the value computed from simulations by $\triangle T \lesssim 10$, with the maximum deviation occurring for periods below $T = 100$. As expected, the agreement improves for larger periods and away from the cliff: the top of the subregion ${}^{-3}O_{+7}^{+10}$ is predicted to be at $(r_0, T) \approx (-0.2633, 373)$ but is located at $(r_0, T) \approx (-0.2637, 377)$ in the simulations.

Two-frequency time-dependence

Once the front depinning times $T_{\pm}^{\rm dpn}(r)$ and amplitude collapse time $T_{sn}^{\rm col}(r)$ are known as a function of the forcing parameter r with constant forcing, the adiabatic theory described by Eq. (4.59) can be applied for forcing with arbitrary time-dependence. Here we consider the effect of a second harmonic by taking the forcing to be of the form

$$r(t) = \rho \sin(2\pi t/T) + \rho_2 \sin(4\pi t/T + \phi_2). \tag{4.62}$$

The forcing function can now enter each of the depinning regions $\mathcal{D}_{\pm}$ more than once in a single cycle and can thus have more than one growth or decay phase. Sample trajectories from simulations of SHE23 with $\rho = 0.8$ and $T = 200$ are shown in Fig. 4.22. We note that this choice of parameters puts the system within PO when $\rho_2 = 0$. All three cases are initialized with a state that is stable when $\rho = \rho_2 = 0$ and have one long growth phase and two shorter decay phases. Figure 4.22(a) shows a trajectory with one wavelength added on each side per cycle of the forcing with three added during the single growth phase and two lost over the decay phases. A periodic orbit is shown in Fig. 4.22(b) that varies by four wavelengths over the cycle, and Fig. 4.22(c) shows a solution that loses two wavelengths on each side per cycle. The parameter space (ρ_2, ϕ_2) is shown in Fig. 4.23 where the right panel is colored by the average net front motion $\langle \Delta f \rangle$ per forcing cycle as computed from simulations while the right panel shows the prediction of the adiabatic theory described by Eq. (4.58).

The net change in the number of wavelengths shown on the right panel of Fig. 4.23 is computed by generalizing the adiabatic theory of the sinusoidal case to include multiple growth and decay phases:

$$N = \sum_j [n_+^j] + \sum_k [n_-^k]. \tag{4.63}$$

Each $n_{\pm}^l$ represents the number of growth or decay events occurring during a continuous interval outside of the pinning range computed using Eq. (4.58). The state is said to collapse if too much time is spent with $r < r_{sn}$ for any one of the decay intervals. The fact that there are two decay phases in the forcing cycle allows for a sweet spot and pinching structure to form *within* regions where a constant number of wavelength are added during the growth phase. We see three sweet spots in PO between approximately $0.06 < \rho_2 < 0.08$ and $-\pi/2 < \phi_2 < -\pi/4$ and this structure appears entirely within a region of parameter space

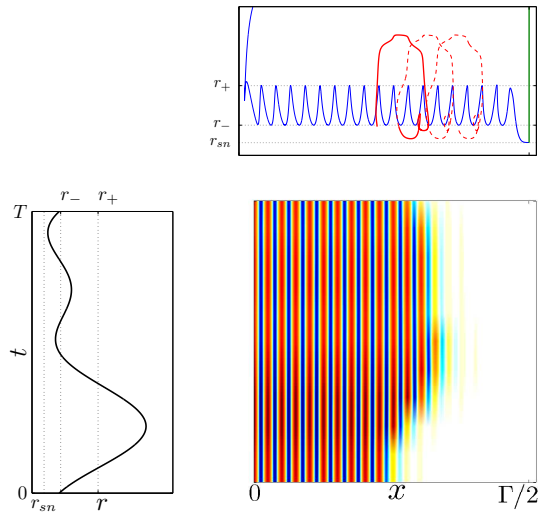

(a) $\rho_2 = 0.05325$, $\phi_2 = -55\pi/128$

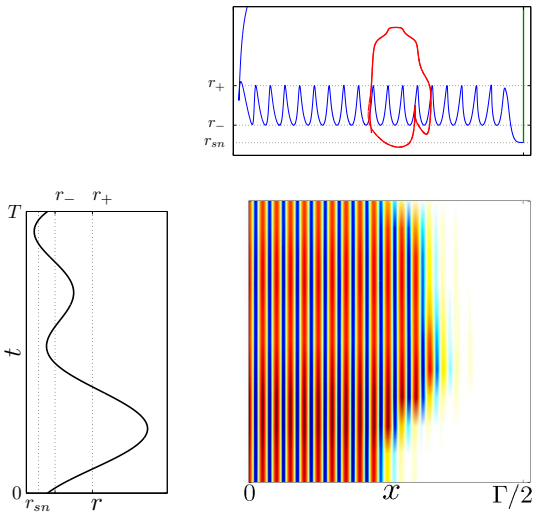

(b) $\rho_2 = 0.069$, $\phi_2 = -50\pi/128$

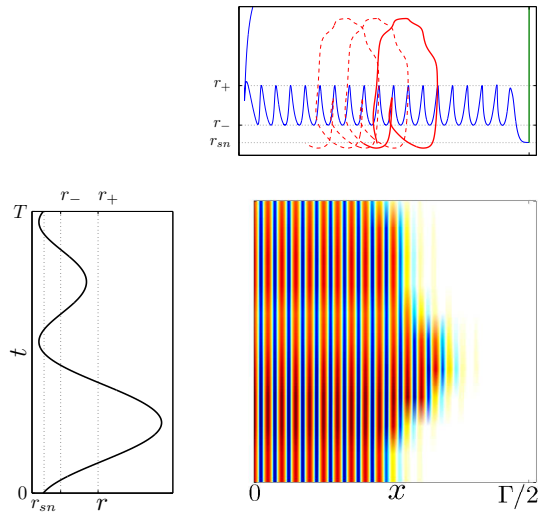

(c) $\rho_2 = 0.086$, $\phi_2 = -\pi/2$

Figure 4.22: Breathing localized structures observed in SHE23 (4.1) with two-frequency forcing (4.62), $\rho = 0.08$, $T = 200$, and $b = 1.8$. Space-time diagrams over one forcing cycle are shown for the right half of a state with positive (negative) values of the field u shown in red (blue). To the left is plot of the forcing function with dashed lines indicating the boundaries of the pinning, depinning, and bistability regions in the time-independent SHE23. Time along the vertical axis is aligned to the vertical axis of the space-time diagram. The upper panel provides a phase diagram plotting the trajectory of the front $x = f$ of the localized state as a function of the forcing and the horizontal axis is aligned with the horizontal axis of the space-time diagram below. The blue line in the background indicates time-independent solutions to SHE with constant forcing $r = r_0$.

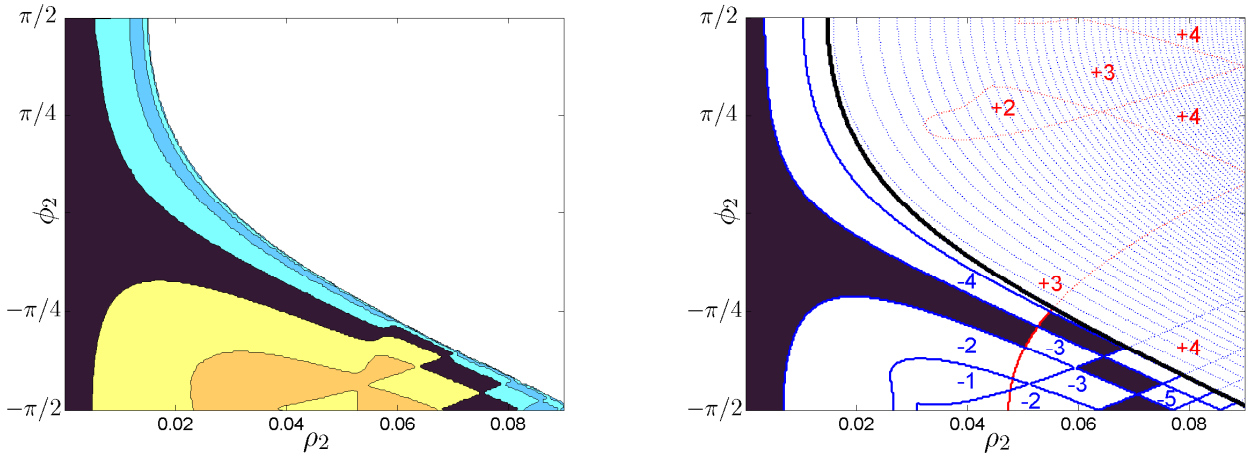

Figure 4.23: Color map of the different dynamics observed from simulations of SHE23 with two-frequency forcing (4.62) in the (ρ_2, ϕ_2) plane for $r_0 = -0.29$, $\rho = 0.08$, $T = 200$, and $b = 1.8$. Periodic orbits exist within region PO, which is defined by $-0.5 < \langle \Delta f \rangle / 2\pi < 0.5$. The regions to the right (left) of PO contain, in order, growing (decaying) solutions where the pattern experiences net growth (decay) by $1, 2, \ldots$ wavelengths on either side per cycle. The white region indicates parameter values at which the amplitude of the localized pattern decays within one cycle independently of its original size. The red (blue) lines show the quasi-static predictions for the transitions between bands with a constant number of nucleation (decay) events within a period of the forcing cycle. The bands are labeled with red (blue) signed integers, and the thick black line marks the quasi-static prediction of the cliff beyond which amplitude decay is expected.

where 4 wavelengths are added to each side during the growth phase. The sweet spot and pinching structure in this case forms from intersections of resonance bands of the two decay phases of the forcing cycle.

4.5 Canards

We have, up to this point, described *stable* localized breathing states that we obtained by time-stepping a *stable* steady-state solution to SHE23 (4.1) with constant forcing $r = r_0$. As the snaking structure (Fig. 4.1) indicates, the localized states alternate between stable and unstable as the branch snakes back and forth within the pinning region. The unstable solutions also generate spatially localized periodic orbits under periodic forcing. These orbits are similar to those presented in the previous sections of this chapter but instead of tracking the stable part of the snaking branches as the forcing varies, they track the unstable part and are therefore unstable as well. By virtue of being unstable, these states cannot be obtained by direct numerical simulation but the analogous orbits for the periodically modulated Adler equation have been studied via numerical continuation in Sec. 3.2.

In this section, we use time-simulations to locate trajectories in SHE23 with sinusoidal forcing (4.2) analogous to the canard trajectories shown in Figs. 3.10 and 3.12 for the periodically modulated Adler equation. Just as with the periodically modulated Adler equation, these trajectories appear near the transitions between neighboring resonance regions. They follow a stable snaking branch during one traversal of the pinning region and begin to follow an unstable one during the return trip and, by finely tuning parameters, one can control when along the unstable branch a jump to one of the two nearby stable solution branches occurs. During such a jump the fronts bounding the localized state move outward or inward depending on whether the stable state reached is longer or shorter than the unstable state. As the forcing period T increases, a separation of timescales between the slow tracking of the equilibria and the fast jumps between them begins to develop. We refer to trajectories that slowly drift along unstable states for part of the forcing cycle before undergoing a quick jump to a stable state as *canard* trajectories [89]. We note that, even though these orbits follow an unstable state for part of the trajectory, we are able to locate at least some of them by numerically time-evolving an appropriate initial condition until it converges to a periodic orbit. As is the case for the periodically modulated Adler equation, however, there are likely also unstable canard trajectories (cf. Fig. 3.11) that cannot be found by this method.

We have in fact already seen evidence that canard trajectories exist in the asymptotic limit that captures the formation of sweet spots and pinching described in Sec. 4.3. Figure 4.17 shows trajectories of the amplitude a of the depinning mode near r_+ (Eq. (4.49)) which can follow the constant forcing state through the fold for specific parameter of r_2, δ and ω such that $\nu = 0$. Tuning of parameters can control if the amplitude jumps up ($\nu > 0$) indicating a depinning event followed by an approach to a longer stable localized state or if it jumps down ($\nu < 0$) indicating an approach to a shorter stable localized state. Moreover, fine tuning near $\nu = 0$ can control where along the unstable solution branch this jump takes place.

More generally, this type of canard behavior is predicted by Eq. (4.49) near integer values of ν which correspond to transitions between the resonance bands generated by the periodic forcing. Near $\nu = n$ where $n \geq 0$, there will be n depinning events before the trajectory begins to track the unstable branch. The system can then, depending on parameter values, execute a jump to one of two nearby stable states as described above. Analogous canard dynamics are also predicted near r_- and we will refer to trajectories that exhibit such behavior near both edges of the pinning region as "double-headed" canards. We note that the trajectories predicted by this calculation follow an unstable state for an asymptotically small distance in r as Eq. (4.49) only describes the trajectory in a small neighborhood of $r = r_+$. Tuning parameters so that $\nu = 0$, including second higher-order corrections to the parameters, and continuing the calculation to higher order may allow for an analytic expression for canards that follow the unstable solution branch arbitrarily far into the pinning region. In what follows, we use the asymptotically small canards predicted by the theory as a starting point to numerically compute canards that follow an unstable state a $\mathcal{O}(1)$ distance into the pinning region.

By varying parameters of the forcing near predicted transition between resonance regions,

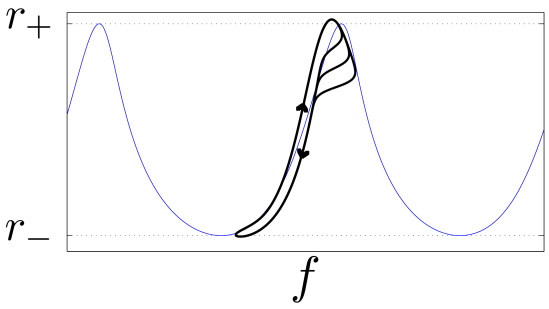

(a) $r_0 = -0.298525000000000$, $T = 1000$
$r_0 = -0.298514648437500$, $T = 1000$
$r_0 = -0.298514516258240$, $T = 1000$

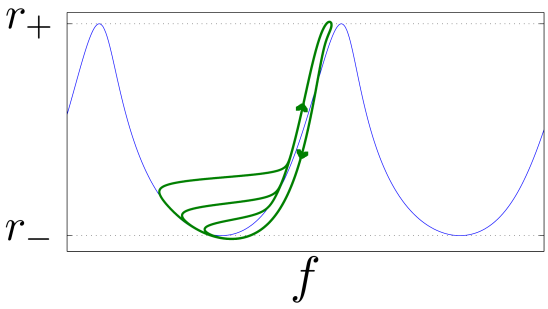

(b) $r_0 = -0.299390000000000$, $T = 1000$
$r_0 = -0.299414375000000$, $T = 1000$
$r_0 = -0.299414733886719$, $T = 1000$

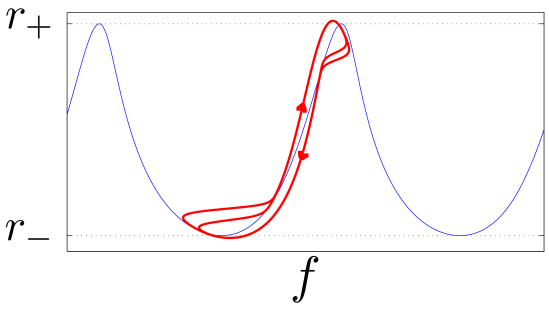

(c) $r_0 = -0.299025000000000$, $T = 1442$
$r_0 = -0.299026550000000$, $T = 1444$

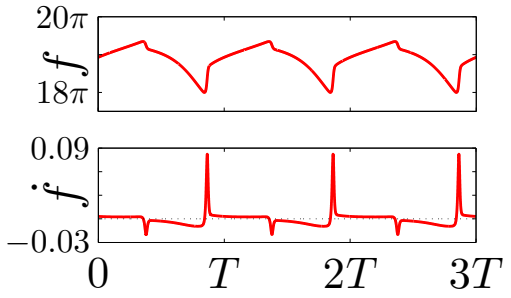

(d) $r_0 = -0.299026550000000$, $T = 1444$

Figure 4.24: For the periodically forced SHE23: (a) C^+ canards, (b) C_- canards and (c) C_-^+ canards represented through the front location $f(t)$ versus the forcing strength $r(t)$ for $\rho - p = 0.001$ (Fig. 4.17(c)). The thin blue line represents the stable ($\partial_f r > 0$) and unstable ($\partial_f r < 0$) parts of the branch of localized solutions for constant forcing ($\rho = 0$). In each case the parameters are listed in order of increasing time spent on the unstable branch. (d) Three periods of a two-headed C_-^+ canard from panel (c) shown using the front location $x = f$ and its speed $\dot{f}$ as functions of time.

we can control how far along the unstable solution branch the trajectory reaches before jumping to a stable branch and thereby generate a family of canard trajectories. Figure 4.24 shows three families of periodic canard trajectories computed from the periodically forced SHE23 such that $||u(t) - u(t+T)||_{L^2} < 10^{-10}$ for some sufficiently large t. Solutions in the family of C^+ canards follow the unstable branch close to the saddle-node at $r = r_+$ but deviate before reaching the saddle-node at $r = r_-$ (panel (a)). Solutions of this type are found near the transition between one growth band and the next. The C_- canards shown in panel (b) follow the unstable branch close to the r_- saddle-node but do not reach the r_+ saddle-node; these are found near transitions between adjacent decay bands. Both sets of transitions are approximated by Eq. (4.57). In regions where both bands intersect, it is

possible to obtain C_-^+ canards (panel (c)) which temporarily follow two different unstable branches; the associated front location $x = f$ and its speed $\dot{f}$ is represented in panels (d). When the trajectory is drifting along the branch of steady states the fronts move slowly inward or outward; however, the jumps from the unstable state to the stable state manifest themselves in abrupt changes in the front location, or equivalently in dramatic peaks in the front speed $\dot{f}$. Figure 4.25 shows how a small change in r_0 (T remaining fixed) impacts the time evolution of canard trajectories. Decreasing r_0 delays the onset of the bursts and

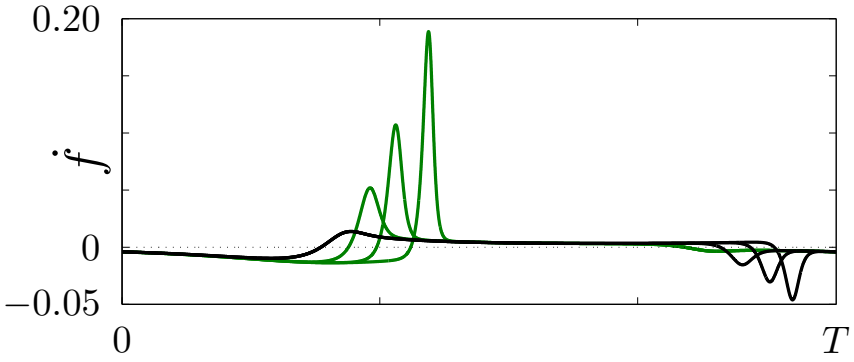

Figure 4.25: One period of the C_- (green) and C^+ (black) canards in the periodically forced SHE23 from Fig. 4.24(a) and Fig. 4.24(b) represented through the speed $\dot{f}$ of the right front as a function of time. The larger amplitude peaks are associated with the larger canards in Fig. 4.24.

increases the front speed, a consequence of the fact that the trajectory now departs from an unstable state farther from the saddle-node and hence with a larger unstable eigenvalue. However, canards that manage to traverse almost the entire unstable part of the branch of steady states are expected to display once again slower dynamics.

The canards shown in Fig. 4.24 correspond to the simplest canard families, organized by a single stable portion of the branch of steady states with no depinning. However, a careful tuning of the parameters reveals the presence of canards displaying depinning. Figure 4.26 shows several examples of the corresponding trajectories. The periodic orbits described by these canards are organized around *two* segments of stable steady states and the adjacent unstable steady states. The transitions between these segments are associated with the addition or loss of one wavelength on either side of the localized structure. A whole flock of canards can thus be obtained involving more segments of stable states and therefore displaying more depinning events per cycle.

In a similar fashion, we can obtain periodic orbits whose solution amplitude follows that of the lower branch spatially periodic state of the steady SHE. This gives rise to C_- canards characterized by a monotonic decrease in amplitude followed by a sudden jump to larger amplitude. Since the spatially periodic state u_p only displays one saddle-node no C^+ or C_-^+ canards can be obtained. These canard trajectories, represented in Fig. 4.27 (left panel),

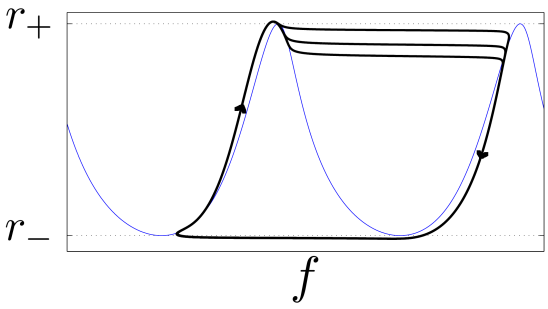

(a) $r_0 = -0.299300000000000$, $T = 2000$
$r_0 = -0.299336718750000$, $T = 2000$
$r_0 = -0.299336845397949$, $T = 2000$

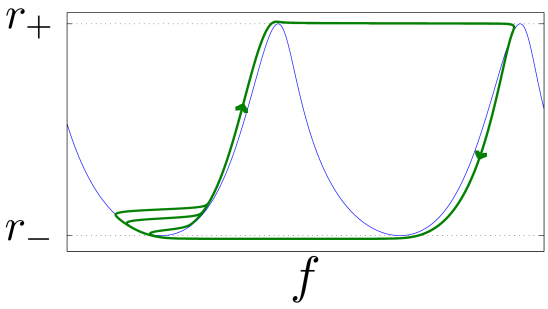

(b) $r_0 = -0.299350000000000$, $T = 3000$
$r_0 = -0.299361282348633$, $T = 3000$
$r_0 = -0.299361284373701$, $T = 3000$

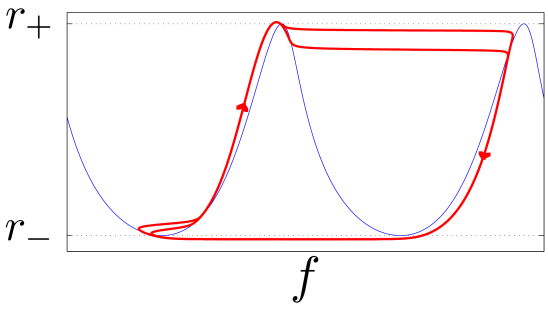

(c) $r_0 = -0.299530000000000$, $T = 2621$
$r_0 = -0.299532712097168$, $T = 2622$

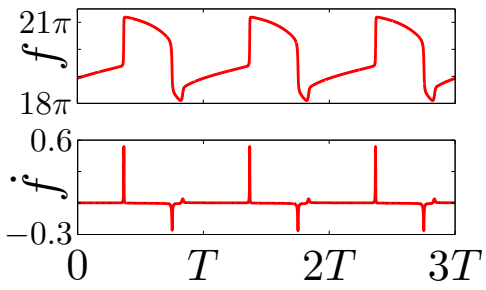

(d) $r_0 = -0.299532712097168$, $T = 2622$

Figure 4.26: "Larger" canards of the periodically forced SHE23 represented in the same fashion as in Fig. 4.24.

can be made to follow the unstable periodic state for a longer amount of time by choosing r_0 closer to the transition to amplitude collapse. Such trajectories spend more time in the depinning regime ($r < r_-$) as well as more time in the collapse regime ($r < r_{sn}$). As a result this regime is characterized by a competition between depinning and amplitude collapse as illustrated in Fig. 4.28(a) but the state ultimately collapses as exemplified by the spiraling trajectory in Fig. 4.27 (right panel). It may be possible, however, to generate similar front creation and annihilation dynamics in a periodic orbit by considering a periodic array of localized states that can interact. The simulation shown in Fig. 4.28(b) uses copies of the interior of the state shown at $2.5T$ for the simulation in Fig. 4.28(a) as an initial condition. While not periodic, it provides evidence that a periodic state could be located by varying the initial condition as well as the parameters of the simulation. Moreover, taking a single copy of the initial condition on a smaller domain will reduce the computation time.

As a final note, we point out that more complicated canard behavior can be predicted and controlled when a more general forcing function is considered. Ref. [118] provides conditions sufficient for the existence of canards with m downward jumps in an equation of the form

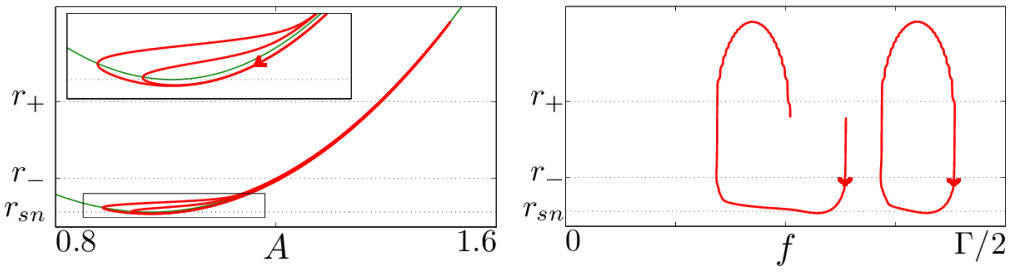

Figure 4.27: Amplitude and front position of canard trajectories of spatially *localized* states in the periodically forced SHE23 that follow the unstable amplitude of the spatially *periodic* state u_p for some amount of time. Here $\rho = -0.1$, $r_0 = -0.276055,\ -0.276220$, $T = 1100$, and $\Gamma = 640\pi$. The fold on the u_p branch is at $r_{sn} \approx -0.374370$.

$y' = h(\epsilon t, \mu) - f(y)$ with $\epsilon \ll 1$, h a C^2 periodic function with m local maxima per period, f a continuous and strictly increasing function and μ a set of m real parameters. Moreover, the theorem specifies that the location of each of the m jumps can be controlled by tuning μ. These results indicate that the simple sinusoidal forcing (4.2) is sufficient for canards with at most two jumps as shown in Figs. 4.24(c) and 4.26(c). The two-frequency forcing (4.62), on the other hand, allows the existence of canards that contain a total of three jumps along the orbit.

4.6 Discussion

We have considered the effects of parametric time-periodic forcing on the dynamics of localized structures in SHE23. In the high frequency limit averaging theory yields an averaged system that is also of Swift–Hohenberg-type. When oscillations are large enough, the time-varying forcing affects the averaged dynamics by modifying the coefficients of the nonlinear terms, thereby reducing the region of existence of spatially localized states (the pinning region in the case of constant forcing) and displacing it to larger values of r_0. For intermediate frequencies, the dynamics become more complex owing to depinning of the fronts bounding the localized structure over a significant fraction of the forcing cycle, resulting in breathing localized structures exhibiting behavior analogous to pinning, depinning, and amplitude collapse familiar from the constant forcing case.

Of particular significance is the observation of a new resonance phenomenon between the forcing period and the time required to nucleate a new wavelength of the pattern. The presence of this resonance is responsible for the complex structure of the parameter space, which breaks up into regions labeled by a pair of integers (m, q) denoting the number of wavelengths lost (m) per cycle and the number gained (q). When $n \equiv q - m = 0$ the resulting state is periodic in time, and corresponds to a state that on average neither expands nor shrinks. We have described the resulting structure of the parameter space in terms of

(a)

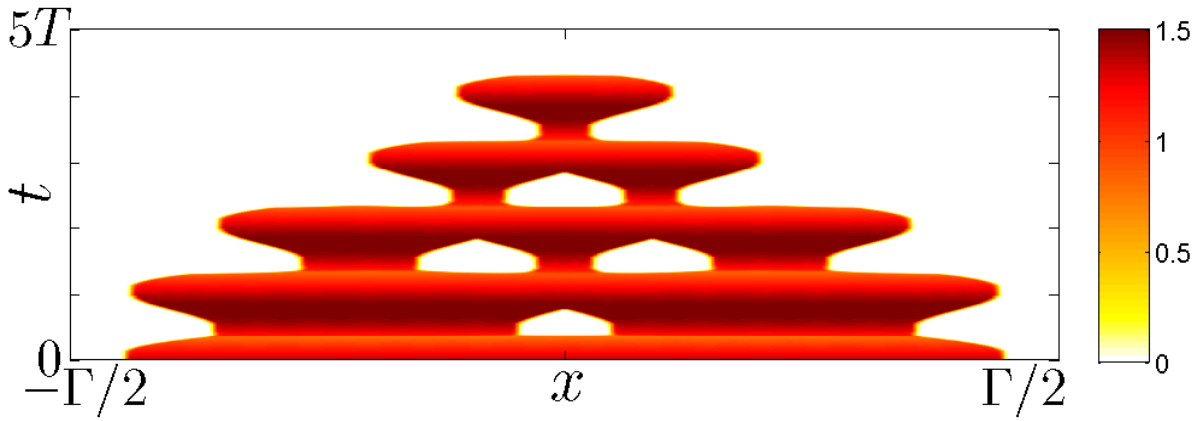

(b)

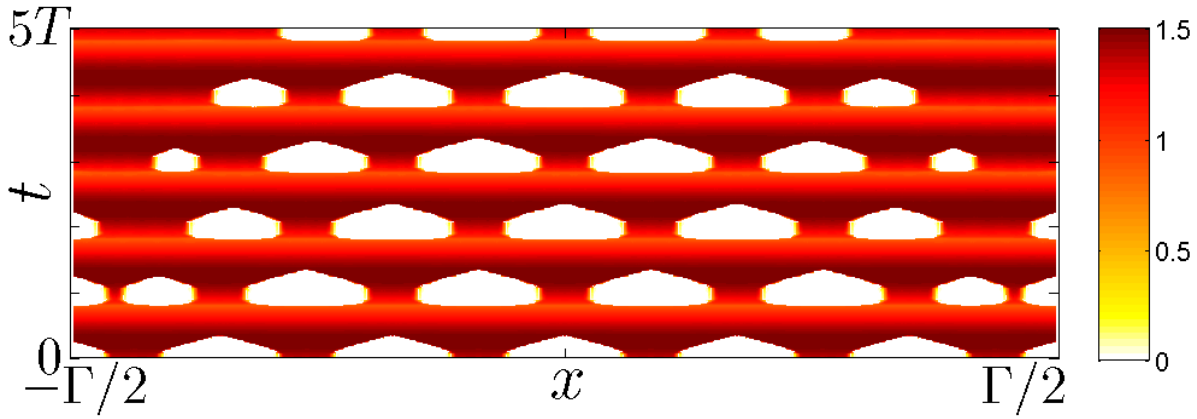

Figure 4.28: Space-time plot of amplitude canard trajectories of the periodically forced SHE23 with parameters $\rho = -0.1$, $r_0 = -0.276228387$, $T = 1100$, and $\Gamma = 640\pi$. Owing to the large extent of the domain, the pattern is not fully represented, only its local maxima are plotted against time. (a) A nearly domain-filling localized state used as an initial condition produces dynamics similar to the shrinking canard seen in Fig. 4.27. Here, new fronts are generated in the interior in addition to the breathing dynamics at the edges. (b) A simulation using $\rho = 0.1$, $r_0 = -0.276228387$, $T = 1100$, and $\Gamma = 640\pi$ is initialized with a multipulse state comprised of copies of the interior of the state shown at $2.5T$ for the simulation in panel (a).

sweet spots favoring the existence of such "pinned" states and pinched regions where the resonance was destructive and periodic localized structures absent. We found that these properties could be understood on the basis of appropriate asymptotics, valid either when the forcing cycle did not penetrate far into the depinning regions, or for low frequency forcing.

In both cases we showed that the number of nucleation/annihilation events can be computed by adapting existing theory of the depinning process, and used these results to partition the parameter space. A similar approach was successful in obtaining the accumulation point of the decay regions beyond which all initial conditions collapse to the trivial state within one forcing cycle. Our calculations suggest that this accumulation is exponential and involves regions of frequency locking corresponding to all rational numbers.

We found that asymptotic theory provided an excellent qualitative description of the resonance phenomenon, and moreover that quantitative agreement could often be obtained by augmenting the leading order nucleation theory with numerical fits to the nucleation times adopted from the time-independent case, thereby greatly extending the range of validity of the theory.

In view of the success of the Swift–Hohenberg equation in modeling localization in a great variety of systems with bistability between a homogeneous and a patterned state we expect that the model studied here, Eq. (4.1), captures faithfully the phenomenology arising from a resonance between the forcing period and the nucleation time in systems undergoing temporary depinning as a result of the forcing. As such we envisage numerous applications of the theory presented here to temporally forced systems such as models of vegetation growth in arid regions subject to seasonal forcing [33, 138].

In future work it will be of interest to extend the present analysis to systems with time-periodic forcing that is not purely sinusoidal and in particular to periodic forcing with asymmetry between the rise and fall phases. In addition, many experimental systems exhibiting spatially localized states, including binary fluid convection [139] and plane Couette flow [69], possess an additional midplane reflection symmetry whose effects are well modeled by the Swift–Hohenberg equation with a cubic-quintic nonlinearity [140, 141]. This motivates investigation of the properties of temporally-forced cubic-quintic Swift–Hohenberg equation with a view to elucidating the behavior expected when such systems are forced periodically.

Chapter 5

Localized stripes in two dimensions with time-periodic forcing

We now consider localized patterns in two spatial dimensions subject to time-periodic forcing. The dynamics here are complicated by the fact that the system can exhibit various kinds of patterns such as stripes of different orientation and hexagons or squares. Moreover, localized structures such as targets, spots, hexagonal or square arrays, and stripes of different orientations can all co-exist stably in certain parameter regimes. Figure 5.1 shows a numerical example of coexisting localized structures in the quadratic-cubic Swift–Hohenberg equation (SHE23) along with regions of existence of different types of localized states as a function of the forcing strength r and the magnitude of the quadratic nonlinearity coefficient b taken from [142]. Stationary target patterns in SHE23 have been studied in further detail in Ref. [143] by making use of radial symmetry to reduce the spatial dynamics of the stationary states to a one-dimensional nonautonomous problem.

In this chapter, we study time-periodic forcing of the cubic-quintic Swift–Hohenberg equation (SHE35) that exhibits squares and fully localized stripes as opposed to hexagonal patterns which are favored by the quadratic nonlinearity of SHE23. We write SHE35 as

$$u_t = ru - (1 + \nabla^2)^2 u + bu^3 - u^5, \tag{5.1}$$

and study the dynamics under an imposed sinusoidally varying forcing parameter of the form

$$r = r_0 + \rho \sin 2\pi t/T. \tag{5.2}$$

This forcing function, familiar from Chs. 3 and 4, is characterized by the average forcing strength r_0, the amplitude of modulation ρ and the period T. We consider localized stripes that are a two-dimensional extension of the one-dimensional states of Ch. 4 and whose stability properties have been discussed in Ref. [42]. We also study interfaces of stripes with different orientation and fully localized stripe patterns [59]. In analogy to the dynamics seen in Ch. 4, we find that the localized states begin to breathe when time-periodic forcing is introduced. We again use *PO* to refer to the region of existence in parameter space of

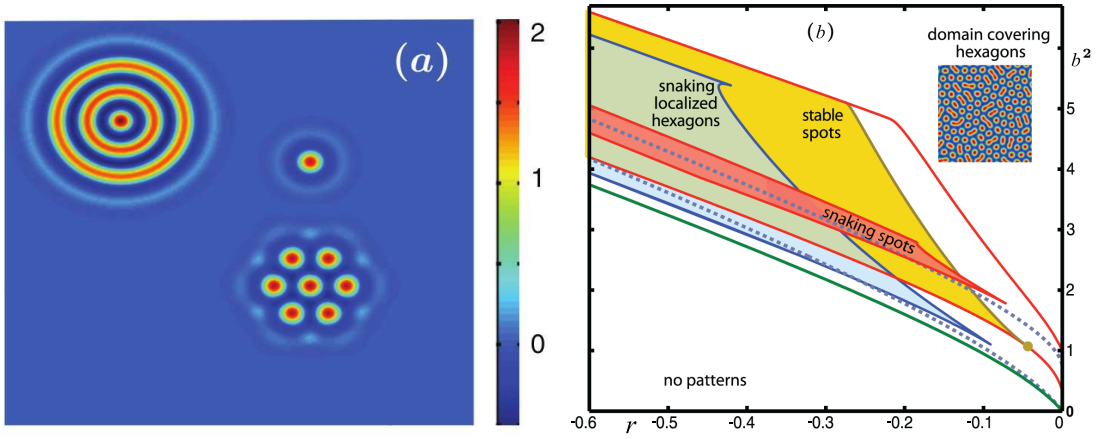

Figure 5.1: Coexisting localized target, hexagon, and spot patterns for SHE23 with constant forcing found by time simulation of an initial condition consisting of three different finite amplitude perturbations. Parameters: $b = 2.2$ and $r = -0.5$. (b) A summary of the region of existence for various localized patterns in SHE23 in the parameter space (r, b^2). Both panels are adapted from Ref. [142].

periodic orbits consisting of breathing states that remain stationary on average. We also find states that grow or decay on average but, because we do not explore forcing parameters that take the system outside of the region of bistability, do not see amplitude collapse.

The first section (5.1) reviews what is already known about stationary localized stripes and squares in SHE35 with constant forcing. Section 5.2 discusses the dynamics of various stripe patterns that are localized along one dimension when time-periodic forcing is introduced. We then turn to the effect of time-periodic forcing on the dynamics of fully localized stripe patterns in Sec. 5.3 before summarizing current progress and discussing future work in Sec. 5.4.

We take a numerical approach in this chapter, relying solely on time-simulations to study the dynamics of the planar patterns in SHE35 with time-periodic forcing. As with the one-dimensional SHE23 in Ch. 4, we integrate the equation forward in time using a fourth order exponential time differencing scheme [136] on an equidistributed mesh. Our calculations are performed in Fourier space and are fully dealiased. We use a periodic domain $(-L_x, L_x) \times (-L_y, L_y)$ with typical values $L_x = 20\pi$, $L_y = 10\pi$ and a grid with 1024×512 points. When we require a different domain size, we keep the same density of grid points. Because of the quintic nonlinearity of SHE35, we can only keep 1/3 of the modes along each spatial direction instead of 1/2 the modes for SHE23 in order to be fully dealiased. See App. A for more details about the numerical methods used. This chapter represents ongoing work and future plans involve a combination of numerical continuation, asymptotic analysis and time simulations to develop a more complete understanding of the dynamics of localized states in two dimensions with both constant and time-periodic forcing.

5.1 Stationary patterns with constant forcing

Early numerical studies of localized structures in the two-dimensional SHE relied on time-simulation [144, 40, 41]. More recent work, such as Refs. [42, 142, 143, 59], that employs numerical continuation to follow the stationary solutions as a function of the parameters has allowed for significant progress towards the development of a theoretical framework for understanding the solution structure of these states via spatial dynamics. This section summarizes parts of the work described in Refs. [42, 59] pertaining to stripe patterns that are localized along one or both directions in space.

Longitudinally invariant stripes

One-dimensional periodic patterns describe *longitudinally invariant stripes* in two dimensions. Likewise, localized states in one dimension describe longitudinally invariant stripes that are localized along the direction transverse to the stripes. In addition to the longitudinally invariant dynamics described by the one-dimensional SHE, these localized stripes can undergo instabilities along the length of the stripes in two dimensions. Figure 5.2 shows a bifurcation diagram of the snakes-and-ladders structure of SHE35 for $b = 2$ in one dimension in panel (a) and a zoom-in of the pinning region for two-dimensional localized stripes in panel (b). The region of bistability between the trivial state $u = 0$ and the periodic state P extends from $r_{SN} < r < 0$ where $r_{SN} = -0.8990$ and the Maxwell point of these two states is at $r_M \approx -0.6752$. The left (E_-) and right (E_+) edges of the one-dimensional pinning region occur at $r_- \approx -0.7126$ and $r_+ \approx -0.6267$, respectively, while the two-dimensional localized stripes are stable within approximately $-0.70 < r < -0.65$.

In Fig. 5.2(b), dotted lines indicate where the state is unstable in one dimension while bold lines indicate stability in two dimensions. The solid unbolded lines represent the sections of solution branches that are unstable along the direction of the stripes. Such longitudinal instabilities can be localized to the fronts at the edges of the states (*wall* modes) or can develop within the interior of the pattern (*body* modes). Figure 5.3 shows the time dynamics of a localized stripe state undergoing instabilities through a wall mode (panel (a)) and through a body mode (panel (b)). The parameters are within the pinning region of the one-dimensional SHE35 in both cases, and the dynamics depicted occur on longer time scales than the characteristic depinning time outside of the pinning region. The wall mode, for the parameters in the simulation ($r = -0.7105$, $b = 2$), generates periodically structured fronts on a relatively slow timescale that remain stationary. The wavelength of the structure is of the same magnitude as the wavelength of the stripe pattern. The body mode (shown for $r = -0.9183$, $b = 2.5$) causes a long wavelength zigzag on the stripes and creates local curvature at the fronts causing them to depin and propagate outward on an even slower timescale. Figure 5.4 summarizes the stability of the localized stripes to different wavelengths along the longitudinal direction k_y as a function of the forcing parameter r for $b = 2$ and $b = 2.5$. We see that the body mode (B) becomes more important for the larger value of b and is first unstable for $k_y = 0$.

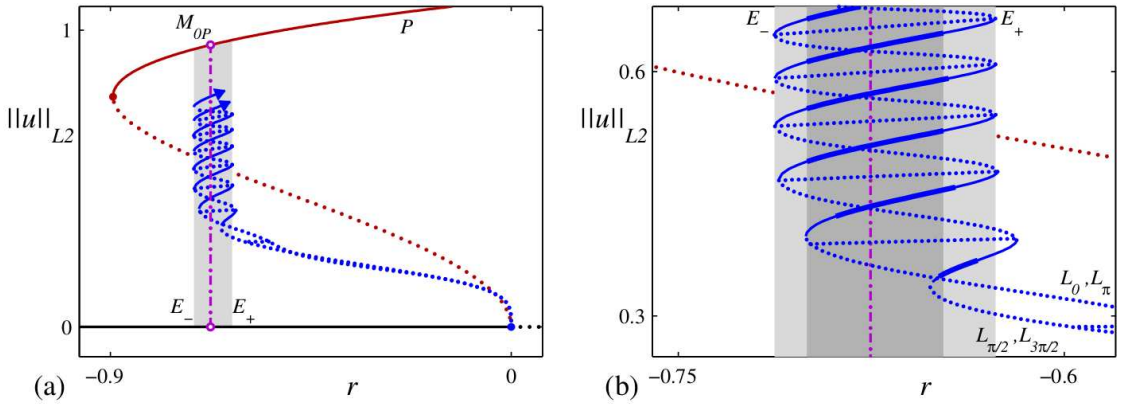

Figure 5.2: (a) A bifurcation diagram of the snakes-and-ladders structure SHE35 in one dimension with constant forcing and $b = 2$. The periodic solution P is shown in red, the spatially localized solutions are shown in blue, and the trivial solution $u = 0$ is shown in black. Dotted lines indicate unstable stationary solutions while solid lines indicate stable ones. The pinning region where the spatially localized states exist is shaded in gray and found approximately for $-0.7126 < r < -0.6267$. The Maxwell point between the periodic state and trivial state is at $r_M \approx -0.6752$. (b) A bifurcation diagram showing a portion of the pinning region for longitudinally invariant stripes of SHE35 in two dimensions. The bold blue lines indicate spatially localized stripes that are stable in two dimensions, while the dotted lines indicate solutions that are unstable in the one-dimensional case. The unbolded lines indicate where the state is unstable to longitudinal perturbations along the stripes. Both panels are taken from Ref. [44] and the corresponding results were first published in Ref. [42].

Stripes of different orientation

Though the stability properties and resulting dynamics are different, stationary localized solutions comprised of longitudinally invariant stripes exhibit the same snakes-and-ladders structure as the one-dimensional localized states owing to front pinning. Localized solutions with fronts that are transverse to the stripes can also be constructed, and these states exhibit *collapsed snaking*. The fronts transverse to the stripes are not pinned and thus the localized state is only stationary at the Maxwell point once fully formed (cf. lower part of branch in Fig. 5.5(b)). We will refer to these patterns as *unpinned stripes*. Collapsed snaking is also seen in one spatial dimension when a heteroclinic connection between the trivial state and a nonzero uniform state forms [24]. Figure 5.5 compares bifurcation diagrams of the two orientations of stripes localized along one direction and provides sample solutions for each.

In addition to having localized patterns with fronts along the stripes or transverse to them, stationary states comprised of a mix of the two orientations exist for SHE35 in two dimensions. Longitudinally invariant stripes can connect to unpinned stripes via fronts

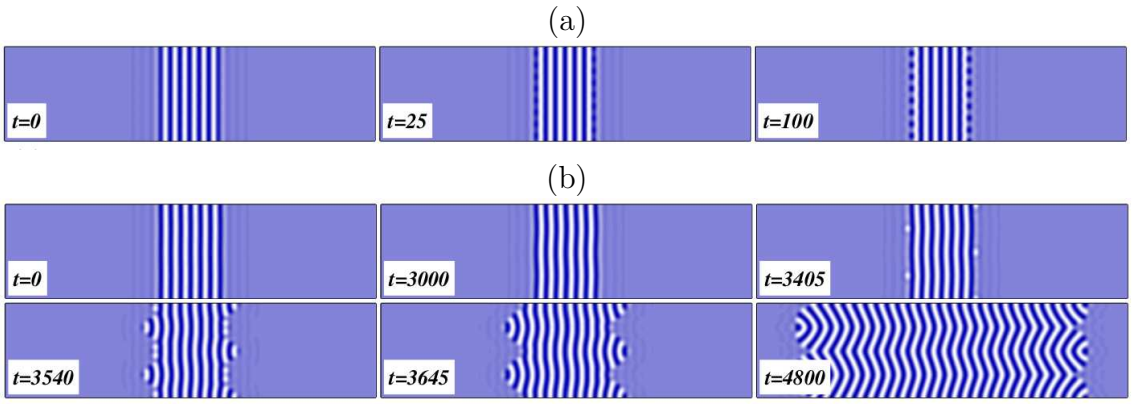

Figure 5.3: Frames from a time simulation of longitudinally invariant, spatially localized stripes in SHE35 with constant forcing undergoing (a) a wall instability (W_-) with $r = -0.7105$ and $b = 2$ and (b) a body instability (B) with $r = -0.9183$ and $b = 2.5$. Both panels are taken from Ref. [42].

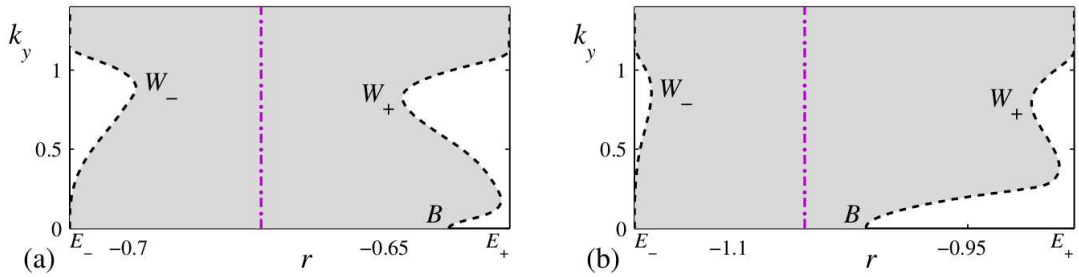

Figure 5.4: A summary of the stability of longitudinally invariant, spatially localized stripes of SHE35 as a function of the longitudinal wavenumber k_y along the stripe and the constant forcing parameter r for (a) $b = 2$ and (b) $b = 2.5$. At the specified value of r within the shaded region the stripes are stable to all perturbations with wavenumber k_y. The dashed lines represent onset of transverse instability due to wall modes ($W_\pm$) or body modes (B). The pink dashed-dotted line marks the Maxwell point between the periodic stripe state and trivial state. Both panels are taken from Ref. [44] and the corresponding results were first published in Ref. [42].

made of squares similar to what is produced by the wall instability seen in Fig. 5.3(a). Figure 5.6 shows a single branch of stationary solutions that exhibits both snaking and collapsed snaking. The single longitudinally invariant stripe surrounded by squares shown in panel (1) can, by varying the forcing parameter, grow via the generation of unpinned stripes from the outer squares (panel (2)) or grow by forming additional longitudinally invariant stripes from the inner squares (panel (3)).

We conclude this subsection by mentioning localized square patterns because of the role

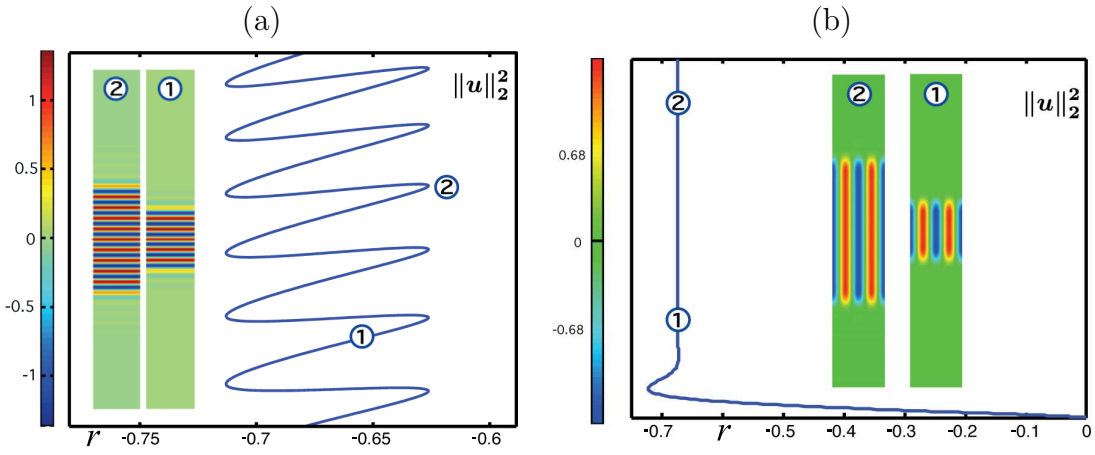

Figure 5.5: Bifurcation diagrams of SHE35 with constant forcing and $b = 2$ showing (a) longitudinally invariant, spatially localized stripes and (b) localized stripes with fronts perpendicular to the direction along the stripes. Sample solutions are shown in each case. The longitudinally invariant stripes exhibit snaking while the stripes with a transverse front exhibit collapsed snaking. Adapted from Ref. [59].

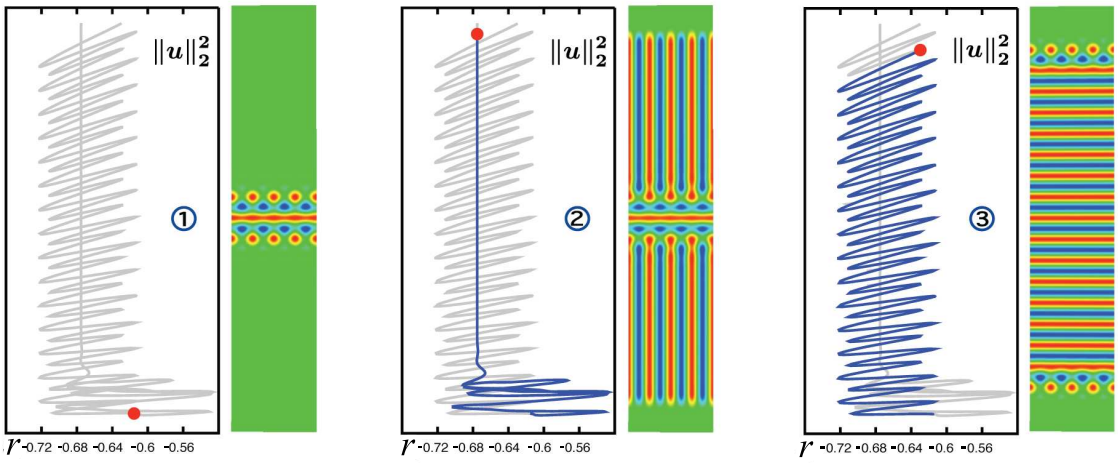

Figure 5.6: A single solution branch of SHE35 with constant forcing and $b = 2$ that exhibits collapsed snaking by developing perpendicular stripes from the outer squares along the longitudinally invariant stripe and exhibits snaking by generating longitudinally invariant stripes from the inner squares of the front. A bifurcation diagram highlighting the appropriate section is given along with a sample solution at the location marked by a red dot. Adapted from Ref. [59].

squares appear to play in the fronts between longitudinally invariant stripes and unpinned stripes. The Maxwell point between homogeneous squares and the trivial state occurs at

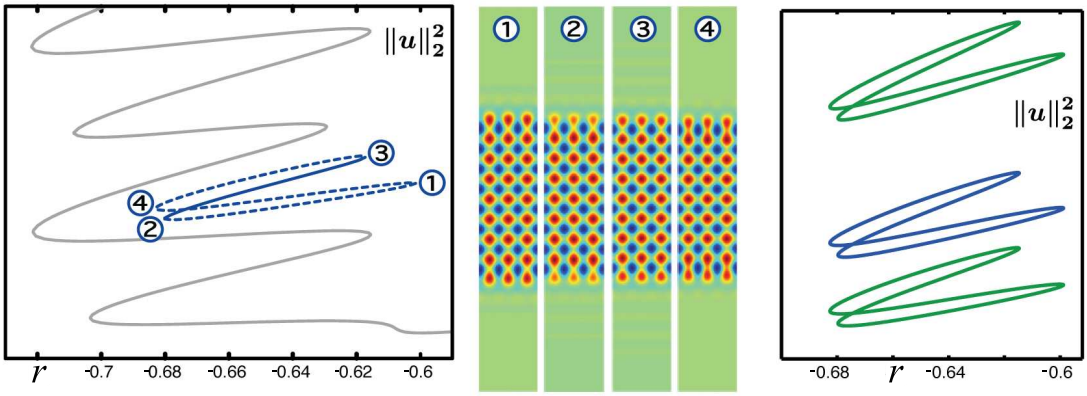

Figure 5.7: Localized square patterns in SHE35 with constant forcing and $b = 2$. The left panel shows a bifurcation diagram of an isola drawn in blue containing square patterns that are localized along one spatial direction. The state is stable where the line is solid and unstable where it is dashed. The gray snaking diagram shows the part of the bifurcation diagram in panel (3) of Fig. 5.6 for reference. Solutions at each of the folds of the isola are given in the central panel and two additional isolas with localized squares of longer and shorter spatial extent are shown in green in the right panel. Adapted from Ref. [59].

$r_s \approx -0.609$ and the localized square patterns shown in Fig. 5.7 are found on isolas that are contained mostly within the pinning region of longitudinally invariant stripes.

Fully localized stripes

Thus far we have described states that are localized along one spatial dimension, but stationary stripe patterns that are fully localized also have been found in SHE35 [41, 59]. Figure 5.8 shows a bifurcation diagram of these so-called "worm" states along with a few sample solutions at different points along the snaking branch. As expected for SHE35, a half-wavelength (e.g. a positive or negative stripe) is added to the structure for each back-and-forth excursion of the solution branch. In addition, the longitudinal length of the stripes on the structure increases as the forcing increases for a state with a given number of wavelengths. The pinning mechanism that allows these states to remain stationary over a finite parameter interval is not yet fully understood, though we do note a striking similarity between the "tips" of the fully localized stripes and the structures that form along the fronts when longitudinally invariant stripes undergo a body mode instability ($t = 3645$ in Fig. 5.3(b)).

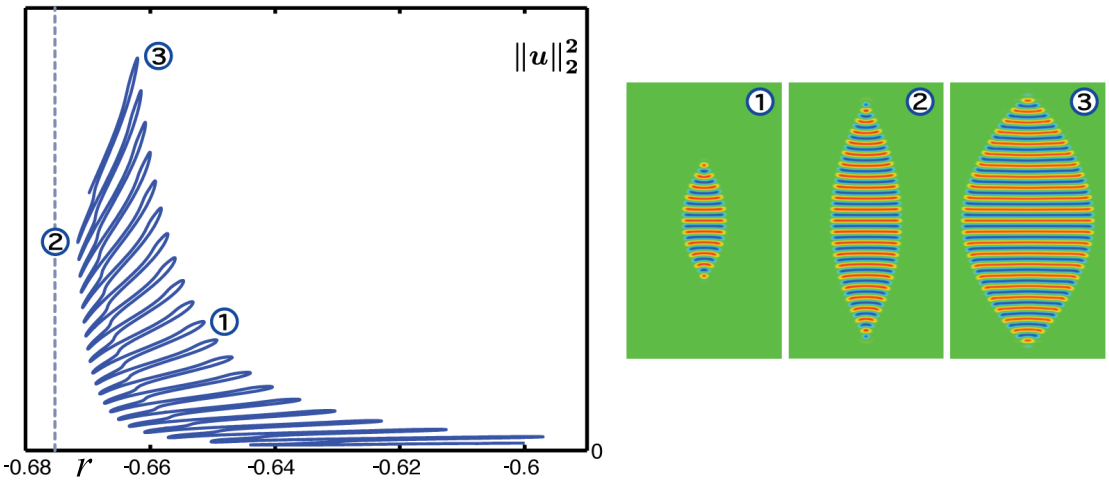

Figure 5.8: Fully localized stripe patterns in SHE35 with constant forcing and $b = 2$. A bifurcation diagram is shown in the left panel and sample solutions along the branch are shown in the right panel. The Maxwell point between the one-dimensional periodic state and the trivial state occurs at $r_M = -0.6753$ and is shown as a vertical dashed line. Adapted from Ref. [59].

5.2 Dynamics of partially localized stripes under time-periodic forcing

in the absence of longitudinal instabilities, longitudinally invariant stripes reproduce the dynamics observed for the one-dimensional patterns of Ch. 4 when time-periodic forcing is introduced. In this section we consider such perturbations to these patterns as well as patterns composed of stripes with different orientations. We restrict our attention to the periodically forced SHE35 (Eqs. (5.1)-(5.2)) with cubic nonlinearity coefficient $b = 2$, forcing period $T = 100$ and modulation amplitude $\rho = 0.12$. We report the dynamics that result from various initial conditions and scans over the average forcing r_0.

Wavy stripes

As seen in Fig. 5.3(b), longitudinally invariant stripes can undergo a long wavelength zigzag instability that results in wavy stripes. We therefore initialize a simulation using the state shown in Fig. 5.9(a), and find that periodic orbits are possible with Fig. 5.9(b) and (c) showing the pattern at the start and halfway point of the final forcing period of a simulation with $r_0 = -0.655$. The computation is done on a periodic domain with $L_x = 20\pi$, $L_y = 10\pi$ and with a grid of 1024×512 points. The pattern in Fig. 5.9 consists of fully-formed wavy stripes on the interior with curved partially formed stripes that arrange into a series of structures along the front. "Tips" appear where the pattern extends farthest along the $\pm x$

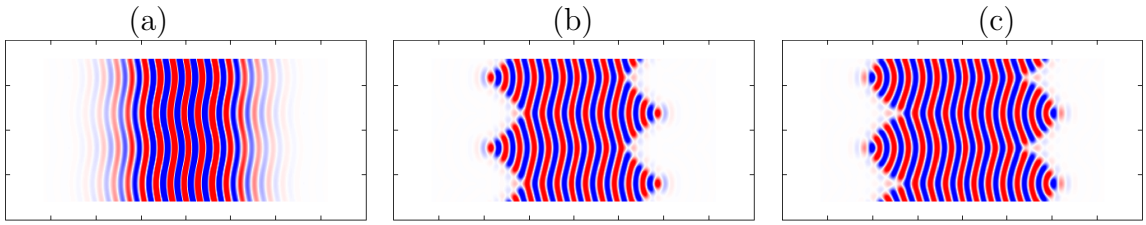

Figure 5.9: Wavy stripe patterns in the periodically forced SHE35 with parameters $r_0 = -0.655$, $\rho = 0.12$, $T = 100$ and $b = 2$. (a) Initial condition used to find a periodic orbit of wavy stripes. Solutions during (b) the initial phase of the final forcing cycle at $t = 2400$ and (c) the middle of the last forcing cycle at $t = 2450$ are also shown. The solutions in (b) and (c) correspond to times along the forcing cycle when $r(t) = r_0$.

direction and grow from concave regions along the front of the initial state. The partially formed stripes lengthen moving inward from the tips until they intersect at "valleys" that form the innermost parts of the front. Not surprisingly given the initial condition, the state along the periodic orbit is not symmetric under $x \to -x$: the tips on the $+x$ front (right side) appear at the same y value as the valleys on the $-x$ front (left side). During each forcing cycle one stripe (a half-wavelength) is added to and subtracted from each side of the pattern at both the tips and valleys of the front. The structures of partially formed stripes along the fronts bulge and narrow in a smooth way as the forcing increases and decreases.

The periodic orbit is found by time-simulation for 25 cycles of the forcing and Fig. 5.10(a) shows that the L^2 norm of the difference of the solution at the start of successive cycles decreases exponentially, reaching $||u(2500) - u(2400)|| \approx 10^{-6}$ by the end of the simulation. As in the one-dimensional case (Eq. (4.3)), we can describe the dynamics in terms of the location of the fronts defining the edge of the localized state. In this case, however, we will employ several front variables in an attempt to characterize the longitudinally varying front. We define the location of the right ($+x$) front at $y = 0$ to be

$$f_x(t) = 2\frac{\int_0^{L_x} xu(x,0,t)^2 dx}{\int_0^{L_x} u(x,0,t)^2 dx}. \tag{5.3}$$

In addition, we define the location of the tip f_x^+ and valley f_x^- of the front to be

$$f_x^{\pm}(t) = 2\frac{\int_0^{L_x} xu(x,y^{\pm},t)^2 dx}{\int_0^{L_x} u(x,y^{\pm},t)^2 dx}, \tag{5.4}$$

where $y^+ = 5\pi$ is the location of a tip and $y^- = -5\pi$ is the location of a valley on the right ($+x$) front. Figure 5.10(b) shows the front positions defined by Eqs. (5.3)-(5.4) as a function of time for the final three forcing cycles of the simulation. The tip and valley locations $f_x^{\pm}$ both vary by approximately π, consistent with the addition and subtraction of a half-wavelength on each side, and fast jumps in the value indicate when the number

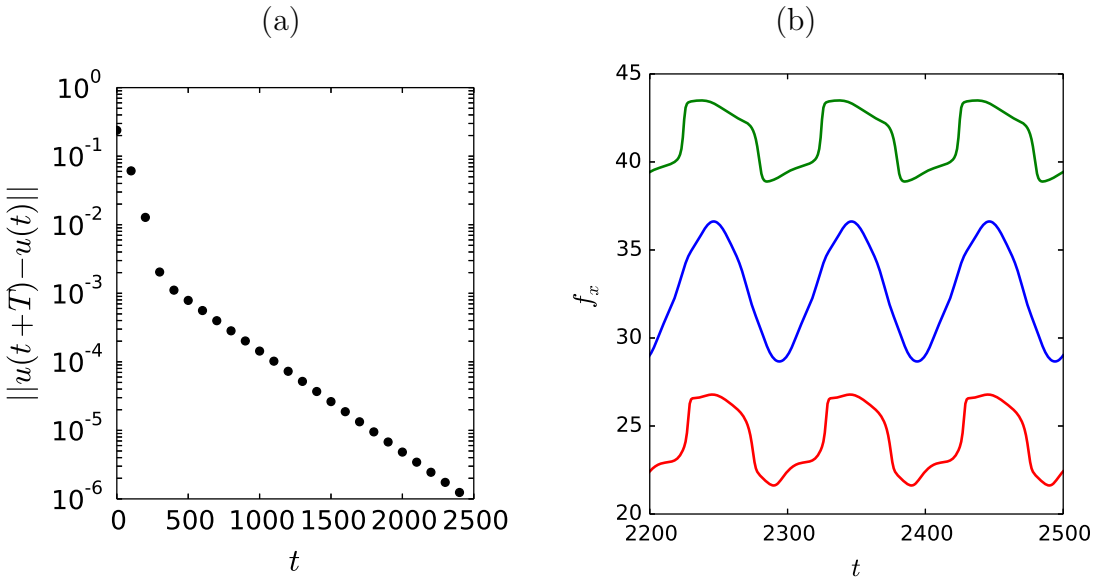

Figure 5.10: The periodic orbit consisting of wavy stripe patterns shown in Fig. 5.9 for the periodically forced SHE35. (a) Convergence to a periodic orbit as measured by the L^2 norm of the difference of the solution at the start of successive periods. (b) The x-front position of the solution along $y = 5\pi$ (green), $y = 0$ (blue) and $y = -5\pi$ (red) as a function of time for the final three forcing cycles of the simulation. The y locations at which the front is computed correspond to the "tip" of the front, the center value, and the "valley" of the front, respectively. Parameters: $r_0 = -0.655$, $\rho = 0.12$, $T = 100$ and $b = 2$.

of wavelengths changes. The front f_x along $y = 0$ varies smoothly with a larger amplitude owing to the bulging and narrowing dynamics of the structures along the fronts.

A plot of the average change $\langle \Delta f_x \rangle$ in front location f_x as a function of the average forcing r_0 reveals a finite region of parameter space, PO, where periodic orbits exist (Fig. 5.11). The width of PO, $\Delta r_0 \approx 0.08$, is about 1/10 the size of the pinning region for one-dimensional localized states under constant forcing and lies within the portion that is stable to body mode instabilities. Periodic forcing with amplitude $\rho = 0.12$, however, takes the system through regions unstable to body modes and outside of the one-dimensional pinning region on either side. Interestingly, periodic orbits exist for values of r_0 completely within the pinning region for fully localized stripes comprised of between approximately 4 and 10 wavelengths (Fig. 5.8). This may be more than a coincidence given that the structures along the fronts in Fig. 5.9 appear to be portions of fully localized stripe states.

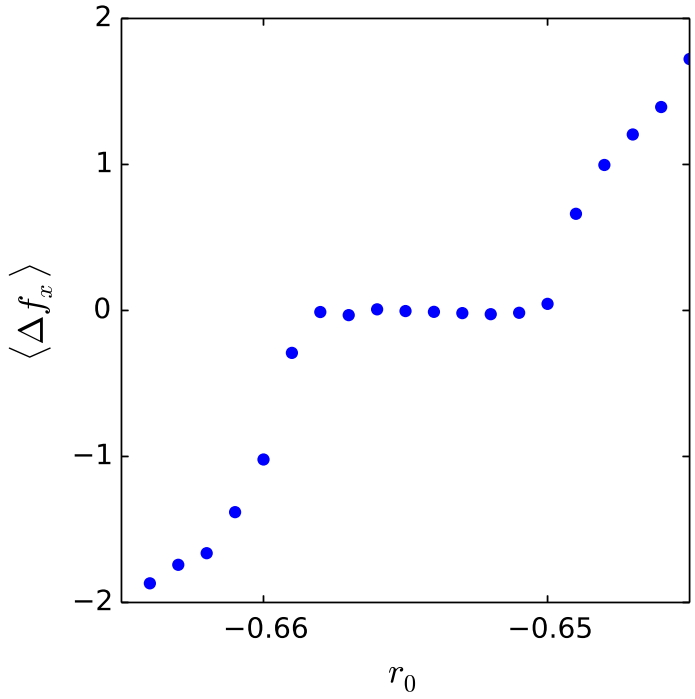

Figure 5.11: The average change $\langle \Delta f_x \rangle$ in location of the front f_x along $y = 0$ as a function of the average forcing parameter r_0 for wavy stripe initial conditions in periodically forced SHE35 with $b = 2$, $T = 100$ and $\rho = 0.12$.

Stripe-stripe interfaces

We now look at interfaces between longitudinally invariant stripes and unpinned stripes (cf. Fig. 5.6). Squares tend to form at these grain boundaries between the sections of stripes with different orientation. We take a (spatially periodic) domain-filling initial condition of alternating patches of longitudinally invariant stripes and unpinned stripes in order to examine the response of the interface to time-periodic forcing. Throughout this subsection, as with the last, we consider the periodically forced SHE35 (Eqs. (5.1)-(5.2)) with cubic nonlinearity coefficient $b = 2$, forcing period $T = 100$ and modulation amplitude $\rho = 0.12$. The computation is done on a periodic domain with $L_x = 20\pi$, $L_y = 10\pi$ and with a grid of 1024×512 points. Figure 5.12 shows the result of three simulations with this initial condition using $r_0 = -0.691$, -0.693 and -0.695. To provide some context, we note that these values are less than the Maxwell point r_M for the stripe solutions (Fig. 5.5(b)), within the pinning region of longitudinally invariant stripes with squares at the fronts (Fig. 5.6(c)), and less than the values of r where localized squares exist (Fig. 5.7).

For $r_0 = -0.691$, the system quickly approaches a periodic orbit in which a row of squares is first added to and then subtracted from each interface (Fig. 5.12(a)). For $r_0 = -0.693$, the

Figure 5.12: Each column is a simulation of the periodically forced SHE35 using a domain-filling initial condition consisting of patches of stripes with perpendicular orientation and (a) $r_0 = -0.691$, (b) $r_0 = -0.695$, (c) $r_0 = -0.695$. The rows, from top to bottom, show the state at $t = 100$, $t = 150$, $t = 200$, $t = 250$ and $t = 300$. Solutions in columns (a) and (b) approach periodic orbits while (c) approaches the trivial state. Parameters: $b = 2$, $T = 100$ and $\rho = 0.12$.

system approaches a periodic orbit in which each interface breaks and reforms during the course of the forcing cycle (Fig. 5.12(b)). The squares remain attached to the longitudinally

invariant stripes and generate a localized structure similar to what the wall instability creates (Figs. 5.3(a) and 5.6(c)). Figure 5.13 shows the convergence to a periodic orbit in the case shown in Fig. 5.12(b) with $r_0 = -0.693$. While the simulation has not yet converged in

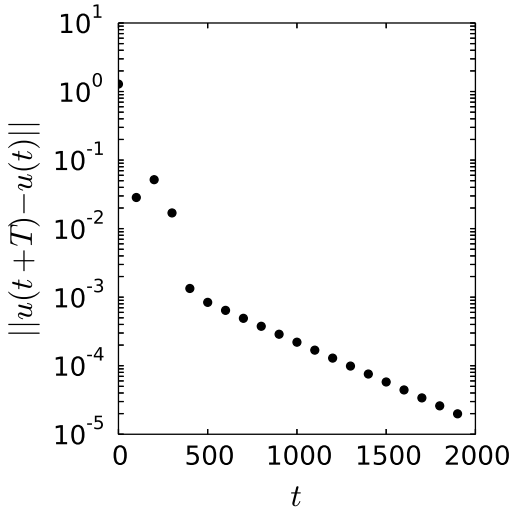

Figure 5.13: Convergence to a periodic orbit consisting of patches of stripes with perpendicular orientation in the simulation of the periodically forced SHE35 depicted in Fig. 5.12(b). The simulation is terminated at $t = 2000$. Parameters: $b = 2$, $T = 100$, $\rho = 0.12$ and $r_0 = -0.693$.

Fig. 5.12(b), the last two states shown at times $t = 250$ and $t = 300$ are visually similar to the corresponding frames along the periodic orbit at times $t = 2450$ and $t = 2500$.

During the first forcing cycle (not shown in Fig. 5.12(c)) for the case of $r_0 = -0.695$, the stripes detach and reconnect in a similar way as is seen in Fig. 5.12(b). During the second forcing cycle the stripes detach but fail to reconnect as is shown in the middle row of Fig. 5.12(c). After this failure to reconnect, the once domain-filling state is now comprised of alternating localized patches of unpinned stripes and longitudinally invariant stripes with squares at the edges. The newly created localized patterns exhibit similar front speeds to the $r_0 = -0.693$ case during the growth phase of the forcing cycle but significantly faster front motion during the decay phase. The localized patches thus decay on average and the system approaches the trivial state. The longitudinally invariant stripes disappear first (at around $t = 400$) and the unpinned stripes only persist for about two forcing cycles longer (approximately to $t = 600$).

We can also construct spatially localized initial conditions that consist of stripes with different orientation embedded in a trivial background. One example is shown in the first panel of Fig. 5.14 and the subsequent panels show results from the first forcing cycle of a simulation with $r_0 = -0.665$. The computation is done on a periodic domain with $L_x = 5\pi$,

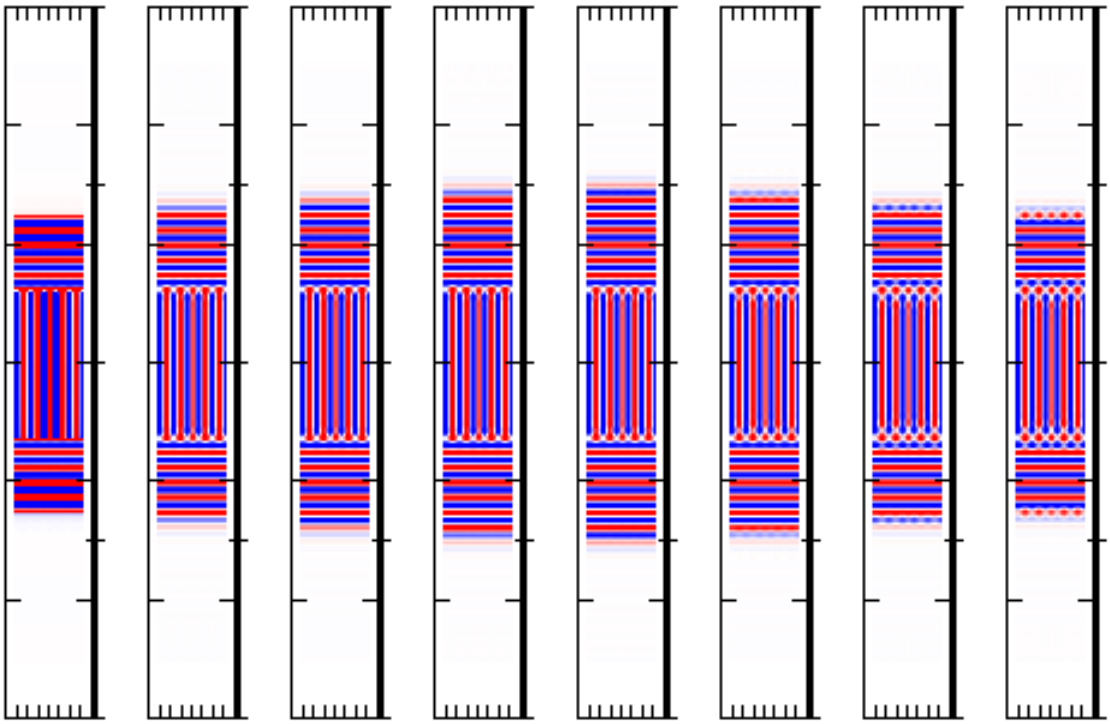

Figure 5.14: The first forcing cycle of a simulation of the periodically forced SHE35 with parameters $b = 2$, $T = 100$, $\rho = 0.12$ and $r_0 = -0.665$. The panels show, from left to right, the state at $t = 0$, 10, 20, 30, 70, 80, 90 and 100. The first four panels are from the growth phase of the forcing cycle while the last four are from the decay phase. This state begins to grow on average after the transition depicted in Fig. 5.15.

$L_y = 40\pi$ and with a grid of 256×2048 points. The average forcing r_0 for this simulation is slightly greater than the Maxwell point between the stripes and trivial state but within the region of stability for longitudinally invariant localized stripes (Fig. 5.2(b)). With this initial condition, the state can begin to breathe when time-periodic forcing is introduced. The outer longitudinally invariant stripes act as anchors, preventing the inner unpinned stripes from growing or decaying in spatial extent on average. A row of squares alternatingly forms and disappears at the grain boundaries on the interior of the state in a similar way to what is seen in Fig. 5.12(a). The outer fronts that define the edge of the localized state breathe as longitudinally invariant stripes are first added and then subtracted, although for the parameters used there is a net loss of these stripes. Figure 5.14 shows the growth and decay of the state over the first forcing cycle with $r_0 = -0.665$. The longitudinally invariant stripe at the outer front remains intact during the growing phase and only develops into squares through a wall instability (cf. Fig. 5.3(a)) during the decay phase. The squares at the outer edges of the state persist until the longitudinally invariant stripes that experience average decay disappear near $t = 800$. After this transition, shown in Fig. 5.15, only the

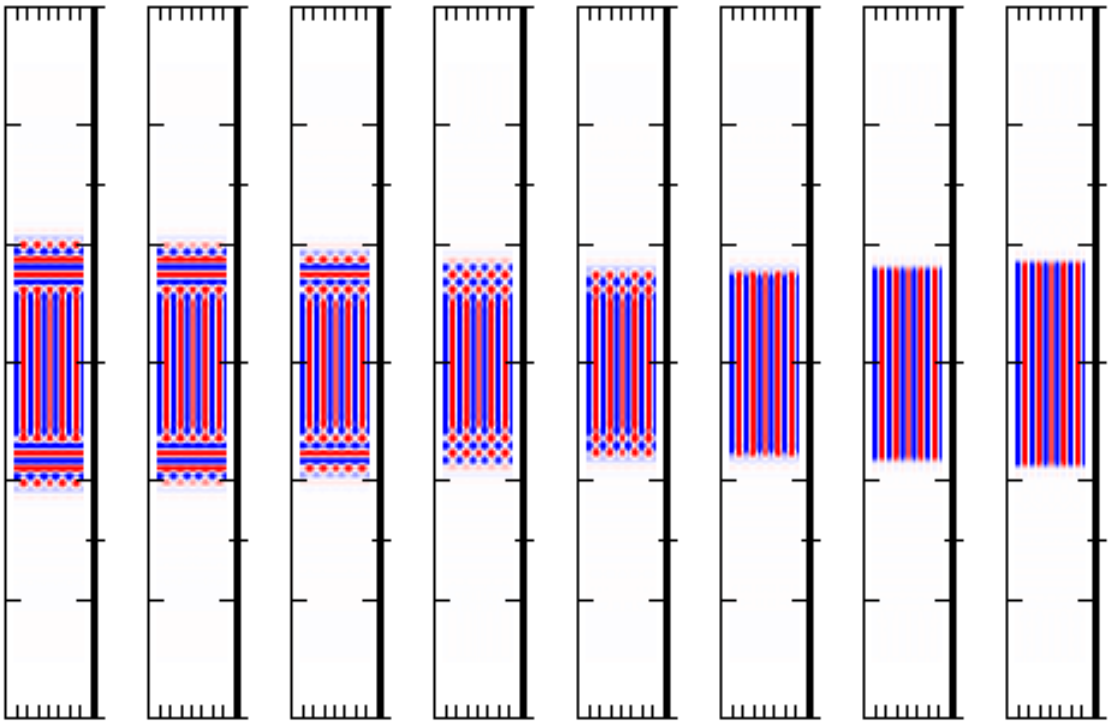

Figure 5.15: Transition in which outer longitudinally invariant stripes disappear in a simulation of the periodically forced SHE35 with parameters $b = 2$, $T = 100$, $\rho = 0.12$ and $r_0 = -0.665$. The initial condition is shown in first panel of Fig. 5.14 and the panels here show, from left to right, the state at $t = 770$, 780, 790, 800, 810, 820, 830 and 840. The first forcing cycle of this simulation is depicted in Fig. 5.14.

central unpinned stripes remain and they begin to breathe via smooth front motion as the state begins to now grow on average. We define the front location $y = f_y$ at $x = 0$ using

$$f_y(t) = 2\frac{\int_0^{L_y} yu(0,y,t)^2 dy}{\int_0^{L_y} u(0,y,t)^2 dy}. \tag{5.5}$$

While Eq. (5.5) only provides an accurate value of the front location for states composed of one type of pattern (e.g. only longitudinally invariant stripes or only unpinned stripes and not both), it does give a numerical measure for the spatial extent of states of the type shown in Fig. 5.14. Figure 5.16 shows f_y for the y-front location as a function of time for the entire simulation. Both the initial average decay of the state by loss of longitudinally invariant stripes and the average growth by lengthening of unpinned stripes are clearly visible with a sharp transition near $t = 800$.

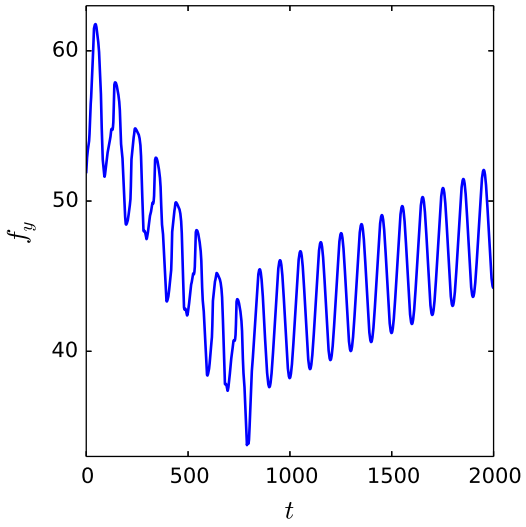

Figure 5.16: The location $f_y(t)$ of the front along $x = 0$ as computed from Eq. (5.5) for the simulation of periodically forced SHE35 shown in Figs. 5.14 and 5.15. While $f_y(t)$ does not accurately represent the location of the front when $t < 800$, it does provide a useful proxy for the dynamics throughout the entire simulation. Parameters: $b = 2$, $T = 100$, $\rho = 0.12$ and $r_0 = -0.665$.

5.3 Dynamics of fully localized stripes under time-periodic forcing

We now describe progress towards a systematic study of the effect of time-periodic forcing on fully localized stripes. We note that stability and depinning dynamics of these states for constant forcing has not been characterized and that even the mechanism for pinning of these states is poorly understood. Therefore any truly systematic study would need to begin with a thorough analysis of the constant forcing case. This section describes preliminary results for the dynamics with time-periodic forcing and details the beginnings of a numerical characterization of the depinning dynamics that will be used to develop a theoretical framework for the observed behavior. We choose the coefficient of nonlinearity to be $b = 2$, fix the period of the forcing cycle to $T = 100$ and examine the dynamics in the (r_0, ρ) plane. The average forcing r_0 is typically taken to be within the pinning region of the longitudinally invariant localized stripes, and we consider values of the forcing amplitude $\rho \leq 0.18$. The system therefore never leaves the region of bistability between the trivial state and the periodic state.

As with localized states in one dimension, periodic forcing can lead to breathing states that remain stationary, or grow or decay on average. We begin this section with a discussion of periodic orbits whose fronts remain stationary on average before turning to states that

exhibit average growth. We consider states that are symmetric about the x and y spatial axes and characterize the state in terms of the location of its fronts f_x along $y = 0$ (Eq. (5.3)) and f_y along $x = 0$ (Eq. (5.5)).

Periodic Orbits

Periodic orbits are found by allowing an initial condition consisting of an approximate fully localized stripe pattern with 11.5 wavelengths (23 stripes) to evolve in time towards the orbit. We show the details of three sample orbits found in this way on a spatial domain with $L_x = 20\pi$, $L_y = 10\pi$, a grid of 1024×512 points and simulation time of 25 forcing cycles with $T = 100$. The samples are taken with different choices of ρ and r_0 and are classified as ${}^{-0}O_0^{-0}$, ${}^{-1/2}O_0^{-1/2}$, and ${}^{-1}O_0^{-1}$ since there are 0, 1/2, and 1 wavelengths added and subtracted from each side over the course of the forcing cycle. Figure 5.17 shows snapshots of the state at times 0, $T/4$, $T/2$, and $3T/4$ of the last forcing cycle of the simulation. The pattern has its minimum number of wavelengths along the orbit at $t = 0$ and is the same for the three examples shown. The maximum number of wavelengths appears at $T/2$ and varies for the three different cases. Figure 5.18 shows the exponential convergence of the state toward a periodic orbit, though we do not run the simulation to machine precision as we did for the one-dimensional case (Fig. 4.8). The location of the fronts along $y = 0$ and $x = 0$ given by $f_x(t)$ and $f_y(t)$ are shown in Fig. 5.19 for the final three forcing cycles of the simulations. The front position f_x follows a slow-fast behavior similar to what has been observed for the one-dimensional localized states (Ch. 4) while the front position f_y varies smoothly in time. We also show the orbit as a trajectory in the (f_x, f_y) plane, anticipating that such a representation will play a role analogous to the front-amplitude picture of the one-dimensional case (Fig. 4.6, for example). Figure 5.21 shows a summary in the (r_0, ρ) plane of the different periodic orbits computed with $T = 100$, $b = 2$ and an initial condition with 11.5 wavelengths. Each orbit has a minimum number of 11.5 wavelengths as shown in the first row of Fig. 5.17 and the overall structure is similar to what is seen in Fig. 4.20 for the one-dimensional localized states. There exist periodic orbits with $\rho > 0$ for values of r_0 where a stationary state does not exist for $\rho = 0$. The region PO of existence of periodic orbits therefore stretches outside of the pinning region for fully localized stripes with constant forcing.

The bifurcation diagram for the constant forcing case in Fig. 5.8 shows that the edges of the pinning region associated with fully localized stripe patterns depend on the width of the state. There is a slant in the snaking diagram such that the pinning region shifts to lower values of r for states with more stripes. The PO region is likewise shifted to lower values of r_0 when computed using a broader initial condition. Figure 5.22 compares the periodic orbits shown in Fig. 5.21 to those computed using an initial condition with 17.5 wavelengths instead of 11.5. A domain with $L_x = 40\pi$, $L_y = 20\pi$ and a grid that is 2048×1024 is used for the simulations with the broader initial condition. The PO region for the broader initial condition appears to be roughly the same shape and carries a similar slant for the parameters

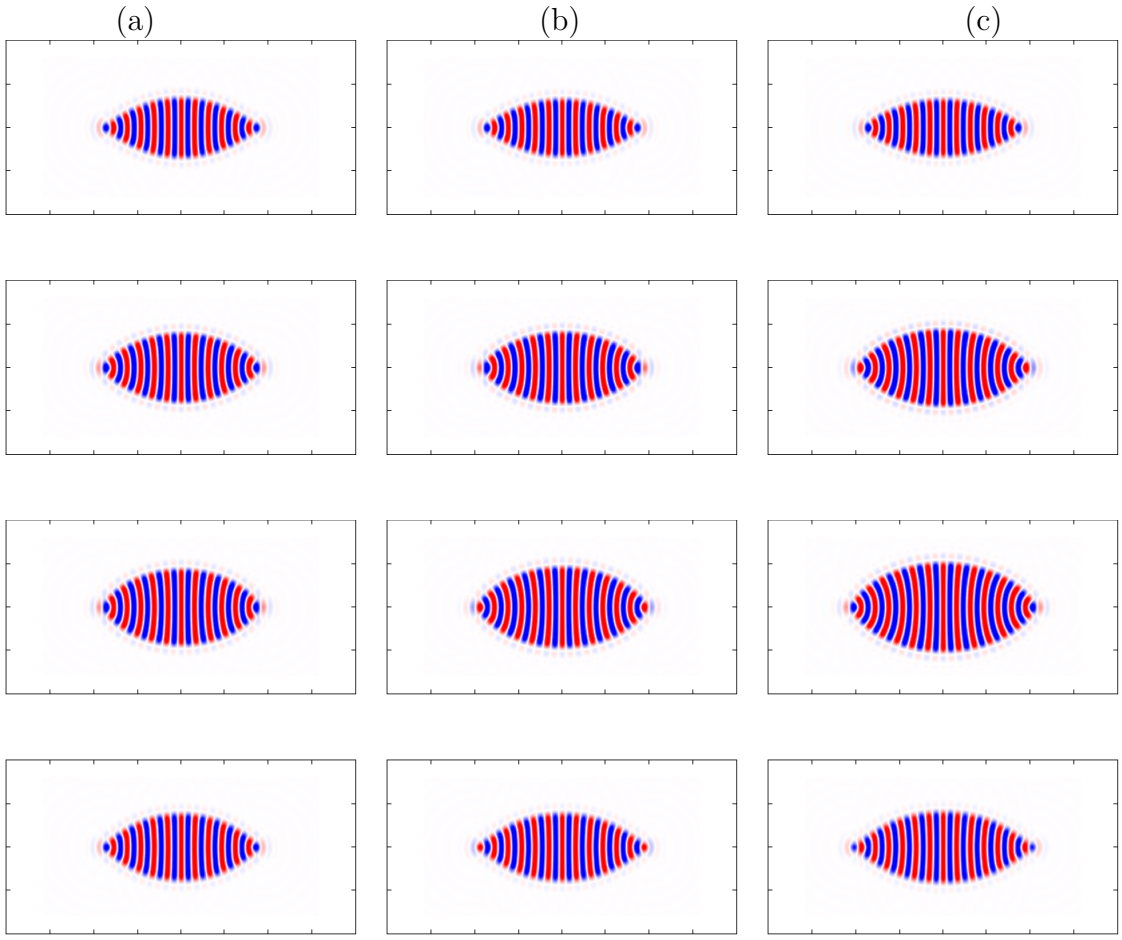

Figure 5.17: Plots showing time evolution of fully localized stripe patterns over the course of a period $T = 100$ of the forcing cycle in the periodically forced SHE35 with $b = 2$. Each column depicts a periodic orbit: (a) $\rho = 0.07$, $r_0 = -0.653$, (b) $\rho = 0.10$, $r_0 = -0.648$ and (c) $\rho = 0.14$, $r_0 = -0.636$. The rows, going from top to bottom, show the solutions at $t = 2400$, 2425, 2450 and 2475.

shown in Fig. 5.22, but more work needs to be done to characterize the dependence of PO on the spatial extent of the pattern.

Average growth

The fact that the edges of the pinning region for fully localized stripes depend on the spatial extent of the pattern means that the time it takes for the pattern to nucleate wavelengths also depends on number of wavelengths the pattern has. This complicates the picture for states that grow on average, as the state can be in a resonance region for particular sizes but may fall out as the size increases over time. We begin the study of growing states by

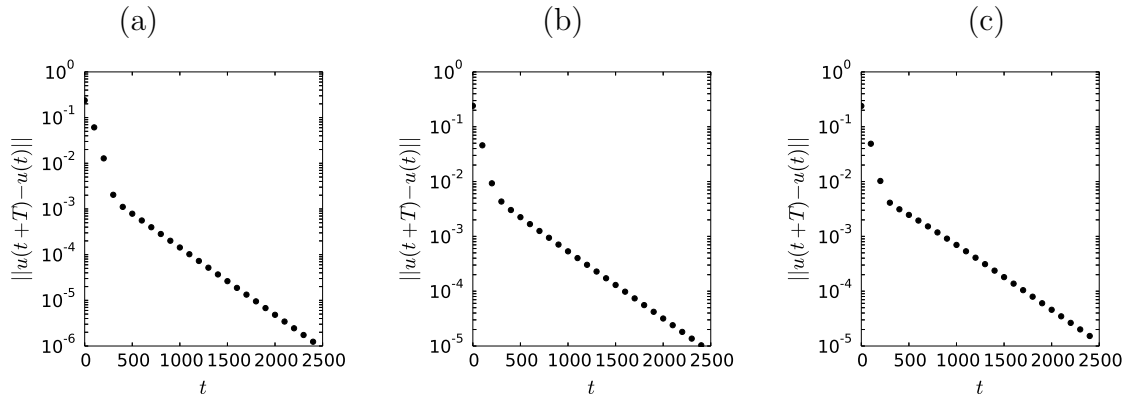

Figure 5.18: Convergence towards a periodic orbit consisting of a fully localized stripe pattern in the periodically forced SHE35 as a function of time for the periodic orbits depicted in Fig. 5.17 with (a) $\rho = 0.07$, $r_0 = -0.653$, (b) $\rho = 0.10$, $r_0 = -0.648$ and (c) $\rho = 0.14$, $r_0 = -0.636$. Parameters: $b = 2$ and $T = 100$.

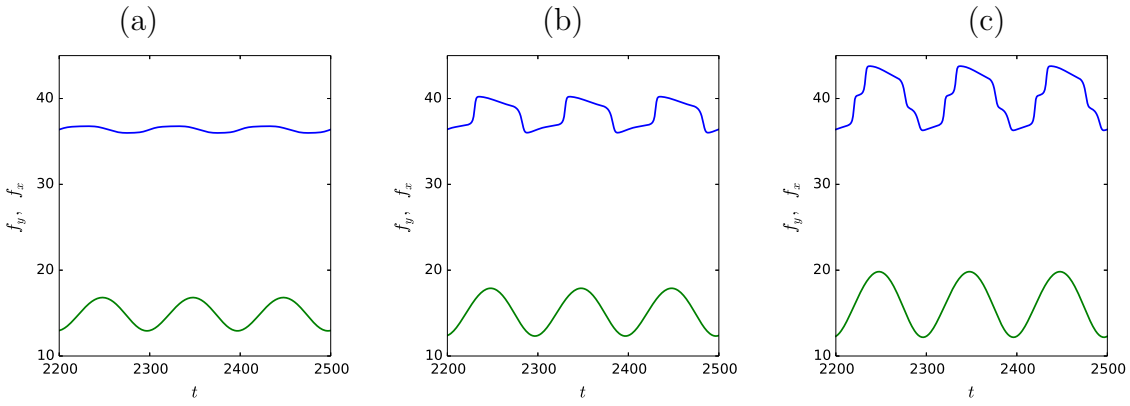

Figure 5.19: The locations of the front along $x = 0$ (f_y in green) and $y = 0$ (f_x in blue) during three forcing cycles of the periodically forced SHE35 for the periodic orbits of fully localized stripe patterns depicted in Fig. 5.17 with (a) $\rho = 0.07$, $r_0 = -0.653$, (b) $\rho = 0.10$, $r_0 = -0.648$ and (c) $\rho = 0.14$, $r_0 = -0.636$. Parameters: $b = 2$ and $T = 100$.

considering constant forcing ($\rho = 0$, $r = r_0$) and mapping out the time to nucleate half of a wavelength on each side as a function of both the constant forcing parameter r and the front position f_x. The calculations used a spatial domain with $L_x = 40\pi$, $L_y = 20\pi$ and a grid of 2048×1024 points. This depinning time T_{dpn} can vary significantly for a particular value of r: at $r = -0.649$, for example, $T_{\text{dpn}} \approx 521$ for a state with 12.5 wavelengths ($f_x \approx 39.2$) and $T_{\text{dpn}} \approx 106$ for a state with 31.5 wavelengths ($f_x \approx 98.6$). Figure 5.23 shows a contour plot where the depinning time at $T_{\text{dpn}}(r, f_x)$ is computed by numerically finding the time between two subsequent peaks in front velocity $\dot{f}_x$ corresponding to adding half-wavelengths to each

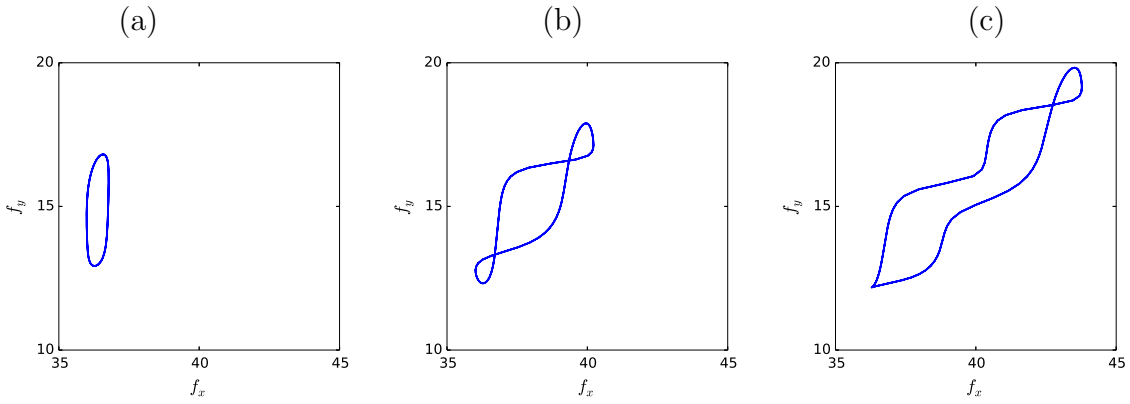

Figure 5.20: Trajectories in the (f_x, f_y) plane for the periodic orbits of the periodically forced SHE35 consisting of fully localized stripes depicted in Fig. 5.17 with (a) $\rho = 0.07$, $r_0 = -0.653$, (b) $\rho = 0.10$, $r_0 = -0.648$ and (c) $\rho = 0.14$, $r_0 = -0.636$. Parameters: $b = 2$ and $T = 100$.

side. This depinning time is associated with the front position at a time halfway between the two peaks. The left panel is colored by $T_{\rm dpn}$ while the right is colored by $T_{\rm dpn}^{-2}$. Each vertical column of data comes from a single simulation and the dots indicate the data points where the calculation has been done while the colors represent an interpolation of the data. The plot of $T_{\rm dpn}^{-2}$ shows bands that are roughly evenly spaced and follow a slant similar to what is seen for the right edge of the pinning region for fully localized stripes (Fig. 5.8).

The dynamics are complicated further by a body instability that begins to appear with constant forcing ($\rho = 0$) near $r \approx -0.62$. Figure 5.24 shows the solutions from a simulation with $r_0 = -0.59$ and $\rho = 0$. A zigzag that is symmetric about $x = 0$ starts to be noticeable on the stripes of the state at around $t = 500$ and results in a drastic change in the depinning dynamics by $t = 800$. We note that there is no evidence of this body instability appearing in any of the simulations conducted with time-periodic forcing for the parameters presented here ($0.07 \leq \rho \leq 0.17$ and $T = 100$). While the system reaches values of forcing $r > -0.62$ for all of the simulations depicted in Fig. 5.21, we conjecture that not enough time is spent in this regime for the mode to develop. However, a more detailed study along with simulations using different forcing periods and conducted over longer times is needed to understand better when this mode becomes important.

Even with the complications that arise from a size-dependent pinning region and additional instabilities, fully-localized stripe patterns still exhibit evidence of resonances in their average growth. We take an initial condition with 14.5 wavelengths and compute the average change $\langle \Delta f_x \rangle$ in the front position f_x per forcing cycle as a function of r_0 when $\rho = 0.12$ (Fig. 5.25(a)). The resonance associated with periodic orbits appears clearly near $-0.649 < r_0 < -0.648$, but there is also a secondary region where the curve appears to flatten out near $-0.647 < r_0 < -0.646$ with a value $\langle \Delta f_x \rangle \approx \pi$. A plot of f_x as a function

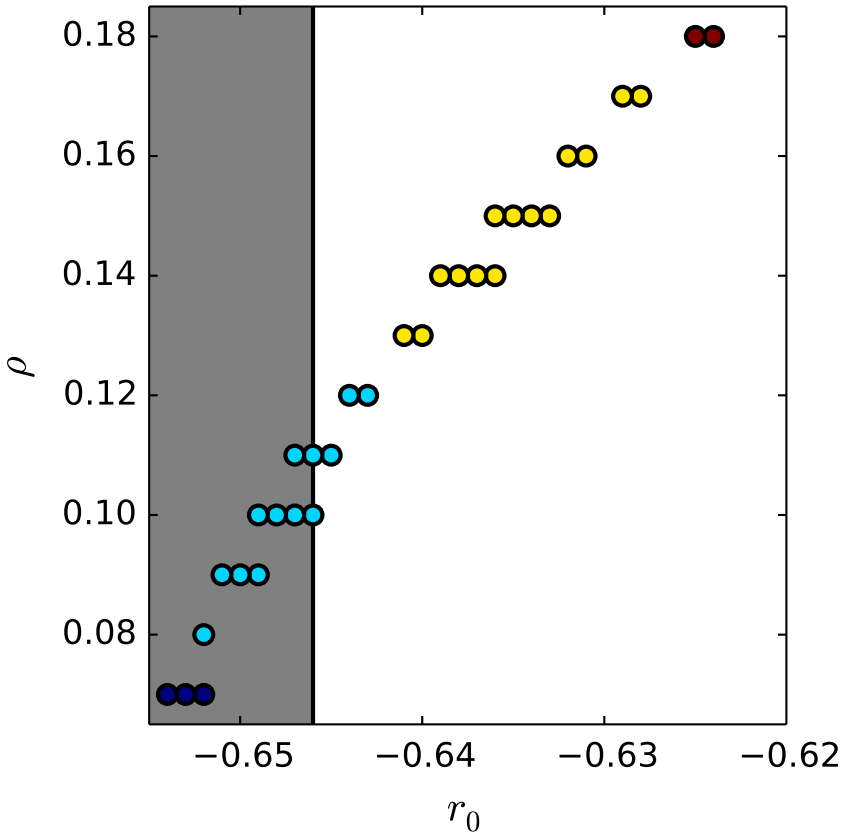

Figure 5.21: Periodic orbits of periodically forced SHE35 in the (r_0, ρ) plane computed using an initial condition that approximates the first row of solutions in Fig. 5.17 containing 11.5 wavelengths. The initial condition is found to be stable under constant forcing ($\rho = 0$) for values of r_0 shaded in gray. The data points are colored by the number of wavelengths added and subtracted from each side of the pattern over the course of one forcing cycle: ± 0 (dark blue), $\pm 1/2$ (light blue), ± 1 (yellow) and $\pm 3/2$ (red). Parameters: $b = 2$ and $T = 100$.

of time in Fig. 5.25(b) shows that the state falls into a $1 : 2$ resonance in which half of a wavelength is added to each side every other cycle of the forcing after about $t = 500$. The trajectory in the (f_x, f_y) plane shown in Fig. 5.25(c) indicates, however, that the shape of the orbit changes as the state grows. Thus it appears that the system would fall out of the resonance after enough time if the simulation were continued on a larger domain. This is presumably due to the size dependence of the depinning time, but it could also be that the state is only in a transition zone near the resonance to begin with.

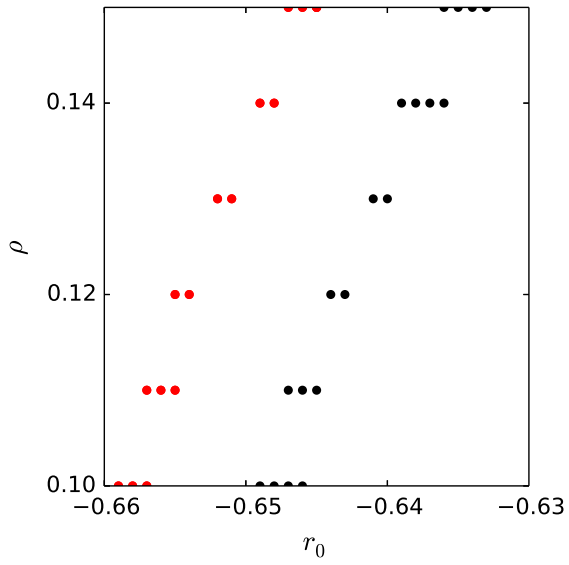

Figure 5.22: Periodic orbits of periodically forced SHE35 in the (r_0, ρ) plane computed with fully localized stripes of 11.5 wavelengths (black) and 17.5 wavelengths (red) as initial conditions. Parameters: $b = 2$ and $T = 100$.

5.4 Discussion

This chapter describes work in progress towards understanding the effects of time-periodic forcing on two-dimensional patterns. In particular, we have studied various configurations of stripe patterns that are localized along one and two spatial directions. Results from numerical simulations show breathing dynamics similar to what has been described for the one-dimensional SHE23 in Ch. 4 and provide evidence that the resonance mechanism underlying Fig. 4.10 and Fig. 3.15 exists for localized states in two dimensions as well. A more detailed understanding of dynamics in the two-dimensional SHE35 with constant forcing will be required to extend the theory from one dimension to two.

Much of the theory developed for understanding localized states with time-periodic forcing in the context of the one-dimensional Swift–Hohenberg equation relies on depinning dynamics under constant forcing. The adiabatic theory described in Sec. 4.4, for example, requires a full characterization of the front speed in order to be applied. While the linear stability of longitudinally invariant stripes has been worked out [42], this is the closest to which time-dependence has been studied for localized states in two dimensions. In addition to stability analysis for the other types of patterns, an analysis of the depinning dynamics via asymptotics is necessary for these two-dimensional localized states. The calculation would follow what is done in Ref. [24] and described in Sec. 4.1 for SHE23 in one dimension. This calculation could then be extended to include time-dependent forcing for certain limits such as the small amplitude case described in Sec. 4.3 for one-dimensional localized states.

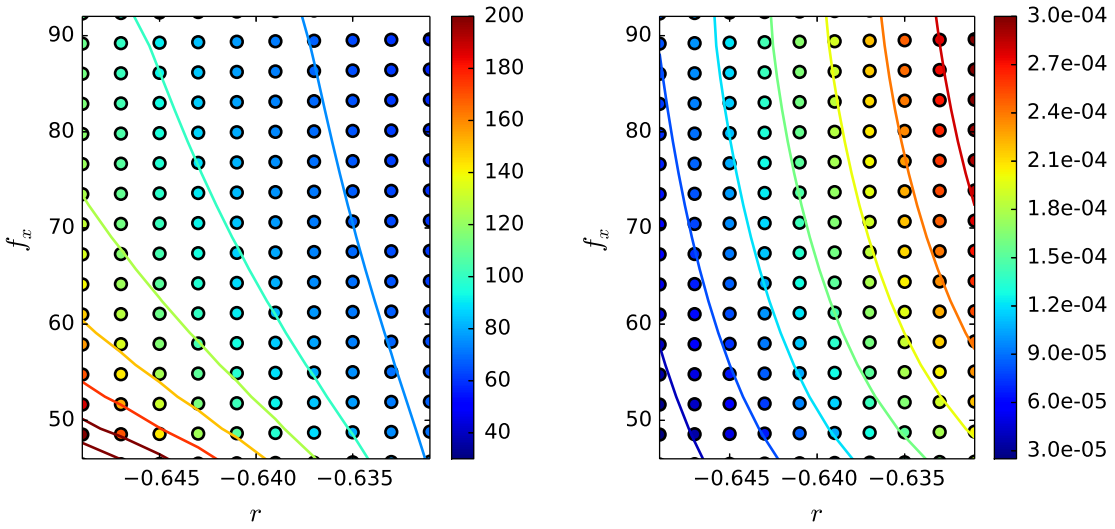

Figure 5.23: Depinning time for growing fully localized stripe patterns in SHE35 as a function of the front location f_x and the constant forcing r with $b = 2$. The dots indicate data from the simulations while the lines are contours from interpolation of the data for (a) T_{dpn} and (b) T_{dpn}^{-2}.

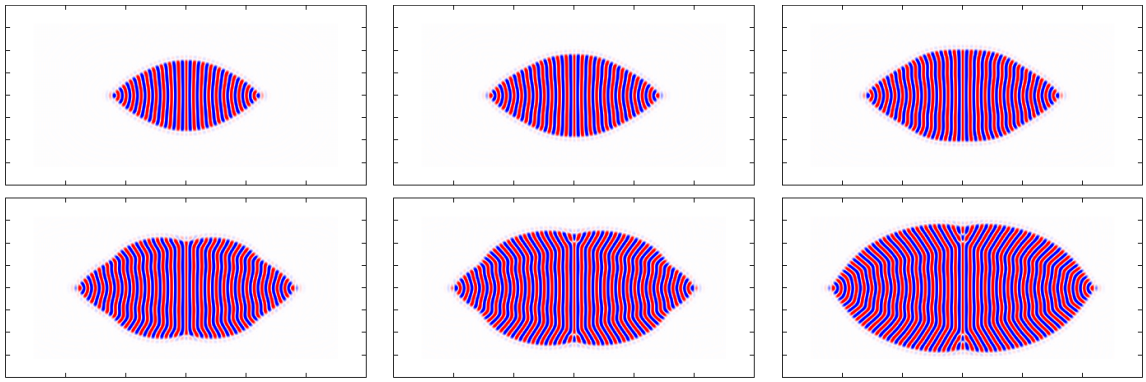

Figure 5.24: Growth of a body instability in a simulation of a fully localized stripe pattern in SHE35 with constant forcing and parameters $b = 2$, $r = -0.59$. The panels in the top row, from left to right, show the state at $t = 400$, 500 and 600 as the body instability develops. The panels in the bottom row show the state at $t = 700$, 800 and 900 and exhibit drastically different depinning dynamics once the instability has developed.

There is also the more basic question that remains unanswered for the fully localized stripe patterns: what is the pinning mechanism? The curvature of the front transverse to the stripes presumably plays a role, but it is unclear exactly how this can pin the front. Curvature-driven

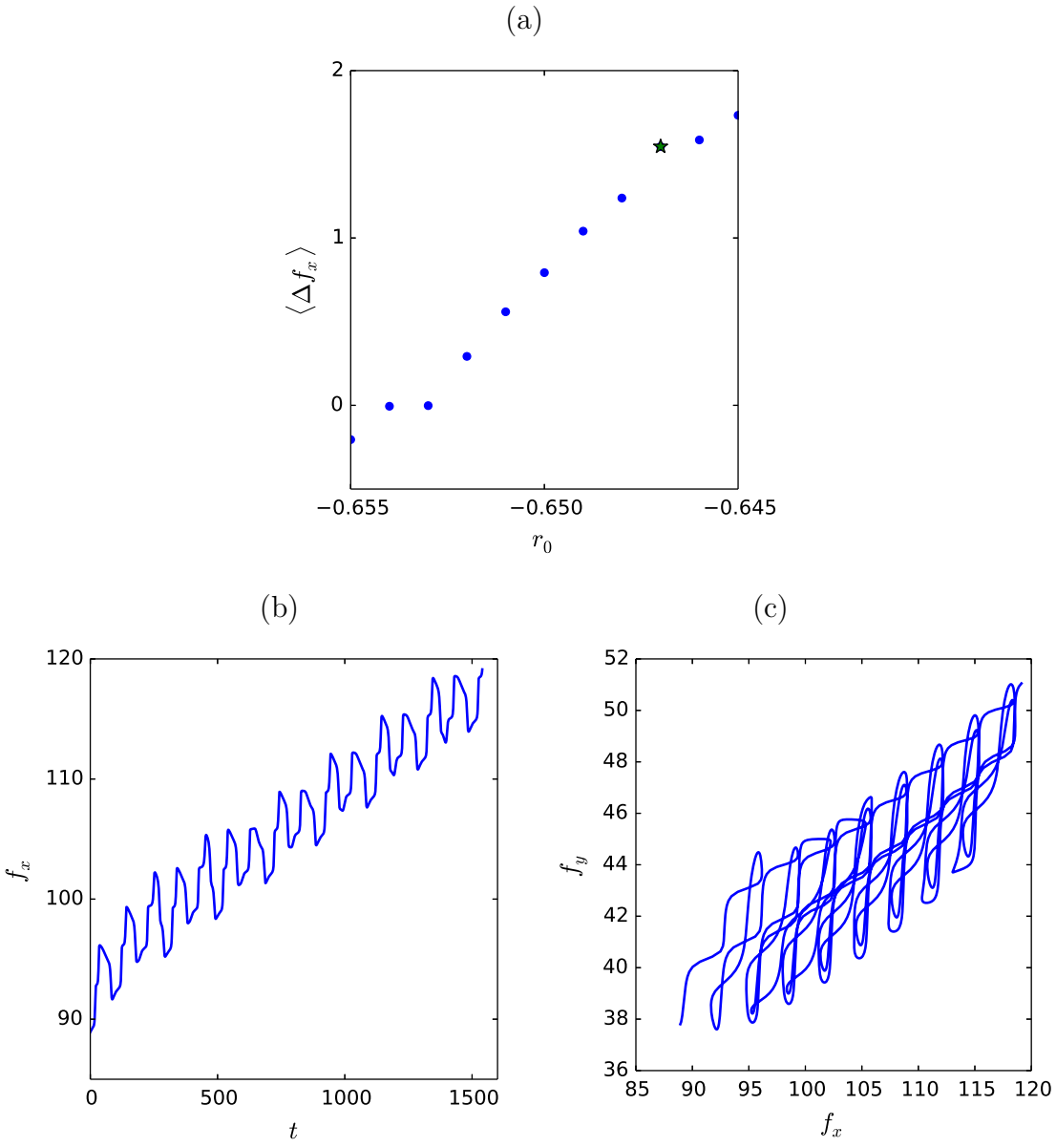

Figure 5.25: (a) The average change $\langle \Delta f_x \rangle$ in location f_x of the front along $y = 0$ as a function of the average forcing parameter r_0 for fully localized stripe patterns in the periodically forced SHE35 with $b = 2$, $T = 100$ and $\rho = 0.12$. For the simulation at $r_0 = -0.647$ indicated by a star (b) shows the position of the front f_x as a function of time and (c) shows the trajectory in the (f_x, f_y) plane.

front propagation has been studied extensively [145] and may provide useful tools for this situation. Figure 5.9 shows results from a simulation in which structures consisting of pieces

of fully localized stripe patterns grow from a concave curvature at the front of a wavy stripe pattern and this may lead to additional insight. Further investigation into, for example, how the number of partially formed stripes in these structures depends on the curvature of the wavy stripe pattern might prove to be relevant. A more complete understanding of the possible instabilities that can lead to the break up of fully localized stripe patterns (e.g. Fig. 5.25) may also provide some hints.

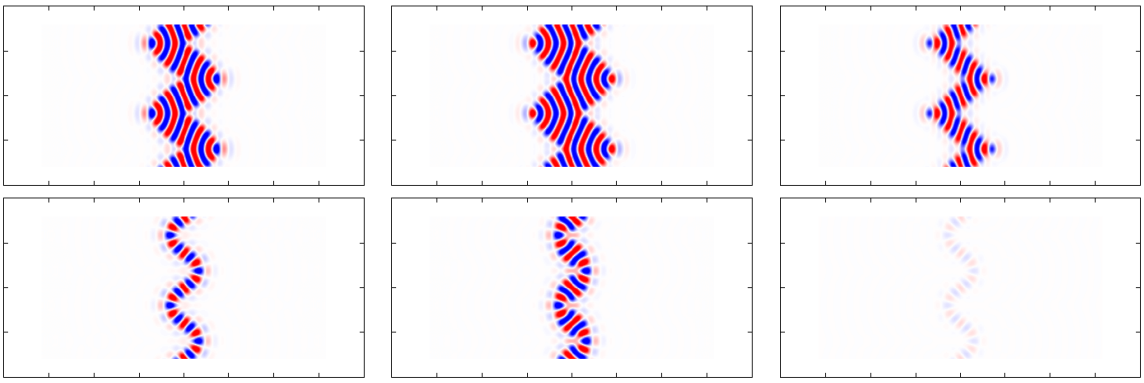

Figure 5.26: Collapse of a wavy stripe pattern in periodically forced SHE35 with parameters $b = 2$, $\rho = 0.12$, $T = 100$ and $r_0 = -0.675$. The panels show the state at (top, from left to right) $t = 520$, $t = 550$, $t = 580$, (bottom, left to right) $t = 610$, $t = 640$ and $t = 670$. The pattern has nearly collapsed to the trivial state by $t = 670$, and is thus only barely visible in the final frame.

As a final note, canard trajectories that appear near transitions of resonance regions for both the periodically modulated Adler equation (Sec. 3.2) and the one-dimensional Swift–Hohenberg equation with periodic forcing (Sec. 4.5) have not yet been examined in two dimensions. We have seen peculiar canard dynamics that result from fine tuning the forcing parameters near the edge of collapse of the localized state (Fig. 4.28), and analogous but more complex behaviors are likely to exist in the two-dimensional case. Figure 5.26 is from a simulation of the periodically forced SHE35 with an initial condition of wavy stripes and parameters $b = 2$, $\rho = 0.12$, $T = 100$ and $r_0 = -0.675$. The state decays on average and the pattern is shown at several times just before collapse. We see the state transition from a wavy vertical stripe pattern to a wavy row of horizontal stripes at $t = 610$. The horizontal stripes then bulge as if the state is composed of a series of fully localized stripe patterns connected end to end at $t = 640$ before decaying to the trivial state at $t = 670$. While the cause of these dynamics is unclear, it could provide some guidance on where to look for possible canard behavior.

Chapter 6

Conclusion

This dissertation describes a resonance mechanism that appears in periodically modulated systems such as the Adler equation with time-periodic frequency parameter and the Swift–Hohenberg equation (SHE) with time-periodic forcing. We consider an external time-periodic modulation that causes the system to sample parameters in which certain dynamics occur in a "forward" direction at some times and a "backward" direction during others. The modulation results in resonances between the period of modulation and the characteristic time on which the dynamics of the unmodulated system occur. The dynamics of the periodically modulated system organizes around the resonances to create a partitioning of the parameter space into regions with distinct behaviors. In particular, a sweet-spot and pinching structure is generated as resonance bands associated with forward and backward dynamics cross. The behavior in each region can, in this case, be characterized by the two resonance numbers of the bands that overlap there. Canard trajectories that track unstable equilibria for some time before quickly jumping to stable ones appear near the edges of these resonance regions. Between the resonance regions are transition zones where dynamics are not locked to the period of the modulation, but are either locked to a multiple of the modulation period or are quasiperiodic. The transition zones narrow and canards become more pronounced as the modulation period increases.

This chapter gives an outlook for future work to extend our understanding of the resonance mechanism described above, explore other applications where it may appear and follow new research directions it motivates. We first summarize the main results in Sec. 6.1, before discussing physical systems where periodic modulation appears or could be introduced (Sec. 6.2) and finally provide directions for future work on localized states in model systems with time-periodic forcing (Sec. 6.3).

6.1 Summary

Chapter 3 introduces the resonance mechanism at the heart of this dissertation in the context of coupled oscillators by studying the periodically modulated Adler equation. In this case the

modulation appears in the frequency parameter, and the forward and backward dynamics of interest are positive and negative phase slips, respectively. The parameter space defined by the average value of the frequency parameter and its modulation period is partitioned into regions that remain phase-locked on average or drift via an imbalance of positive and negative phase slips. Resonance regions where a fixed number of positive and negative phase slips occur in each modulation cycle are separated by transition zones with non-integer winding numbers. The resonance regions as well as the canard trajectories near the edges are computed via numerical continuation. Asymptotic analysis provides a detailed understanding of the dynamics in several limits and an adiabatic theory based on WKB analysis provides excellent agreement with the numerical results even beyond the low-frequency limit where it is valid.

In addition to providing valuable insight into the resonance mechanism that is the main subject of this thesis in a very simple and general context, the work of Ch. 3 opens up several interesting applications to phase-coupled oscillator systems. A more complete analysis of the system described by the Hamiltonian (3.68) would help make a direct link from the results of Ch. 3 to globally coupled systems of active rotators. It would also be interesting to consider systems in which multiple populations of coupled oscillators interact, a situation that could be described in terms of coupled Adler equations. Finally, we note that chimera states [146, 147] that consist of a localized patch of synchronized oscillators in an asynchronous background have been observed for oscillators that are nonlocally (but not globally) coupled and it would be interesting to examine the dynamics of such partially synchronized states when time-periodic modulation is introduced into the system.

Chapter 4 employs the one-dimensional quadratic-cubic Swift–Hohenberg equation (SHE23) with time-periodic forcing as a second example of the resonance mechanism. The fronts that define the edges of spatially localized states can, upon exiting the pinning region, move outwards (forward dynamics) or inwards (backward dynamics) via episodic nucleation or annihilation of wavelengths of the pattern. The sweet-spot and pinching structure, mapped out in this case by time-simulations, consists of regions defined by the number of wavelengths gained and lost over a period of the forcing cycle. There is also an additional region of the parameter space in which the localized state collapses via amplitude decay. This region of collapse, not present for the periodically modulated Adler equation, is linked to the amplitude dynamics that overtake the front dynamics outside of the region of bistability between the trivial state and homogeneous patterned state.

The same asymptotic limits considered for the periodically modulated Adler equation are considered for SHE23 with time-periodic forcing, and Tab. 6.1 provides a summary. While the corresponding results for the two examples are similar in most cases, one notable difference appears in the high frequency, large amplitude limit. This limit predicts a collapse of the region PO where breathing states that remain localized on average for SHE23 while the analogous region in the Adler equation persists in this limit, a difference caused by amplitude dynamics in SHE23.

Chapter 5 explores the dynamics of stripe patterns localized along one and two dimensions in the two-dimensional cubic-quintic Swift–Hohenberg equation (SHE35) with time-periodic

Table 6.1: Summary of the various asymptotic limits of SHE23 with time-periodic forcing (Ch. 4) in terms of the frequency $\omega = 2\pi/T$, amplitude ρ, and average value r_0 of the forcing. $r_\pm$ define the edges of the pinning region, $r_c = (r_+ + r_-)/2$ is the center of the pinning region, and $p = (r_+ - r_-)/2$ is its half-width. We assume that $0 < \epsilon \ll 1$ is a small quantity and all others are $\sim \mathcal{O}(1)$.

Limit	Frequency	Amplitude	Avg. Value	Predictions
High-Freq. (HF)	ω/ϵ	ρ	r_0	*PO* narrows $\sim \epsilon^2(\rho/\omega)^2$
HF, Large-Amp.	ω/ϵ	ρ/ϵ	r_0	*PO* collapses for $\rho/\omega \sim \mathcal{O}(1)$
Small-Amp.	$\epsilon\omega$	$\epsilon^2\rho$	$r_\pm + \epsilon^2\delta$	resonance bands and transition zones
Asymptotic sweet spots	$\epsilon^2\omega$	$p + \epsilon^2\rho$	$r_c + \epsilon^2\delta$	resonance bands cross to form $\sim \mathcal{O}(\epsilon^2)$ sweet spots and pinching

forcing. While this is work in progress, the numerical results provide evidence that the same resonance mechanism is at play for the localized states in two dimensions. Longitudinally invariant stripe patterns localized along one direction can undergo instabilities along the stripe and one such instability leads to wavy stripes. Structures composed of partially formed stripes also appear along the fronts at the edges of the state. These states undergo breathing dynamics analogous to what is seen in the one-dimensional case and the *PO* region has been identified through numerical simulation. Analysis of the other resonance regions is not yet complete, but it appears that the transition zones for wavy stripe patterns of the two-dimensional SHE35 take up a larger fraction of the parameter space than the analogous transition zones for one-dimensional localized states in SHE23. The *PO* region and evidence of a $1:2$ resonance region has also been mapped out for fully localized stripe patterns. The region of existence of the resonance regions in this case depends on the spatial extent of the localized state, an effect that can be traced back to a slant in the snaking diagram for the states under constant forcing. As noted in Sec. 5.4, the pinning mechanisms and depinning dynamics for the fully localized stripe patterns under constant forcing are not yet well understood.

It will be interesting to consider other types of patterns and parameter regimes where the various patterns interact more strongly. All of the results of Ch. 5 are taken with cubic nonlinearity coefficient $b = 2$ but, with larger values of b, the Maxwell point associated with the stripes and the Maxwell point associated with the squares are closer together. A larger value of b can also produce more complex behavior when considering only longitudinally invariant stripe patterns. The body mode can lead to the growth of a labyrinth pattern in the wake

of the outward propagating front instead of the wavy stripes generated in Fig. 5.3(b) [42]. Finally, we note that preliminary numerical simulations indicate that time-periodic forcing can induce drift of defects in two-dimensions that would otherwise be frozen into the pattern under constant forcing. Fronts opens up around the defect during the decaying phase of the forcing cycle and move before closing during the growing phase. This allows for an annealing process to take place in which the defects drift towards a lower energy configuration for the system.

6.2 Applications to systems with time-periodic modulation

As discussed in Sec. 1.3, the SHE provides a qualitative description for spatially localized states in a number of different physical systems. However it is useful to consider more realistic models in order to develop a better understanding of the essential features in the system. This can motivate extensions of SHE or other model systems that better capture the mechanisms at play in specific systems and thus provide a more complete understanding of the effects of time-periodic forcing. We also note that understanding the effects of stochastic noise on the resonances generated by time-periodic forcing will be necessary for applying the results of this dissertation to physical systems where random fluctuations play an important role. This section is divided into two subsections, one focusing on vegetation patterns in semi-arid regions and the other focusing on localized states in a table-top nonlinear optics experiment.

Vegetation patterns in semi-arid regions

We discuss three models of vegetation patterns in order of increasing complexity. Each successive model incorporates more realistic details of the system in order to better capture the physical mechanisms involved in the pattern formation process.

The first model proposed by Lefever and Lejeune [148, 149] describes the dynamics of the vegetation density ρ in terms of a nonlocal PDE. Using Gaussian weighting functions, a Taylor expansion of the biomass, and appropriate nondimensionalization, this integro-differential equation has been approximated to fourth order as

$$\partial_t \rho = (1-\mu)\rho + (\Lambda - 1)\rho^2 - \rho^3 + \frac{1}{2}(L^2 - \rho)\nabla^2\rho - \frac{1}{8}\rho\nabla^4\rho, \tag{6.1}$$

where μ is the ratio of mortality to growth, Λ is the degree of facilitation relative to competition in the local interactions between plants, and L is the ratio of the length scales for facilitation to competition. The local approximation given by Eq. (6.1) is very similar to SHE (1.6) except with more complicated nonlinearities, most notably the $\rho\nabla^4\rho$ term. While the additional nonlinearities complicate the bifurcation analysis, initial work on the model indicates the emergence of localized states in a previously unstudied manner and has led

to the discovery of new localized states in SHE. In particular, weakly nonlinear analysis points to the emergence of a spatially modulated solution from the transcritical bifurcation at $\mu = 1$ in Eq. (6.1) and at $r = 1$ in SHE. Future work will be to develop a theoretical understanding of these new states and continue to analyze the Lefever–Lejeune equation (6.1) to better characterize what is gained in terms of modeling by including more complicated nonlinearities.

The Klausmeier model [150] and its extensions describe the dynamics of the water and biomass in a pair of reaction-diffusion-advection equations. A generalized version [151] reduces to the Gray–Scott system [152, 153, 154] in a particular limit, which has found broad application in chemistry and biology. The second model that we consider is a non-standard form of the Gray–Scott model,

$$W_t = d\nabla^2 W - WB^2 - W + a \tag{6.2}$$

$$B_t = \nabla^2 B + WB^2 - mB, \tag{6.3}$$

that has been motivated by the Klausmeier model. The system (6.2)-(6.3) models the interaction between water concentration W and biomass concentration B. Precipitation increases the concentration of water spatially uniformly at a constant rate a and water can be converted to biomass at a rate WB^2 or lost by evaporation at a rate normalized to W. In addition to being created with water, the biomass dies at a rate mB. Finally, both the biomass and water diffuse in space with the water diffusing d times faster. The original Klausmeier model, which was developed for vegetation on a hill, has $d = 0$ and an advective term proportional to W_x to model the flow of water downhill. Recently patterns in an "extended Klausmeier model" have been considered [138, 155] with the inclusion of both diffusive and advective terms in the water dynamics. This model employs a generalization the diffusive term in the water equation (6.2) of the form $d\nabla^2 W^\gamma$, but the inclusion of nonlinear diffusion does not qualitatively change the dynamics for physically relevant values of γ [151]. The Gray–Scott model has been studied extensively in the limit of large d [156]. Intermediate values of d have been mostly overlooked in the literature but homoclinic snaking has been identified in this regime [157]. More analysis will provide insight into the existence and dynamics of localized states in this intermediate parameter regime $2 < dm < 20$ as well as the non-standard way at which the homoclinic snaking structure breaks apart at $dm \approx 3.67$.

Rietkerk et al. proposed the third model considered here in which the dynamics of water is split into a groundwater component and a surface water component to produce a system of three coupled equations for water and biomass [158]. A more realistic variant distinguishes the biomass field as describing above-ground biomass by explicitly modeling feedback associated with the nonlocal root systems of the plants [159]. The large-scale redistribution of water in semi-arid environments through surface flow may be the essential feature of these types of models that is not captured by SHE. Fast diffusion and slow infiltration into the soil makes the surface water behave approximately like a conserved quantity. Surface water flow allows the existence of a localized patch of vegetation to globally alter the water level of the background bare soil state, and this in turn alters the effective forcing felt by the vegetation

patch. Simple models of pattern formation in the presence of a conserved quantity [160, 161] may provide a good starting point for understanding the effects of large-scale redistribution of a limited resource in ecological systems such as vegetation in semi-arid regions.

Nonlinear optics

Nonlinear optical media provide a setting in which spatially localized structures can be experimentally created and manipulated in a highly controlled fashion. Moreover, the experiments are usually set up on a single optical table and the resulting localized structures can often be imaged in real time with just a ccd camera. A liquid crystal light valve (LCLV) setup with optical feedback has experimentally demonstrated pinning and depinning of fronts connecting a spatially periodic pattern to a uniform background state [162, 163, 164]. The experiment has generated one-dimensional localized structures consisting of any number of wavelengths of the pattern that exist stably within a pinning region. Outside of the pinning region, the fronts that define the edges of the state depin and the front propagation speed has been measured as function of the control parameter. The dynamics of these localized states qualitatively follow SHE with constant forcing and can provide an experimental realization of the resonance mechanism that occurs when time-periodic forcing is introduced.

The setup consists of a thin nematic liquid crystal layer, a photoconductive wall and transparent electrodes that allow for an applied external voltage. A collimated laser beam passes through the liquid crystal layer and is reflected back though the layer by a dielectric mirror deposited on the back. The light experiences a phase shift within the liquid crystal that depends on the voltage across the layer. A polarizing beam splitter and mirrors direct the component of the reflected light with a particular polarization into a light valve that uses a bundle of fiber optic cables to transport the light onto the photoconductive wall at the back of the liquid crystal layer. This optical feedback is designed to be local in the sense that the reflected light illuminates a spatial location on the photoconductive wall corresponding to where it passed through the liquid crystal layer. Therefore, in addition to the uniformly applied external voltage, the layer experiences local fluctuations in the effective voltage from feedback generated by the light at each particular location in the layer. The effective voltage reorients the liquid crystals and thus controls the index of refraction experienced by the light.

The net effect of the LCLV setup with optical feedback is that the liquid crystal layer behaves like a Kerr medium in which the local index of refraction depends on the local intensity of the light. The system exhibits bistability between two spatially homogeneous states which can be distinguished by the light intensity of the reflected laser beam. When a spatial light modulator is used to impose a spatially periodic intensity profile on the input laser beam, one of the homogeneous states develops a spatially periodic profile and fronts between the states can now be pinned by the structure of the periodic state. The spatially periodic forcing generates stationary localized states in the system that exhibit characteristics of homoclinic snaking [165]. A time-periodic forcing can be introduced into the system via the spatial light modulator which uses a computer to control the light intensity profile of

the incident laser beam. The computer can be programmed to generate a spatially uniform time-periodic modulation of the light intensity on top of the spatial modulation.

6.3 Localized states in model systems with time-periodic forcing

The work in Ch. 4 provides a foundation for understanding the dynamics that result from introducing time-periodic forcing to spatially localized structures and a number of additional effects can be explored via variations of SHE or other model systems. Unlike the results in Ch. 3 that were obtained by numerical continuation, much of the numerical results on SHE23 in Ch. 4 rely on time-simulations. Numerical continuation has been used to study periodic orbits in a Ginzburg–Landau type equation with time-periodic forcing [128], though a very coarse time-discretization was employed (four spectral modes were used). Techniques for the computation of highly accurate periodic orbits of PDEs in one spatial dimension through numerical continuation have been developed in the context of water waves [166] and mode-locked lasers [167], and such techniques could prove very useful if adopted for the future studies described below.

Additional symmetries and broken symmetries

Because it is the simplest choice that allows for localized states, Ch. 4 adopts SHE23 to study periodically forced patterns in one dimension. In two dimensions, however, quadratic nonlinearities favor hexagonal patterns and Ch. 5 thus uses SHE35 in order to study localized stripe patterns subject to time-periodic forcing. While the behavior of localized states is not fundamentally changed in going from quadratic-cubic to cubic-quintic nonlinearity, there are several consequences of the additional "up-down" symmetry $u \to -u$ that are worth exploring in systems with time-periodic forcing. As mentioned in Sec. 1.3, the depinning dynamics of SHE35 involves nucleation and annihilation of half-wavelengths of the pattern at a time instead of full wavelengths. The additional symmetry also means that the spatial dynamics are reversible under the two involutions $(x, u) \to (-x, \pm u)$ and thus both symmetric and antisymmetric states can be stationary.

It may also be interesting to consider systems with broken symmetries instead of additional ones. A breaking of the spatial reflection symmetry, for example, will generically cause localized states to drift [134] though it is possible to break the reflection symmetry and maintain stationary localized states by protecting the spatial Hamiltonian structure [168]. A time-periodic modulation of a symmetry-breaking term in SHE could lead to resonances that maintain the dynamic consequences of the symmetry on average over a finite parameter range. The addition of the dispersion term $\gamma(t)\partial_x^3 u$ to SHE where $\gamma(t) = \gamma_0 + \rho \sin(2\pi t/T))$ will cause the localized states to drift, but it may be possible for the state to maintain zero average velocity over a finite range of γ_0. Moreover, the introduction of an asymmetry between the increasing and decreasing phases of $\gamma(t)$ could allow for ratcheting behavior in

which the state drifts on average even though $\langle \gamma(t) \rangle = 0$ when averaged over a modulation period. Finally, we note that this dispersion term induces a phase velocity of the periodic pattern within its localized envelope with a constant parameter γ and this may also have interesting consequences when the system is periodically modulated.

Collapsed snaking

This dissertation focuses on localized states with pinned fronts that exist on snaking solution branches that are stable over a finite range of parameters. The pinning in the cases discussed here results from the spatial periodicity of the homogeneous patterned state that is bistable with the trivial state. We have, however, encountered unpinned fronts when considering localized stripe patterns with fronts transverse to the direction along the stripes (Fig. 5.5(b)). Unpinned fronts can also appear in one-dimensional systems through a bistability between two spatially uniform states. A spatially uniform state bifurcates from the trivial state of SHE at $r = 1$ and localized states can result from bistability of this uniform state with the trivial one [24]. Localized states on the so-called collapsed snaking branch can take on a continuous range of spatial lengths and remain stationary only at the Maxwell point.

Pinning is not necessary for the creation of the resonance regions, as can be seen in the limit of small amplitude forcing modulation (Fig. 4.14) by the fact that the resonance tongues persist beyond $\delta/\rho = 1$ to where the system no longer enters the pinning region. The resonance tongues continue to exist because the parameter dependence of the depinning time couples the time-periodic forcing to the front motion. The introduction of time-periodic forcing is thus expected to create resonance regions where the localized states can remain stationary on average for a finite range of parameters on a collapsed snaking branch. These resonance regions are likely be much smaller than what has been seen for pinned fronts, and may be difficult to locate numerically. Asymptotics in the limit of small amplitude forcing modulation should, however, provide some theoretical understanding as well as a starting point for numerical studies.

Slanted snaking

The conserved Swift–Hohenberg equation has been studied in connection with front propagation in phase transitions of supercooled liquids [169] and the coupling of SHE to a large-scale conserved mode has appeared in connection to descriptions of vertically vibrated granular material [161]. In both models, the snaking branch of spatially localized states exhibits a slant such that the location of the pinning region in parameter space depends on the spatial extent of the state. This slant is linked to the existence of a conserved quantity that makes the presence of the localized state alter the background state (see Ref. [170] for an excellent review). In addition to appearing in a number of applications, these systems provide a one-dimensional realization of a complication that arises in the study of fully localized stripes in two dimensions. It will thus be useful to understand the effect of slanted snaking on the resonance structure induced by time-periodic forcing in one spatial dimension. Depending

on the application in mind, time-periodic modulation could be introduced into the systems in ways other than through the forcing. For example it might be interesting to indirectly force the localized state by periodically modulating the large-scale mode. This might have relevance to a photo-sensitive chemical reaction where catalyst production is modulated by time-periodic illumination [171]. Such a system may also provide a simple model that captures the essential dynamics associated with the large-scale redistribution of limited resources in ecological systems such as vegetation patterns in semi-arid regions (Sec. 6.2).

Oscillatory systems

The gradient structure of SHE does not permit oscillatory dynamics and the system thus has limited applicability to situations with inherent periodic dynamics. The forced complex Ginzburg-Landau equation

$$\partial_t A = (\mu + i\nu)A - (1 + i\beta)|A|^2 A + (1 + i\alpha)\nabla^2 A + \gamma \bar{A}^{n-1} \tag{6.4}$$

describes the long-time and large-scale evolution of the envelope of patterns in parametrically driven systems near a $n : 1$ temporal resonance. Here, μ represents dissipation ($\mu < 0$) or a constant drive ($\mu > 0$) in the system, ν is the detuning from the unforced frequency, α is the dispersion, β characterizes the nonlinear frequency dependence, and γ is the amplitude of the periodic forcing. Both self-oscillatory and damped dynamics are possible for this system. The $n = 2$ case appears frequently in applications and an exhaustive classification of localized states for this case has been carried out in Ref. [133]. In addition to standard snaking exemplified by SHE, Eq. (6.4) exhibits defect-mediated snaking in which the localized state grows by nucleating wavelengths of the pattern from a central defect [172]. Moreover, a wealth of unexpected dynamics has been uncovered for two-dimensional patterns in this system [173]. Coupling such an equation to a conserved mode has provided a description for oscillons in granular material [174] and proven successful as phenomenological model for recently discovered localized Faraday patterns [175].

The steady state solutions and dynamics of Eq. (6.4) have been well studied and it has proven a useful description in a number of applications, so it would be an ideal starting point for exploring the role time-periodic modulation in oscillatory systems. The equation describes the slow dynamics of an envelope of a pattern that is oscillating in resonance with a parametric forcing, and so explicit time dependence in parameters of Eq. (6.4) correspond to modulation on a long timescale. This could be achieved, for example, via a slow modulation of the parametric forcing. We also note that a special case of multi-frequency forcing leads to a generalization of Eq. (6.4) with time-independent parameters [176] but one expects the description to generically include explicit periodic time dependence.

Appendix A

Numerical methods

The two main methods used to obtain the numerical results that appear throughout this dissertation are numerical continuation and time integration. The dynamics of a system are computed through time integration. It is thus useful for exploring the evolution of a system from some initial condition and for studying transient behavior or complicated time-dependent states. Numerical integration in time can also provide a straightforward way to compute the parameter dependence of an attractor by allowing simulations using different parameter values to converge to the attractor of interest. Numerical continuation, on the other hand, has the advantage of being able to compute the parameter dependence of both stable and unstable solutions. Moreover, the publicly available package AUTO [115] provides an accessible way to perform continuation on ordinary differential equations (ODEs) and time-independent solutions of partial differential equations (PDEs) in one spatial dimension. There are also a number of other publicly available packages, including pde2path which has the capability to continue time-independent solutions of PDEs in two dimensions [177, 178, 179]. Techniques for numerical continuation of periodic orbits in PDEs have been developed in other contexts [166, 167] and would prove useful if adopted for periodically forced systems of the type studied in this dissertation.

A.1 Numerical continuation

In this section we describe some basic methods of numerical continuation following Refs. [180, 181] with a particular emphasis on the implementation in AUTO. Numerical continuation provides an approach for computing solutions to the dynamical system

$$\mathbf{u}' = f(\mathbf{u}, \mu) \tag{A.1}$$

for $\mathbf{u} \in \mathbb{R}^n$ as a function of a parameter of the system $\mu \in \mathbb{R}$. The prime here denotes derivative with respect to x. Given some $\mathbf{u}_0(x)$ that solves the system (A.1) for $\mu = \mu_0$ along with boundary conditions or integral constraints, we would like to find other solutions and associated parameters $(\mathbf{u}, \mu)$ that also satisfy Eq. (A.1). A solution branch is a set of

continuously varying solutions and parameter values $(\mathbf{u}(x;s), \mu(s))$ where s denotes some parametrization. We are often interested in the case that $\mathbf{u}(x;s)$ is a fixed point, but it can also be a periodic orbit or have more general x dependence. The bifurcation diagrams depicting these solution branches use a scalar measure of the state and the parameter value in order to create a representation in the plane.

The implicit function theorem provides a foundation for the basic theory of continuation. Assume $G : \mathbb{R}^{n+m} \to \mathbb{R}^m$ is a continuously differentiable function such that $G(\mathbf{v}_0, \mathbf{w}_0) = 0$ for $\mathbf{v}_0 \in \mathbb{R}^n$ and $\mathbf{w}_0 \in \mathbb{R}^m$. If G_w is invertible where $[G_w]_{ij} = \partial G_i / \partial w_j$ then there exists a unique continuously differentiable function $g : \mathbb{R}^n \to \mathbb{R}^m$ in a neighborhood around $(\mathbf{v}_0, \mathbf{w}_0)$ such that $G(\mathbf{v}, g(\mathbf{v})) = 0$. If we consider a dynamical system $\dot{\mathbf{w}} = G(\mathbf{v}, \mathbf{w})$ and take $\mathbf{v}$ to be a set of parameters, then the interpretation becomes: if the Jacobian G_w is invertible then the fixed point $\mathbf{w}_0$ persists for parameter values near $\mathbf{v}_0$. Moreover the solution branch $(g(\mathbf{v}), \mathbf{v})$ passing through the point $(\mathbf{w}_0, \mathbf{v}_0)$ is unique.

The basic procedure for numerically computing solution branches involves approximating the problem as a set of algebraic equations, producing an initial guess $(\mathbf{u}_1^{(0)}, \mu_1^{(0)})$ for a new point on the branch based on the currently known point $(\mathbf{u}_0, \mu_0)$, and then finding an actual point $(\mathbf{u}_1, \mu_1)$ on the branch near the initial guess. The approach taken by AUTO for iteratively approaching the point $(\mathbf{u}_1, \mu_1)$ from a guess $(\mathbf{u}_1^{(\nu)}, \mu_1^{(\nu)})$ relies on Newton's method. This technique generates a sequence of successively better approximations to zeros of a function and we demonstrate the method for a real-valued function g. If we are looking for solutions to $g(x) = 0$ and have an initial guess $x^{(0)}$, we can use a linear approximation of the function

$$g(y) = g(x^{(0)}) + g'(x^{(0)})(y - x^{(0)}) + \mathcal{O}((y - x^{(0)})^2), \tag{A.2}$$

to provide a new point $x^{(1)}$. Solving the approximation for $g(x^{(1)}) = 0$ gives $x^{(1)} = x^{(0)} - g(x^{(0)})/g'(x^{(0)})$. The point $x^{(1)}$ is the intersection of the line tangent to g at $x^{(0)}$ with the x-axis. Iterating on this process ν more times gives

$$x^{(\nu+1)} = x^{(\nu)} - \frac{g(x^{(\nu)})}{g'(x^{(\nu)})}. \tag{A.3}$$

If $g(z) = 0$ and $g'(z) \neq 0$, then the sequence $x^{(\nu)} \to z$ as long as $x^{(0)}$ is sufficiently close to the zero z. Moreover, the convergence is quadratic and "sufficiently close" can be defined in terms of where the linear approximation (Eq. (A.2)) is valid.

Discretization by method of collocation

A discretization scheme is necessary to approximate Eq. (A.1) as an algebraic system. The method of orthogonal collocation is employed by AUTO because of its nice convergence properties [182]. The domain is scaled to $[0, 1]$ and divided into a mesh of N elements by the points $0 = x_0 < x_1 < ... < x_N = 1$.

These elements are not necessarily uniform in size and the code periodically adapts the mesh in order to equidistribute the local discretization error as the continuation proceeds [183]. Each element $[x_{j-1}, x_j]$ is further divided into $2 \leq m \leq 7$ sections by uniformly

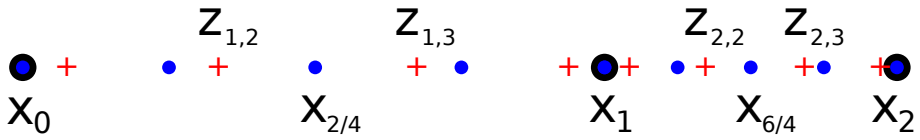

Figure A.1: A sample discretization with two elements ($N = 2$) and four collocation points ($m = 4$). The edges of the elements are marked with large black circles and the jth element is subdivided by the equally spaced small blue circles corresponding to the points $x_{j-k/m}$. The calculations are done at the collocation points $z_{j,k}$ marked by red crosses and interpolated to the points $x_{j-k/m}$.

spaced points $x_{j-k/m} = x_j - k\Delta x_j/m$ where $\Delta x_j = x_j - x_{j-1}$ and $0 \le k \le m$. The notation used here involving fractional subindices is meant to emphasize that there are N elements each subdivided into m pieces. The actual calculation is done at m collocation points $z_{j,k}$ that correspond to zeros of the mth degree Legendre polynomial P_m relative to the jth element, and the zeros thus satisfy $P_m(2(z_{j,k} - x_{j-1})/\Delta x_j - 1) = 0$. Lagrange polynomials

$$\ell_{j,k}(x) = \prod_{\substack{i=0 \\ i\neq k}}^{m} \frac{x - x_{j-i/m}}{x_{j-i/m} - x_{j-k/m}}, \tag{A.4}$$

are used to interpolate from the collocation points $z_{j,k}$ to the uniformly space points $x_{j-k/m}$. The m Lagrange polynomials $\ell_{j,k}(x)$ are constructed so that $\ell_{j,k}(x_{j-k/m}) = 1$ and $\ell_{j,k}(x_{j-i/m}) = 0$ for $i \neq k$. Figure A.1 provides an illustration of the discretization scheme.

The solution on each element $[x_{j-1}, x_j]$ is approximated in terms of the Lagrange polynomials as

$$\mathbf{p}_j(x) = \sum_{k=0}^{m} \mathbf{u}_{j-k/m}\ell_{j,k}(x), \tag{A.5}$$

where the $m+1$ unknown coefficients $\mathbf{u}_{j-k/m}$ approximate the values of the field $\mathbf{u}(x_{j-k/m})$. Adjacent elements share the coefficient associated with the common edge and so there are a total of $mN + 1$ points on the grid. Substituting into Eq. (A.1) and evaluating at the collocation points $z_{j,k}$ provides mN equations of the form

$$\mathbf{p}_j'(z_{j,k}) - f(\mathbf{p}_j(z_{j,k}), \mu) = 0. \tag{A.6}$$

The derivative term $\mathbf{p}_j'(z_{j,k})$ can be explicitly computed since it is just a sum of polynomials and, because the coefficients $\mathbf{u}_{j-k/m}$ each have n components, this is in fact a system of nmN algebraic equations for $n(mN + 1) + 1$ unknown components of the coefficients $\mathbf{u}_{j-k/m}$ and the parameter μ.

A standard situation is that an additional n equations come from boundary conditions and a final equation for the system comes from the continuation procedure for choosing the next point on the branch. In this case the next point on the branch is uniquely determined

as long as the matrix corresponding to the algebraic system has full rank. Because we are often looking for symmetric or antisymmetric solutions in a reversible system, we may take advantage of symmetry to perform the computation on only half of the domain of interest. For symmetric states, Neumann boundary conditions on half of the domain can be used to obtain the state on the full domain with periodic boundary conditions. Similarly, antisymmetric states on a periodic domain can be computed on a half-domain using Dirichlet boundary conditions.

Pseudo-arclength continuation

Let us now assume that we have a system of algebraic equations that approximate Eq. (A.1) in the form

$$F(\mathbf{u}, \mu) = 0, \tag{A.7}$$

where $\mathbf{u}, F(\mathbf{u}, \mu) \in \mathbb{R}^{n_t}$, and $\mu \in \mathbb{R}$. In the case that we are continuing a branch of fixed points in one parameter and use the discretization by method of collocation as described above, we have $n_t = n(mN + 1)$. For periodic orbits or multi-parameter continuation the algebraic system (A.7) that approximates Eq. (A.1) will generally need to be augmented so that $n_t > n(mN+1)$, but the general continuation procedure still applies. AUTO employs the method of pseudo-arclength continuation, an approximation to arclength continuation, to step along the solution branch of the algebraic system. This approach, while more complicated to implement than natural continuation, has the advantage of being able to negotiate folds of a solution branch. Other packages, such as pde2path, employ natural continuation until approach to a potential fold is detected and then switch to pseudo-arclength continuation. Figure A.2 graphically depicts the continuation step for natural continuation, arclength continuation, and pseudo-arclength continuation.

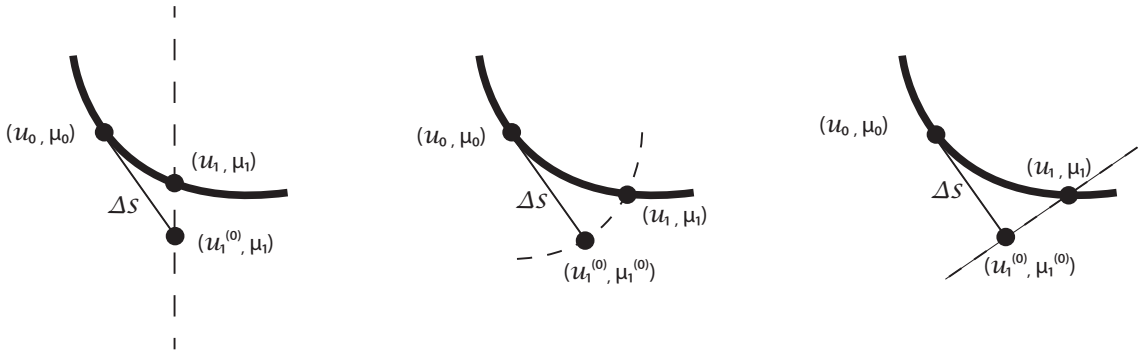

Figure A.2: A step along the solution branch starting from the point $(\mathbf{u}_0, \mu_0)$ via (a) natural continuation, (b) arclength continuation (c) pseudo-arclength continuation. The initial guess is taken a distance Δs along the direction tangent to the solution branch in all three cases. Newton's method is used to approach the point $(\mathbf{u}_1, \mu_1)$ along the dotted line.

We first discuss natural continuation (Fig. A.2(a)) which is the most straightforward way to numerically follow a solution branch in order to provide some intuition for the process. Given $(\mathbf{u}_0, \mu_0)$ on a solution branch, a naive way to guess a new point $(\mathbf{u}_1, \mu_1)$ on the branch might be to parametrize the branch by the parameter μ so that the next point is at $\mu_1 = \mu_0 + \Delta\mu$. An initial guess for the solution $\mathbf{u}_1$ at μ_1 is given by the linearization in μ about μ_0,

$$\mathbf{u}_1^{(0)} = \mathbf{u}_0 + \Delta\mu \frac{d\mathbf{u}_0}{d\mu}. \tag{A.8}$$

The guess $\mathbf{u}_1^{(0)}$ then becomes the starting point for a recursively defined sequence $\mathbf{u}_1^{(\nu)}$ that approaches a point on the solution branch corresponding to $\mu = \mu_1$ as $\nu \to \infty$. The convergence is achieved via Newton's method by iteratively solving

$$F_u(\mathbf{u}_1^{(\nu)}, \mu_1) \cdot \Delta\mathbf{u}_1^{(\nu)} = -F(\mathbf{u}_1^{(\nu)}, \mu_1) \tag{A.9}$$

$$\mathbf{u}_1^{(\nu+1)} = \mathbf{u}_1^{(\nu)} + \Delta\mathbf{u}_1^{(\nu)}, \tag{A.10}$$

where $[F_u]_{ij} = \partial F_i/\partial u_j$, $[F_\mu]_i = \partial F_i/\partial\mu$ and the dot product represents the standard vector dot product on $\mathbb{R}^{n_t}$. This approach, known as *natural* continuation, fails at folds where the solution branch does not persist beyond a particular value of μ.

Arclength continuation (Fig. A.2(b)), a conceptually useful but difficult to implement approach, instead takes a step of fixed length in $(\mathbf{u}, \mu)$ space. This procedure can be formulated as

$$F(\mathbf{u}(x; s), \mu(s)) = 0, \qquad \left\| \frac{d\mathbf{u}}{ds} \right\|^2 + \left(\frac{d\mu}{ds} \right)^2 = 1. \tag{A.11}$$

Because we are interpreting the vector $\mathbf{u} \in \mathbb{R}^{n_t}$ as a discretization of a continuous function $u(x)$ on $\mathbb{R}^n$, we can choose the norm in Eq. (A.11) to approximate the norm $\|u\|^2 = \int u(x) \cdot u(x)dx$, where the dot represents the standard vector dot product on $\mathbb{R}^n$. Newton's method can use an initial guess that is along the direction tangent to the solution branch at $(\mathbf{u}_0, \mu_0)$ to generate successively closer approximations to a point on the solution branch at $(\mathbf{u}_1, \mu_1)$ by varying the direction and fixing Δs. In practice, it is easier to implement *pseudo-arclength* continuation (Fig. A.2(c)) in which the arclength formulation (Eq. (A.11)) is approximated by

$$F(\mathbf{u}_1, \mu_1) = 0, \qquad \left\langle (\mathbf{u}_1 - \mathbf{u}_0), \frac{d\mathbf{u}_0}{ds} \right\rangle + (\mu_1 - \mu_0)\frac{d\mu_0}{ds} - \Delta s = 0, \tag{A.12}$$

where the inner product $\langle \mathbf{u}, \mathbf{v} \rangle$ on $\mathbb{R}^{n_t}$ should approximate the inner product $\langle u, v \rangle = \int u(x) \cdot v(x)dx$ of functions on $\mathbb{R}^n$. AUTO approximates the integral by quadrature to give

$$\langle u, v \rangle = \sum_{j,k} \omega_{j,k} \mathbf{u}_{j-k/m} \cdot \mathbf{v}_{j-k/m}, \qquad \omega_{j,k} = \int_{x_{j-1}}^{x_j} \ell_{j,k}(x)dx, \tag{A.13}$$

where the quadrature coefficients $\omega_{j,k}$ are independent of j apart from an overall scaling, $\mathbf{u}_{j-k/m}, \mathbf{v}_{j-k/m} \in \mathbb{R}^n$ correspond to values of the functions evaluated at the grid point $x_{j-k/m}$, and the dot in the expressions again represents the standard vector dot product on $\mathbb{R}^n$.

Geometrically, the interpretation is that a step is taken along the hyperplane perpendicular to the direction $(d\mathbf{u}_0/ds, d\mu_0/ds)$ tangent to the solution branch at $(\mathbf{u}_0, \mu_0)$ and a distance Δs away. The additional constraint comes from the condition defining the hyperplane that the projection of the step from $(\mathbf{u}_0, \mu_0)$ onto the tangent direction $(d\mathbf{u}_0/ds, d\mu_0/ds)$ must be Δs. The initial guess, which is still taken to be along the direction tangent to the solution branch, is given by

$$\mathbf{u}_1^{(0)} = \mathbf{u}_0 + \Delta s \frac{d\mathbf{u}_0}{ds} \tag{A.14}$$

$$\mu_1^{(0)} = \mu_0 + \Delta s \frac{d\mu_0}{ds}, \tag{A.15}$$

with $(d\mathbf{u}_0/ds, d\mu_0/ds)$ known from the previous step.

The Newton method AUTO uses for convergence to a point on the branch is given by

$$\begin{pmatrix} F_u(\mathbf{u}_1^{(\nu)}, \lambda_1^{(\nu)}) & F_\mu(\mathbf{u}_1^{(\nu)}, \lambda_1^{(\nu)}) \\ \frac{d\mathbf{u}_0}{ds} & \frac{d\mu_0}{ds} \end{pmatrix} \begin{pmatrix} \Delta\mathbf{u}_1^{(\nu)} \\ \Delta\mu_1^{(\nu)} \end{pmatrix}$$

$$= - \begin{pmatrix} F(\mathbf{u}_1^{(\nu)}, \lambda_1^{(\nu)}) \\ \left\langle (\mathbf{u}_1^{(\nu)} - \mathbf{u}_0), \frac{d\mathbf{u}_0}{ds} \right\rangle + (\mu_1^{(\nu)} - \mu_0)\frac{d\mu_0}{ds} - \Delta s \end{pmatrix} \tag{A.16}$$

Because inverting the $(n_t + 1) \times (n_t + 1)$ matrix on the left-hand side of Eq. (A.16) at each iteration is costly, the code employs a Newton–Chord method where the inverse is updated for only a user-specified number of Newton iterations before being frozen and Chord iterations are used.

The direction tangent to the solution branch at $(\mathbf{u}_1, \mu_1)$ can be computed from differentiation of Eq. (A.12) to get

$$\begin{pmatrix} F_u(\mathbf{u}_1, \lambda_1) & F_\mu(\mathbf{u}_1, \lambda_1) \\ \frac{d\mathbf{u}_0}{ds} & \frac{d\mu_0}{ds} \end{pmatrix} \begin{pmatrix} \frac{d\mathbf{u}_1}{ds} \\ \frac{d\mu_1}{ds} \end{pmatrix} = \begin{pmatrix} 0 \\ 1 \end{pmatrix}, \tag{A.17}$$

which is solved using the same matrix inversion that appears in the Newton iteration. The pseudo-arclength continuation procedure can then be repeated to trace out a particular solution branch. AUTO adapts the size of each step in Δs based on how fast the Newton method converges. If Δs falls below a user-specified minimum value or if the Newton algorithm doesn't converge within a user-specified number of iterations then the procedure is terminated. The tolerance that defines convergence is also specified by the user.

Bifurcation detection and branch switching

A regular solution $\mathbf{u} = \mathbf{u}_0$ to Eq. (A.7) at $\mu = \mu_0$ is defined by the property that $F_u(\mathbf{u}_0, \mu_0)$ has rank n_t. The implicit function theorem ensures that a unique solution branch $(\mathbf{u}(x; s), \mu(s))$

passes through a regular solution at the point $(\mathbf{u}_0, \mu_0)$. The implicit function theorem also ensures a unique solution branch passes through a point $(\mathbf{u}, \mu)$ with rank $(F_u(\mathbf{u}, \mu)) = n_t - 1$ as long as the augmented matrix $[F_u|F_\mu]$ has rank n_t. The point $(\mathbf{u}, \mu)$ is known as a simple fold in the latter case and the saddle-node bifurcation provides an example where such a point occurs.

Regular points and folds have a unique solution branch passing through, but additional branches can emerge at singular points with rank $(F_u(\mathbf{u}, \mu)) < n_t$. Additional solutions can also be created though a Hopf bifurcation at points where an eigenvalue has zero real part even if rank $(F_u(\mathbf{u}, \mu)) = n_t$. The detection of these Hopf bifurcation points must be handled separately and will not be discussed here. We focus on new solution branches created at local steady state bifurcations which occur at singular points owing to least one zero eigenvalue. A *simple* singular point occurs where rank $([F_u|F_\mu]) = n_t - 1$ which happens when either rank $(F_u) = n_t - 1$, or rank $(F_u) = n_t - 2$ and F_μ is not in the span of the columns of F_u. We expect that one additional solution branch can emerge from a simple singular point. In order to detect potential steady state bifurcations AUTO tracks the value of $q(s) = \det([F_u(s)|F_\mu(s)])$ as a function of the parametrization along the solution branch. When a sign change is detected, a secant method is used to approximate the location of the zero. Essentially a finite difference approximation to Newton's method, the secant method finds the zero by iterating the recursive formula

$$s^{\nu+1} = s^\nu - \frac{s^\nu - s^{\nu-1}}{q(s^\nu) - q(s^{\nu-1})} q(s^\nu). \tag{A.18}$$

This method fails to detect codimension-two bifurcations where two eigenvalues pass through zero and thus $q(s)$ has a zero without changing sign. While the determinant $q(s)$ does not cross zero at a simple fold, the solution branch changes direction in μ at folds. A fold point is therefore a zero of $d\mu/ds$ along the branch and can be found using secant method where a change in sign of $d\mu/ds$ is detected. Because AUTO must already compute $d\mu/ds$ (Eq. A.17) in order to determine the direction tangent to the branch, this provides an efficient method for determining potential folds.

At steady state bifurcation points where a second solution emerges, AUTO can attempt to continue along the current solution branch or try to switch onto the new branch. As discussed, the initial guess for continuing along the current branch is obtained by stepping along the direction $(d\mathbf{u}/ds, d\mu/ds)$ tangent to the branch. The tangent direction is in the nullspace of $[F_u|F_\mu]$, and the second branch also emerges along a direction within this two-dimensional nullspace. Computing the actual direction that the second branch emerges requires the evaluation of second order derivatives of F [184]. AUTO instead uses the direction orthogonal to $(d\mathbf{u}/ds, d\mu/ds)$ in the nullpace as an initial guess for the pseudo-arclength continuation procedure in order to attempt to switch branches, and this has been found to be successful in most applications.

Multiple continuation parameters and periodic orbits

The previous discussion has considered only a single bifurcation parameter, but it is often useful to follow a particular solution as a function of two or more parameters. The approach outlined above can be generalized to consider any number of bifurcation parameters by noting that the continuation procedure makes no real distinction between the discretized field variables and the continuation parameter. There just needs to be an additional boundary condition, integral constraint or other imposed constraint on the system for each additional bifurcation parameter considered. For example we may want to track the location of the Maxwell point between the periodic state and trivial state in SHE as a function of two parameters. This can be accomplished by including an integral constraint that specifies that the value of the free energy for the periodic state is fixed at zero. Another example might be to follow a fold point in two parameters. AUTO can handle this situation by automatically extending the system to include the zero eigenvector and the additional constraint enforcing that F_u has a one-dimensional zero eigenspace.

Following periodic orbits involves two-parameter continuation since the period of the orbit can change along the solution branch in addition to the bifurcation parameter. Because the domain is scaled to the unit interval in AUTO, the period of the orbit appears as an additional parameter of the system. AUTO can thus automatically extend a given system to be able to perform the required two-parameter continuation for periodic orbits. Periodic boundary conditions are necessary to make the orbit periodic but this is not enough to uniquely specify the solution since x translations of a solution also solve the system. AUTO implements the following additional integral constraint that fixes the phase of the orbit when performing continuation on periodic orbits:

$$\langle \mathbf{u}_1', \mathbf{u}_1 - \mathbf{u}_0 \rangle = 0, \tag{A.19}$$

where $\mathbf{u}_1'$ is the discretization of the derivative of the function $u_1(x)$ on $\mathbb{R}^n$ with respect to x and the inner product is computed by the method used for Eq. (A.12). This phase condition minimizes the distance in function space between the solution being computed and the solution at the previously computed point on the branch. The advantage of this method is that it prevents sharp fronts or peaks from drifting along the domain as successive solutions are computed along the branch.

A.2 Time integration

PDEs are often solved numerically by reducing the system to a set of N ODEs and integrating them forward in time. This can be accomplished by approximating the solution on a discrete spatial grid where the ODEs describe the time-dynamics at a set of points $\mathbf{x}_j$ and finite difference methods to approximate the coupling between the points due to spatial derivative terms. A better approximation to the derivative terms can be achieved in Fourier space and this approach is straightforward to implement when the system is subject to periodic boundary conditions and the grid points are uniformly distributed. The code we have written

to numerically integrate SHE in one and two dimensions thus performs the calculations in Fourier space.

In Fourier space, SHE can be written as

$$\frac{d\hat{u}_j}{dt} = \left(r_0 - (1 - k_j^2)^2\right) \hat{u}_j + \widehat{NL}_j, \tag{A.20}$$

where the hat denotes a Fourier transform, the jth Fourier mode has wavenumber k_j, r_0 is the time-independent component of the forcing, and NL contains the nonlinear terms from N_{23} or N_{35} and explicitly time-dependent terms such as $\rho \sin(2\pi t/T)u$. At each time step $\hat{u}$ is transformed to real space via inverse Fourier transform, NL is computed on the spatial grid as a function of u and t, and then NL is transformed back to Fourier space to get $\widehat{NL}_j$. In one spatial dimension, the simulation is set up on a grid of N_x equidistant points on a spatial domain with $-L_x < x \leq L_x$ and subject to periodic boundary conditions. In Fourier space, the modes are given by $k_n = n\pi/2L_x$ for $-N/2 < n \leq N/2$. Because u is a real-valued function, $\hat{u}_{-j}$ is the complex conjugate of $\hat{u}_j$ and it is only necessary to compute half of the modes. In two spatial dimensions, the grid becomes $N_x \times N_y$ points on a domain with $-L_x < x \leq L_x$, $-L_y < y \leq L_y$ and subject to periodic boundary conditions in both directions. It is only necessary to compute half the modes for the two-dimensional case again owing to the fact that u is real-valued.

Nonlinear terms in the system generate large wavenumbers that are subject to *aliasing* when computing in Fourier space. A nonlinear term u^p produces a response with wavenumber as large as pk from a mode with wavenumber k. One must take care that these short wavelength (large wavenumber) responses do not alias onto long wavelength modes of the discretized system. This aliasing occurs when the discrete spatial sampling cannot distinguish the high frequency spatial oscillation from a low frequency one (Fig. A.3). The short wavelength response thus spuriously contributes to the amplitude of a long wavelength mode resulting in numerical inaccuracies.

In order to prevent large wavenumber contamination due to aliasing, we filter out modes from our computation by manually setting their amplitudes to zero. The general rule for filtering in a system with highest order nonlinearity u^p is that the top $(p-1)/(p+1)$ fraction of modes must be set to zero in order to prevent aliasing. This condition can be understood by considering N equally spaced points on a one-dimensional spatial domain with periodic boundary conditions. In Fourier space the modes range from $-N/2$ to $N/2$ and the highest mode generated by the nonlinear term from a particular mode n is pn. When $N/2 < pn < 3N/2$, the mode pn is aliased onto $pn - N$. In order to determine the largest mode that does not contaminate any modes lower than it, we must find the mode that just aliases onto itself. The condition for this to happen is $-n = pn - N$, implying that the modes $-N/(p+1) < n < N/(p+1)$ is be safe from contamination if we filter the modes $|n| \geq N/(p+1)$. In two dimensions, the same argument holds for each spatial direction independently and the fraction of modes kept after filtering is $4/(p+1)^2$. Therefore only 1/9 of the modes remain after filtering in the two-dimensional SHE with a quintic nonlinearity.

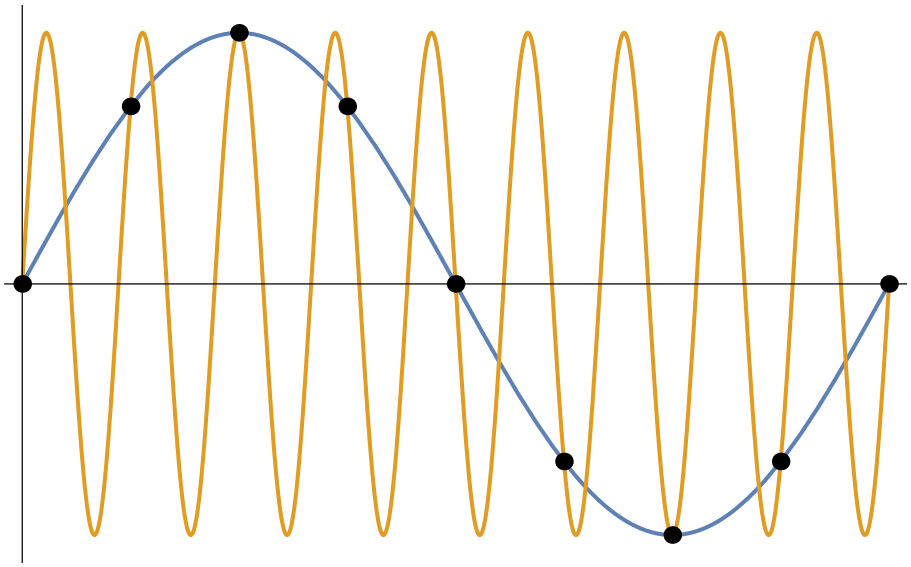

Figure A.3: Aliasing of $\sin 9x$ onto $\sin x$ using a grid with $N = 8$.

Exponential time differencing

Special care must be taken with the time integration of Fourier modes of a system like SHE because it contains a fourth order spatial derivative. The modes with short wavelength evolve on fast time scales because of the k^4 term in Eq. (A.20). The ratio of the slowest to the fastest time scale in the system scales exponentially with the order of highest spatial derivative. When this ratio is large, the system is considered *stiff*. Such systems are numerically challenging to integrate in time because they require a time step small enough to capture the fastest time scales and must be integrated long enough to capture the slowest time scales. If the time step is too large the numerical scheme may be unstable and if it is too short the computation time will be unnecessarily long.

It is often the case that the stiffness of a system stems from the linear terms as they typically contain the high order spatial derivatives. The method of exponential time differencing [136] provides an efficient way of dealing with stiffness in these cases by exactly solving the linear autonomous part of the problem and employing a numerical scheme to approximate the nonlinear and explicitly time-dependent contributions.

Consider an ODE of the form

$$\dot{v} = cv + F(v, t) \tag{A.21}$$

where c is a constant and $F(v, t)$ represents nonlinear and explicitly time-dependent terms. There are N equations of this form to integrate forward in time for SHE where $v = \hat{u}_j$, $c = r_0 - (1 - k_j^2)^2$ and $F(v, t) = \widehat{NL}_j$. The term $F(v, t)$ is computed from v in practice by taking an inverse Fourier transform of v, evaluating the nonlinear and explicitly time-dependent terms in real space, and the transforming back to Fourier space. We would like

an approximation of $v(t_{n+1})$ given $v(t_n)$. The first step is to solve the linear part of the equation exactly. Thus we multiply Eq. (A.21) by the integrating factor e^{-ct} and integrate the equation from $t = t_n$ to $t = t_{n+1} = t_n + h$ to get

$$ve^{-ct}\Big|_{t_n}^{t_n+h} = \int_{t_n}^{t_n+h} e^{-c\tau} F\left(v(\tau), \tau\right) d\tau. \tag{A.22}$$

Equation (A.22), which is still exact, simplifies to

$$v(t_{n+1}) = v(t_n)e^{ch} + e^{ch} \int_0^h e^{-c\tau} F(v(t_n + \tau), t_n + \tau) d\tau. \tag{A.23}$$

The numerical approximation in this scheme appears in computing the contribution from the integral involving nonlinear and explicitly time-dependent terms on the right-hand side of Eq. (A.23). We use a fourth order approximation based on the Runge–Kutta method. The solution v_{n+1} at time t_{n+1} is computed from v_n through four intermediate steps, and the full procedure is

$$\begin{aligned}
a_n =& v_n e^{ch/2} + \alpha_0 h F(v_n, t_n) && \text{(A.24)}\\
b_n =& v_n e^{ch/2} + \alpha_0 h F(a_n, t_n + h/2) && \text{(A.25)}\\
c_n =& a_n e^{ch/2} + \alpha_0 h \left(2F(b_n, t_n + h/2) - F(v_n, t_n)\right) && \text{(A.26)}\\
v_{n+1} =& v_n e^{ch} + \alpha_1 h F(v_n, t_n) + \alpha_2 h \left(F(a_n, t_n + h/2) + F(b_n, t_n + h/2)\right)\\
&+ \alpha_3 h F(c_n, t_n + h). && \text{(A.27)}
\end{aligned}$$

In order to calculate the contribution from F at each intermediate step, we perform an inverse Fourier transform of an intermediate field, compute the nonlinear terms in real space, and a transform back to Fourier space. This process must be repeated four times at every time step. The coefficients α_j, which only need to be computed once as long as the time step is fixed, are given by

$$\begin{aligned}
\alpha_0 &= \left(e^{ch/2} - 1\right)/ch && \text{(A.28)}\\
\alpha_1 &= \left(-4 - ch + e^{ch}(4 - 3ch + c^2h^2)\right)/c^3h^3 && \text{(A.29)}\\
\alpha_2 &= 2\left(2 + ch + e^{ch}(-2 + ch)\right)/c^3h^3 && \text{(A.30)}\\
\alpha_3 &= \left(-4 - 3ch - c^2h^2 + e^{ch}(4 - ch)\right)/c^3h^3. && \text{(A.31)}
\end{aligned}$$

These coefficients suffer from numerical inaccuracies due to cancellation errors when $ch \ll 1$. One approach is to compute these terms from a Taylor expansion when the value is below a certain threshold. A more robust approach, which we employ, is to compute the coefficients from a contour integral [185]. Taking the coefficients to be functions of ch, we can make use of the residue theorem to write

$$\alpha_j(ch) = \frac{1}{2\pi i} \int_\Gamma \frac{\alpha_j(z)}{z - ch} dz, \tag{A.32}$$

where Γ is a contour sufficiently large to enclose ch. This method has the advantage over the Taylor expansion approach of being accurate for both large and small values of ch. Moreover it is generalizable to higher-dimensional systems where c becomes a linear operator that is not necessarily diagonalizable. In practice, we only employ Eq. (A.32) when $ch < 0.1$ and we use a Riemann sum to numerically compute the integral along a unit circle centered about the origin.

Parameter scans

The most straightforward way to characterize the dependence of an attractor on parameters of the system using time integration is to numerically evolve an initial state within the basin of attraction to the attractor at a set of grid points that cover the parameter space. Some knowledge of the structure of the dynamics in the parameter space can allow for intelligent choices for the grid points in order to minimize the number of simulations necessary to map out the parameter space. Moreover, knowledge of how to distinguish between attractors of interest can allow for reduction in length of each simulation.

For initial parameter explorations of SHE23 with time-periodic forcing (cf. Fig. 4.10), we use an evenly spaced grid and scanned horizontally ($\Delta r_0 = -10^{-4}$) before making each vertical step ($\Delta T = 1$) thus going from the bottom right to the top left of the parameter space. We begin each horizontal scan at the right-hand side of the parameter space $r_0 = r_+$ and, anticipating average growth (yellow and orange regions), take a relatively narrow initial condition that consists of five wavelengths of the periodic pattern. Once PO (dark region) is detected during a horizontal scan, the initial condition switches to a state that fills approximately 3/4 of the domain in preparation for average decay (light and dark blue regions). We stop each simulation after the state reaches the domain edge, collapses to $u = 0$ or after a maximum time (typically $t_{\max} = 2000$ or 4000). We stop each horizontal scan and step up vertically when a simulation first indicates amplitude collapse (white region). At $T = 200$, the domain size of the simulation is doubled in order to capture the larger fluctuations in front position allowed by the longer forcing period. Specifically, we go from computation with $L_x = 40\pi$ and $N_x = 1024$ to $L_x = 80\pi$ and $N_x = 2048$.

This initial parameter provides a picture of the parameter space as being composed of relatively large regions with constant values of $\langle \Delta f \rangle$ approximately 2π apart. These regions are separated by relatively narrow transition bands between where $\langle \Delta f \rangle$ changes rapidly. Subsequent parameter scans (cf. Figs. 4.18, 4.19 and 4.23) make use of this information to intelligently select grid points such that they are more dense near the transition zones. A coarse and evenly spaced mesh is first used to cover the parameter space that does not experience amplitude collapse. The mesh is then iteratively refined in the following way. Each grid point computed during the first iteration is taken to be the lower right corner of a rectangular element of the parameter space whose other corners are adjacent grid points. If the value of $\langle \Delta f \rangle$ differs by some threshold value (typically $\pi/10$) on any of the four corners of the element, we assume the element contains a transition zone. We refine the element by performing simulations at the midpoints of the all the edges and at the center. This divides

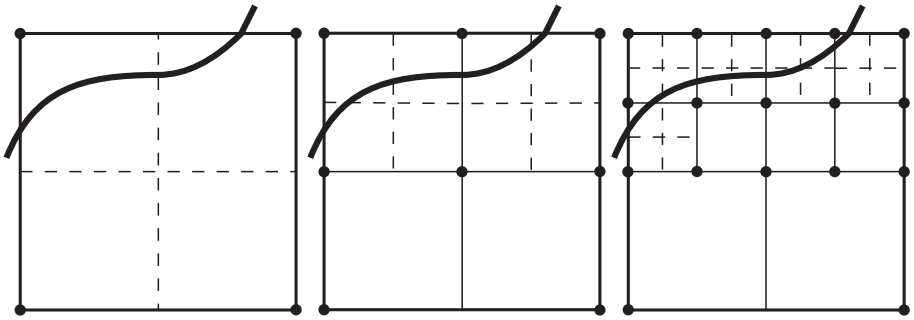

Figure A.4: Refinement of mesh in parameter space near a transition zone depicted by the bold curve.

the element into four sub-elements that are each 1/4 the size of the original. The procedure is then repeated for all of the sub-elements created during the previous iteration. In this way, the grid points where simulations are performed accumulate on the transition zones and the procedure is terminated once the desired resolution in parameter space is reached. Three iterations of the process are depicted in Fig. A.4.

Bibliography

[1] A. T. Winfree. *The Geometry of Biological Time*. Springer, New York, 1980.

[2] A. M. Turing. "The chemical basis of morphogenesis". In: *Phil. Trans. Royal Soc. B* 237.641 (1952), pp. 37–72.

[3] A. Gierer and H. Meinhardt. "A theory of biological pattern formation". In: *Kybernetik* 12.1 (1972), pp. 30–39.

[4] Q. Ouyang, J. Boissonade, J. C. Roux, and P. De Kepper. "Sustained reaction-diffusion structures in an open reactor". In: *Phys. Lett. A* 134.5 (1989), pp. 282–286.

[5] Q. Ouyang and H. L. Swinney. "Transition from a uniform state to hexagonal and striped Turing patterns". In: *Nature* 352.6336 (1991), pp. 610–612.

[6] M. C. Cross and P. C. Hohenberg. "Pattern formation outside of equilibrium". In: *Rev. Mod. Phys.* 65.3 (1993), p. 851.

[7] R. B. Hoyle. *Pattern Formation: An Introduction to Methods*. Cambridge University Press, 2006.

[8] H. Meinhardt. *The Algorithmic Beauty of Sea Shells*. Springer Science & Business Media, 2009.

[9] M. B. Short, M. R. D'Orsogna, V. B. Pasour, G. E. Tita, P. J. Brantingham, A. L. Bertozzi, and L. B. Chayes. "A statistical model of criminal behavior". In: *Math. Mod. Meth. Appl. Sci.* 18.supp01 (2008), pp. 1249–1267.

[10] E. Pampaloni, P. L. Ramazza, S. Residori, and F. T. Arecchi. "Two-dimensional crystals and quasicrystals in nonlinear optics". In: *Phys. Rev. Lett.* 74.2 (1995), p. 258.

[11] J. M. Sakoda. "The checkerboard model of social interaction". In: *J. of Math. Sociol.* 1.1 (1971), pp. 119–132.

[12] T. C. Schelling. "Dynamic models of segregation". In: *J. Math. Sociol.* 1.2 (1971), pp. 143–186.

[13] A. Boettiger, B. Ermentrout, and G. Oster. "The neural origins of shell structure and pattern in aquatic mollusks". In: *Proc. Natl. Acad. Sci.* 106.16 (2009), pp. 6837–6842.

[14] S. Residori. "Patterns, fronts and structures in a liquid-crystal-light-valve with optical feedback". In: *Phys. Rep.* 416.5 (2005), pp. 201–272.

[15] P. B. Umbanhowar, F. Melo, and H. L. Swinney. "Localized excitations in a vertically vibrated granular layer". In: *Nature* 382.6594 (1996), pp. 793–796.

[16] V. Petrov, Q. Ouyang, and H. L. Swinney. "Resonant pattern formation in achemical system". In: *Nature* 388.6643 (1997), pp. 655–657.

[17] Y. A. Astrov and Y. A. Logvin. "Formation of clusters of localized states in a gas discharge system via a self-completion scenario". In: *Phys. Rev. Lett.* 79.16 (1997), p. 2983.

[18] C. R. Laing, W. C. Troy, B. Gutkin, and G. B. Ermentrout. "Multiple bumps in a neuronal model of working memory". In: *SIAM J. Appl. Math.* 63.1 (2002), pp. 62–97.

[19] D. Avitabile and H. Schmidt. "Snakes and ladders in an inhomogeneous neural field model". In: *Physica D.* 294 (2015), pp. 24–36.

[20] N. J. Balmforth. "Solitary waves and homoclinic orbits". In: *Annu. Rev. Fluid Mech.* 27.1 (1995), pp. 335–373.

[21] P. D. Woods and A. R. Champneys. "Heteroclinic tangles and homoclinic snaking in the unfolding of a degenerate reversible Hamiltonian–Hopf bifurcation". In: *Physica D* 129.3 (1999), pp. 147–170.

[22] Y. Pomeau. "Front motion, metastability and subcritical bifurcations in hydrodynamics". In: *Physica D* 23.1–3 (1986), pp. 3–11.

[23] G. W. Hunt, M. A. Peletier, A. R. Champneys, P. D. Woods, M. A. Wadee, C. J. Budd, and G. J. Lord. "Cellular buckling in long structures". In: *Nonlinear Dynamics* 21 (2000), pp. 3–29.

[24] J. Burke and E. Knobloch. "Localized states in the generalized Swift-Hohenberg equation". In: *Phys. Rev. E* 73.5 (2006), p. 056211.

[25] J. Burke and E. Knobloch. "Snakes and ladders: localized states in the Swift–Hohenberg equation". In: *Phys. Lett. A* 360.6 (2007), pp. 681–688.

[26] E. Knobloch. "Spatial localization in dissipative systems". In: *Annu. Rev. Conden. Matter Phys.* 6 (2015), pp. 325–359.

[27] *R. Lefever*. `http://www.ulb.ac.be/sciences/nlpc/rlefever.html`.

[28] J. A. Sherratt. "An analysis of vegetation stripe formation in semi-arid landscapes". In: *J. Math. Biol.* 51.2 (2005), pp. 183–197.

[29] M. Tlidi, R. Lefever, and A. Vladimirov. "On vegetation clustering, localized bare soil spots and fairy circles". In: *Dissipative Solitons: From Optics to Biology and Medicine*. Vol. 751. Lecture Notes in Physics. Springer, Berlin, 2008, pp. 1–22.

[30] J. A. Sherratt. "Pattern solutions of the Klausmeier model for banded vegetation in semi-arid environments I". In: *Nonlinearity* 23.10 (2010), pp. 2657–2675.

[31] A. Y. Kletter, J. von Hardenberg, and E. Meron. "Ostwald ripening in dryland vegetation". In: *Comm. Pure Appl. Anal.* 11 (2012), pp. 261–273.

[32] E. Meron. "Pattern-formation approach to modelling spatially extended ecosystems". In: *Ecol. Model.* 234 (2012), pp. 70–82.

[33] V. Guttal and C. Jayaprakash. "Self-organization and productivity in semi-arid ecosystems: Implications of seasonality in rainfall". In: *J. Theor. Biol.* 248.3 (2007), pp. 490–500.

[34] A. Y. Kletter, J. Von Hardenberg, E. Meron, and A. Provenzale. "Patterned vegetation and rainfall intermittency". In: *J. Theor. Biol.* 256.4 (2009), pp. 574–583.

[35] X.-X. Zhao and J.-Z. Wang. "Rich spatiotemporal dynamics of a vegetation model with noise and periodic forcing". In: *Discrete Dyn. Nat. Soc.* 2014 (2014).

[36] Y. R. Zelnik, E. Meron, and G. Bel. "Localized states qualitatively change the response of ecosystems to varying conditions and local disturbances". In: *Ecol. Complex.* 25 (2016), pp. 26–34.

[37] E. Meron. *Nonlinear Physics of Ecosystems*. CRC Press, 2015.

[38] M. K. Davidson, J. R. Lindsey, and J. K. Davis. "Requirements and selection of an animal model". In: *Isr. J Med. Sci.* 23.6 (1987), pp. 551–555.

[39] E. Bier. "Drosophila, the golden bug, emerges as a tool for human genetics". In: *Nature Rev. Gen.* 6.1 (2005), pp. 9–23.

[40] M'F. Hilali, S. Métens, P. Borckmans, and G. Dewel. "Pattern selection in the generalized Swift–Hohenberg model". In: *Phys. Rev. E* 51.3 (1995), p. 2046.

[41] H. Sakaguchi and H. R. Brand. "Stable localized solutions of arbitrary length for the quintic Swift–Hohenberg equation". In: *Physica D* 97.1 (1996), pp. 274–285.

[42] J. Burke and E. Knobloch. "Homoclinic snaking: Structure and stability". In: *Chaos* 17.3 (2007), pp. 037102–037102.

[43] J. Swift and P. C. Hohenberg. "Hydrodynamic fluctuations at the convective instability". In: *Phys. Rev. A* 15.1 (1977), p. 319.

[44] J. Burke. *Localized states in driven dissipative systems*. Ph.D. Thesis. University of California, Berkeley, 2008.

[45] A. Bergeon, J. Burke, E. Knobloch, and I. Mercader. "Eckhaus instability and homoclinic snaking". In: *Phys. Rev. E* 78.4 (2008), p. 046201.

[46] J. Burke and J. H. P. Dawes. "Localized states in an extended Swift–Hohenberg equation". In: *SIAM J Appl. Dyn. Sys.* 11.1 (2012), pp. 261–284.

[47] E. Knobloch. "Spatially localized structures in dissipative systems: Open problems". In: *Nonlinearity* 21.4 (2008), T45–T60.

[48] P. Gandhi, E. Knobloch, and C. Beaume. "Dynamics of phase slips in systems with time-periodic modulation". In: *Physical Review E* 92.6 (2015), p. 062914.

[49] P. Gandhi, E. Knobloch, and C. Beaume. "Localized states in periodically forced systems". In: *Phys. Rev. Lett.* 114.3 (2015), p. 034102.

[50] P. Gandhi, C. Beaume, and E. Knobloch. "A new resonance mechanism in the Swift–Hohenberg equation with time-periodic forcing". In: *SIAM J. Appl. Dyn. Sys.* 14 (2015), pp. 860–892.

[51] P. Gandhi, C. Beaume, and E. Knobloch. "Time-periodic forcing of spatially localized structures". In: *Nonlinear Dynamics: Materials, Theory and Experiments*. Ed. by M. G. Clerc and M. Tlidi. Springer Proceedings in Physics. Springer International Publishing, 2016, pp. 303–316.

[52] C. M. Bender and S. A. Orszag. *Advanced Mathematical Methods for Scientists and Engineers*. Springer Science & Business Media, 1999.

[53] D. W. Jordan and P. Smith. *Nonlinear Ordinary Differential Equations: An Introduction to Dynamical Systems*. Vol. 2. Oxford University Press, USA, 1999.

[54] S. Wiggins. *Introduction to Applied Nonlinear Dynamical Systems and Chaos*. Vol. 2. Springer Science & Business Media, 2003.

[55] J. Guckenheimer and P. Holmes. *Nonlinear Oscillations, Dynamical Systems, and Bifurcations of Vector Fields*. Vol. 42. Springer Science & Business Media, 2013.

[56] S. H. Strogatz. *Nonlinear Dynamics and Chaos: With Applications to Physics, Biology, Chemistry, and Engineering*. Westview press, 2014.

[57] J. D. Crawford. "Introduction to bifurcation theory". In: *Rev. Mod. Phys.* 63.4 (1991), p. 991.

[58] G. Hu, T. Ditzinger, C. Ning, and H. Haken. "Stochastic resonance without external periodic force". In: *Phys. Rev. Lett.* 71.6 (1993), p. 807.

[59] D. Avitabile, D. J. B. Lloyd, J. Burke, E. Knobloch, and B. Sandstede. "To snake or not to snake in the planar Swift–Hohenberg equation". In: *SIAM J. Appl. Dyn. Sys.* 9.3 (2010), pp. 704–733.

[60] R. L. Devaney. "Reversible diffeomorphisms and flows". In: *Trans. Am. Math. Soc.* 218 (1976), pp. 89–113.

[61] J. S. W. Lamb and J. A. G. Roberts. "Time-reversal symmetry in dynamical systems: A survey". In: *Physica D* 112.1 (1998), pp. 1–39.

[62] A. R. Champneys. "Homoclinic orbits in reversible systems and their applications in mechanics, fluids and optics". In: *Physica D* 112.1 (1998), pp. 158–186.

[63] C. Elphick, E. Tirapegui, M. E. Brachet, P. Coullet, and G. Iooss. "A simple global characterization for normal forms of singular vector fields". In: *Physica D* 29.1 (1987), pp. 95–127.

[64] G. Iooss and M. C. Pérouème. "Perturbed homoclinic solutions in reversible 1:1 resonance vector fields". In: *J. Diff. Eqns.* 102.1 (1993), pp. 62–88.

[65] G. W. Hunt, G. J. Lord, and A. R. Champneys. "Homoclinic and heteroclinic orbits underlying the post-buckling of axially-compressed cylindrical shells". In: *Comput. Meth. Appl. Mech. Eng.* 170.3 (1999), pp. 239–251.

[66] J. V. José and E. J. Saletan. *Classical Dynamics: A Contemporary Approach*. Cambridge University Press, 1998.

[67] M. Beck, J. Knobloch, D. J. B. Lloyd, B. Sandstede, and T. Wagenknecht. "Snakes, ladders, and isolas of localized patterns". In: *SIAM J. Math. Anal.* 41.3 (2009), pp. 936–972.

[68] G. W. Hunt, H. M. Bolt, and J. M. T. Thompson. "Structural localization phenomena and the dynamical phase-space analogy". In: *Proc. R. Soc. London A* 425.1869 (1989), pp. 245–267.

[69] T. M. Schneider, J. Gibson, and J. Burke. "Snakes and ladders: Localized solutions of plane Couette flow". In: *Phys. Rev. Lett.* 104 (2010), p. 104501.

[70] I. Mercader, O. Batiste, A. Alonso, and E. Knobloch. "Convectons, anticonvectons and multiconvectons in binary fluid convection". In: *J. Fluid Mech.* 667 (2011), pp. 586–606.

[71] C. Beaume, A. Bergeon, and E. Knobloch. "Convectons and secondary snaking in three-dimensional natural doubly diffusive convection". In: *Phys. Fluids* 25 (2013), p. 024105.

[72] C. Beaume, E. Knobloch, and A. Bergeon. "Nonsnaking doubly diffusive convectons and the twist instability". In: *Phys. Fluids* 25 (2013), p. 114102.

[73] D. Lo Jacono, A. Bergeon, and E. Knobloch. "Three-dimensional binary fluid convection in a porous medium". In: *J. Fluid Mech.* 730 (2013), R2.

[74] C. Beaume, H.-C. Kao, E. Knobloch, and A. Bergeon. "Localized rotating convection with no-slip boundary conditions". In: *Phys. Fluids* 25 (2013), p. 124105.

[75] L. Y. Glebsky and L. M. Lerman. "On small stationary localized solutions for the generalized 1-D Swift–Hohenberg equation". In: *Chaos* 5.2 (1995), pp. 424–431.

[76] G. Kozyreff and S. J. Chapman. "Asymptotics of large bound states of localized structures". In: *Phys. Rev. Lett.* 97.4 (2006), p. 044502.

[77] S. J. Chapman and G. Kozyreff. "Exponential asymptotics of localised patterns and snaking bifurcation diagrams". In: *Physica D* 238.3 (2009), pp. 319–354.

[78] N. W. McLachlan. *Theory and Application of Mathieu Functions*. Clarendon Press, 1951.

[79] F. Verhulst. *Nonlinear Differential Equations and Dynamical Systems*. Springer Science & Business Media, 2006.

[80] A. T. Winfree. "Biological rhythms and the behavior of populations of coupled oscillators". In: *J. Theoret. Biol.* 16.1 (1967), pp. 15–42.

[81] R. E. Mirollo and S. H. Strogatz. "Synchronization of pulse-coupled biological oscillators". In: *SIAM J. Appl. Math.* 50.6 (1990), pp. 1645–1662.

[82] C. S. Peskin. *Mathematical Aspects of Heart Physiology*. Courant Institute of Mathematical Sciences, New York University, 1975.

[83] C. Hammond, H. Bergman, and P. Brown. "Pathological synchronization in Parkinson's disease: Networks, models and treatments". In: *Trends Neurosci.* 30.7 (2007), pp. 357–364.

[84] Y. Kuramoto. *Chemical Oscillations, Waves, and Turbulence*. Springer, New York, 1984.

[85] J. Guckenheimer. "Isochrons and phaseless sets". In: *J. Math. Biol.* 1.3 (1975), pp. 259–273.

[86] E. N. Brown, J. Moehlis, and P. Holmes. "On the phase reduction and response dynamics of neural oscillator populations". In: *Neural Comput.* 16.4 (2004), pp. 673–715.

[87] Y. Kuramoto. "Self-entrainment of a population of coupled non-linear oscillators". In: *International Symposium on Mathematical Problems in Theoretical Physics*. Ed. by H. Araki. Vol. 39. Lecture Notes in Physics. Springer: Berlin, Heidelberg, 1975, pp. 420–422.

[88] E. Benoît, J. L. Callot, F. Diener, and M. Diener. "Chasse au canard". In: *Collectanea Mathematica* 32.1 (1981), pp. 37–76.

[89] W. Eckhaus. "Relaxation oscillations, including a standard chase on French ducks". In: *Asymptotic Analysis II*. Vol. 985. Lecture Notes in Mathematics. Springer, New York, 1983, pp. 449–494.

[90] E. M. Izhikevich. "Neural excitability, spiking and bursting". In: *Int. J. Bifurcat. Chaos* 10.06 (2000), pp. 1171–1266.

[91] M. Brøns and K. Bar-Eli. "Canard explosion and excitation in a model of the Belousov–Zhabotinskii reaction". In: *J. Phys. Chem.* 95.22 (1991), pp. 8706–8713.

[92] M. Wechselberger and G. J. Pettet. "Folds, canards and shocks in advection-reaction-diffusion models". In: *Nonlinearity* 23.8 (2010), p. 1949.

[93] K. Harley, P. van Heijster, R. Marangell, G. J. Pettet, and M. Wechselberger. "Novel solutions for a model of wound healing angiogenesis". In: *Nonlinearity* 27.12 (2014), p. 2975.

[94] P. Carter, E. Knobloch, and M. Wechselberger. "Transonic canards and stellar wind". In: *Preprint* (2015).

[95] M. Wechselberger. "Canards". In: *Scholarpedia* 2.4 (2007), p. 1356.

[96] R. Adler. "A study of locking phenomena in oscillators". In: *Proc. IRE* 34.6 (1946), pp. 351–357.

[97] S. Shinomoto and Y. Kuramoto. "Phase transitions in active rotator systems". In: *Prog. Theor. Phys.* 75 (1986), pp. 1105–1110.

[98] L. F. Lafuerza, P. Colet, and R. Toral. "Nonuniversal results induced by diversity distribution in coupled excitable systems". In: *Phys. Rev. Lett.* 105 (2010), p. 084101.

[99] S. Watanabe and S. H. Strogatz. "Constants of motion for superconducting Josephson arrays". In: *Physica D* 74.3–4 (1994), pp. 197–253.

[100] M. Y. Choi, Y. W. Kim, and D. C. Hong. "Periodic synchronization in a driven system of coupled oscillators". In: *Phys. Rev. E* 49.5 (1994), pp. 3825–3832.

[101] D. Cumin and C. P. Unsworth. "Generalising the Kuramoto model for the study of neuronal synchronisation in the brain". In: *Physica D* 226 (2007), pp. 181–196.

[102] P. So, B. C. Cotton, and E. Barreto. "Synchronization in interacting populations of heterogeneous oscillators with time-varying coupling". In: *Chaos* 18 (2008), p. 037114.

[103] P. So and E. Barreto. "Generating macroscopic chaos in a network of globally coupled phase oscillators". In: *Chaos* 21 (2011), p. 033127.

[104] S. Petkoski and A. Stefanovska. "Kuramoto model with time-varying parameters". In: *Phys. Rev. E* 86 (2012), p. 046212.

[105] S. H. Lee, S. Lee, S.-W. Son, and P. Holme. "Phase-shift inversion in oscillator systems with periodically switching couplings". In: *Phys. Rev. E* 85 (2012), p. 027202.

[106] J. H. Sheeba, A. Stefanovska, and P. V. E. McClintock. "Neural synchrony during anesthesia: a thalamocortical model". In: *Biophys. J.* 95 (2008), pp. 2722–2727.

[107] D. Taylor, E. Ott, and J. G. Restrepo. "Spontaneous synchronization of coupled oscillator systems with frequency adaptation". In: *Phys. Rev. E* 81 (2010), p. 046214.

[108] P. T. Clemson, S. Petkoski, T. Stankovski, and A. Stefanovska. "Coupled nonautonomous oscillators". In: *Nonautonomous Dynamical Systems in the Life Sciences*. Springer, 2013, pp. 163–197.

[109] K. K. Likharev. *Dynamics of Josephson Junctions and Circuits*. Gordon and Breach, 1986.

[110] S. Shapiro. "Microwave harmonic generation from Josephson junctions". In: *J. Appl. Phys.* 38.4 (1967), pp. 1879–1884.

[111] P. Russer. "Influence of microwave radiation on current-voltage characteristic of superconducting weak links". In: *J. Appl. Phys.* 43.4 (1972), pp. 2008–2010.

[112] M. J. Renne and D. Polder. "Some analytical results for the resistively shunted Josephson junction". In: *Rev. Phys. Appl. (Paris)* 9.1 (1974), pp. 25–28.

[113] A. A. Abidi and L. O. Chua. "On the dynamics of Josephson-junction circuits". In: *IEEE J. Electron. Circ. Syst.* 3.4 (1979), pp. 186–200.

[114] K. Wiesenfeld, P. Colet, and S. H. Strogatz. "Frequency locking in Josephson arrays: Connection with the Kuramoto model". In: *Phys. Rev. E* 57 (2 1998), pp. 1563–1569.

[115] E. J. Doedel and B. E. Oldeman. "AUTO-07P: Continuation and bifurcation software for ordinary differential equations". In: *Concordia University* Montreal, Canada (2010). URL: `http://cmvl.cs.concordia.ca/auto/`.

[116] M. Abramowitz and I. A. Stegun. *Handbook of Mathematical Functions*. Vol. 1. 5. Dover, New York, 1972.

[117] P. Hartman. *Ordinary Differential Equations, Society for Industrial and Applied Mathematics (SIAM), Philadelphia, PA*. Tech. rep. Corrected reprint of the second (1982) edition [Birkhäuser, Boston, MA], 2002.

[118] A. M. Krasnosel'skii, E. O'Grady, A. Pokrovskii, and D. I. Rachinskii. "Periodic canard trajectories with multiple segments following the unstable part of critical manifold". In: *Discrete Contin. Dyn. Syst. Ser. B* 18.2 (2013), pp. 467–482.

[119] B. Schäpers, M. Feldmann, T. Ackemann, and W. Lange. "Interaction of localized structures in an optical pattern-forming system". In: *Phys. Rev. Lett.* 85.4 (2000), pp. 748–751.

[120] A. Prigent, G. Grégoire, H. Chaté, O. Dauchot, and W. van Saarloos. "Large-scale finite-wavelength modulation within turbulent shear flows". In: *Phys. Rev. Lett.* 89 (2002), p. 014501.

[121] D. Barkley and L. S. Tuckerman. "Computational study of turbulent laminar patterns in Couette flow". In: *Phys. Rev. Lett.* 94 (2005), p. 014502.

[122] M. G. Clerc, C. Falcon, and E. Tirapegui. "Additive noise induces front propagation". In: *Phys. Rev. Lett.* 94.14 (2005), p. 148302.

[123] J. M. G. Vilar and J. M. Rubi. "Spatiotemporal stochastic resonance in the Swift–Hohenberg equation". In: *Phys. Rev. Lett.* 78 (1997), pp. 2886–2889.

[124] O. Lioubashevski, Y. Hamiel, A. Agnon, Z. Reches, and J. Fineberg. "Oscillons and propagating solitary waves in a vertically vibrated colloidal suspension". In: *Phys. Rev. Lett.* 83.16 (1999), pp. 3190–3193.

[125] P. Binder, D. Abraimov, A. V. Ustinov, S. Flach, and Y. Zolotaryuk. "Observation of breathers in Josephson ladders". In: *Phys. Rev. Lett.* 84.4 (2000), pp. 745–748.

[126] A. M. Rucklidge and M. Silber. "Design of parametrically forced patterns and quasipatterns". In: *SIAM J. Appl. Math.* 8 (2009), pp. 298–347.

[127] J. V. I. Timonen, M. Latikka, L. Leibler, R. H. A. Ras, and O. Ikkala. "Switchable static and dynamic self-assembly of magnetic droplets on superhydrophobic surfaces". In: *Science* 341 (2013), pp. 253–257.

[128] A. S. Alnahdi, J. Niesen, and A. M. Rucklidge. "Localized patterns in periodically forced systems". In: *SIAM J. Appl. Dyn. Sys.* 13.3 (2014), pp. 1311–1327.

[129] A. Yochelis, C. Elphick, A. Hagberg, and E. Meron. "Frequency locking in extended systems: The impact of a Turing mode". In: *Europhys. Lett.* 69.2 (2005), pp. 170–176.

[130] B. Marts, A. Hagberg, E. Meron, and A. L. Lin. "Resonant and nonresonant patterns in forced oscillators". In: *Chaos* 16.3 (2006), p. 037113.

[131] J. Buceta, K. Lindenberg, and J. M. R. Parrondo. "Stationary and oscillatory spatial patterns induced by global periodic switching". In: *Phys. Rev. Lett.* 88.2 (2001), p. 024103.

[132] I. Belykh, V. Belykh, R. Jeter, and M. Hasler. "Multistable randomly switching oscillators: The odds of meeting a ghost". In: *Euro. Phys. J. Spec. Top.* 222.10 (2013), pp. 2497–2507.

[133] J. Burke, A. Yochelis, and E. Knobloch. "Classification of spatially localized oscillations in periodically forced dissipative systems". In: *SIAM J. Appl. Dyn. Sys.* 7.3 (2008), pp. 651–711.

[134] J. Burke, S. M. Houghton, and E. Knobloch. "Swift–Hohenberg equation with broken reflection symmetry". In: *Phys. Rev. E* 80 (2009), p. 036202.

[135] H.-C. Kao, C. Beaume, and E. Knobloch. "Spatial localization in heterogeneous systems". In: *Phys. Rev. E* 89 (2014), p. 012903.

[136] S. M. Cox and P. C. Matthews. "Exponential time differencing for stiff systems". In: *J. Comp. Phys.* 176.2 (2002), pp. 430–455.

[137] J. Hinch. *Perturbation Methods*. Cambridge University Press, Cambridge, 1991.

[138] K. Siteur, E. Siero, M. B. Eppinga, J. D. M. Rademacher, A. Doelman, and M. Rietkerk. "Beyond Turing: The response of patterned ecosystems to environmental change". In: *Ecol. Complex.* 20 (2014), pp. 81–96.

[139] O. Batiste, E. Knobloch, A. Alonso, and I. Mercader. "Spatially localized binary-fluid convection". In: *J. Fluid Mech.* 560 (2006), pp. 149–158.

[140] S. M. Houghton and E. Knobloch. "Swift–Hohenberg equation with broken cubic-quintic nonlinearity". In: *Phys. Rev. E* 84 (2011), p. 016204.

[141] I. Mercader, O. Batiste, A. Alonso, and E. Knobloch. "Travelling convectons in binary fluid convection". In: *J. Fluid Mech.* 772 (2013), pp. 240–266.

[142] D. J. B. Lloyd and B. Sandstede. "Localized radial solutions of the Swift–Hohenberg equation". In: *Nonlinearity* 22.2 (2009), p. 485.

[143] S. McCalla and B. Sandstede. "Snaking of radial solutions of the multi-dimensional Swift–Hohenberg equation: A numerical study". In: *Physica D* 239.16 (2010), pp. 1581–1592.

[144] I. S. Aranson, K. A. Gorshkov, A. S. Lomov, and M. I. Rabinovich. "Stable particle-like solutions of multidimensional nonlinear fields". In: *Physica D* 43.2 (1990), pp. 435–453.

[145] P. Pelcé and A. Libchaber. *Dynamics of Curved Fronts*. Elsevier, 2012.

[146] Y. Kuramoto and D. Battogtokh. "Coexistence of coherence and incoherence in nonlocally coupled phase oscillators." In: *Nonl. Phen. Compl. Sys.* 5.4 (2002), pp. 380–385.

[147] D. M. Abrams and S. H. Strogatz. "Chimera states for coupled oscillators". In: *Phys. Rev. Lett.* 93.17 (2004), p. 174102.

[148] R. Lefever and O. Lejeune. "On the origin of tiger bush". In: *Bull. Math. Biol.* 59.2 (1997), pp. 263–294.

[149] O. Lejeune, M. Tlidi, and P. Couteron. "Localized vegetation patches: A self-organized response to resource scarcity". In: *Phys. Rev. E* 66 (2002), p. 010901.

[150] C. A. Klausmeier. "Regular and irregular patterns in semiarid vegetation". In: *Science* 284.5421 (1999), pp. 1826–1828.

[151] S. van der Stelt, A. Doelman, G. Hek, and J. D. M. Rademacher. "Rise and fall of periodic patterns for a generalized Klausmeier–Gray–Scott model". In: *J. Nonlinear Sci.* 23.1 (2013), pp. 39–95.

[152] P. Gray and S. K. Scott. "Autocatalytic reactions in the isothermal, continuous stirred tank reactor: Isolas and other forms of multistability". In: *Chem. Eng. Sci.* 38.1 (1983), pp. 29–43.

[153] P. Gray and S. K. Scott. "Autocatalytic reactions in the isothermal, continuous stirred tank reactor: Oscillations and instabilities in the system $A + 2B \to 3B$; $B \to C$". In: *Chem. Eng. Sci.* 39.6 (1984), pp. 1087–1097.

[154] P. Gray and S. K. Scott. "Sustained oscillations and other exotic patterns of behavior in isothermal reactions". In: *J. Phys. Chem.* 89.1 (1985), pp. 22–32.

[155] E. Siero, A. Doelman, M. B. Eppinga, J. D. M. Rademacher, M. Rietkerk, and K. Siteur. "Striped pattern selection by advective reaction-diffusion systems: Resilience of banded vegetation on slopes". In: *Chaos* 25.3 (2015), p. 036411.

[156] D. S. Morgan, A. Doelman, and T. J. Kaper. "Stationary periodic patterns in the 1D Gray–Scott model". In: *Meth. Appl. Anal.* 7.1 (2000), pp. 105–150.

[157] Y. Zelnik. private communication. 2015.

[158] M. Rietkerk, M. C. Boerlijst, F. van Langevelde, R. HilleRisLambers, J. van de Koppel, L. Kumar, H. H. T. Prins, and A. M. de Roos. "Self-organization of vegetation in arid ecosystems". In: *Amer. Nat.* 160.4 (2002), pp. 524–530.

[159] E. Gilad, J. Von Hardenberg, A. Provenzale, M. Shachak, and E. Meron. "Ecosystem engineers: From pattern formation to habitat creation". In: *Phys. Rev. Lett.* 93.9 (2004), p. 098105.

[160] P. C. Matthews and S. M. Cox. "Pattern formation with a conservation law". In: *Nonlinearity* 13.4 (2000), pp. 1293–1320.

[161] J. H. P. Dawes. "Localized pattern formation with a large-scale mode: Slanted snaking". In: *SIAM J. Appl. Dyn. Sys.* 7.1 (2008), pp. 186–206.

[162] F. Haudin, R. G. Elías, R. G. Rojas, U. Bortolozzo, M. G. Clerc, and S. Residori. "Driven front propagation in 1D spatially periodic media". In: *Phys. Rev. Lett.* 103.12 (2009), p. 128003.

[163] F. Haudin, R. G. Elías, R. G. Rojas, U. Bortolozzo, M. G. Clerc, and S. Residori. "Front dynamics and pinning-depinning phenomenon in spatially periodic media". In: *Phys. Rev. E* 81.5 (2010), p. 056203.

[164] F. Haudin, R. G. Rojas, U. Bortolozzo, S. Residori, and M. G. Clerc. "Homoclinic snaking of localized patterns in a spatially forced system". In: *Phys. Rev. Lett.* 107.26 (2011), p. 264101.

[165] B. Ponedel and E. Knobloch. "Forced Snaking: Localized structures in the real Ginzburg-Landau equation with spatially periodic parametric forcing". In: *Eur. Phys. J. Spec. Top.* (Submitted).

[166] D. M. Ambrose and J. Wilkening. "Computation of time-periodic solutions of the Benjamin-Ono equation". In: *J. Nonlinear Sci.* 20.3 (2010), pp. 277–308.

[167] M. O. Williams, J. Wilkening, E. Shlizerman, and J. N. Kutz. "Continuation of periodic solutions in the waveguide array mode-locked laser". In: *Physica D* 240.22 (2011), pp. 1791–1804.

[168] J. Knobloch, M. Vielitz, and T. Wagenknecht. "Non-reversible perturbations of homoclinic snaking scenarios". In: *Nonlinearity* 25.12 (2012), p. 3469.

[169] U. Thiele, A. J. Archer, M. J. Robbins, H. Gomez, and E. Knobloch. "Localized states in the conserved Swift-Hohenberg equation with cubic nonlinearity". In: *Phys. Rev. E* 87.4 (2013), p. 042915.

[170] E. Knobloch. "Localized structures and front propagation in systems with a conservation law". In: *IMA J. Appl. Math.* (Submitted).

[171] H. Luo, C. Wang, L. Ren, Q. Gao, C. Pan, and I. R. Epstein. "Light-Modulated Intermittent Wave Groups in a Diffusively Fed Reactive Gel". In: *Angewandte Chemie* 128 (2016), pp. 4988–4991.

[172] Y.-P. Ma, J. Burke, and E. Knobloch. "Defect-mediated snaking: A new growth mechanism for localized structures". In: *Physica D* 239.19 (2010), pp. 1867–1883.

[173] Y.-P. Ma and E. Knobloch. "Two-dimensional localized structures in harmonically forced oscillatory systems". In: *arXiv:1508.03521* (2015).

[174] J. H. P. Dawes and S. Lilley. "Localized states in a model of pattern formation in a vertically vibrated layer". In: *SIAM J. Appl. Dyn. Sys.* 9.1 (2010), pp. 238–260.

[175] B. Pradenas, M. G. Clerc, C. Falcón, P. Gandhi, and E. Knobloch. *Slanted homoclinic snaking in a Faraday experiment*. Manuscript in preperation. 2016.

[176] J. M. Conway and H. Riecke. "Multiresonant forcing of the complex Ginzburg–Landau equation: Pattern selection". In: *Phys. Rev. E* 76.5 (2007), p. 057202.

[177] K. Engelborghs, T. Luzyanina, and D. Roose. "Numerical bifurcation analysis of delay differential equations using DDE-BIFTOOL". In: *ACM Trans. Math. Softw.* 28.1 (2002), pp. 1–21.

[178] R. H. Clewley, W. E. Sherwood, M. D. LaMar, and J. M. Guckenheimer. "PyDSTool, a software environment for dynamical systems modeling". In: *URL http://pydstool.sourceforge.net* (2007).

[179] H. Uecker, D. Wetzel, and J. D. M. Rademacher. "pde2path - A Matlab package for continuation and bifurcation in 2D elliptic systems". In: *Numer. Math. Theory, Me.* 7.01 (2014), pp. 58–106.

[180] E. Doedel, H. B. Keller, and J. P. Kernevez. "Numerical analysis and control of bifurcation problems (I): Bifurcation in finite dimensions". In: *Int. J. Bifurcat. Chaos* 1.03 (1991), pp. 493–520.

[181] E. Doedel, H. B. Keller, and J. P. Kernevez. "Numerical analysis and control of bifurcation problems (II): Bifurcation in infinite dimensions". In: *Int. J. Bifurcat. Chaos* 1.04 (1991), pp. 745–772.

[182] C. De Boor and B. Swartz. "Collocation at Gaussian points". In: *SIAM J. Numer. Anal.* 10.4 (1973), pp. 582–606.

[183] R. D. Russell and J. Christiansen. "Adaptive mesh selection strategies for solving boundary value problems". In: *SIAM J. Numer. Anal.* 15.1 (1978), pp. 59–80.

[184] H. B. Keller. "Numerical solution of bifurcation and nonlinear eigenvalue problems". In: *Applications of Bifurcation Theory* 1.38 (1977), pp. 359–384.

[185] A.-K. Kassam and L. N. Trefethen. "Fourth-order time-stepping for stiff PDEs". In: *SIAM J. Sci. Comput.* 26.4 (2005), pp. 1214–1233.